



CRAS 2018 Workshop Program



Queen Mary
University of London

Imperial College
London



Program Overview

Schedule		Monday, 10 September
8:55	9:00	Welcome from Organisers
9:00	10:00	Session 1: Novel Robotics Hardware for Medical Applications
10:00	10:45	Keynote talk by Prof Alberto Arezzo
10:45	11:00	Morning coffee break
11:00	12:15	Session 2: Tracking and Guidance for Surgical Systems
12:15	13:00	Keynote talk by Prof Pietro Valdastri
13:00	14:00	Lunch
14:00	15:15	Poster Teaser Session 1
15:15	15:45	Afternoon coffee break
15:30	17:00	Exhibition and poster session
18:30	23:00	Social Dinner at HMS Belfast
		Tuesday, 10 September
9:00	9:45	Keynote by Prof Jessica Burgner-Kahrs
9:45	10:30	Session 3: Image processing, modelling and learning
10:30	10:45	Morning coffee break
10:45	12:15	Session 4: Real-time sensing and haptic feedback
12:15	13:00	Keynote by Prof Sanja Dogramadzi
13:00	14:00	Lunch
14:00	14:10	CRAS 2019 announcement
14:10	15:30	Poster Teaser Session 2
15:30	17:00	Exhibition and poster session
16:30	17:00	Wine reception

Monday, 10th of September

8:00 - 17:00 Registration

8:55 - 9:00 Welcome from Organisers by Prof Kaspar Althoefer, The Centre for Advanced Robotics @ Queen Mary, Queen Mary University of London

9:00 - 10:00 Session 1: Novel Robotics Hardware for Medical Applications

Chairs: Emmanuel Vander Poorten and Brian Davies

From a Disposable Ureteroscope to an Active Lightweight Fetoscope

9:00 - 09:15 Julie Legrand, Mouloud Ourak, Allan Javaux, Caspar Gruijthuisen, Tom Vercauteren, Jan Deprest, Sebastien Ourselin and Emmanuel Vander Poorten

Deployable, Disposable, Self-Propelling and Variable Stiffness Devices for Minimally Invasive Surgery

09:15 - 09:30 Mark Runciman, Ara Darzi and George Mylonas

An Ex-vivo Demonstration of a Robotic Laser Tissue Soldering System

09:30 - 09:45 Amit Milstein, Svetlana Basov, Erez Sulimani, Max Platkov, Eli Peretz, Uri Netz, Abraham Katzir and Ilana Nisky

Novel Design of Two Degrees of Freedom Laparoscopic Liver Retractor Based on Local Magnetic Actuators

09:45 - 10:00 Nicola Fornarelli, Manish Chauhan, Arianna Menciassi and Pietro Valdastri

10:00 - 10:45 Keynote talk by Alberto Arezzo (Chair: Arianna Menciassi)

Department of Surgical Sciences, University of Torino, Italy

10:45 - 11:00 Morning coffee break

11:00 - 12:15 Session 2: Tracking and Guidance for Surgical Systems

Chairs: Ferdinando Rodriguez Y Baena and Elena De Momi

Real-time electromagnetic tracking of orthopaedic pins for robot-assisted fracture surgery

11:00 - 11:15 Beatriz Martins, Giulio Dagnino and Sanja Dogramadzi

Towards Accurate Drilling Guidance for Orthopaedic Surgery

11:15 - 11:30 Ioannis Georgilas, Grey Giddins and Jonathan du Bois

- 11:30 - 11:45 *Steerable needle DBS path planning safeguards deep nuclei and white matter tracts*
Alberto Favaro, Valentina Pieri, Alice Segato, Andrea Falini, Elena De Momi and Antonella Castellano
- 11:45 - 12:00 *A Virtual Fixture Adaptation Strategy for MIRS Dissection Tasks*
Mario Selvaggio, Giuseppe Andrea Fontanelli, Fanny Ficuciello, Luigi Villani and Bruno Siciliano
- 12:00 - 12:15 *Stereoscopic Near-Infrared Fluorescence Imaging: A Proof of Concept towards Real-Time Depth Perception in Surgical Robotics*
Maxwell Munford, Ferdinando Rogriguez Y Baena and Stuart Bowyer
- 12:15 - 13:00 Keynote talk by Prof. Pietro Valdastri (Chair: Helge Wurdemann)
Lifesaving Capsule Robots

13:00 - 14:00

Lunch

14:00 - 15:15

Poster teaser session 1

Chair: Kaspar Althoefer

- 14:00 - 14:05 *Development of an Innovative Sleeve-Based Robotic Catheter Driver*
Poster 1.1 Omar Al-Ahmad, Moloud Ourak, Simon Jeanquart, Nick Deserranno, Felix Bernhard, Yohannes Kassahun, Bingbin Yu and Emmanuel Vander Poorten
- 14:05 - 14:10 *Fulcrum Effect on Stiffness Virtual Fixtures at Distal Tip*
Poster 1.2 Caspar Gruijthuijsen, Gianni Borghesan and Emmanuel Vander Poorten
- 14:10 - 14:15 *An Endoscopic Laser Scanner for Soft Tissue Microsurgery*
Poster 1.3 Alperen Acemoglu and Leonardo Mattos
- 14:15 - 14:20 *A SIMPLE surgical robot concept: a bimanual single-port system with intrinsic force-sensing capability*
Poster 1.4 Timo Oude Vrielink, Ara Darzi and George Mylonas
- 14:20 - 14:25 *Motion-based skill analysis in a fetoscopic spina-bifida repair training model*
Poster 1.5 Allan Javaux, Luc Joyeux, Jan Deprest, Kathleen Denis and Emmanuel Vander Poorten
- 14:25 - 14:30 *Towards actuating soft robotic manipulators for MIS using stiffness-controllable low melting point alloy*
Poster 1.6 Samuel Suchal, Alberto Arezzo, Mark Miodownik, Sarah Spurgeon and Helge Wurdemann
- 14:30 - 14:35 *Educational Workshop for Image-Guided Therapy and Medical Robotics*
Poster 1.7 John O'Neill, Sebastien Ourselin, Christos Bergeles and Tom Vercauteren

14:35 - 14:40

Poster 1.8

FCNN-based segmentation of kidney vessels - Towards constraints definition for safe robot-assisted nephrectomy

Sara Moccia, Simone Foti, Silvia Maddalena Rossi, Ilaria Rota, Matteo Scotti, Simone Toffoli, Leonardo Mattos, Elena De Momi and Emanuele Frontoni

14:40 - 14:45

Poster 1.9

Advanced User Interface for Augmented Information Display on Endoscopic Surgical Images

Simone Foti, Andrea Mariani, Thibaud Chupin, Diego Dall'Alba, Zhuoqi Cheng, Leonardo Mattos, Darwin Caldwell, Paolo Fiorini, Elena De Momi and Giancarlo Ferrigno

14:45 - 14:50

Poster 1.10

ORPlanner - Towards Enhanced Operating Room Planning Tools

Mark Stacey, Sam Muscroft, Andre Chow, Jean Nehme and Danail Stoyanov

14:50 - 14:55

Poster 1.11

Haptics-enabled palpation for intraoperative tumour detection using a cable-driven parallel manipulator

Arianna Saracino, Timo Joric Corman Oude-Vrielink, Edoardo Sinibaldi, Arianna Menciassi and George Mylonas

14:55 - 15:00

Poster 1.12

Force Sensing for Measuring Vaginal Wall Interaction Forces during Laparoscopic Sacrocolpopexy

Jef De Smet, Jan Deprest, André Thys and Emmanuel Vander Poorten
Design and Evaluation of an Intraoperative Safety Constraints Definition and Enforcement System for Robot-Assisted Minimally Invasive Surgery
Luca Vantadori, Andrea Mariani, Thibaud Chupin, Elena De Momi and Giancarlo Ferrigno

15:05 - 15:10

Poster 1.14

Design of an ergonomic upper gastro-intestinal endoscopic device for gastric cancer diagnosis

Manish Chauhan, James Chandler, Pietro Valdastrì and Keith Obstein

15:10 - 15:15

Poster 1.15

Human-Robot Shared Control for Split-Site Interaction and Disabled Assistance

Alaa Al-Ibadi, Samia Nefti-Meziani and Steve Davis

15:15 - 15:45

Afternoon coffee break

15:30 - 17:00

Exhibition and poster session

18:30 - 23:00

Social dinner **at HMS Belfast**

Tuesday, 11th of September

9:00 - 9:45 Keynote talk by Prof Jessica Burgner-Kahrs

Keyhole Surgery with Continuum Robots

9:45 - 10:30 Session 3

Image processing, modelling and learning

9:45 - 10:00 *Patient specific FE modeling for deformable breast registration*

Eleonora Tagliabue, Bogdan Maris, Andrea Roberti, Anton Nikolaev, Leon De Jong and Paolo Fiorini

10:00 - 10:15 *Vision-based pose estimation of a continuum robot using optical flow and kinematic robot model*

Valentin Bordoux, Benoît Rosa and Florent Nageotte

10:15 - 10:30 *Track-Guided Ultrasound Scanning for Tumour Margins Outlining in Robot-Assisted Partial Nephrectomy*

Agostino Stilli, Manios Dimitrakakis, Maxine Tran and Danail Stoyanov

10:30 - 10:45 Morning coffee break

10:45 - 12:15 Session 4: Real-time sensing and haptic feedback

10:45 - 11:00 *Contact Force Estimation for Minimally Invasive Robot-assisted Laser Osteotomy in the Human Knee*

Manuela Eugster, Esther Isabel Zoller, Lorin Fasel, Philippe C. Cattin, Niklaus Felix Friederich, Azhar Zam and Georg Rauter

11:00 - 11:15 *Design and integration of electrical bio-impedance sensing in surgical robotic tools for tissue identification*

Zhuoqi Cheng, Diego Dall'Alba, Simone Foti, Andrea Mariani, Thibaud Chupin, Darwin Caldwell, Paolo Fiorini, Elena De Momi, Giancarlo Ferrigno and Leonardo Mattos

11:15 - 11:30 *Haptic Feedback Helps Surgeons with Different Level of Expertise on Bimanual Laser Surgery*

Sergio Portoles Diez, Mizra Awais Ahmad, Gianni Borghesan, Christel Meuleman and Emmanuel Vander Poorten

11:30 - 11:45 *Soft and Inflatable Hand Rehabilitation Device with Haptic Perception, Evaluation of Applied Forces*

Jelizaveta Konstantinova, Caroline Yan Zheng and Kaspar Althoefer

- 11:45 - 12:00 *Contact Force Measurement for Medical Ultrasound Imaging*
Ata Otaran, Halime Gulle Gulle, Stuart Miller and Ildar Farkhatdinov
- 12:00 - 12:15 *Development of a non-contact device for detecting small animal breathing in dedicated whole-body imaging instruments based on fibre optics and CCD camera*
Dalia Osman, Gilbert Fruhwirth, Rhode Kawal and Yohan Noh

- 12:15 - 13:00 Keynote talk by Prof Sanja Dogramadzi (Chair: Kathleen Denis)
Surgeon-centred RAMIS design

13:00 - 14:00

Lunch

- 14:00 - 14:10 CRAS 2019 announcement by Dr Leonardo De Mattos, Italian Institute of Technology

14:10 - 15:30

Poster teaser session 2

Chair: Jelizaveta Konstantinova

- 14:10 - 14:15 *A Long Short-Term Memory Network for Vessel Detection with a Steerable Needle*
Poster 2.1
Vani Virdiyawan and Ferdinando Rodriguez Y Baena
- 14:15 - 14:20 *Gesture Classification in Robotic Surgery using Recurrent Neural Networks with Kinematic Information*
Poster 2.2
Evangelos Mazomenos, Dave Watson, Rado Kotorov and Danail Stoyanov
- 14:20 - 14:25 *Incision Port Displacement Modelling Verification in Minimally Invasive Surgical Robots*
Poster 2.3
Iman Delshad, Efi Psomopoulou, Sajeeva Abeywardena, Antonia Tzemanaki and Sanja Dogramadzi
- 14:25 - 14:30 *Monocular 3D Reconstruction of the Colon Using CNNs Trained on Synthetic Data*
Poster 2.4
Anita Rau, Francois Chadebecq, Paul Riordan and Danail Stoyanov
- 14:30 - 14:35 *Power Augmentation and Rehabilitation Exoskeleton Robot based on Variable Stiffness Soft Actuators*
Poster 2.5
Hassanin Al-Fahaam, Samia Nefti-Meziani and Steve Davis
- 14:35 - 14:40 *Toward effective three-dimensional control of an epicardial wire robot*
Poster 2.6
Sumit Dan, Yiyi Ren, Nicole A. Bustos, Nathan A. Wood, Michael J. Passineau, Robert J. Moraca and Cameron N. Riviere
- 14:40 - 14:45 *Soft Wearable Glove for Tele-Rehabilitation Therapy of Clenched Hand/Fingers Patients*
Poster 2.7
Taqi Abrar, Fabrizio Putzu and Kaspar Althoefer

- 14:45 - 14:50 *Using current measurement to estimate palpation and grasping forces in robot-assisted minimally invasive surgery*
Poster 2.8
Antonia Tzemanaki, Sajeeva Abeywardena, Efi Psomopoulou, Chris Melhuish and Sanja Dogramadzi
- 14:50 - 14:55 *Free-view Gaze Controlled Image Navigation: One application of a Perceptually-enabled Smart Operating Room*
Poster 2.9
Alexandros Kogkas, Ahmed Ezzat, Ara Darzi and George Mylonas
- 14:55 - 15:00 *Augmented Reality Based External Fixation Training*
Poster 2.10
Paul Riordan, Sam Muscroft, Mark Stacey, Anthony Inwood, Lucy Greenlee, Ruth Connaghan, Sam Oussedik and Danail Stoyanov.
- 15:00 - 15:05 *Design, Fabrication and Testing of an Inflatable Variable Stiffness Retractor Prototype for Minimally Invasive Colorectal Surgery*
Poster 2.11
Stephen Agha, Aly Abidali, Kaspar Althoefer, Mohamed A. Thaha and Hasan Shaheed.
- 15:05 - 15:10 *Development of a Soft Inflatable Structure with Variable Stiffness for Hand Rehabilitation*
Poster 2.12
Fabrizio Putzu, Taqi Abrar and Kaspar Althoefer
- 15:15 - 15:20 *Medical Virtual Reality Palpation Training using Ultrasound Based Haptics and Image Processing*
Poster 2.13
L. Puertolas Balint and Kaspar Althoefer
- 15:20 - 15:25 *Fetoscopic Scene Orientation Estimation From a Single 2D Image Using Convolutional Neural Networks*
Poster 2.14
Mirza Awais Ahmad, Caspar Gruijthuijsen, Jan Deprest and Emmanuel Vander Poorten
- 15:25 - 15:30 *Fuzzy Logic Control of a Tele-Robotic Manipulator Assistant for Laparoscopic Surgery*
Poster 2.15
Ololade O. Obadina, Mohamed A. Thaha, Kaspar Althoefer and M. Hasan Shaheed
- 15:30 - 17:00 Exhibition and poster session

16:30 - 17:30 Wine reception

Keynote speakers



Prof. Alberto Arezzo

Department of Surgical Science,
University of Torino, Turin, Italy

Prof. Alberto Arezzo is Associate Professor at the University of Torino, Italy. Since the beginning of his career he is serving both as conventional endoscopist and endoscopic surgeon. Being member of the Technology Committee of the European Association for Endoscopic Surgery (EAES) and of the Board of the Society for Medical Innovation and Technology (SMIT) and of the Italian Society for Digestive Endoscopy (SIED), Prof. Arezzo is also the Former scientist at the Section for Minimally Invasive Surgery at Eberhart Karls University of Tuebingen, Germany, consultant in the field of Endoscopic Surgery and Flexible Endoscopy of Ethicon Endosurgery (Johnson & Johnson Medical), Boston Scientific, Microvasive Endoscopy, Karl Storz Endoskope GmbH and Partner of different FP5/FP6/FP7 projects CLEANTEST, VECTOR and STIFF- FLOP.

He has been Coordinator of several international multicentre studies and projects. Prof. Arezzo is the Founder of the start-up company RED, Robot for Endoscopic Dissection. Prof. Arezzo is Teacher of Emergency Surgery at the VI year of the School of Medicine and teacher or tutor of courses at the School of Surgery, such as Scientific English, Surgical Anatomy and Digestive Surgery. He is the Vice-Coordinator of the PhD Course in Technology Applied to Surgical Sciences and Faculty and Tutor of the II Level University Master course in Advanced Laparoscopy for MDs. He is Coordinator, Faculty and Tutor of the II Level University Master course in Operative Digestive Endoscopy for MDs.



Prof Pietro Valdastri
University of Leeds

Lifesaving Capsule Robots

The talk will focus on *Medical Capsule Robots*. Capsule robots are cm-size devices that leverage extreme miniaturization to access and operate in environments that are out of reach for larger robots. In medicine, capsule robots can be designed to be swallowed like a pill and to diagnose and treat mortal diseases, such as cancer. The talk will focus on capsule robots for the inspection of the digestive tract with a focus on autonomy and frugal innovation. During the talk, we will discuss the recent enabling technologies that are being developed at the University of Leeds to transform medical robotics. These technologies include magnetic manipulation of capsule robots, water jet propulsion, real-time tracking of capsule position and orientation, and autonomy in robotic endoscopy.

Biography

Prof. Pietro Valdastri is a Royal Society Wolfson Research Merit Award holder, a Senior Member of the Institute of Electrical and Electronics Engineers (IEEE), one of the Editors of the IEEE International Conference on Robotics and Automation, a member of the Technology Committee of the European Association for Endoscopic Surgery (EAES), and an Associate Editor of the Journal of Medical Robotics Research. He co-founded a successful medical start-up (WinMedical, www.winmedical.com), and received several prestigious awards, including the Wolfson Research Merit Award and the Hamlyn Symposium Surgical Robot Challenge Award in 2016, the NSF CAREER Award in 2015, the Sensys 2014 Best Paper Award, the OLYMPUS Best Laparoscopy/Robotic Paper Award 2013, the OLYMPUS ISCAS Best Paper Award 2012, the ASME Design of Medical Devices Conference Best Paper Award 2012, the Hamlyn Symposium on Medical Robotics Best Oral Presentation Award 2011, and the European Association of Endoscopic Surgery Best Technology Presentation Award 2011.



Prof Jessica Burgner-Kahrs

The Centre of Mechatronics of Leibniz Universität Hannover

Keyhole Surgery with Continuum Robots

Continuum robots are composed of flexible, elastic, or soft materials such that complex bending and twisting motions can be achieved. Thanks to their small size and high dexterity, continuum robots have the potential to revolutionise keyhole surgery through small incisions or natural orifices. Physicians can rethink their approach to minimally invasive surgery as surgical sites become accessible on highly tortuous trajectories and unimagined surgical manoeuvres become feasible. The presentation provides an overview of the current state of continuum robotics research for surgical applications. Open research questions and cross-disciplinary challenges are discussed.

Biography

Prof. Jessica Burgner-Kahrs is head of the Laboratory for Continuum Robotics at the Center of Mechatronics of Leibniz Universität Hannover since November 2015. The lab originates from her Emmy Noether Research Group CROSS which is funded by the German Research Foundation since 2013.

Jessica Burgner-Kahrs graduated from Universität Karlsruhe (TH), Germany in computer science and got her Ph.D. at Karlsruhe Institute of Technology (KIT), Germany. Before she started at Leibniz Universität Hannover in 2013, she was Research Associate at Vanderbilt University, USA for two years.

Her research focus lies on continuum robotics. In 2015 she was awarded with the Heinz Maier-Leibnitz Prize and the Lower Saxony Science Award in the category Young Researcher. She was also nominated Young Researcher of the Year 2015 from academics and ZEIT publishers. The Berlin-Brandenburg Academy of Sciences awarded her the Engineering Science Prize in 2016.



Prof. Sanja Dogramadzi
Bristol Robotics Laboratory

Surgeon-centred RAMIS design

Professor Sanja Dogramadzi is leading Healthcare Robotics group in Bristol Robotics Laboratory. She completed a PhD in medical robotics at University of Newcastle in 2001 and joined University of Leeds in 2002 as a postdoctoral researcher. She got a lectureship post at Bristol Robotics Laboratory (University of the West of England) in 2007 and was promoted to Reader and Professor in 2012 and 2017, respectively. Her research interests include design and control of surgical robots for minimally invasive fracture surgery and robot-assisted MIS, rehabilitation robots, physical assistance robots and safe and ethical human-robot interaction. She has led many research projects funded by UK councils and European Commission and is currently a coordinator and PI of EC H2020 funded SMARTurg project (www.smartsurg-project.eu) and PI for EPSRC funded I-DRESS project (<https://i-dress-project.eu>) and the EC H2020 funded Marie Curie ITN Socrates (www.socrates-project.eu). She was also the technical lead for Innovate UK funded CHIRON project (<https://chiron.org.uk>). She is a member of BSI committee for developing standards for medical and service robots from 2008.

Workshop Dinner – Monday 10th September

The networking dinner will start at 18:30 until 23:00 at HMS Belfast, on Monday 10th September. If you booked a ticket to the workshop dinner on Monday 10th September during the registration process, you will find this detailed on your registration confirmation email.

Please note that guests will be required to make their own way to the venue. The nearest tube station and train station is London Bridge, at around a 5 minute walk to HMS Belfast. Tower Hill tube station is also only a 15 - 20 minute walk away from HMS Belfast.

Venue

HMS Belfast,
The Queen's Walk,
London,
SE1 2JH

Please note; if you did not book a ticket to the workshop dinner during the registration process, then a place will not have been reserved for you.



CRAS 2018 Proceedings



Queen Mary
University of London

Imperial College
London



From a Disposable Ureteroscope to an Active Lightweight Fetoscope

Julie Legrand¹, Mouloud Ourak¹, Allan Javaux¹, Caspar Gruijthuijsen¹, Tom Vercauteren^{2,3}, Jan Deprest³, Sebastien Ourselin² and Emmanuel Vander Poorten¹

¹*Departement of Mechanical Engineering, KULeuven, Leuven Belgium.,*

²*Departement of Imaging and Biomedical Engineering, King's College London, United Kingdom.,*

³*Departement of Development and Regeneration, KULeuven, Leuven, Belgium.*

julie.legrand@kuleuven.be

INTRODUCTION

The twin-to-twin transfusion syndrome (TTTS) is a serious fetal complication occurring in monozygotic twins sharing a single placenta, but separate amniotic sacs. This fetal anomaly, which occurs in 10 to 15% of monochorionic twin pregnancies [1], results from a disproportional blood transfusion from one twin to the other. If left untreated, severe TTTS can lead to a near-100% mortality rate. However, endoscopic laser ablation (ELA) of placental vessels allows a trend reversal and can guarantee the survival of at least one twin in 75 to 80% of the cases [1]. This minimally invasive surgery (MIS) consists in inserting a straight fetoscope equipped with a therapeutic laser fiber in a cannula through the maternal abdominal and uterine wall. The fetoscope is used to visualize the blood vessels on the placenta surface, as the embedded laser allows to coagulate the placental vessels responsible for the blood transfusion [2].

Compared to other forms of surgery, ELA presents important challenges partially caused by the rigid nature of current instruments (rigid and semi-rigid scopes) (Fig.1) and their poor controllability. More specifically, when operating anterior located placentas (Fig.1b), surgeons are forced to approach the targets under obtuse angles, worsening the visualization, limiting the ablation precision and causing to apply large forces at the incision site that may lead to iatrogenic preterm premature rupture of membranes (IPROM) [3]. In order to solve the above-mentioned issues and limitation, this paper proposes a steerable flexible instrument with large laser and vision steering angle range. This single instrument contains all the necessary tools to perform a TTTS procedure, namely a camera, an illumination fiber and a working channel, allowing the insertion of a coagulation laser while keeping similar external diameter dimensions than proposed fetoscopes in the literature. Moreover, this novel fetoscope has been designed to be comfortably single-handed-controlled, which limits the number of surgeons needed for the surgical procedure.

MATERIALS AND METHODS

In order to keep the instrument approval process towards animal and human trials short, an add-on housing and actuation system on a commercially available

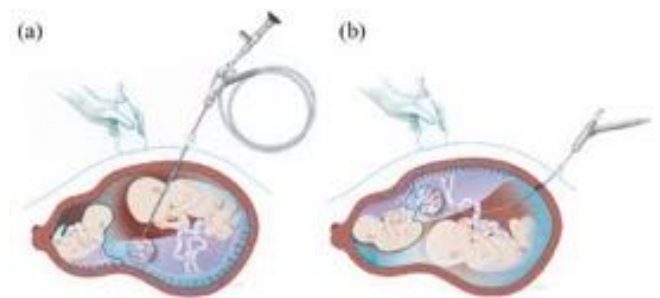


Figure. 1. Possible positions of the placenta in the uterus and corresponding used instrument. a. use of a straight fetoscope for posterior positioning of the placenta. b. use of a curved fetoscope for anterior positioning of the placenta (Courtesy of UZ Leuven).

ureteroscope, the LithoVue (Boston Scientific, Natick, USA), is proposed. This cable-driven flexible ureteroscope has a small external diameter (≤ 3.23 mm), a large working channel (1.2 mm ID) as well as an integrated light source and a chip-on-tip sensor. Moreover, the deflection of its distal flexible tip actuated via a lever at the back of the instrument is large (max 270° in both directions), making the LithoVue an excellent candidate for use in fetal surgery. However, some modifications have been made to the instrument in order to meet the active fetoscope specifications. The cable system present in the LithoVue has been modified, limiting the bending angle to 135° in one direction. A spring has also been foreseen inside the instrument ensuring the return to 0° when no load is applied on the cable. The non-rigid proximal part has been shortened and rigidified by sliding a rigid tube over that part. Finally, a compact and light-weight add-on frame with integrated actuation has been fixed on the LithoVue allowing the distal flexible tip to be precisely single-handed operated in an intuitive way (Fig.2). The used actuation system is a McKibben muscle, which forms a thin and extremely light weight linear actuator. The latter is attached at one end to the LithoVue lever as the other end is attached to the distal part of the handle (Fig.2). A pair of low-profile buttons are embedded in the external housing. The location was chosen such that it would be easy for the operator to manipulate the scope with one hand and at the same time access the buttons to control the distal tip. By pushing one button or the other, the surgeon commands the pressure inside the muscle. As a

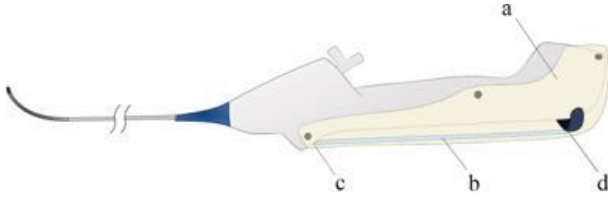


Figure. 2. Adapted LithoVue for fetal surgery. a. external housing. b. McKibben muscle. c. anchor point McKibben muscle-frame. d. anchor point McKibben muscle-LithoVue lever.

result, the position of the lever is adjusted, which through the cable thus controls the bending angle of the distal tip. When actuating the instrument, a large hysteretic effect is observed that is linked to the nonlinear behavior of the McKibben muscle as well as to the friction induced by the cable actuation inside the LithoVue.

In order to keep the setup simple in the following, it is explored in how far an open-loop feed-forward control can be set to “linearize” the behavior and compensates the hysteresis. By doing so, all system nonlinearities can be made to some extent invisible to the surgeon. To this end, the characteristic curve linking the input pressure and the resulting bending has been modeled as the concatenation of two constant functions and two 1st order polynomials.

RESULTS

A first human-in-the-loop experiment was designed using the active LithoVue fetoscope once with the implemented openloop control, and once with no control at all. The user was asked to orient the flexible tip on several specific angles using the buttons in both operation modes. Beginning at rest position ($\alpha = 156^\circ$), the flexible tip was then driven to successively reach $\alpha = 90^\circ$, 135° , 110° and finally 156° . An angle of 180° corresponds to a flexible distal tip perfectly aligned with the rigid shaft. Once a target is reached, the user was asked to maintain this position for a brief period of time. Fig. 3 depicts the results of the experiment. The benefits of the open-loop control are clearly visible. The response is faster when using the implemented control. Also, higher levels of precision are reached. The prototype has also been evaluated by two surgeons with experience in fetal surgery. They were asked to compare two instruments : 1) an original LithoVue of which the proximal part was shortened and made stiffer by adding a rigid shaft and 2) the proposed active LithoVue fetoscope. The surgeons

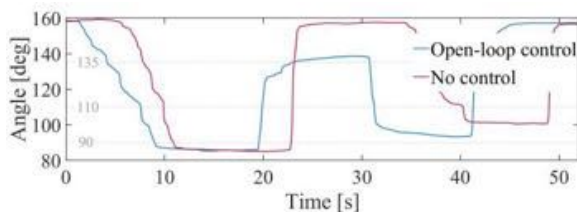


Figure. 3. Human-in-the-loop experiment, comparison of the controllability of the device with and without open-loop control.

were asked to test both instruments in virtual reality, using a validated simulator [4]. Then, they were asked to fill in a questionnaire to evaluate the ergonomics and the ease of manipulation of these instruments. A trend can be observed on Fig.4, that the new instrument enhances the manipulation comfort and ease of treating TTTS. This tendency shows that even though the instrument control is not fully optimized, the single-handed active button-controlled fetoscope is already preferred for TTTS treatment.

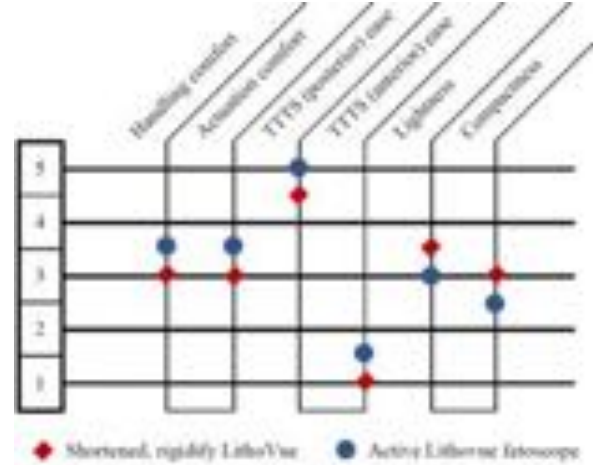


Figure. 4. Mean results of the testing of a shortened, rigidified LithoVue and active LithoVue fetoscope on a virtual TTTS task.

CONCLUSION AND DISCUSSION

An improved flexible fetoscope tailored for TTTS treatment was presented in this paper. This device, being an adaptation of the passive flexible ureterscope LithoVue (Boston Scientific, Natick, USA), has shown a good potential for use in TTTS surgery. Compared to a passive, lever-actuated fetoscope, the active LithoVue fetoscope was evaluated as being more comfortable and allowing an easier accomplishment of typical TTTS treatment tasks.

REFERENCES

- [1] C. S. Muratore et al., “Survival after laser surgery for twin-to-twin transfusion syndrome: when are they out of the woods?” *Journal of Pediatric Surgery*, vol. 44, no. 1, pp. 66-69; discussion 70, Jan. 2009.
- [2] “Intrauterine laser ablation of placental vessels for the treatment of twin-to-twin transfusion syndrome [Guidance and guidelines] NICE.” [Online]. Available: <https://www.nice.org.uk/guidance/ipg198>
- [3] E. E. Maradny, N. Kanayama, A. Halim, K. Maehara, and T. Terao, “Stretching of fetal membranes increases the concentration of interleukin-8 and collagenase activity,” *American Journal of Obstetrics and Gynecology*, vol. 174, no. 3, pp. 843-849, Mar. 1996.
- [4] A. Javaux et al., “A mixed-reality surgical trainer with comprehensive sensing for fetal laser minimally invasive surgery,” *CARS* (accepted), 2018.

Deployable, Disposable, Self-Propelling and Variable Stiffness Devices for Minimally Invasive Surgery

M. Runciman, A. Darzi, G. P. Mylonas

hARMS Lab, Department of Surgery and Cancer, Imperial College London

m.runciman@imperial.ac.uk

INTRODUCTION

Current minimally invasive surgery (MIS) procedures rely heavily on rigid devices that are still difficult to use and can therefore cause undesirable damage and patient pain. In colonoscopy, for example, the cecum is difficult to reach in as many as 10% - 20% of cases [1] and deformation of the colon by the stiff endoscope causes patient discomfort [2]. Furthermore, rigid devices cannot easily deform or conform to their environment. In contrast, soft robotic devices made of compliant materials can change their shape to fit their surroundings and avoid exerting large forces. Current approaches to soft robotics in MIS are typically pneumatically driven continuum style devices made from fibre reinforced moulded elastomer. Limitations of these approaches include limited space for channels to accommodate diagnostic or therapeutic instruments, the need to position the devices manually, limited force exertion, controllability and sensor integration. To address some of these problems we have produced customisable, pneumatically actuated soft robotic devices capable of large volume and workspace change, stiffness variation and self-propulsion. These devices are manufactured from readily available plastic sheet with only one preparatory step, various automated laser welding steps depending on the design, and up to two assembly steps. A soft, deployable, peristaltic crawling robot and a deployable, variable stiffness structure are manufactured as exemplars of the concept.

MATERIALS AND METHODS

A laser welding system capable of rapid, highly adaptable manufacture was developed in order to make patient-specific devices feasible economically and in terms of manufacture time. As shown in Figure 1, a robotic arm (Universal Robots, UR5, Denmark) guides a collimated laser beam of wavelength 940 nm that is focused with a beam diameter of 0.8 mm at the interface of two thermoplastic film sheets, which are placed on a vacuum table to ensure good contact between the plastic film layers while the welding process is carried out. These sheets are made from a polyethylene (PE), polyethylene terephthalate (PET) triple laminate and an infrared absorbing dye is applied evenly at their interface, which locally heats up upon exposure to the laser beam, thereby welding the sheets together. The welding parameters laser power, welding speed and focus of the beam were adjusted to levels that produced smooth, unbroken seals such that airtight chambers are formed.

The 2D weld patterns can be rapidly designed and adapted using CAD software and this, together with the rapid and precise manufacturing method, enables

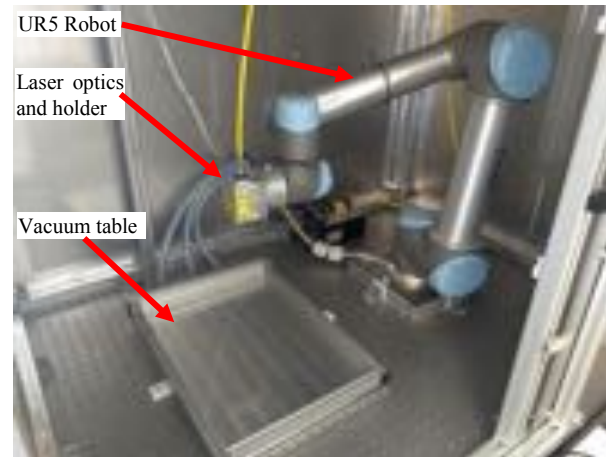


Figure 1: Robotically guided laser welding system.

customisable designs. The welding steps typically take less than 5 minutes to complete, depending on the design. When the welding process has been completed, the next step before connecting the air supply to the pneumatic chambers is to cut the excess plastic sheet from around the welded design or around hinges, allowing them to bend. Then, the 2D welded plastic sheets can be manipulated into a 3D shape, as appropriate for their application. In the examples used here, the devices are rolled into cylinders and a simple adhesive applied to join their edges. The pneumatic supply is connected and the soft robotic devices are ready to use. By welding multiple chambers into a single layer and also welding multiple layers, each possibly containing multiple chambers, devices capable of deployment, stiffness variation and self-propulsion can be made.

RESULTS

Peristaltic Robot

A soft, peristaltic crawling robot for applications in the GI tract was manufactured in a single welding step and with only two assembly steps, cutting and adhesion, taking less than an hour to produce from start to finish. The sides that were joined to form a cylinder were the two sides highlighted in red in Figure 2A overleaf. By sequentially pressurising each chamber, locomotion is achieved. Anchoring is achieved when either of the rings at the head and tail is pressurised, causing radial expansion and increasing friction. Simultaneously, the device's body is contracted by pneumatic hinges or extended by pneumatic beams, depending on which chamber is pressurised. Figure 2E and 2F, show a difference in length of around 1 cm between the extended and contracted states when the respective chambers were pressurised at 1 bar. Ten of these two chambered

inchworm-inspired robots were manufactured, three of which had minor faults. The average burst pressures of each chamber were 1.82 bar and 2.53 bar respectively. The method is repeatable and both the pressure capacity and reliability can be improved by simple measures.

Variable Stiffness Structure

A deployable structure was manufactured whose stiffness can be varied by changing the pressure in auxiliary pneumatic chambers positioned at each joint, which can be seen in Figure 3A along the inside corner of the hollow rectangular structure. Three automated welding steps were used to produce the multiple layers and multiple chambers of this device, taking under an hour to manufacture from start to finish. Firstly, a single chamber is welded that will produce the basic cuboid structure is welded, then, a single chamber with four beams that will fit into each of the corners is separately welded. Lastly, the two designs are aligned and welded together to permanently join them. As previously, the welded 2D sheet was formed into a cylinder by joining the edges, shown in red in Figure 3A. Pressurising the chambers at the corners has the effect of increasing the shear stiffness and can be controlled independently from the main structure itself. A pressure of 1 bar was used as the operating pressure for all chambers in this case, although variable stiffness structures and robots manufactured in this way can withstand higher pressures.

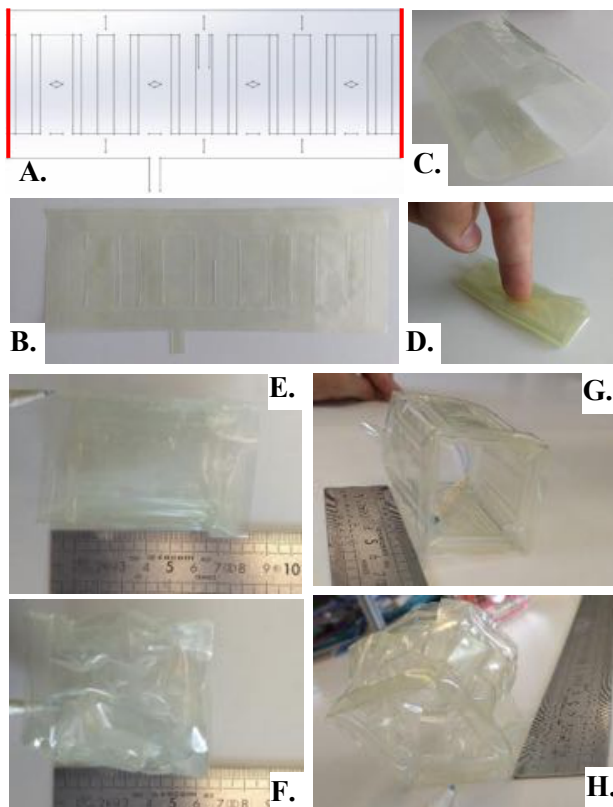


Figure 2: A) Weld pattern for soft inchworm robot, where the welded plastic is rolled into a cylinder and joined at the red lines. B) Plastic sheets welded and cut. C) Welded sheets in cylindrical configuration. D) Small packing size of the soft robot, showing deployability. E) Peristaltic crawler in extended state. F) In contracted state. G) Angled view in extended state. H) Angled view in contracted state.

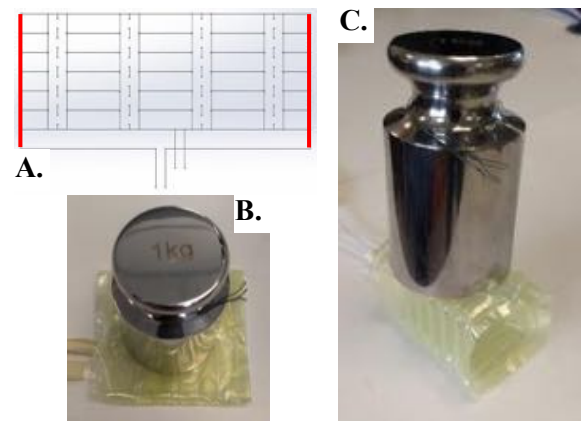


Figure 3: A) Weld pattern for variable stiffness structure where the welded plastic is rolled into a cylinder and joined at the red lines B) Uninflated robot deforming under the 1 kg load. C) The pressurised structure supporting a load of 1 kg.

The approximately 37.5 x 37.5 x 70 mm hollow rectangle structure can easily support a 1 kg load when pressurised, as can be seen in Figure 3C.

CONCLUSION AND DISCUSSION

A peristaltic mechanism and a variable stiffness structure were manufactured that may enable automated exploration of the GI tract and support of a surgical platform in MIS procedures. Self-propelling devices would help to increase colonoscopy completion rates, to reduce procedure times and patient pain. Deployable variable stiffness structures may enable higher force exertion of surgical platforms integrated within them. There are improvements to be made and functionalities to be added to these robotic devices, for example an anchoring mechanism aimed at producing as little stretching of the colon as possible. The capability to weld 3D as well as 2D patterns is also being investigated. The laser welding manufacturing method is particularly useful because it is repeatable and little time and very few steps are needed to produce fully functional soft robotic devices. To the authors' knowledge, this method has not been used before to make soft robotic devices for MIS applications and the economic, rapid and highly adaptable manufacturing method will enable manufacture of disposable patient specific devices. Manufacturing small devices with features down to 1 mm is also possible, which other techniques have difficulty with. Ongoing work focuses on using this manufacturing methodology to integrate diagnostic, therapeutic and sensing equipment into this type of soft robotic device.

MR's PhD is supported by the NIHR Imperial Biomedical Research Centre (BRC).

REFERENCES

- [1] T. N. Witte and R. Enns, "The difficult colonoscopy," *Can. J. Gastroenterol.*, vol. 21, no. 8, pp. 487–490, 2007.
- [2] S. G. Shah, B. P. Saunders, J. C. Brooker, and C. B. Williams, "Magnetic imaging of colonoscopy: An audit of looping, accuracy and ancillary maneuvers," *Gastrointest. Endosc.*, vol. 52, no. 1, pp. 1–8, 2000.

An Ex-vivo Demonstration of a Robotic Laser Tissue Soldering System

Amit Milstein¹, Svetlana Basov³, Erez Sulimani¹, Max Platkov², Eli Peretz¹, Uri Netz^{4,5}, Abraham Katzir⁶, Ilana Nisky¹

¹Department of Biomedical Engineering, Ben-Gurion University of the Negev, ²Nuclear Research Center Negev, ³Department of Biomedical Engineering, Tel-Aviv University, ⁴Soroka University Medical Center, ⁵Faculty of Health Sciences, Ben-Gurion University of the Negev, ⁶School of Physics and Astronomy, Tel-Aviv University
nisky@bgu.ac.il

INTRODUCTION

One of the mundane yet challenging tasks in any, and especially minimally invasive surgery, is the suturing of incisions [1]. Laser technology provides a promising alternative to suturing by connecting the tissues with heat formed by a laser beam. In laser tissue soldering (LTS), the approximated edges of an incision are covered by a biological solder (e.g. albumin, fibrin), and a spot on the incision is heated by a laser beam to a temperature (T) for a time (t). The heated biological solder biochemically links to the surrounding tissue and creates a clot, thereby sealing the incision. The beam is then moved to a neighboring spot and the heating resumes until the full length of the incision is heated. Different variations of LTS techniques have been developed, but none have achieved wide clinical use.

Most of the prior studies did not control the temperature during the laser soldering act [2]. In recent experiments, we utilized a two-fiber hand-piece, one for delivering laser light to heat a spot on the tissue and one for measuring the temperature of the target spot [3]. A feedback-loop allowed for continuously adjusting the laser intensity to obtain a constant T. These experiments demonstrated that both under-heating and over-heating of the incision resulted in a weak bond. Over-heating additionally resulted in thermal damage and scarring. Using these experiments, we have made considerable advances in deciphering the optimal dose (T and t) to obtain the strongest bonding without thermal damage. Successful *ex-vivo* and *in-vivo* tissue soldering of incisions in skin, bowel, dura and thin corneal tissues in pig models have yielded record-high bond strength [3]. Successful incision closure in human abdominal skin, following laparoscopic cholecystectomy also demonstrated strong bonding and negligible scarring [4]. All these LTS experiments were performed manually: the surgeon held the hand-piece so that the distal tip of the fiber was fixed at an approximate height H above the incision. Heating the incisions was accomplished through setting T and t to optimal values and manually moving the tip of the fiber along the incision. One of the challenges for the surgeon using this technique was maintaining consistent tip-sample height, heated-spot-separation and tip-dwell time on a heated spot. As a result, variations were registered, resulting in less-than-uniform bonding.

Currently, many surgical interventions are performed with the assistance of robotic systems. In robot-assisted

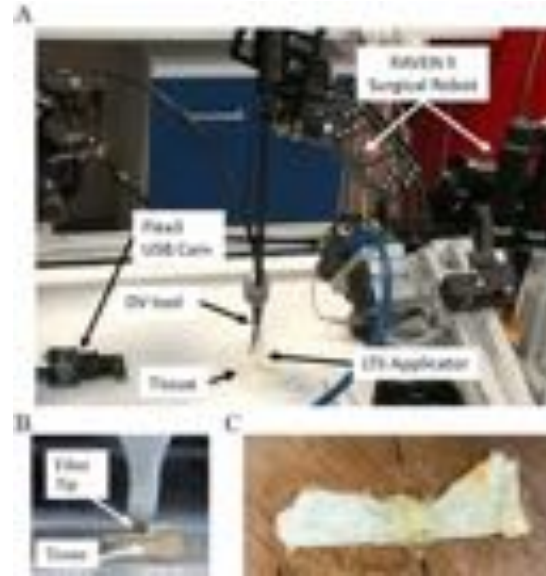


Fig. 1. Experimental system. (A) The RAVEN II Surgical Robot connected to the LTS applicator and the experimental workspace. (B) The LTS applicator connected to the RAMIS tool. (C) The resulting soldered specimen.

minimally invasive surgery (RAMIS), suturing and incision-closure is even more complicated, because in state-of-the-art systems, the surgeons currently do not receive touch feedback, leading to undesirable tearing of tissues and sutures. LTS, unlike suturing, does not require complex dexterous manipulation and it does not require a contact with the tissue. Therefore, LTS can improve RAMIS by improving the quality of incisions closure and reducing their completion time.

We present a novel Robotic LTS (RLTS) system that integrates LTS with an existing RAMIS platform (Fig. 1). Such automated RLTS holds the potential to result in reproducible bond-strength, avoid tissue damage, and reduce post-operative complications. In this work, as a proof of feasibility of such a system, we present a preliminary demonstration of RLTS soldering of incisions in mouse skin and a mechanical testing of the strength of the resulting bonded tissue.

MATERIALS AND METHODS

Hardware and Software

Our RLTS system is divided into three subsystems: the surgeon's console, the surgical robot, and the LTS unit.

We used the Raven II (Applied Dexterity) surgical robot (Fig. 1A)[5]. The arm of the Raven II is a cable-driven manipulator with seven degrees-of-freedom. The surgeon's operating console is based on a haptic manipulator, connected to a PC. A Da Vinci Tool was attached to the Raven II arm with a tool adapter, and the LTS applicator was attached to the Da Vinci Tool, as presented (Fig 1A). The LTS applicator, (identical to the model previously used in our manual experiments), was mounted on the robot arm (Fig. 1B).

Control of the surgical robot by the surgeon can be achieved in three different modes via a custom-built graphic user interface: manual control, keyboard control, and automatic control. By using the haptic manipulator, the manual control allows the surgeon to position the robot arm carrying the LTS applicator, to a desired location in the remote scene (SIGMA 7, Force Dimension). The surgeon can then perform fine position and orientation corrections of the applicator by way of keyboard control of the distal fiber-tip. Finally, the automatic control allows the surgeon to program a 3D path (a straight line in the current demonstration), controlling the direction and amplitude of the motion, the increments of each segment of the motion, the total motion time, the time of each increment, and the hold time between increments. In the current demonstration we used manual control to bring the applicator to the general workspace close to the tissue, then keyboard for fine tuning of the beginning of the soldering, and automatic open loop control during the soldering.

Optical Platform. The laser used was a custom made, Fiber-Coupled, Semiconductor Disc Laser (SDL, Fraunhofer Institute, Freiburg, Germany) operating at $\lambda=1900$ nanometers. The laser intensity was controlled to a constant temperature of 60°C with a controller based on feedback from a custom-built infrared thermometer as described in details in [3-4].

Biological Samples

Tissues. Mouse skin tissues were used in the soldering experiment. They were stored in a freezer at -4°C and defrosted prior to the experiment. Samples of 1 by 5 cm and ~1mm thick were cut to two segments, the segments were approximated, and the samples, in petri-dishes, were placed under the distal tip of the power delivery fiber.

Solder. We used an albumin solder, prepared from bovine albumin solution (Sigma-Aldrich Inc.), in water. The solder was spread along the area planned for soldering.

Protocol

We used two experimental protocols: (1) discrete, where multiple spots were heated one-by-one along the incision line, for a predefined dwell-time of 12 seconds (that was found to be optimal in [3-4]), resulting in about 900 seconds of soldering. (2) continuous, where the heated spot was constantly moved along the incision at a predefined speed of 1.1 mm/sec, resulting in about 700 seconds of soldering. In both conditions, we strived for the applicator to maintain a distance of $H=3$ mm throughout the soldering run, but because the control of

the trajectory was open loop this was not feedback enforced. Immediately after the experiment, we measured the maximal tensile strength of tissue rupture in a tension-machine. To provide a benchmark for the best possible tensile strength we also measured a control sample without an incision.

Bond strength measurement

Bond strength was measured using a universal testing machine (Lloyd LC2.5, Lloyd instruments). A pull-to-break protocol was used to measure the maximum bond strength [N] prior to bond failure.

RESULTS

We repeated the protocol in four trials: two discrete trials, and two continuous trials. A sample of the result of the process is depicted in Fig. 1C. The maximum strength measured in the discrete trials, was 2.1 N, and in the continuous trials was 2.7 N. The maximum strength of a control sample (without incision) was 3.7 N.

CONCLUSION AND FUTURE WORK

We present an integration of a fiber-optic LTS device with a robot-assisted surgery platform. We demonstrated a continuous and a discrete precise open loop movement of the distal tip of the LTS applicator along the incision. The best bonding strength was 73% of the strength of the control sample without incision. Future directions of development of our novel RTLS system will aim at seamless integration of LTS with existing RAMIS platforms to achieve: (1) faster and more precise tissue bonding, (2) satisfactory and uniform bond strength throughout the incision, and (3) fully automated or shared control soldering with a fast learning curve of operating the device. In addition, it is important to test the effect of the novel soldering on tissue pathology and healing.

ACKNOWLEDGEMENTS

Supported by the ABC Robotics Initiative at BGU, by the ISF (grant number 823/15), and Alon Fellowship. AM is supported by a fellowship from the Ministry of Science and Technology, Israel, ES is supported by BGU Kreitman Fellowship. We thank the Fraunhofer Institute for the laser.

REFERENCES.

- [1] M. Severin and K.-U. Bartz-Schmidt, *Penetrating Keratoplasty: Diagnosis and Treatment of Postoperative Complications*. Berlin Heidelberg: Springer-Verlag, 2000.
- [2] C. Matossian, S. Makari, and R. Potvin, "Cataract surgery and methods of wound closure: a review," *Clin. Ophthalmol. Auckl. NZ*, vol. 9, pp. 921–928, May 2015.
- [3] I. Gabay *et al.*, "Closure of incision in cataract surgery in vivo using a temperature controlled laser soldering system based on a 1.9 μ m semiconductor laser," presented at the Optical Fibers and Sensors for Medical Diagnostics and Treatment Applications XVI, 2016, vol. 9702, p. 97020B.
- [4] D. Simhon *et al.*, "Temperature-controlled laser-soldering system and its clinical application for bonding skin incisions," *J. Biomed. Opt.*, vol. 20, no. 12, p. 128002, 2015.
- [5] A. Milstein, T. Ganel, S. Berman, and I. Nisky, "Human-Centered Transparency of Grasping via a Robot-Assisted Minimally Invasive Surgery System," *IEEE Trans. Hum.-Mach. Syst.*, vol. 48, no. 4, p. 349 – 358.

Novel Design of Two Degrees of Freedom Laparoscopic Liver Retractor Based on Local Magnetic Actuators

N. Fornarelli¹, M. Chauhan¹, A. Mencias², P. Valdastrì¹

¹STORM LAB UK, University of Leeds, UK

²BioRobotics Institute, Scuola Superiore Sant'Anna, Pontedera (PI), Italy
n.fornarelli@leeds.ac.uk

INTRODUCTION

In this paper we propose a novel design of a laparoscopic liver retractor based on Local Magnetic Actuation (LMA) [1][3] with 2 degrees of freedom (DoFs). The LMA concept, already introduced in [1], represents a good solution to the typical issues in laparoscopic surgery (i.e. tissue distress, limited view for surgeon, low dexterity tools). By combining the benefits of Minimally Invasive Surgery (MIS) and Single Port Laparoscopy (SPL), an LMA-actuated instrument can be introduced in a limited workspace through a single incision without losing power transmission.

In order to tackle some of the complications related to organ retraction in laparoscopy, the 2-DoFs LMA-based instrument is designed taking into account: motion dexterity in the surgical workspace, materials and dimensions of either inner or outer environment. Compared to LapR-LMA [1], the retractor we propose can lift the liver by means of a flexible End-Effector (EE) which adapts to the shape of the organ. This solution, hence, permits to support the organ without the need to grasp it with pincers, avoiding tissue damages. Moreover, a simplified mechanical structure is designed to ease the instrument disposal and sterilization. The additional introduction of another DoF would let the liver retractor cover a larger range of motion, by exposing the underneath tissue and provide the surgeon with a better view and awareness. Furthermore, a more dexterous device would allow the surgeon assistant a better position in external area of operation. Eventually, in relation to traditional laparoscopic tools used for retraction (e.g. Nathanson's liver retraction), the 2-DoFs instrument LMA-based has the advantage of an easier insertion and a better positioning inside the abdominal cavity.



Figure 1. Representation of liver retractor function inside the abdominal cavity.

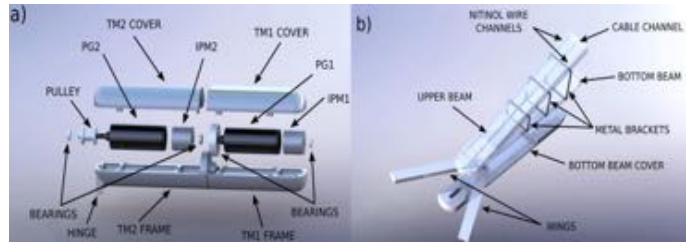


Figure 2. (a) Module Transmissions components. (b) End-Effector design with upper beam inner structure

In the following we discuss the proposed mechanical design, focusing on the description of static analysis and innovative features. Eventually, preliminary experimental results are reported.

MATERIALS AND METHODS

The device, shown in Fig. 1, is based on a transmission motion mechanism already proposed in [2]. This mechanism is composed of two *transmission modules* (TM1, TM2) each activated by an *actuation unit*, composed of a DC Motor and an External Permanent Magnet (EPM). The modules provide a flexible cable-driven end-effector to rotate around x and y axes, from inside the cavity, while the actuation units lie on the outside of the abdominal wall.

a. Transmission Modules

The Transmission Modules (TMs), presented in Fig. 2(a), have an overall weight of 41.35g. The internal frames, including TM1 and TM2, have a length of 46.27mm and 58.7mm respectively and diameters of 12.5mm, 3D printed with Photopolymer Resin (Rigid, Formlabs Inc., USA). Each TM is equipped with an internal permanent magnet (IPM), made of NdFeB, grade N42, with length and diameter of 9.5mm, connected to a planetary gear (PG) (110312, Maxon Planetary Gearbox, Sachseln, Switzerland) with ratio 1024:1. The PG1 shaft is directly inserted inside the TM2 frame, allowing the frame rotation around x. The two modules decoupling is obtained by using a ceramic bearing, placed in the TM1 frame by the outside diameter (12mm) and connected to TM2 frame by internal diameter (6mm). In the TM2, the PG2 shaft is linked to a 9mm long pulley.

b. End-effector Mechanism

The flexible EE, shown in Fig. 2(b), is 3D printed with Photopolymer Resin (Durable, Formlabs Inc., USA) with a Tensile Modulus of 1.26GPa and a Flexural Modulus of 0.82GPa post-curing and has an overall length of

103,37mm and weight of 9.15g. The tool structure is composed of an upper and bottom beam fixed together by one end. The other end of the bottom beam is hinged to the TM2 frame. The tool is actuated by TM2, by pulling two cables (Fishing line nylon, capacity = 15Kg, diameter = 0.3mm) passing through the upper beam. Each of the cables is fixed inside two 50mm long wings, hinged onto the bottom beam surface. The function of wings is to extend the length of the end-effector, enhancing support and contact with tissue. The bottom beam is designed to allow the wings of a maximum opening range of 160°, when pulled by cables. A linear spring, placed between the wings, brings them back to the initial configuration, when cables are loose. Moreover, the flexibility of the tool is enhanced by inserting metal brackets between the two beams. In this way, the end-effector can be modeled adapting its shape and reducing the distress of the organ, due to the contact. Finally, a possible mechanical failure, induced by the tool deformation, can be limited by using nitinol wires (45087, superelastic, Alloy N, Alfa Aesar, UK) of 1mm diameter, fixed inside the upper beam.

c. Static Analysis of the Device Model

With the aim to predict the weight the device can support, a structural model with loads and forces distribution is studied and represented in Fig 4(a).

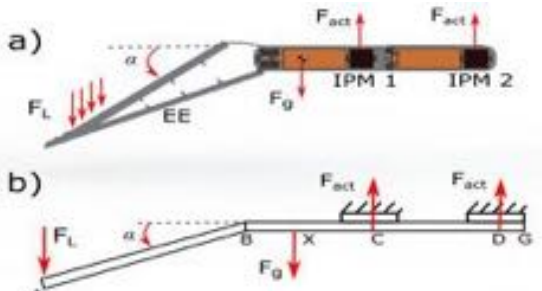


Figure 4. Structural model of the retractor used for weight supporting estimation. (a) Cross section of the device with point of application of forces and loads acting on. (b) Free body diagram of the device.

In the design of this device we take advantage of the introduction of the second DoF which can be used as anchoring. In this way, when one external magnet is activated, the second one doesn't transmit any torque, keeping the internal structure anchored to the abdominal wall. The resulting disadvantage is the inability to activate both DoFs simultaneously. However, this allows a further reduction of the internal device dimensions, by avoiding the insertion of another magnet for anchoring. In Fig. 4(b), the free-body diagram is presented: in this case IPM1 and IPM2 are subject to a vertical attraction force F_{act}^1 , due to the magnetic couplings with the external magnets. We also consider F_g the weight force acting on the device in center of mass positioned in X and F_L the force needed by the EE for lifting the load. The condition for a stable anchoring is expressed by considering the rotational equilibrium in the point G :

¹The values of the forces used in simulations are the ones in [1].

$$F_L < \frac{F_{act} \cdot CG + F_{act} \cdot DG - F_g \cdot GX}{AB \cdot \cos(\alpha) + BG} \quad (1)$$

RESULTS

Two mathematical models are developed to provide an estimation of the tissue lifting performance compared to the predicted load W_L , statically supported by magnetic attraction forces, expressed in (1).

The tissue lifting model is implemented by considering

$$W_L < \frac{10^3 (\tau \cdot GR_{PG} \cdot \eta_{PG})}{9.8 AB} \quad (2)$$

where τ is the torque transferred [3] by IPM2 to PG2, GR_{PG} and η_{PG} are the gear ratio and efficiency of PG2, respectively. The combination of the plots of the two models, obtained via FEA simulation and presented in Fig. 5, shows the operative range for the device.

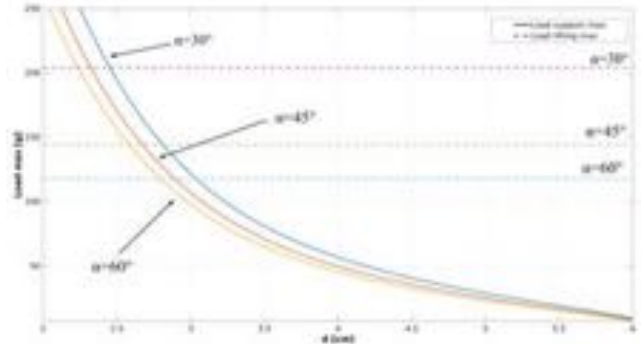


Figure 5. Maximum load lifted by the device (dashed line) and maximum load statically supported by the device (solid line). Load limitations are function of intermagnetic distance d between EPs and IPMs, at three different values of angular position α (30°, 45°, 60°) of EE.

CONCLUSION AND DISCUSSION

This work presents the design of a novel 2-Dofs LMA-based liver retractor, by introducing some mechanical features that can improve previous solutions.

The FEA simulations show the feasible operative range of the device.

Future developments would include the motion analysis of the second DoF, by introducing the control scheme in [3]. Moreover, experimental analysis will be considered to validate our preliminary numerical study.

REFERENCES

- [1] N. Garbin, C. Di Natali, J. Buzzi, E. De Momi, and P. Valdastrì, "Laparoscopic Tissue Retractor Based on Local Magnetic Actuation", *Journal of Medical Devices*, vol. 9, no. 1, p. 011005, 2015.
- [2] A. Mohammadi, F. Leong, Y. Tan, P. Valdastrì and D. Oetomo, "Control of Camera Motion in Laparoscopic Surgery Using Local Magnetic Actuation", *Australasian Conference on Robotics and Automation (ACRA)*, October 2015.
- [3] B. Scaglioni, N. Fornarelli, N. Garbin, A. Menciassi, P. Valdastrì, "Independent Control of Multiple Degrees of Freedom Local Magnetic Actuators with Magnetic Cross-coupling Compensation", *IEEE Robotics and Automation Letters (RAL)*, June 2018.

Real-time electromagnetic tracking of orthopaedic pins for robot-assisted fracture surgery

B. Martins¹, G. Dagnino^{2,3}, S. Dogramadzi³

¹ *Instituto de Biofísica e Engenharia Biomédica, Faculdade de Ciências da Universidade de Lisboa, Campo Grande, 1749-016, Lisboa, Portugal*

² *The Hamlyn Centre for Robotic Surgery, Imperial College London, United Kingdom*

³ *Bristol Robotics Laboratory – UWE, Bristol, United Kingdom*

bea.alvesmartins@gmail.com

INTRODUCTION

Traumatic fractures often involve large incisions where broken bone fragments are manually aligned and secured together using a metallic plate and screws, or intramedullary nails, leading to long stays in hospitals and place a burden on the National Health Service (NHS) [1]. To reduce recovery time and risk of infection, percutaneous techniques, using 2D intra-operative medical imaging, have been developed which allow the surgeon to manipulate the fractured fragments using pins, through small incisions in patient's flesh [2].

Robotic assistance and image guidance could have a positive impact on fracture reduction accuracy and pre- and intra-operative 3D imaging. Robot-assisted fracture surgery (RAFS) system is under research at Bristol Robotics Laboratory [2] with the aim to perform fracture reduction surgeries that involve joints using orthopaedic pins attached to the bone fragments which have to be tracked in real-time. The current RAFS system (Fig.1) consists of: 1) two *Robotic Fracture Manipulator (RFM)*, 2) Two *Carrier Platform (CP)*, 3) one *External Robot (ER)*, and 4) one *System Workstation (SW)*.

The system workstation supports the surgeon to operate the robot and provides real-time navigation using an optical tracking system (Polaris Spectra, NDI Inc.) which tracks pins' pose in real time and allows accurate repositioning of fracture fragments. It consists of a graphical user interface (GUI) that enables the surgeon to interact with the robotic system and allows manipulation of the 3D models of the broken bones generated by the pre-operative CT data. The optical tracker also provides intra-operative image guidance by updating, in real time, the position of the 3D models of the bones during the surgery, through optical tools placed on the orthopaedic pins inserted into the bones. This is possible through to surgical registration as described in [3]. The tracking system requires line of sight between the optical tracker and the optical tools at any time [4]. Unfortunately, given the complexity of the robotic system and the procedure, this is not always achievable, thus representing one of the main limitations of this tracking methodology.

OBJECTIVES

Tracking devices are an essential component in image guided surgery particularly when precise treatment or

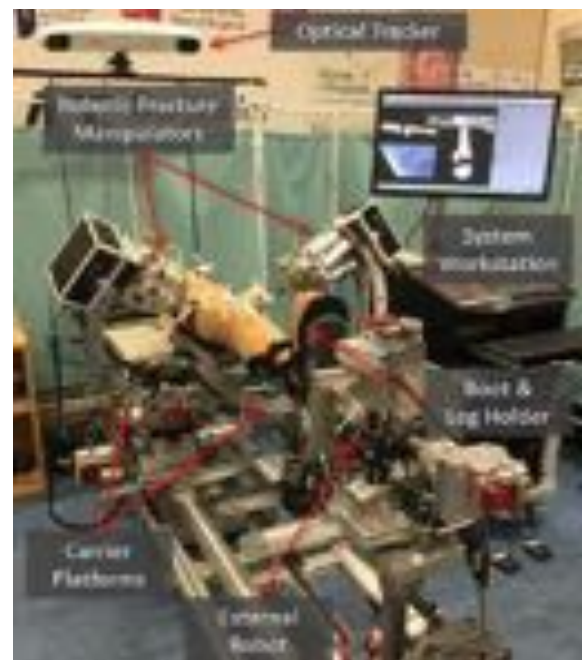


Figure 1 RAFS surgical system [4]

implant positioning are required. In this paper we explore the use of an electromagnetic tracking device (Polaris Aurora, NDI Inc.) as an alternative to the optical tracking system within the RAFS platform. The proposed solution includes:

1. Development of a software to calculate the actual pose of the pin in the workspace;
2. Design and development of a novel orthopaedic manipulation pin with an embedded electromagnetic tracking sensor;
3. Comparison of the performance of the two tracking systems in RAFS context.

METHODOLOGY

A graphical user interface (GUI) for NDI Aurora was created in LabView. The first step involved analysing a simplified version of the existing LabVIEW user - interface for Polaris Spectra, NDI.

To verify Aurora's volume, measurements were made in the cube and dome mode (i.e in the different volume modes of Aurora's data acquisition) with both the reference sensor (Aurora 6DOF Reference) and the measurement sensor (Aurora 6DOF Cable Tool).

Measurements were carried out on a flat table, away from ferromagnetic materials as much as possible.

To create a new orthopaedic pin with embedded electromagnetic sensor, an existing orthopaedic pin (please refer to the pin described in [4]) was modified. In order to insert the sensor in the pin's distal tip, to facilitate alignment with the optical tool, a thin cavity was created inside the pin's body. As a result, the sensor was aligned with the longitudinal axis of the pin and placed as closest as possible to the end of its threaded section (Fig. 2).

Finally, we have tested accuracy of the new pin on ex-vivo animal samples. Four bending experiments were performed using a pork leg. Furthermore, a comparison of the two tracking systems has been performed.



Figure 2 New orthopaedic for electromagnetic sensor. 2-A: front view with the anchoring system section and the cavity, 2-B: side view.

RESULTS

The relative pose of the Aurora sensor and the Polaris optical tool (both placed in one pin as shown in Fig. 3A) was measured with respect to their references (placed on another pin with a fixed and known position as shown in Fig. 3B). A LabVIEW user interface (running at 60Hz) was created to acquire actual and relative poses of the Aurora and Polaris sensors. According to the manufacturer (NDI), the position accuracy (RMS) of the Aurora and Polaris sensors is 0.48mm and 0.25mm respectively. In order to better understand the pin's dynamics, manipulation forces were measured through a load cell placed on the top end of the pin. Before starting the data acquisition, the relative pose between the optical tool and the electromagnetic sensor was settled as zero. The orientation, represented in roll, pitch and yaw, was a way to represent an object's orientation through the angles of the principal axis, respectively. The numerical derivative of relative difference of the Aurora pose relative to Polaris pose measurement was calculated (Fig 4). It is observed that when forces are applied, there is an increase of the position and orientation difference, being greater in x-axis, because the hole for placing the electromagnetic sensor, which is along this direction, makes the pin more fragile, increasing the probability of bending. When force is applied to y-axis, bending is observed which can be due to the geometry of the pin. In



Figure 3 Attached pins. A: electromagnetic pin with embedded Aurora's sensor, Polaris' optical tool and load cell. B: reference pin, Polaris' reference optical tool and Aurora's reference sensor.

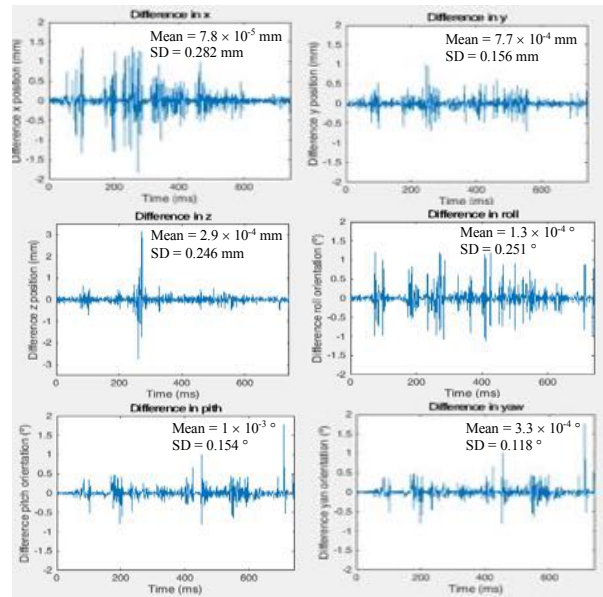


Figure 4 Relative difference of position and orientation in time. Mean and SD (standard deviation) calculated over 740 data points.

z-axis, the peaks observed can be neglected since, in those time frames, no forces were applied in this axis.

DISCUSSION AND FUTURE WORK

After the experimental tests, it was obvious that Aurora system has a smaller workspace, when compared to Polaris optical tracking system, but, despite magnetic field interferences from ferromagnetic materials, Aurora has the added advantage of not requiring a line-of-sight. The pin, however needs redesigning to avoid bending. In a clinical environment, higher forces and torques could be applied and pin bending might compromise the accuracy and safety of the surgical procedure. A prototype of a new orthopaedic pin with the space for an embedded electro-magnetic sensor is required, to include a larger section where the cavity is created. Contrary to the pin used in the experimental tests, the new prototype can be closed using a door fixed with screws, increasing the resistance of the pin, thus reducing the bending and improving safety and accuracy. Future work will include the use of non-ferromagnetic materials (e.g. carbon fibres) to manufacture the RFMs, in order to minimise the interferences with the Aurora system and facilitate their integration and usability.

REFERENCES

- [1] J. Bizzarro and P. Regazzoni, "Principles of fracture fixation," [AOTrauma](#).
- [2] G. Dagnino *et al.*, "Image - Based Robotic System for Enhanced Minimally Invasive Intra - Articular Fracture Surgeries," ICRA 2016.
- [3] G. Dagnino *et al.*, "Intra-operative fiducial-based CT/fluoroscope image registration framework for image-guided robot-assisted joint fracture surgery," *Int. J. Comput. Assist. Radiol. Surg.*, May 2017.
- [4] G. Dagnino *et al.*, "RAFS: a computer - assisted robotic system for minimally invasive joint fracture surgery, based on pre - and intra - operative imaging," ICRA 2017.

Towards Accurate Drilling Guidance for Orthopaedic Surgery

I. Georgilas¹, G. Giddins², J. du Bois¹

¹*Department of Mechanical Engineering, University of Bath, Bath, United Kingdom*

²*Royal United Hospitals Bath NHS Foundation Trust, Bath, United Kingdom*

i.georgilas@bath.ac.uk

INTRODUCTION

In orthopaedic surgery, drilling accuracy is very important. Depending on the procedure, the exact placement of a screw or wire can affect the quality of the surgical outcome. This in turn affects patient health and costs of further treatment. Currently surgeons have only 2D imaging from peri-operative radiographs (X-rays). This can work adequately, but not infallibly, for bones with simple shapes but not for complex bones such as the scaphoid (wrist), distal humerus (elbow) and talus/calcaneus (ankle). In such cases, surgeons, even experienced ones, often have to re-drill multiple times before they are satisfied with the placement of their hole or wire. This increases the duration of surgery, the risks for the patient and the costs for the health system. Inaccurate drilling can also damage delicate tissue around the bone, leading to complications for the patient. Sometimes imperfect screw positioning may be (or must be) accepted. This comes in contrast to general guidelines of surgical practice, for example in the UK the Getting It Right First Time (GIRFT) initiative [1].

One potential solution to this issue is the use of computer-assisted techniques. Computer-assisted surgery utilizes computer technology for preoperative planning and intraoperative guidance of surgical interventions either manually or semi-automatically. Initially developed for use in neurosurgery, this technology has become prominent in several orthopaedic applications. The main concept is the use of segmented radiographs (CT and/or X-rays), for planning and registration of bones, and some form of external navigation system [2]. In [3] this is achieved for the scaphoid, a small, complex bone in the wrist area. Liverneaux et al. used only intra-operative fluoroscopy and continuous update of the registration model to ensure correct navigation registration with the navigation system. Although the system operated well it was limited by the use of intra-operative fluoroscopy, complex registration, limited access, and a global image navigation system that can be subject to occlusions.

A potential solution can be the use of a localised vision-based navigation system. The use of a camera system on-board the acting device addresses the issue of occlusions since in small distances such an event is less likely to occur. Moreover, it has been demonstrated that in other demanding and rapidly changing application this approach can be implemented in real-time control cases ensuring accurate and precise results [4].

With this work, the authors are proposing a new system that can be used in small, complex bones where precise drilling is required. The system will enable the surgeon

to accurately guide a wire or make a hole in a single pass. The system will be using a local imaging system and a special probe, to address the occlusion concerns and remove the need for any registration of radiographs.

MATERIALS AND METHODS

Hardware

The system will be composed by two elements. The first is the *tracking unit*, Figure 1a, that is active and composed of a) a set of cameras, b) a control unit, c) an indicator system, and d) a battery. The tracking unit will be mounted on existing drilling systems; facilitating a universal mounting approach. The second element is the *guidance probe*, Figure 1b, which will have a) a metal tip and b) a number of optically detectable features.

All computational operations take place in the tracking unit. Namely, tracking of the probe, calculation of relevant posture, and updating the surgeon. The tracking unit is using the camera to detect the features on the probe; these can be a number of reflective spheres, or 2D QR-like images to allow 3D tracking. Based on the relative position and orientation of the features the necessary transformation is computed and an indication is provided to the surgeon to adjust drilling

Workflow

The workflow, Figure 2, will consist of two distinctive phases, the setup, and the operation phase. In the setup phase, the tracking unit is placed on the drill. Since the unit will be in the surgical field a suitable sterilisation

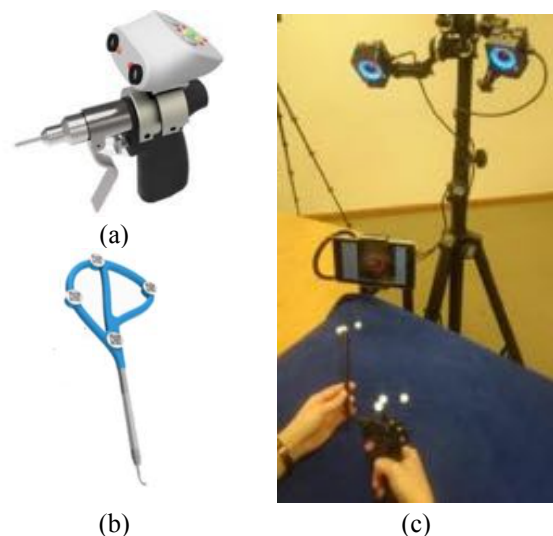


Figure. 1. System versions. Proposed final prototype, (a) tracking unit and (b) guidance probe. (c) Evaluation setup with optical tracker (OptiTrack®) and feedback screen.

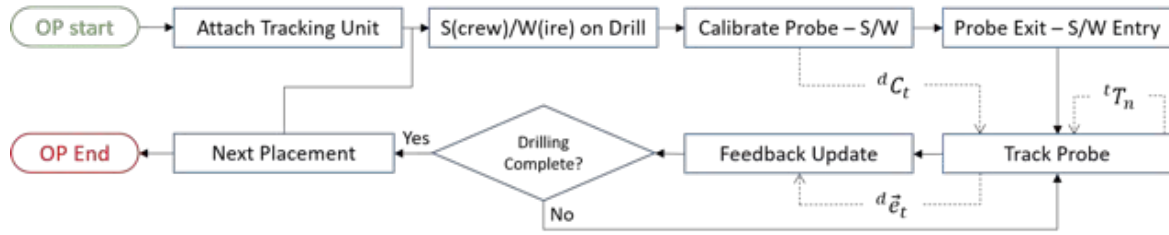


Figure. 2. Proposed system workflow. Continuous lines are the sequence of the steps and dotted lines the exchange of data between steps, either transformation matrices for calibration and tracking or error data for feedback.

regime will be followed, i.e. either the entire unit be sterilisable or the use of a sterile drape. Moreover, the guidance probe, which will be sterile, is placed close to the surgeon for fast access.

For the tracking phase, the surgeon will place the wire or screw on the drill and manual calibration will take place. A potential calibration approach will be for the surgeon to touch the tip of wire/screw to the tip of the probe and the tracking unit will register their relative position and orientation and generate, internally, a calibration transformation matrix dC_t , from the tip to the drill reference frame. Following this, the surgeon will select an exit point on the operated bone and place the tip of the probe on this while placing the wire/screw tip on the entrance point. The final step will be to pivot the drill so they can align the tip with the exit point, using the indication on the tracking unit. The unit will be calculating the desired motion to achieve the alignment (e.g. pivot left/right/up/down). The unit will perform the calculations by generating the transformation matrices between the tip and the markers, n , tT_n and then the error vector from the tip to the drill ${}^d\vec{z}_t$ taking into account the calibration matrix. The indication will be given based on the error vector information.

Prototype testing

Evaluation of the principle of operation was done by using an external tracking device (OptiTrack®) and a feedback screen, Figure 1c. Users of varying experience (surgeons and engineering students) were asked to drill a wire into material mimicking bone. The test aimed to evaluate the accuracy of the system in terms of distance from target, but not orientation error. The users were given a drill and a probe with optical markers, and asked to drill from one point, through the material to an exit point using the probe and feedback screen. The average distance from the desired exit point, standard deviation and confidence interval at 50% are reported.

RESULTS

The users completed 25 attempts of the evaluation experiment, which involved drilling a route of average length of 8mm. The average distance from the desired exit point was 2.10mm, SD 0.87mm, CI_{50%} 0.12mm. The errors can be attributed to the following sources, accuracy of the optical tracker, precision of the marker holder geometry, and bending of the wire during drilling.

CONCLUSION AND DISCUSSION

This work proposed a new way to assist orthopaedic surgeons when performing high precision drilling

operations in small or complex geometry bones. The first prototype showed promising results and demonstrated the potential of the approach. The benefits can be significant and further work is required to enable this method to reach the operating theatre. Although other commercial options are available, the authors believe that this solution can prove more cost effective.

A faster operation can be a significant cost saving where by improved efficiency certain procedures will take less time, allowing additional procedures to be performed in a given period. The improvement of accuracy will have a direct positive effect to patient outcomes. Moreover, the system can be used as a training aid for surgeons, to help improve their accuracy, reducing risk, meaning that surgeons in training can get experience with complex cases in a controlled and safe environment.

The next steps are to develop the stand-alone version with the on-board camera and feedback and investigate an appropriate geometry for the probe. Improve the accuracy of the system to sub-millimetre levels and compensate for the other error sources identified, as well as evaluate orientation accuracy. The more compact version will be tested for sterilisation getting closer to marker and allowing clinical testing to be conducted, demonstrating the efficacy of the method in a real setting.

ACKNOWLEDGMENT

This is a summary of independent research funded by the National Institute for Health Research (NIHR)'s Invention for Innovation (i4i) Programme. The views expressed are those of the author(s) and not necessarily those of the NHS, the NIHR or the Department of Health.

REFERENCES

- [1] Abercrombie J. "General Surgery Specialty Report" GIRFT Programme London 2017.
- [2] Dagnino G, Georgilas I, Köhler P, Morad S, Atkins R, Dogramadzi S. "Navigation system for robot-assisted intra-articular lower-limb fracture surgery." Int J Comput Assist Radiol Surg Springer Berlin Heidelberg 2016.
- [3] Liverneaux PA, Gherissi A, Stefanelli MB. "Kirschner wire placement in scaphoid bones using fluoroscopic navigation: a cadaver study comparing conventional techniques with navigation." Int J Med Robot Comput Assist Surg Wiley-Blackwell 2008.
- [4] Martinez C, Richardson T, Thomas P, du Bois JL, Campoy P. "A vision-based strategy for autonomous aerial refuelling tasks." Rob Auton Syst. North-Holland 2013.

Steerable needle DBS path planning safeguards deep nuclei and white matter tracts

Alberto Favaro¹, Valentina Pieri², Alice Segato¹, Andrea Falini², Elena De Momi¹ & Antonella Castellano²

¹Department of Electronics, Information and Bioengineering, Politecnico di Milano;

²Neuroradiology Unit and CERMAC, Vita-Salute San Raffaele University, Milano, Italy

alberto.favaro@polimi.it; pieri.valentina@hsr.it

INTRODUCTION

Deep Brain Stimulation (DBS) has been increasingly employed to treat motor symptoms of Parkinson's Disease (PD) inhibiting the indirect dopaminergic pathway via the Subthalamic Nuclei (STN) stimulation [1]. DBS planning is challenging due to the risk of haemorrhages, seizures and, importantly, the critical STN position [2]. Therefore, planning algorithms for automatically computing DBS trajectories represent a breakthrough in this field. The capability to calculate a path able to provide an appropriate targeting of the STN also safeguarding the relevant anatomical obstacles (AOs) is a key requisite for a competitive algorithm. In literature, planning solutions able to estimate only rectilinear trajectories (RTs) for rigid electrodes have been proposed, as in [3], [4]. In these cases, the impossibility to follow curvilinear trajectories (CTs) may limit the chances to obtain an optimal targeting of the STN with the proper AOs avoidance. Contrariwise, flexible electrodes can mitigate limitations of their rigid counterparts through their ability to steer along CTs [5]. In particular, the present work focuses on an electrode whose design mimics the EDEN2020* programmable bevel-tip needle, where the displacement among four interlocked sections generates an offset on its tip so that the tool can follow CTs [6].

The aim of this work is to present a planning algorithm for DBS able to estimate a pool of CTs for an accurate targeting of the STN, ensuring a higher level of safety with respect to the standard rectilinear approach.

SUBJECTS AND METHODS

- MRI acquisitions and AOs segmentation - In 15 healthy human controls, a T1-weighted volumetric sequence and a high-resolution diffusion MRI sequence (HARDI: 60 diffusion gradient directions, b -value=3000 s/mm² and two b0 volumes without diffusion-weighting) were acquired on a 3 Tesla Philips scanner (Ingenia CX) at the Excellence Centre for High Field MR (CERMAC). HARDI datasets were corrected for movement and eddy-current distortions using the FMRIB Software Library (FSL). Diffusion Imaging in Python (Dipy) software was used for q-ball residual-bootstrap fibre tracking (FA threshold=0.1; max turning angle=60°) and bilateral corticospinal tracts (CST) were reconstructed. All images and the reconstructed tracts were co-registered to the Montreal Neurological Institute (MNI) space (resolution: 2 mm × 2 mm × 2 mm) by 3D affine transformation using the FSL FLIRT registration tool. Specifically, for

HARDI images, the b0 volume was firstly co-registered to the MNI image, then the same transformation was applied to the tracts, while the T1 volumetric images were directly co-registered to the MNI volume. All MR images thus reside in the same space as the targets (STN) and the AOs [thalamus (THA), globus pallidus (GP), caudate nucleus (CN)] obtained from the segmented atlas in 3D Slicer©. In this work, preliminary tests were conducted bilaterally on one case-study.

- Selection of target points (TPs) and entry points (EPs)

The TPs were established on the anterior STN on the basis of current clinical practice [2]. In a selected 1cm-diameter entry area (EA) on the caudal middle frontal gyrus, 10 EPs resulted viable for 10 obstacle-free RTs, following the procedure described in [5] (cfr. Fig. 1).

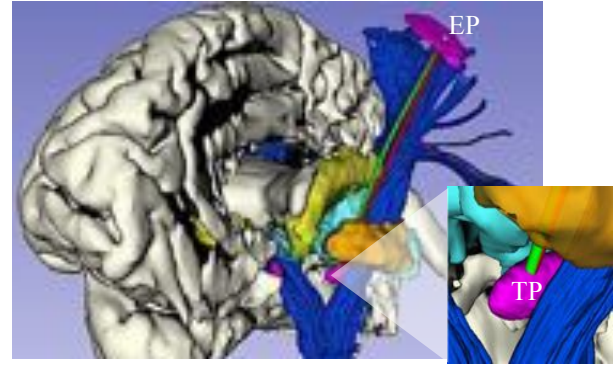


Fig. 1: Planning case on the left hemisphere. RT (red) and CT (green) are shown. EP is located on the purple EA, while TP is placed within the left one of the STN (fuchsia). The picture shows THA (cyan), GP (brown), CN (yellow) and CST (blue).

- Algorithm - The curvilinear planning algorithm is similar to the one proposed in [5]. In the present work, the interpolation step is performed using Non-Uniform Rational Beta Splines (NURBS), which allow to obtain a more precise tuning of the trajectories thanks to NURBS local controllability. The method benefits from a genetic algorithm (GA) for minimizing a fitness function:

$$F_{fit} = \alpha P_{saf} + \beta \ell + \gamma SD + \delta P_{fea}$$

it includes, respectively, the points exceeding a distance threshold from the AOs, the trajectory length, the standard deviation of the curvature (k) and the points beyond the curvature limit (k_{max}).

- 1st test: RTs vs CTs - The RTs, formerly computed for identifying the EPs on the two hemispheres, were compared against the CTs in terms of distance from the AOs. The EPs and TPs were kept constant. An electrode with outer diameter (EOD) of 1.3 mm was considered. For the flexible electrode, a k_{max} of 0.015 mm⁻¹ was considered, as reported in [6]. The minimum (d_{min}) and

* This project has received founding from the European Union Horizon 2020 research and innovation program under grant agreement No 688279.

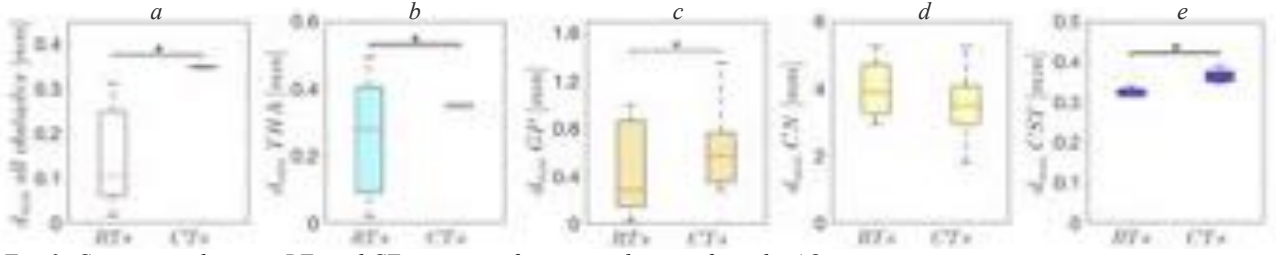


Fig. 2: Comparison between RTs and CTs in terms of minimum distance from the AOs.

mean distance (\bar{d}) from THA, GP, CN and CST were computed both for the RTs and CTs.

- **2nd test: feasibility study** - As a reference model, the objective of the test was to evaluate the performance of the curvilinear planner in response to variations in EOD and k . Again, the STN were set as target. The EPs that had given origin to the best and worst CTs in the 1st test were used to evaluate the best and worst-case scenarios.

- **3rd test: targeting STN's centre of mass (COM)** - A better PD clinical outcome can results by placing the tip of the electrode in the proximity of STN's COM, as stated in [3]. The aim of the test was to verify the ability to find viable RTs and CTs using these points as targets.

RESULTS

- **1st test: CTs are safer than RTs** - Overall, the value of the d_{min} was significantly greater in 100% of the computed CTs with respect to the corresponding RTs (Fig. 2a), while \bar{d} resulted larger in 15 over the 20 CTs examined. The CTs kept a greater d_{min} also examining each AO independently (Fig. 2b,c,d,e). Statistical significance (Lilliefors test for data normality, pairwise comparison with Wilcoxon matched pairs test, $p < 0.05$) is proved for the global d_{min} as well as the THA, GP and CST evaluation.

- **2nd test: viable CTs can be planned for larger EOD by increasing k** - Five EODs were tested, starting from the standard 1.3 mm applied in clinic up to 2.5 mm. The value of k was augmented stepwise from 0.015 mm⁻¹ (the minimum for computing a viable trajectory) to 0.055 mm⁻¹. The performance in terms of d_{min} from the AOs in response to variations in EOD and k was computed (Fig. 3). Viable trajectories could be determined even for a 2.5mm-EOD with a k of 0.055 mm⁻¹.

- **3rd test: only CTs allow to reach the COMs of STN** -

In this experiment, the existence of RTs and CTs able to reach the COMs of the STN using the same EPs from the previous tests was assessed. In this scenario, no RTs could be found, while a total of 6 and 3 CTs (with \bar{d} equal to 1.36 mm and 1.16 mm) were estimated for the left and right hemisphere, respectively.

DISCUSSION AND CONCLUSIONS

This work aimed at proving the benefits of using steerable electrodes, associated with a bespoke curvilinear planner, for safety and targeting optimization in DBS. Compared to a rectilinear approach, the curvilinear planner was able to determine solutions which, in most of the cases, could provide a larger d_{min} from the AOs (Fig. 2), even with the most conservative value of k_{max} . With a larger k_{max} , better results were

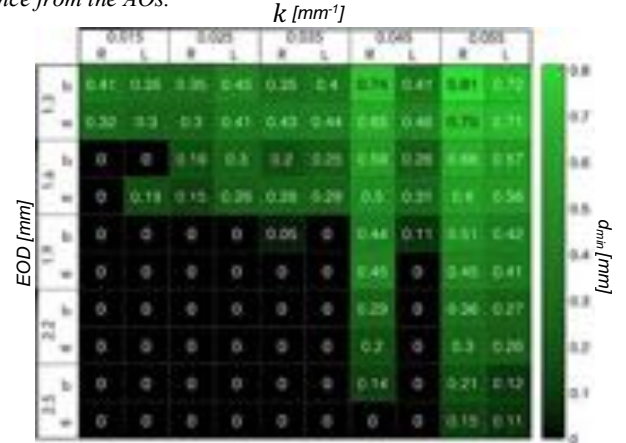


Fig. 3: Feasibility heatmap for the best (b) and worst (w) EP of the right (R) and left (L) hemisphere.

obtained (Fig. 3). The same test, performed over multiple EODs, demonstrated that solutions for curvilinear planning do exist. A further point is represented by the possibility to reach the COMs of the STN, accessible exclusively by using a curvilinear approach.

Overall, such notable results may be traced back to the combination of NURBS and GA implemented in CTs planning which demonstrates, on average, larger d_{min} and \bar{d} (+145%, +22%) and a reduction in the rate of failure (-62%) with respect to [5].

In conclusion, our algorithm is able to compute CTs that precisely reach the targets, preserving the AOs more efficiently than standard RTs.

REFERENCES

- [1] P. Hickey and M. Stacy, "Deep brain stimulation: a paradigm shifting approach to treat Parkinson's disease," *Front. Neurosci.*, vol. 10, p. 173, 2016.
- [2] P. S. Larson, "Deep brain stimulation for movement disorders," *Neurotherapeutics*, vol. 11, no. 3, pp. 465–474, 2014.
- [3] C. Essert, C. Haegelen, F. Lalys, A. Abadie, and P. Jannin, "Automatic computation of electrode trajectories for deep brain stimulation: a hybrid symbolic and numerical approach," *Int. J. Comput. Assist. Radiol. Surg.*, vol. 7, no. 4, pp. 517–532, 2012.
- [4] P. F. D'Haese, E. Cetinkaya, P. E. Konrad, C. Kao, and B. M. Dawant, "Computer-aided placement of deep brain stimulators: From planning to intraoperative guidance," *IEEE Trans. Med. Imaging*, 2005.
- [5] A. Favaro, L. Cerri, D. Scorza, and E. De Momi, "Automatic multi-trajectory planning solution for steerable catheters," in *Medical Robotics (ISMR), 2018 International Symposium on*, 2018, pp. 1–6.
- [6] R. Secoli and F. Rodriguez, "Experimental validation of curvature tracking with a programmable bevel-tip steerable needle," in *Medical Robotics (ISMR), 2018 International Symposium on*, 2018, pp. 1–6.

A Virtual Fixture Adaptation Strategy for MIRS Dissection Tasks

M. Selvaggio¹, G. A. Fontanelli¹, F. Ficuciello¹, L. Villani¹, and B. Siciliano¹

¹*Department of Information Technology and Electrical Engineering, University of Naples "Federico II"*

¹mario.selvaggio@unina.it

INTRODUCTION

Shared-control techniques applied to robotic surgical interventions allow reducing the surgeon's mental workload, increasing the operative precision and/or decreasing the task completion time. Among these techniques, virtual fixtures (VFs) has been identified as one of the most promising approaches in robotic surgery [1]. VFs are software generated constraints which restrict the motion of a robotic manipulator into predefined regions [2]. This technique, although being very effective, is very often not practicable in unstructured surgical environments. In order to comply with the environmental deformation, the VF geometry and its constraint enforcement parameters need to be online adapted [3]. This paper proposes a strategy for an effective use of VF assistance in minimally invasive robotic surgical tasks. Passivity of the overall system is guaranteed by using energy tanks passivity-based control [4]. The proposed method is validated through experiments on the da Vinci Research Kit (dVRK).

MATERIALS AND METHODS

VFs are displayed to the operator through guidance forces applied to the master device of the teleoperation system. The n degree-of-freedom (DoF) manipulator controlled according to an impedance/admittance scheme exhibits the following Cartesian space dynamics

$$\mathbf{M}\ddot{\tilde{\mathbf{x}}} + \mathbf{D}\dot{\tilde{\mathbf{x}}} = \mathbf{f}_h + \mathbf{f}_{vf}(\cdot), \quad (1)$$

where $\tilde{\mathbf{x}} = (\mathbf{x}_d - \mathbf{x})$ with $\mathbf{x} \in \mathbb{R}^r$ being the task space variable, and \mathbf{x}_d its desired value, $\mathbf{M} \in \mathbb{R}^{r \times r}$ and $\mathbf{D} \in \mathbb{R}^{r \times r}$ are fixed, diagonal and positive definite inertia and damping matrices, respectively, $\mathbf{f}_h \in \mathbb{R}^r$ is the external force applied by an interacting user and $\mathbf{f}_{vf}(\cdot)$ is the additional VF force.

A. Virtual Fixtures

A guidance VF exhibits attractive behavior towards a desired geometrical path. The simplest constraint enforcement method consists in applying a spring-damper like force. In the linear case this can be defined as follows

$$\mathbf{f}_{vf}(\tilde{\mathbf{x}}, \dot{\tilde{\mathbf{x}}}) = -\mathbf{K}_{vf}\tilde{\mathbf{x}} - \mathbf{D}_{vf}\dot{\tilde{\mathbf{x}}}, \quad (2)$$

where $\mathbf{K}_{vf} \in \mathbb{R}^{r \times r}$ and $\mathbf{D}_{vf} \in \mathbb{R}^{r \times r}$ are properly designed diagonal and positive definite matrices and \mathbf{x}_d is the set-point belonging to the constraint geometry having minimum distance from \mathbf{x} . An impedance controlled manipulator (1), endowed with VF control forces defined in (2),

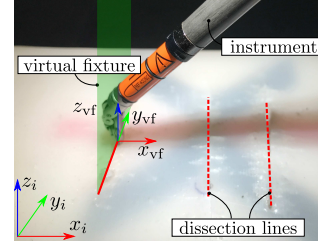


Fig. 1. VF adaptation experimental setup.

exhibits a closed-loop behavior that can be described by

$$\mathbf{M}\ddot{\tilde{\mathbf{x}}} + \hat{\mathbf{D}}\dot{\tilde{\mathbf{x}}} + \mathbf{K}_{vf}\tilde{\mathbf{x}} = \mathbf{f}_h, \quad (3)$$

where $\hat{\mathbf{D}} = \mathbf{D} + \mathbf{D}_{vf}$. To limit the VF spatial influence we adopt a non linear stiffness profile \mathbf{K}_{vf} designed as follows

$$k_{vf}(\tilde{x}) = \beta(\tilde{x})K_{\max}, \quad (4)$$

where $\beta(\tilde{x}, t)$ is a stiffness shaping function and K_{\max} is the predefined maximum stiffness value. For each task space variable $\beta(\tilde{x})$ is mathematically described by

$$\beta(\tilde{x}) = \begin{cases} 0 & \text{if } |\tilde{x}| \geq l \\ \frac{1}{2} \left(1 + \cos \left(\frac{\pi(|\tilde{x}| - d)}{l - d} \right) \right) & \text{otherwise} \\ 1 & \text{if } |\tilde{x}| \leq d \end{cases} \quad (5)$$

where l is the distance at which the VF attractive action vanishes completely and d is the threshold distance value inside which the stiffness perceived is K_{\max} .

B. Virtual Fixture Adaptation

Our aim is to design a system that adapts the VF pose following a human-in-the-loop approach. The strategy consists in detecting interaction points at the slave side and use these to update the VF desired reference frame.

We use the classical least-squares minimization methods to fit a predefined geometry (without loss of generality we consider a vertical plane) onto the set of points. This current VF pose is adapted online by using a simple proportional control law defined on the pose error. In grater details, let $\mathcal{F}_{vf,d}$ and \mathcal{F}_{vf} be the desired and current VF frames, the position error can be defined as

$$\mathbf{e}_p = \mathbf{O}_{vf,d} - \mathbf{O}_{vf} \quad (6)$$

where $\mathbf{O}_{vf,d}$ and $\mathbf{O}_{vf} \in \mathbb{R}^3$ denote the $\mathcal{F}_{vf,d}$ and \mathcal{F}_{vf} origins, respectively. The proportional control law allows obtaining the following VF dynamics

$$\dot{\mathbf{O}}_{vf} = -\Lambda_p \mathbf{e}_p \quad \Lambda_p > 0, \quad (7)$$

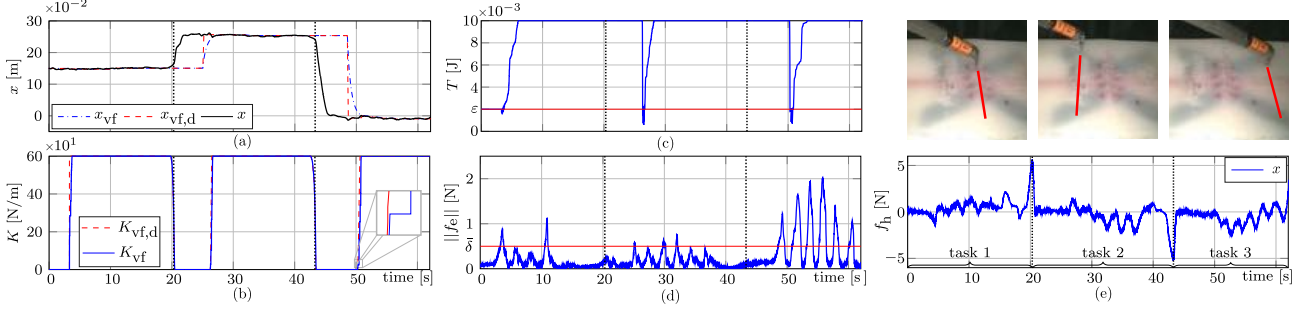


Fig. 2. VF pose adaptation experiment. Time histories of: (a) VF and tool central point pose along the x direction; (b) desired and current stiffness value; (c) energy tank level; (d) slave interaction force; (e) human operator estimated force on the master side.

that exponentially drives \mathbf{O}_{vf} to the desired value $\mathbf{O}_{vf,d}$.

C. Passivity

To preserve the passivity of the resulting variable stiffness system we use the energy tanks-based approach. The extended system dynamics can be rewritten as follows

$$\begin{cases} \mathbf{M}\ddot{\mathbf{x}} + \hat{\mathbf{D}}\dot{\mathbf{x}} + \mathbf{K}_{vf}\mathbf{x} = \mathbf{f}_h \\ \dot{\mathbf{K}}_{vf} = \alpha (\mathbf{\Lambda}_k (\mathbf{K}_{vf,d} - \mathbf{K}_{vf}) + \dot{\mathbf{K}}_{vf,d}) \\ \dot{z} = \frac{\varphi}{z} \dot{\mathbf{x}}^T \hat{\mathbf{D}}\dot{\mathbf{x}} - \frac{\gamma}{z} \frac{1}{2} \dot{\mathbf{x}}^T \mathbf{K}_{vf}\mathbf{x} \end{cases}, \quad (8)$$

where $\mathbf{\Lambda}_k \in \mathbb{R}^{r \times r}$ is a diagonal and positive definite matrix containing the stiffness tracking control parameter, $\alpha \in \{0, 1\}$ is a variable used to activate/deactivate the stiffness variation in case of passivity violation, z is the state of the tank, φ and $\gamma \in \{0, 1\}$ are control parameters. The master system, endowed with the energy tank, has the following energy function

$$\mathcal{H} = H + T = \frac{1}{2} \dot{\mathbf{x}}^T \mathbf{M} \dot{\mathbf{x}} + \frac{1}{2} \mathbf{x}^T \mathbf{K}_{vf} \mathbf{x} + \frac{1}{2} z^2, \quad (9)$$

whose time derivative is given by

$$\dot{\mathcal{H}} = \dot{H} + \dot{T} = \dot{\mathbf{x}}^T \mathbf{M} \ddot{\mathbf{x}} + \mathbf{x}^T \mathbf{K}_{vf} \dot{\mathbf{x}} + \frac{1}{2} \mathbf{x}^T \dot{\mathbf{K}}_{vf} \mathbf{x} + z \dot{z} \quad (10)$$

which, evaluated along the system trajectories, becomes

$$\dot{\mathcal{H}} = \dot{\mathbf{x}}^T \mathbf{f}_h - (1 - \varphi) \dot{\mathbf{x}}^T \hat{\mathbf{D}}\dot{\mathbf{x}} + (1 - \gamma) \frac{1}{2} \mathbf{x}^T \dot{\mathbf{K}}_{vf} \mathbf{x}. \quad (11)$$

By defining the following control laws for α , φ and γ

$$\alpha = \begin{cases} 0 & \text{if } T \leq \varepsilon \text{ \& } \dot{\mathbf{K}}_{vf} > 0 \\ 1 & \text{otherwise} \end{cases} \quad \gamma = \begin{cases} \varphi & \text{if } \dot{\mathbf{K}}_{vf} < 0 \\ 1 & \text{otherwise} \end{cases} \quad (12)$$

$$\varphi = \begin{cases} 1 & \text{if } T \leq \bar{T} \\ 0 & \text{otherwise} \end{cases}$$

the system in (8) is passive with respect to the input-output pair $(\mathbf{f}_h, \dot{\mathbf{x}})$ with storage function (9). \bar{T} and ε in (12) are the upper and lower thresholds for the tank energy, respectively.

RESULTS

The proposed adaptation strategy is evaluated executing multiple dissection tasks in spatially separated regions (see Fig. 1). In the considered case (planar VF), the fitting strategy reduces to a linear regression problem. The desired VF reference frame is fitted using the last fifty recorded interaction poses of the slave robot with the environment.

Fig. 2 contains the results of a performed experiment. The graph 2(a) contains the VF desired and current pose together with the robot tool central point position, while in Fig. 2(b) the user perceived stiffness is shown. The energy tank passivity-based control ensures a passive behavior by implementing the change in stiffness only when sufficient tank energy is at disposal. This is evident looking at Figs. 2(b) and 2(c). In particular, the stiffness is kept constant (*i.e.* $\dot{\mathbf{K}}_{vf} = 0$) when the tank is empty, thus not introducing discontinuities in the system. Fig. 2(b) contains a focus around 50 s that emphasizes this behavior.

Fig. 2(d) shows the interaction force norm measured at the slave side using an ATI nano 17 F/T sensor together with the chosen threshold $\bar{\delta} = 0.5$ N used to discriminate between interaction and free motion.

Finally, looking at the master estimated forces in Fig. 2(e), it can be noticed that relatively high forces (≈ 5 N) are only applied at the task switching.

CONCLUSIONS AND DISCUSSION

In this work we have introduced and experimentally validated the use of adaptive VF for dissection tasks in MIRS. An adaptation strategy is proposed together with a suitable nonlinear stiffness profile for guidance VF. Passivity of the system is preserved by using energy-tank passivity-based control.

Future works will explore the use of online user-defined VF geometries and generalization of the proposed methods to other surgical procedures. In addition, the use of shared control in surgical operations will be further assessed by surgeons user studies.

REFERENCES

- [1] N. Enayati, E. D. Momi, and G. Ferrigno, "Haptics in robot-assisted surgery: Challenges and benefits," *IEEE Rev. Biomed. Eng.*, vol. 9, pp. 49–65, 2016.
- [2] S. A. Bowyer, B. L. Davies, and F. R. y Baena, "Active constraints/virtual fixtures: A survey," *IEEE Trans. Robot.*, vol. 30, no. 1, pp. 138–157, 2014.
- [3] D. Zhang, Q. Zhu, J. Xiong, and L. Wang, "Dynamic virtual fixture on the euclidean group for admittance-type manipulator in deforming environments," *Biomed Eng Online*, vol. 13, no. 1, p. 51, 2014.
- [4] F. Ferraguti, C. Secchi, and C. Fantuzzi, "A tank-based approach to impedance control with variable stiffness," in *IEEE Int. Conf. on Robotics and Automation*, 2013, pp. 4948–4953.
- [5] M. Selvaggio, G. A. Fontanelli, F. Ficuciello, L. Villani, and B. Siciliano, "Passive virtual fixtures adaptation in minimally invasive robotic surgery," *IEEE Robotics and Automation Letters*, vol. 3, no. 4, pp. 3129–3136, Oct 2018.

Stereoscopic Near-Infrared Fluorescence Imaging: A Proof of Concept towards Real-Time Depth Perception in Surgical Robotics

M. J. Munford¹, S. Bowyer¹, F. Rodriguez y Baena¹

¹*Department of Mechanical Engineering, Imperial College London,
f.rodriquez@imperial.ac.uk*

INTRODUCTION

The increasing use of surgical robotics has provoked the necessity for new medical imaging methods. Many assistive surgical robotic systems influence the surgeon's movements based on a model of constraints and boundaries driven by anatomy. This study aimed to demonstrate that Near-Infrared Fluorescence (NIRF) imaging could be applied in surgical applications to provide subsurface mapping of capillaries beneath soft. This study focused on the use of NIRF to determine submersion depth and inclination angle of a phantom below soft tissue.

MATERIALS AND METHODS

All testing was carried out using the custom built test rig shown in Figure 1. It consists of an excitation LED, a 2 degree of freedom translation linear stage and kinematic base, a modified CCD camera and long pass filter. The camera was modified to remove its IR cut filter to allow image capture in the IR spectrum and an additional filter fitted to remove visible light.

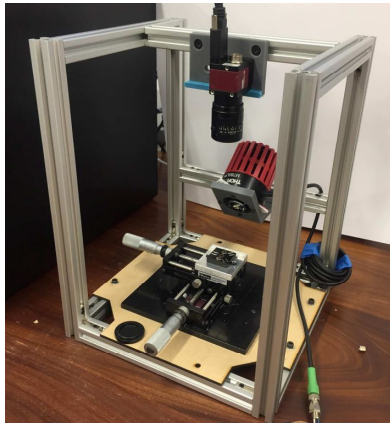


Figure 1. Assembled test rig used for ICG excitation, specimen positioning and data collection.

The excitation LED was a 800 mW source of 780 nm light, chosen to emit on the peak excitation of ICG pigment. ICG pigment was used in solution for fluorescence as it is FDA approved and well-studied. The linear stage and kinematic base allowed for precise and reliable control of the specimen position, an important factor in stereoscopic calibration. Due to budget constraints, imaging proceeded with only one camera. This was translated 0.6 mm between left and right image capture to simulate the separation distance of a stereo pair of cameras. Connection of the camera to a computer was

made using a firewire PCI interface, which allowed image acquisition, and subsequent processing, to be done using MATLAB.

Preliminary work suggested that glass capillaries of 4 mm internal diameter filled with ICG pigment in solution at 1 mg/ml should be used. Capillaries were held in position in a 3D printed test piece filled with a milk and gelatin mixture which replicates the optical properties of soft tissue [1]. The choices made for the concentration of ICG, capillary diameter and soft tissue substitute are all supported by existing literature.

A calibration procedure was run before each series of testing, which formed a model of the stereo extrinsic parameters. This allowed for depth reconstruction of the subsurface scene based on pixel disparities between the left and right images.

Once in position, the capillary specimens were excited at 780 nm and the resulting fluorescence, with peak emission at 815 nm, was captured in stereo. During testing, the whole rig was shielded from ambient light. Depth maps of the field of view were then generated via post-processing in MATLAB.

Stereo post-processing algorithms were written to implement a 'winner-takes-all' strategy and determined corresponding pixels between images based on a normalised cross correlation cost function [2]. Preliminary work identified that an optimal window radius which maximised correspondence could be found, however, this was not implemented in this study.

Testing sought to determine the effect of capillary submersion depth and inclination angle, as per the set up in Figure 2, on the imaging quality. Figures 3 through 6 show key features in the collected data.

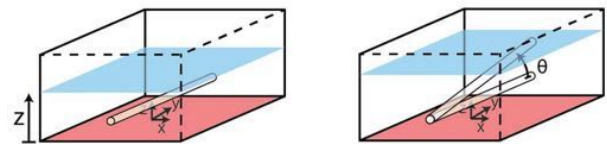


Figure 2. Set up for testing of phantom submersion depth and incline angle. Controlled variables are z and θ .

RESULTS

Figure 3 shows that data from phantom submersion depths below 11 mm exhibited a distinct reduction in the number of corresponding pixels which were found. These

data points were marked as outliers and excluded from further calculation of errors. This was further supported by data collected for phantom inclination angle, where it was observed that larger angles give a reduction in the percentage of corresponding pixels. This was most likely because a greater number of points are below 11 mm for a larger specimen angle.

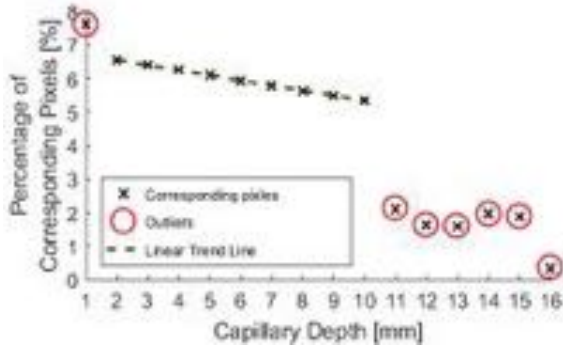


Figure 3. Percentage of pixels for which a corresponding pixel could be found in the partnering stereo image.

Outliers in Figure 4 further supported the hypothesis that the maximum imageable submersion depth was 11 mm as data points beyond this depth were spurious and noisy. Figure 4 suggests that the error in depth measurement was linear, ranging from ± 2.3 mm to ± 3 mm. These values are large compared to the data, however, this can be explained largely by the inherent human error in adjusting the camera separation distance.

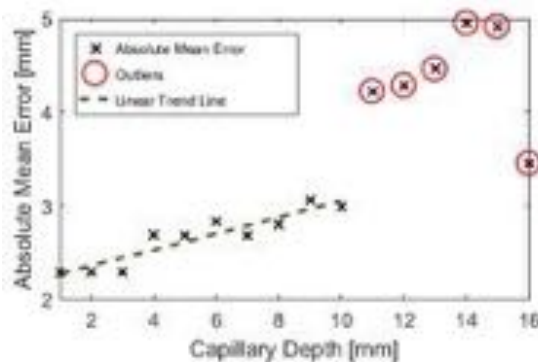


Figure 4. Absolute mean error in depth estimation of the entire field of view against controlled submersion depth.

Post-processing allowed for the inclination angle to be accurately inferred from the depth map data to within $\pm 1.6^\circ$, as shown in Figure 5.

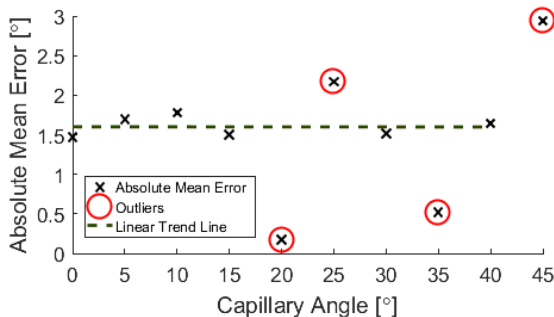


Figure 5. Absolute mean error in phantom angle against controlled angle.

Figures 6 and 7 are examples of the reconstructed depth maps which were produced using NIRF imaging with a subsurface capillary. The data is representative of the original surface, despite being noisy.

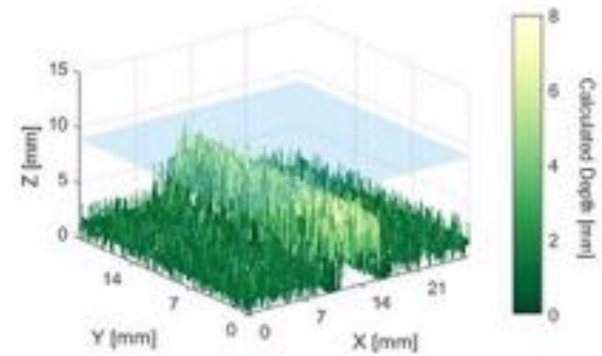


Figure 6. Reconstructed depth map for a capillary phantom 5 mm below the surface of soft tissue emulate, shown in blue.

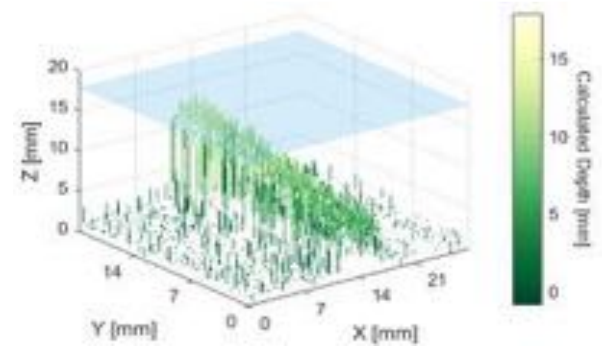


Figure 7. Reconstructed depth map for a capillary phantom inclined at 15° to the plane. Positioned so that the maximum height is 2 mm below the surface of soft tissue emulate, shown in blue.

DISCUSSION AND CONCLUSION

It has been shown that it is possible to use NIRF for the imaging of a capillary submersed up to 11 mm below a soft tissue phantom, over a range of angles from 0° through 45° . Phantom depth has been measured to a worse case accuracy of ± 3 mm and phantom angle to a constant accuracy of $\pm 1.6^\circ$. The errors associated with the test data are within what is deemed acceptable in a prototyped clinical scenario. These profound findings suggest that NIRF could indeed be used for the next generation of medical imaging in surgical robotics and provide a firm basis for future research into real-time depth perception.

REFERENCES

- [1] Waterworth M. D. et al. "Optical transmission properties of homogenised milk used as a phantom material in visible wavelength imaging" in *Australas. Phys. and Eng. Sci. in Med.*, 18(1):39–44, 1995.
- [2] Bhalerao, R. et al. "Modified Dual Winner Takes All Approach for Tri-Stereo Image Matching Using Disparity Space Images" 2017

Patient specific FE modeling for deformable breast registration

E. Tagliabue¹, B. Maris¹, A. Roberti¹, A. Nikolaev², L. De Jong², P Fiorini¹

¹*Dept. of Computer Science, University of Verona, Italy*

²*Radboud University Medical Center, Nijmegen, Netherlands*
eleonora.tagliabue@univr.it

INTRODUCTION

Accurate alignment of prone and supine images of the breast is the first step for many surgical procedures, like image-guided biopsy, where the suspicious lesion is identified in magnetic resonance (MR) images acquired in prone position, while the procedure takes place under ultrasound (US) guidance with the patient lying semi-supine. Due the repositioning of the patient and the gravity load, a non-rigid registration able to recover large deformations is required in these cases. Most of the image registration methods that correct for breast tissues deformation rely on finite element (FE) simulations. These simulations have the ability to provide physically realistic predictions if accurate material properties are considered and reasonable assumptions on physical constraints and loading conditions are made. Most of such studies consider the anatomy composed of at least two internal tissues with different mechanical properties and described by a non-linear constitutive law [1], [2]. Although patient-specific models should be considered to achieve an accurate estimation, due to the fact that the mechanical properties of the breast tissue vary across the population and over time for each person, in these studies, the assignment of material parameters is based on values from literature [3], [4]. Furthermore, FE simulations of the breast usually fix the displacement on the pectoral muscle surface, even though a sliding motion on the chest wall has been observed [1], [2].

In this work, we propose an approach for registration of prone and supine MR acquisitions based on a patient-specific FE model. Breast elastic properties are estimated through a calibration procedure that iteratively aligns prone and supine volumes under gravity load. The patient-specific model obtained is then employed to guide image deformation on the initial prone MR, through thin plate splines interpolation method. We investigate the performance of the proposed registration scheme on a phantom study and on a clinical case. Deformable registration accuracy is assessed by comparing the positions of some anatomical landmarks in the supine and the deformed images. Being this approach totally independent from intensity values, it has the potential to be applied to multi-modal deformable registration problems (e.g., MR/US, MR/X-ray), once initial prone and supine acquisitions are available.

MATERIALS AND METHODS

As a first step in the registration procedure, prone and supine images are rigidly registered by exploiting MR

visible markers. Breast anatomy in prone and supine configurations is then segmented using a semi-automatic procedure based on a snake model, and the associated volumes are meshed using tetrahedral elements. We simplify the FE model by assuming the breast to be composed of a single isotropic linear elastic material, quasi-incompressible (Poisson's ratio 0.49) and with density 1000 kg/m³. Previous studies report that assumption of linear elasticity does not significantly affect the overall accuracy [5]. Furthermore, considering the breast as homogeneous avoids the introduction of inaccuracies due to the segmentation of more structures, and errors that might arise from the interaction between different tissue type. FE modelling is performed using the open-source framework SOFA. At this point, an iterative procedure varying the tissue elastic modulus is performed, until either the matching error between the prone and supine configurations is below a pre-defined threshold (0.1mm) or the maximum number of iterations is exceeded (20). At each iteration, the breast in prone position is deformed under two times the gravity load and Newton's method is used to guess a new value for the elastic parameter, based on the previous estimations and errors. The estimated Young modulus is then exploited to obtain an optimized FE breast model for each case. Such a model can be used to simulate several different scenarios in a patient-specific manner, if loading conditions are known. Nodal positions before and after deformation are used as source and target landmarks to drive thin plate spline deformation of the original prone MR image.

In this work, we use the case-specific FE model to deform the prone breast under gravity load for two case studies. The first dataset corresponds to a breast phantom, composed of a rigid base structure, stiff superficial tissue, soft internal tissue, and four hard lesions. The MR acquisitions of a healthy patient have been obtained at Radboud University Medical Center, where the protocol for prone and supine scanning has received ethical approval. The 3D volumes extracted from these datasets (resulting in 21252 tetrahedra for the phantom and 16490 for the patient) are modelled with the described method. In addition, accurate definition of boundary conditions is necessary to allow FE simulations to converge to a solution. This task is straightforward for the phantom case, where the displacements of all the nodes belonging to its rigid base can be prescribed. However, in the patient case we need to account for the sliding of the breast tissues against the chest wall under gravity. We model this motion by imposing a frictionless contact between these two structures, and we prescribe the displacement

of nodes lying on the sternum (Figure 1). Registration performance is then evaluated by comparing the positions of corresponding landmarks identified on the deformed and supine MR images. Five reference positions are selected for the phantom (4 tumor centroids and 1 point on the nipple) and three for the patient (1 MR-visible artificial marker on the lateral side, 1 point on the nipple and 1 point on the duct branch).

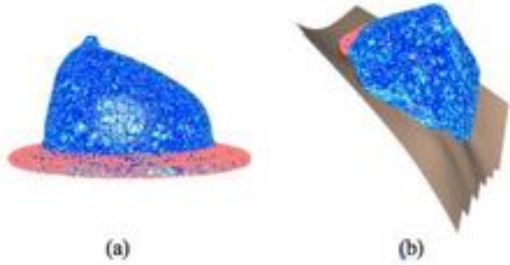


Figure 1. FE modelling scenarios. Tetrahedral meshes are represented in blue, while fixed points are coloured in dark pink. (a) Phantom scenario: points belonging to the rigid base are constrained in all directions. (b) Patient scenario: points on the sternum are kept fixed. The chest wall surface is also considered, to constrain breast deformation.

RESULTS

The estimated values for the Young modulus obtained with the calibration procedure are 4,42kPa and 2,18kPa for the phantom and the patient respectively. Biomechanical models initialized with these values are used to predict anatomy deformations. Figure 2 shows MR slices of breast in both initial and deformed configurations for the patient case. Visually, the FE breast model seems quite able to account for the gravity-induced deformation.

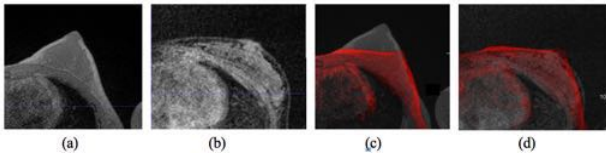


Figure 2. MR images of the patient included in the study. (a) prone MRI, (b) supine MRI, (c) prone MRI (gray) with prone MRI after deformation (red), (d) supine MRI (gray) with prone MRI after deformation (red). All images are rigidly registered to the prone configuration.

Registration performance is further investigated by computing the mean square errors (MSE) between corresponding landmarks identified on the two images. MSE in the three directions before and after deformation is reported in Table 1. Error values related to the phantom case are significantly lower than those obtained for patient case, due to the higher initial matching of the prone and supine volumes already in the initial configuration. A common trend in the reduction of the global error after the deformation can be observed in both the situations, with the only exception of phantom's tumor 3. Overall, the most meaningful results are obtained for the patient, where the matching distance passes from a range of 33-40 mm to 6-9 mm.

PHANTOM

	Tumor1 centroid	Tumor2 centroid	Tumor3 centroid	Tumor4 centroid	Nipple
Initial	5.23	4.22	0.87	2.52	3.64
Final	2.27	2.34	1.04	1.93	2.8

PATIENT

	External MR marker	Nipple	Duct branch
Initial	32.95	39.74	33.1
Final	8.92	5.63	5.89

Table 1. Mean square errors between the corresponding landmarks identified on the prone-deformed and the supine images, before (“initial”) and after (“final”) the registration algorithm is applied. Errors are expressed in mm.

CONCLUSION AND DISCUSSION

We propose a patient-specific framework to first identify breast elastic properties and subsequently register prone and supine breast MRs, through FE modeling. The method has succeeded in recovering the displacements of internal areas with good approximation for a synthetic phantom and a patient case. The patient scenario has turned out to be the most challenging, due to the larger extent of deformations as well as the non-trivial establishment of the boundary conditions. Despite the final error still being large, especially in the patient case, the proposed approach has demonstrated to be a promising initial step towards deformable image registration relying on patient-specific estimation of elastic properties. As a next step, a wider population of patients will be included in the study for a more extensive evaluation. Future work will also involve breast modelling refinement, considering a non-linear constitutive law and possibly including other materials. Furthermore, the independence of this approach on intensity levels paves the way towards a wider validation on multi-modal datasets.

REFERENCES

- [1] L. Han *et al.*, “Development of patient-specific biomechanical models for predicting large breast deformation,” *Phys. Med. Biol.*, 2012.
- [2] a Samani, J. Bishop, M. J. Yaffe, and D. B. Plewes, “Biomechanical 3-D finite element modeling of the human breast using MRI data,” *IEEE Trans. Med. Imaging*, 2001.
- [3] L. Han *et al.*, “A hybrid fem-based method for aligning prone and supine images for image guided breast surgery,” in *Proceedings - International Symposium on Biomedical Imaging*, 2011.
- [4] A. P. del Palomar, B. Calvo, J. Herrero, J. López, and M. Doblaré, “A finite element model to accurately predict real deformations of the breast,” *Med. Eng. Phys.*, 2008.
- [5] C. Tanner, J. A. Schnabel, D. L. G. Hill, D. J. Hawkes, M. O. Leach, and D. R. Hose, “Factors influencing the accuracy of biomechanical breast models,” *Med. Phys.*, 2006.

Vision-based pose estimation of a continuum robot using optical flow and kinematic robot model

V. Bordoux, B. Rosa, F. Nageotte

Icube, University of Strasbourg, CNRS, France

valentin.bordoux@insa-strasbourg.fr

INTRODUCTION

Continuum robots provide great dexterity along tortuous anatomical paths and are therefore promising tools for minimally invasive surgery. The control of such robots is however difficult. State of the art models permit to estimate the shape of a robot knowing forces applied to the robot, but in surgical procedures the load applied to the tool is changing due to interactions with the tissues. Therefore, to control continuum robots, methods based on additional sensors have been explored. Vision-based control offers a low cost and non-invasive method for pose estimation with endoscopic system since a camera is embedded for surgeon visual feedback.

This paper proposes an approach to estimate the pose of a continuum robot without markers, using a monocular vision system. However, instead of using images to estimate the pose as usually done, the method combines the estimation of the optical flow and the use of a simple robot kinematic model, thus making it independent of the visual appearance of the robot. The method and the conditions will first be presented, followed by the results obtained in laboratory and in-vivo datasets.

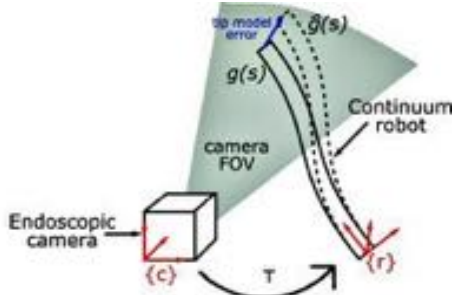


Figure. 1. Continuum robot inserted in working channel of an endoscope and visualized by the endoscopic camera

MATERIALS AND METHODS

Figure 1 presents the situation where we want to estimate the robot pose. The camera projection matrix K is considered as known, as well as the transformation T between the camera frame and the robot frame. The conventional piece-wise constant curvature model of continuum robots is used [1]. This model is simple, expendable to multiple active sections but it is obviously inaccurate. This results in an error on tip pose estimates (Figure 1).

Compensation of the kinematic model error can be realized by using the endoscopic images. A lot of work has been done on the subject [2]. The state of the art accomplishes robust results but heavily relies on trained

machine learning algorithms. Such methods require extensive manual labor as many labeled images are needed.

Our idea is to rely on the measured optical flow in the image and to compare it with the theoretical optical flow obtained from the measured joints movements and the differential kinematics. The rationale of this approach is that the differential kinematic model is generally less erroneous than the position kinematic model. A key advantage of the method is that it does not require information about tool appearance such as color or texture. Moreover, it should help to deal with the model inaccuracy and with projection appearance redundancy of different poses because the speed orientation should help to discriminate the correct pose.

By using the measured velocity at the joint level, the estimated pose parameters and the robot model, a theoretical optical flow can be computed (Fig. 2b), which can be compared with the optical flow measured in the image sequence (Fig. 2a). Starting from the measured joint values, the pose parameters can thus be varied in order to minimize a cost function relating measured optical flow and theoretical one. For this purpose, a specific cost function has been developed to compare the optical flow images, which includes robot position and speed information:

$$e_{tot} = e_q + \lambda_1 \cdot e_{OF} + \lambda_2 \cdot e_{hist}$$

e_q is a function of the pose parameters, which limits the search space around the initial estimation provided by measured joint values.

e_{OF} compares the two optical flow vectors:

$$e_{OF} = \frac{\sum_{x,y} \Delta OF}{\sum_{x,y} M}$$

Where ΔOF is the difference between the measured optical flow and the theoretical optical flow and M the mask of the theoretical optical flow, i.e. the area of the image where the theoretical optical flow is non null.

These two terms are not sufficient to ensure the correct convergence of the pose estimation process because the robot model can converge onto the background or inside the actual robot image.

Therefore, a third component e_{hist} is added to correct those cases, which compares the robot with its close contour assuming that the robot is distinguishable from the background in optical flow measure. The measured optical flow inside the model mask and in the contour around it are compared using histogram correlation.



Figure 2. a. Estimation of the displacement in two successive images using the FlowNet2 algorithm [45]. b. Reconstruction of the theoretical optical flow using the robot kinematic model. c. Contours of the instrument projected onto the original image before optimization (red) and after optimization of the pose parameters (green).

For minimizing the cost function an optimization loop is used, where the pose parameters are iteratively changed. These variations both act on the robot projection in the image and on the theoretical optical flow. After convergence of the optimization (Fig. 2c), the complete robot pose is obtained by putting the optimal pose parameters into the kinematic model.

RESULTS

The algorithm has been implemented in python using the OpenCV library. The optimization algorithm is the differential evolution algorithm provided by the scipy library. The images were acquired on the motorized endoscopic system STRAS [3] in two different environments. The endoscopic camera has a resolution of 580x760 pixels, a model of distortion has been used to rectify the images. A state of the art optical flow algorithm has been used to estimate the motion in images, called FlowNet2 [4]. The robot is a tendon-driven single active section continuum robot. The optimization is run over the three parameters defining its pose: the curvature, the insertion length and the rotation.

First, results were generated on a simulated dataset. Perfect robot poses were obtained by rendering the robot model on a surgical environment video, and pose perturbations were introduced by adding a sinusoidal perturbation on the joint values. The proposed approach was tested on 119 randomly selected images from this dataset. The convergence rate was below 50%. However, considering only the converged results, the average tip error improved from 145.5 pixels to 4.8 pixels in the image, and from 20.7 mm to 1.03 mm in 3D. These results show that despite a lack of robustness the method improves the pose estimation in the case of a perfect hand-eye registration and good optical flow estimation. The second test dataset features images which were acquired during an in-vivo experiment in the colon of a porcine model. No pose ground truth is available, therefore images have been manually labeled in order to compute the projection error in terms of precision and recall. The dataset is very challenging, including images where the tool is not moving or is out of the field of view. As the method cannot be directly applied in these cases, they have to be detected.

Here the test has been performed on 78 manually selected images, in order to assess the method efficiency when the

optical flow estimation is successful. The average precision and recall obtained with these images are respectively 0.70 and 0.87 while they were 0.32 and 0.41 before optimization. Qualitatively, the projection error is good. However, an error in the depth estimation is expected.

Independently of the dataset, the mean pose estimation time is approximately 60 seconds. This is mainly due to the code, which is not optimized, and to the choice for the optimization algorithm which runs many function evaluations. Using GPU computation, a better suited optimization algorithm, and code optimization, it is expected to run much closer to real time (≈ 20 Hz).

Further work is about improving the method's robustness and accuracy. Assuming that a part of the remaining error in the in-vivo dataset is inherited from the camera / robot registration, a local optimization of this transformation could be added to the pose estimation. Ongoing work concerns the automatic selection of adequate images as well as developing a criterion to assess the result quality after convergence.

CONCLUSION AND DISCUSSION

This paper presents an algorithm to estimate the pose of a continuum robot by using motion information in images and the differential kinematic model of the robot. The method could be combined with some other tracking method for 2D tracking, or used as an initialization for automatic segmentation of the robot. With some improvements, the method is expected to be used for 3D pose estimation as well.

REFERENCES

- [1] R.J. Webster *et al*, 2010. Design and kinematic modeling of constant curvature continuum robots: A review, *Int. J. Robotics Res.* **29**(13), 1661–1683
- [2] D. Bouget *et al*, 2017. Vision-based and marker-less surgical tool detection and tracking: a review of the literature. *Med. Image Analysis*, **35**, 633–654.
- [3] L. Zorn *et al*, 2018. A novel telemanipulated robotic assistant for surgical endoscopy: preclinical application to ESD, *IEEE TBME*.
- [4] E. Ilg *et al*, 2016. FlowNet 2.0: Evolution of optical flow estimation with deep networks, *IEEE CVPR*.

Track-Guided Ultrasound Scanning for Tumour Margins Outlining in Robot-Assisted Partial Nephrectomy

Agostino Stilli¹, Manios Dimitrakakis², Maxine Tran³, Danail Stoyanov¹

¹University College London, Department of Computer Science, Surgical Robot Vision Group
a.stilli@ucl.ac.uk, danail.stoyanov@ucl.ac.uk

²University of Patras, Department of Electrical and Computer Engineering, Laboratory of Automation and Robotics

³University College London, Department of Nanotechnology, Div. of Surgery & Interventional Science

INTRODUCTION

Robot-Assisted Partial Nephrectomy (RAPN) is a medical procedure in which part of a kidney is removed, typically because of the presence of a tumour. RAPN is the second most diffused robotically assisted surgical procedure worldwide after prostatectomy [1]. The advantages of this robot-assisted procedure are detailed in [2], and in [3] it is argued that RAPN can be used in place of open surgery or total nephrectomy in some complex renal tumour cases. The RAPN procedure is thoroughly described in [4]. Methods used for the identification of the tumour include pre-operative Computer Tomography (CT) scans, Magnetic Resonance (MR) imaging and intraoperative Ultrasound (US) scans. The use of drop-in US probes for RAPN procedures is widely recognized as the golden standard for the intraoperative detection and margins outlining of the mass targeted. In [5] the authors show that the use of US drop-in probes guided by robotic laparoscopic tools rather than standard laparoscopic tool is beneficial for the surgeon as it significantly increases the dexterity, hence, the field of view of the system. Typically, the probe is inserted through a standard trocar port and the surgeon grasps it with a gripper, picking up the probe from a dedicated slot. The slot is generally designed to match the EndoWrist® Prograsp™ Forceps gripper of the daVinci Surgical System, (Intuitive Surgical Inc., Sunnyvale, CA, US). Once the probe is paired with the gripper, the surgeon can navigate to the target organ to perform the scan: multiple swipes with the US probe are performed on the kidney surface in order to localise the tumour. Section by section the resection area is outlined and marked with an electrocautery tool. The additional degrees of freedom provided by the dexterous wrist of the robot-assisted laparoscopic tool navigating the probe in comparison with the standard laparoscopic scenario ease the swiping process, nonetheless, this procedure is still challenging. The US probe often requires repositioning because of slippage from the target organ surface. Furthermore, the localisation can be inaccurate when tumours are in locations particularly hard to reach, e.g. in the back part of the kidney. In such cases, kidney repositioning could be required. A highly skilled surgeon is typically required to successfully perform this pre-operative procedure. Similar problems exist in many other medical procedures involving the use of drop-in US probes, e.g. prostatectomy. In this paper we propose a novel approach for the navigation of US probes: the use of pneumatically attachable flexible rails to enable swift, effortless and accurate track-guided scanning of the kidney. The

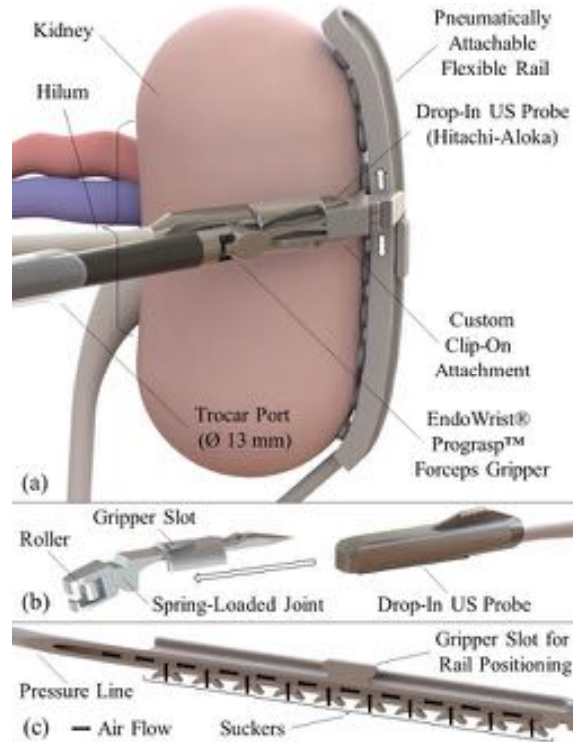


Figure 1 – Pneumatically attachable flexible rails: (a) overview of the system when used to guide a drop-in US probe for tumour margins outlining in RAPN, (b) custom add-on (left) for the drop-in US probe (Hitachi-Aloka pictured on the right) to allow the connection between the probe and the rail; (c) section view of the proposed system, components and air flow.

proposed device, shown in Fig.1 (a, section view in b), is attached on the kidney side surface with the use of a series of bio-inspired vacuum suckers and it is used as a guide on which the surgeon attaches and slides the drop-in US probe. The use of vacuum pressure in surgical applications has been previously investigated to enable the navigation of micro-robotic systems [6], the stabilisation of a beating heart [7], as well as the anchoring of medical devices [8]. Nonetheless, the concept of pneumatically attachable rails, as well as the concept of rail-like systems for track-based navigation of surgical instruments and sensing probes, has never been proposed to date. Given the novelty of the proposed system, a patent application has been filed (United Kingdom Patent Application No. 1808728.8).

MATERIALS AND METHODS

The proposed system is shown in the CAD drawings in Fig.1 (a) and (c). A flexible pressure line supplies the

vacuum pressure to the proximal end of the proposed system. This line connects with a cavity that runs through the entire length of the system: suckers are arranged on a protruding line and connected such cavity by a series of openings, as shown in Fig.1 (c). The distal end of the cavity is sealed. Once vacuum pressure is applied, all the suckers are depressurized. As a result, the suckers, hence, the whole system, firmly connects with any adjacent body surface or organ. As shown in Fig.1 (a), along the whole perimeter of the system, excluding the proximal end, a continuous T-section rail is embedded. A customized slot is also embedded to match the shape of a EndoWrist® Prograsp™ Forceps gripper to facilitate the system positioning during the deployment (Fig.1 (c)).

The deployment process can be summarized as follows:

1. The system is passed through a standard trocar port and grasped by the gripper slot with the EndoWrist® Prograsp™ Forceps gripper.
2. The mid-point of the sucker line is placed in contact with the mid-point of the lateral surface of the kidney, opposed to the hilum, as shown in Fig.1 (a).
3. Vacuum pressure is applied to the sucker line, making the system adhere to the kidney surface in its whole length. Any other robot-assisted tool can be used to apply a small force on those parts of the system not in suction to allow the pneumatic connection.
4. The system is now firmly connected to the kidney and it is released from the gripper.
5. The drop-in US-probe (Hitachi-Aloka pictured in Fig.1 (a) and (b)) with the customized connector (Fig.1 (b) left) already assembled onto it is passed through the same trocar port fitting the pressure line, grasped with EndoWrist® Prograsp™ Forceps gripper by the dedicated slot and attached to the rail.
6. The drop-in US-probe is moved along the rail to perform the scan, outlining the tumour, hence, the margin of resection.

Inherently in its design, the proposed system is flexible enough to match the surfaces of the internal organs and cavity walls, but at the same time stiff enough to provide a rail-like structure for robust coupling with any probe/tool sliding along it. To achieve such characteristics, rubber-like materials with low Shore hardness have been used to provide the required compliance to the suckers. Contextually, materials of higher Shore hardness have been used to build the walls of the pressure line, in order to prevent it from collapsing once vacuumized. Thus, the use of rubber-like materials of different Shore hardness in the same body element is of paramount importance for the correct functionality of the proposed system.

At the current stage we have designed and prototyped the proposed system using multi-material multi-hardness soft 3D-printing (Model: Objet260 Connex, Stratasys, Eden Prairie, MN, USA). The digital material FLX9985-DM (TangoBlackPlus + VeroClear, Shore Hardness 85A) has been used for the walls of the internal cavity and the rail. TangoBlackPlus FLX930 material (Shore Hardness 28A) instead has been used for the suckers.

RESULTS

Preliminary tests have been performed on animal tissue (chicken breasts), showing that it is possible to: 1 – firmly anchor the proposed system to the tissue when a vacuum pressure of 0.092 MPa ($P_a = 9.325 Pa$) is applied, 2 – connect a US-probe paired with the custom attachment and 3 – slide it along the whole length of the rail, without causing the system to detach or damaging the underlying surface of the tissue. Detailed results related to this investigation will be presented in a separate paper.

CONCLUSION AND DISCUSSION

In this work, the concept of pneumatically attachable flexible rails for MIS surgical applications has been introduced for the first time. The proposed system on top of its main function, i.e. to provide a rail-like structure to guide probes along its length, can be used also to:

- actively constrain the shape of the organ/tissue to which it is attached;
- provide a visual reference of known shape and size in the field of view of the endoscope, thus allowing more accurate super-imposition of US-reconstructed 3D images of the tumour in augmented reality (AR).
- create a scaffold to be used to mobilise or retract organs as well as mini- and micro-robotic systems.

The system here presented has been developed for use in RAPN, as this common procedure is among those which can benefit the most of this novel approach, nonetheless its use can be extended to several other procedures (e.g. prostatectomy, partial hepatectomy) and sensing probes (e.g. γ - β -imaging). Not only the abdominal, but also the pelvic and the thoracic cavities and the organs therein can be targeted. Furthermore, the design of the proposed system allows for ease of customization according to the size of the organ or internal body wall targeted. Future work will investigate on the use of the proposed system with peri-operative surgical imaging probes and the coupling with the da Vinci surgical robot system.

REFERENCES

- [1] H. J. Marcus *et al.*, “Trends in the diffusion of robotic surgery: A retrospective observational study,” *Int. J. Med. Robot. Comput. Assist. Surg.*, vol. 13, no. 4, 2017.
- [2] S. Kaul *et al.*, “da Vinci-assisted robotic partial nephrectomy: technique and results at a mean of 15 months of follow-up,” *Eur. Urol.*, vol. 51, no. 1, pp. 186–192, 2007.
- [3] C. G. Rogers, A. Singh, A. M. Blatt, W. M. Linehan, and P. A. Pinto, “Robotic partial nephrectomy for complex renal tumors: surgical technique,” *Eur. Urol.*, vol. 53, no. 3, pp. 514–523, 2008.
- [4] S. B. Bhayani, “da Vinci robotic partial nephrectomy for renal cell carcinoma: an atlas of the four-arm technique,” *J. Robot. Surg.*, vol. 1, no. 4, pp. 279–285, 2008.
- [5] B. F. Kaczmarek *et al.*, “Comparison of robotic and laparoscopic ultrasound probes for robotic partial nephrectomy,” *J. Endourol.*, vol. 27, no. 9, pp. 1137–1140, 2013.
- [6] S. Ohno, C. Hiroki, and W. Yu, “Design and manipulation of a suction-based micro robot for moving in the abdominal cavity,” *Adv. Robot.*, vol. 24, no. 12, pp. 1741–1761, 2010.
- [7] G. Knight, W. D. Fox, and D. R. Schulze, “Cardiac stabilizer device having multiplexed vacuum ports and method of stabilizing a beating heart.” Google Patents, 08-Jul-2003.
- [8] B. Schena, “Extendable suction surface for bracing medial devices during robotically assisted medical procedures.” Google Patents, 19-Feb-2013.

Contact Force Estimation for Minimally Invasive Robot-assisted Laser Osteotomy in the Human Knee

M. Eugster¹, E. I. Zoller¹, L. Fasel¹, P. C. Cattin², N. F. Friederich³, A. Zam⁴, G. Rauter¹

{BIROMED-Lab¹, CIAN², BLOG⁴}, Dept. of Biomedical Engineering, University of Basel, CH

³Dept. of Orthopedic Surgery, University Hospital Basel, CH

manuela.eugster@unibas.ch

INTRODUCTION

We are developing a robotic endoscope with an integrated laser osteotome. The goal of this laser osteotome is to combine the advantages of laser osteotomies with those of minimally invasive surgery. The robotic endoscope is controlled through teleoperation and the laser optics as well as a camera for visual feedback are integrated in the endoscope end-effector. In order to allow precise laser cuts, the end-effector needs to be positioned accurately and stabilized at the cutting location. Therefore, an active parallel mechanism [1] is integrated in the endoscope end-effector which allows attaching the tip of the endoscope to the bone and to manipulate the end-effector accurately within three planar degrees of freedom (DoF) (Fig. 1). Precise bone cuts are relevant in many surgical areas, however, we focus on using our device for unicompartmental knee arthroplasty (UKA). This is a technically challenging surgery where the alignment of the implant and therefore the bone cuts are of uttermost importance with respect to the clinical outcome [2].



Figure 1. The overall system setup consists of a serial robot which holds a robotic endoscope. The tip of the endoscope houses the laser optics and the laser beam exits the endoscope orthogonally to its longitudinal axis in order to ablate the bone below. An integrated parallel mechanism can position and stabilize the endoscope tip on the bone.

One of the main challenges when developing robotic tools for minimally invasive surgery is the lack of a formal design methodology [3]. It is especially difficult to find literature documenting anatomical manipulation requirements such as the forces required to manipulate a robotic tool inside a human joint or the available workspace within human cavities. There is some literature available on interaction forces during laparoscopic surgery [4], but to the best of our knowledge, no such information is available for manipulations within the human knee.

This paper presents experiments for the estimation of expected contact forces between the endoscope end-effector and the surrounding tissue inside the human knee joint. Our aim was to estimate the magnitudes of both axial and lateral forces which have to be overcome in order to move the endoscope tip inside the knee capsule on the femur along the necessary cutting lines for an Aesculap® univation® X knee implant (Aesculap AG, Tuttlingen, Germany).

MATERIALS AND METHODS

The necessary bone cuts for the femoral part of the knee implant were defined together with an orthopedic surgeon by fitting a 3D model of the implant on a 3D model of the femur that was segmented from a high resolution MRI scan and provided by numex GmbH (Dietikon, Switzerland). For the study, only the distal and posterior cuts were selected. These cuts were chosen based on the available workspace inside the knee joint. Thus, the distal cut will have to be executed from the medial side of the medial condyle at approximately 45° knee flexion and the posterior cut will be executed with the end-effector attached to the distal part of the condyle at about 90° knee flexion (Fig. 2). The chamfer cut, which adds a chamfer between the distal and posterior cutting planes, will most likely be executed in a similar fashion as the posterior cut and we therefore do not expect substantial differences in the required forces as compared to the posterior cut.

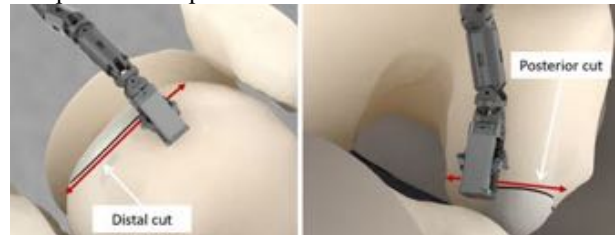


Figure 2. Left side: path for the distal cut of the femur. Right side: path for the posterior cut of the femur.

A probe which in size and form is comparable to our current endoscope end-effector prototype was manufactured and connected to a 6 DoF Nano17 force/torque sensor with calibration SI-12-0.12 (ATI Industrial Automation, Inc., Apex, NC, U.S.A.) by a rod of 60 mm length. The sensor itself was mounted on a cylindrical handle that was manipulated by an orthopedic surgeon, experienced in knee surgery (Fig. 3). To record the measured forces, a control cabinet including an embedded PC which runs TWINCAT3 (Beckhoff

Automation AG, Verl, Germany), a real-time automation software, was used. Prior to measurement the probe was held vertically and offsets were removed. During the experiments, the surgeon was instructed to insert the probe into the knee joint through an incision similar in place to the ones used in current UKA surgeries but of smaller size. The probe was then navigated five times along each of the preplanned cutting paths. The whole experiment was recorded with a standard digital camera. The footage was then synchronized with the force measurements in order to assign the measured forces to the respective movements of the surgeon. All measurements were conducted on a deceased male subject, aged 76, Thiel-embalmed (Ethics Committee of Northwest/Central Switzerland, Basel, Nr. 2018-00158).



Figure. 3 Setup for the force measurements. Left: The surgeon navigates the probe along the preplanned cutting paths. Right: Probe attached to the force/torque sensor mounted on a handle.

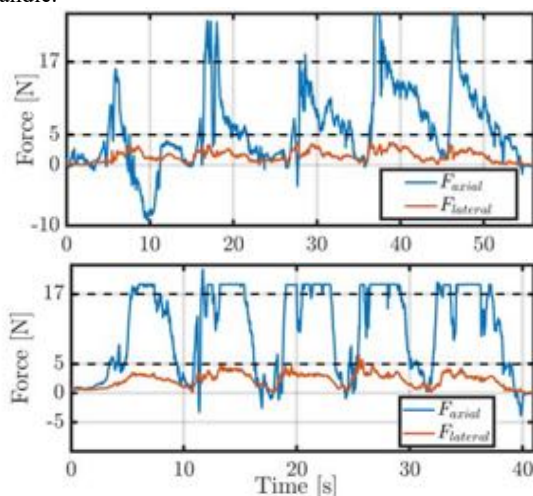


Figure. 4 Force measurement data from the experiments. Top: path along the distal cut of the femur; bottom: path along the posterior cut of the femur. Each cutting path was retraced five times.

RESULTS

The measured forces for the five trials of both cutting paths are shown in Fig. 4. Since the sensor's range limit is specified by the manufacturer to be 17 N, all forces exceeding this force might not be accurate and therefore the plot's y-axis is limited at 25 N. While the lateral forces remained mostly below 5 N, the measured axial forces were much higher and often exceeded the 17 N limit.

CONCLUSION AND DISCUSSION

The presented force estimation experiments provide a rough estimate of the expected contact forces in a minimally invasive UKA. However, it has to be emphasized that these experiments purely allow conclusions about the order of magnitude of the required actuator forces. In addition to the sensing range limit of the force/torque sensor, several other factors might have influenced the results: First, mounting the measurement probe on a rigid link led to the measurement of forces that were acting on the rod in addition to those acting on the endoscope tip. Secondly, since the probe was moved manually in a minimally invasive manner without any visual feedback, the probe tip and the rigid link were sometimes pushed against anatomical constraints such as the border of the knee capsule or the bone. We suspect that this, in combination with the first point, led to higher forces than we expect in the robot-assisted procedure since these constraints would be avoided by the robotic device. Thirdly, even though Thiel embalming conserves the properties of tissue relatively well, there are still significant differences to living tissue.

We conclude that the expected relevant contact forces for minimally invasive UKA will most likely be below 10 N laterally and at around 25 N axially. However, to confirm these values, we will in a next step repeat the measurements with a miniature force sensor attached directly to the mockup end-effector in order to overcome some of the abovementioned limitations.

ACKNOWLEDGEMENT

The authors gratefully acknowledge funding of the Werner Siemens Foundation through the MIRACLE project. Also, we would like to express our gratitude towards Prof. Müller-Gerbl from the Anatomical Institute of the University of Basel, who supported the experiments. Further support was provided by Aesculap AG (Tuttlingen, Germany) and numex GmbH (Dietikon, Switzerland).

REFERENCES

- [1] M. Eugster et al., "Positioning and stabilisation of a minimally invasive laser osteotome," in Hamlyn Symposium on Medical Robotics, 2017.
- [2] M. Roche et al., "Robotic arm-assisted unicompartmental knee arthroplasty: preoperative planning and surgical technique" in American Journal of Orthopedics, vol. 38, 2009.
- [3] N. Simaan et al., "Medical technologies and challenges of robot-assisted minimally invasive intervention and diagnostics" in Annual Review of Control, Robotics and Autonomous Systems, 2018.
- [4] H. Yamanaka et al., "Measurement of the physical properties during laparoscopic surgery performed on pigs by using forceps with pressure sensors," Advances in Urology, vol. 2015, pp. 1-10, 2015.

Design and integration of electrical bio-impedance sensing in surgical robotic tools for tissue identification

Zhuoqi Cheng¹, Diego Dall'Alba², Simone Foti³, Andrea Mariani³, Thibaud Chupin³, Darwin Caldwell¹, Paolo Fiorini², Elena De Momi³, Giancarlo Ferrigno³, Leonardo Mattos¹

¹ADVR, Istituto Italiano di Tecnologia, Genova, Italy,

²Altair Robotics Lab, University of Verona, Verona, Italy,

³NearLab, Electronic Information & Bioengineering Dept., Politecnico di Milano, Milano, Italy.

zhuoqi.cheng@iit.it

INTRODUCTION

The diffusion of Robot-assisted Minimally Invasive Surgery (RMIS) consistently increased over the last 15 years. Thanks to the enhanced dexterity and 3D vision provided to the surgeon, RMIS can translate a conventionally difficult surgical procedure into an easier work for surgeons and, ultimately, better surgical outcomes for patients.

Advanced sensing technologies are of paramount importance for RMIS to ensure a safer and faster procedure. However, vision is currently the only sensing technology that provides real-time feedback from the surgical site on most surgical robotic systems (such as the daVinci robot, Intuitive Surg. Inc.). However, providing additional sensing information to the surgeon would lead to a better understanding of the operational field and, consequently, improve the confidence in performing important surgical actions (e.g. definition of resection margins). Although different sensing technologies (e.g. tactile sensing) have been studied for this purpose, the complexity of the required surgical tools' modifications and integration with the robotic system often make them difficult to be applied.

To address this issue, we proposed to use Electrical Bio-Impedance (EBI) sensing technology. Such sensor can be easily integrated to a standard bipolar tool for providing fast and accurate tissue detection and identification.

MATERIALS AND METHODS

There are several factors that can significantly affect the EBI measurement via a bipolar forceps, including the excitation frequency (f), the jaw opening distance (L) and the pressing depth (d) (Figure. 1(a)). The Cole model [1] describes the tissue as a circuit including one resistor in series with one capacitor, and both in parallel with a resistor. This model interprets the changing trend of EBI when different excitation frequencies are applied. In addition, different jaw opening distances of the forceps can apply different current density to the measuring tissue area, which results to a different EBI value. Moreover, study [1] showed that tissue compression can change the intracellular impedance and extracellular impedance of the tissue, resulting in a significant change of the EBI value.

In this study, an EBI sensing device is designed and integrated to a bipolar forceps. Then an experiment is performed to characterize the above factors and evaluate the efficacy of the sensor for tissue identification.

Figure.1(b) shows the prototype of the designed EBI sensing device which consists of an electrical impedance converter (AD5933) and a micro-controller. The device can be directly mounted on top of a daVinci Maryland bipolar endowrist, and connects to its proximal end for measuring the EBI of the tissue contacting its jaws. The measured value is sent to a computer via USB. The sensing device was calibrated with several known resistors ranging from 786Ω to $8.2k\Omega$, which covers the range of EBI for most tissue types. The error rate was found to be 0.59% in average, and the maximum error rate was found to be 1.2%.

Figure. 1(c) shows the experimental setup. Four types of ex-vivo porcine tissues including liver, lung, muscle and fat were used. A micro-motion stage was used to control the vertical motion of the bipolar forceps. At the beginning of the measurement, the jaw opening distance was fixed to be one of the following: 2, 4, 6, 8, 10 and 12 mm, and the excitation frequency was set to be from 10 to 100 kHz with a step of 10 kHz. The position of the tool was then adjusted to right touch the tissue, and this position was set as zero. Subsequently, we controlled the forceps to move 5 mm downwards, and recorded the EBI values every 1 mm.

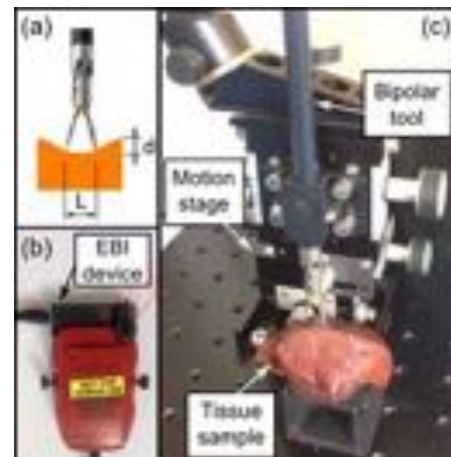


Figure. 1. (a) The model of the EBI measurement; (b) The device is mounted on top of the bipolar tool in use; (c) The experimental setup.

Based on the measured results, a Gaussian model was constructed for each tissue type and each jaw opening distance. Then a tissue classification method based on Gaussian naïve Bayes classifier was designed. Then we performed experimental validation of the proposed tissue classifier considering different value of d and L . For each condition, we collected 20 samples and then the mean value of the samples was used to compute the probabilities given the Gaussian distributions of the corresponding jaw opening distance and different tissue types. The type of contacting tissue was then estimated by the maximum probability value. It took an average of 0.8 s for the system to identify each tissue type.

RESULTS

For each tissue type, excitation frequency (f), pressing depth (d) and jaw opening distance (L), at least 6 EBI measurements were collected for analysis. The experimental results revealed that the EBI values decreased with a higher excitation frequency, a bigger pressing depth and a smaller jaw opening distance.

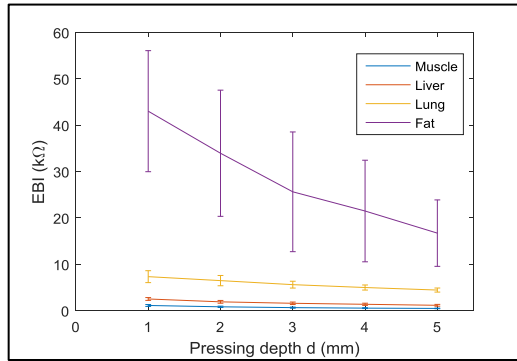


Figure 2. The EBI of 4 tissue types are measured with a 10 mm jaw opening distance, 100 kHz excitation frequency and different pressing depth from 1 mm to 5 mm. The vertical bars indicate the standard deviation of the EBI measurements.

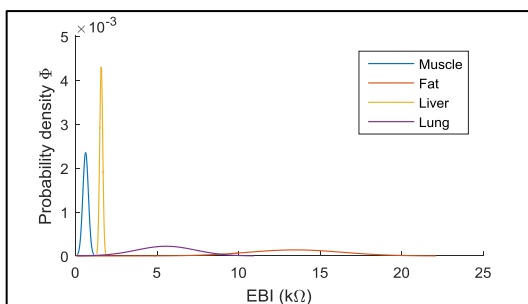


Figure 3. Four Gaussian distributions are formed based on the measured EBI values of 4 types of tissues ($f = 100$ kHz, $L = 8$ mm, $d = 2-5$ mm).

Figure 2 shows an example of the EBI values of 4 tissues types with $L = 10$ mm, $f = 100$ kHz and $d = 1 - 5$ mm. The EBI values at the contact moment ($d = 0$ mm) were discarded due to the huge variance caused by unstable contact between the jaws and the tissue. We found out that using a single excitation frequency ($f = 100$ kHz) is enough for identifying these 4 tissue types, but the pressing depth should be controlled within a

range (d from 2 to 5 mm). In this case, a reliable contact between the jaws and the tissues can be guaranteed, and the distance of the pressing depth is enough to allow good control by the user.

Figure 3 shows an example of four Gaussian distributions of four different tissue types whose EBI values were measured with a 8 mm jaw opening distance. The theoretical misclassification error rates of the classifier were computed and found to be all $< 7.7\%$.

As shown in Figure 4, the system was tested with ex vivo porcine tissues, moving the tool manually with a random jaw opening distance. The tests were repeated 10 times, and in all the trials the designed classifier was capable of identifying different tissues accurately.



Figure 4. The experimental results demonstrate that the EBI sensing system can accurately detect different tissues.

CONCLUSION AND DISCUSSION

This study is a part of the EL.I.S.A. project which aims to apply EBI sensing for various surgical applications. This study presents some preliminary results to demonstrate the feasibility of using EBI sensing for tissue identification. The future study will integrate the EBI sensing technology and augmented reality technology for assisting the surgeon in detecting and tracking different tissue areas such as different organs or cancerous tissue during a RMIS. Also, more tissue types and higher frequencies will be tested in the future study.

REFERENCES

- [1] K. S. Cole, and R. H. Cole. Dispersion and absorption in dielectrics I. Alternating current characteristics. The Journal of chemical physics, 1941.
- [2] O. G. Martinsen and S. Grimnes. Bioimpedance and bioelectricity basics. Academic press, 2011.

Haptic Feedback Helps Surgeons with Different Level of Expertise on Bimanual Laser Surgery

S. Portolés Díez¹, M.A. Ahmad¹, G. Borghesan¹, C. Meuleman², E.B. Vander Poorten¹

¹Mechanical Department, KU Leuven, ²Department of Development and Regeneration, UZ Leuven
Sergio [dot] PortolesDiez [at] kuleuven.be

INTRODUCTION

Robotic minimal invasive surgery is gaining acceptance in surgical care. Whereas 3D vision and enhanced dexterity are typical benefits attributed to commercially available robotic surgical platforms, haptic feedback is not yet offered. For this reason robotics is not considered beneficial for delicate interventions such the endometriosis. Overall, haptic feedback remains debatable and yet unproven except for some simple scenarios such as Fundamentals of Laparoscopic Surgery exercises [1].

A new training exercise, “Endometriosis Surgery Exercise” (ESE) has been devised approximating the setting for monocular robotic endometriosis treatment. A bimanual bilateral teleoperation setup was designed for laparoscopic laser surgery. Haptic guidance and haptic feedback are respectively offered to the operator.

This paper investigates the value of haptics in a more complex scenario, namely on a specially developed model for training surgery for treatment of endometriosis, comparing the performance of experts versus novices.

MATERIALS AND METHODS

Currently there are no golden standard endometriosis training models that can prove effectiveness of a specific surgical practice. We propose a model where the affected organ and endometriotic tissue are represented by the pericarp of a tomato. The exocarp (skin) of the model, which is the stiffer part, takes the role of the fibrotic tissue. The underlying mesocarp (flesh) corresponds then to the healthy organ tissue. In a raw tomato the mesocarp and the exocarp are strongly connected, in fact, stronger than is the case for a typical endometriotic lesion. The raw model makes it overly difficult to separate both. By precisely controlling the conditions of a warm bath the connectivity between layers is adjusted.

A robotic system and a procedural training exercise for RMIS have been designed using the abovementioned training model. The robotic platform has been designed as a laboratory prototype for bimanual laser surgery, however, it is not certified for clinical use. It is equipped with two robotic arms, one holding a laser laparoscope and a second holding a grasper (Fig. 1) and it is used to remove a 21 mm x 13 mm rectangular patch of the exocarp. A patch is colored in green after the cooking (Fig. 2), so that the participant has a clear view on the area to be removed. The participant is asked to remove the entire exocarp patch without leaving behind visual marks. The task consists in edging the perimeter of the

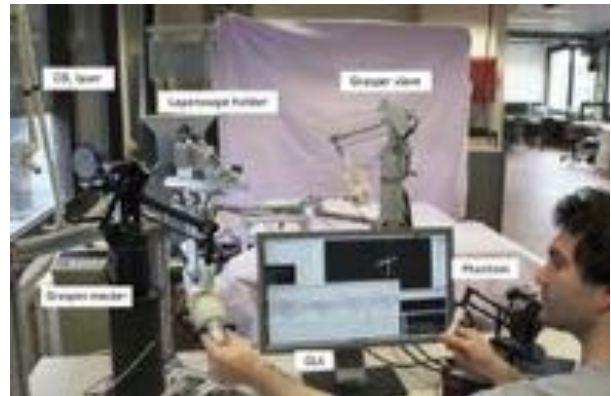


Figure. 1. Overview of experimental bimanual laser surgery setup. Two master joysticks are controlled by the operator. Steering commands are sent to a laser laparoscope holding slave robot and a robot controlling a grasper. The interaction force exerted by the slave is fed back via a bilateral controller and is well perceivable by the operator.

marked patch with the ablation laser. After edging, the patch is to be peeled off. The peeling requires simultaneous and coordinated operation of both laser laparoscope and grasper. By lifting the grasped patch, the ‘cleavage’ plane (plane separating healthy from diseased tissue) becomes visible. During the entire exercise the operator can observe the motion of the instruments and of the endometriosis model on a monitor in front of him/her.

The bimanual robotic platform is composed out of four main components, as presented in Fig. 1. At the slave side one robot is used to steer the laser laparoscope; a second robot controls a MIS grasper. At the master side two haptic joysticks are used to control the pair of slave robots. The surgeon holds these joysticks but also operates three foot-pedal buttons. These are used to control the ablation laser (on/off) or to clutch (decouple) each master-slave pair. Since laser is not supposed to touch the organs, force does not need to be fed back here, and hence a unilateral controller suffices. For the grasping forceps both a unilateral and a bilateral controller have been implemented. The effect of haptic feedback is investigated by comparing the difference in performance between the two controllers.

USER CAMPAIGN AND RESULTS

A user campaign has been organized. Subjects were invited to execute the ESE, described in previous section, three times under two conditions in random order. Nine

Table. 1. Comparison of the metrics grouped by level of expertise and type of controller.

	Novices						Licensed					
	No Haptic		Haptic		P-value		No Haptic		Haptic		P-value	
	Mean	STD	Mean	STD			Mean	STD	Mean	STD		
Max Force	7,47	4,35	4,16	1,7	0,0014	**	5,67	3,06	4,52	2,53	0,37	
Mean Force	0,87	0,43	0,54	0,34	0,032	*	0,66	0,4	0,34	0,08	0,09	
Time End	638	255	653	377	0,93		508	124	666	302	0,35	
Accidents	1,11	1,08	0,47	0,71	0,07		0,88	0,92	0,125	0,35	0,044 *	

	No Haptic		Haptic		P-value		Novices		Licensed		P-value			
	Novices		Licensed				Novices		Licensed					
	Mean	STD	Mean	STD			Mean	STD	Mean	STD				
Max Force	7,47	4,35	5,67	3,06	0,25		4,16	1,7	4,52	2,53	>0,99			
Mean Force	0,87	0,43	0,66	0,4	0,19		0,54	0,34	0,34	0,08	0,47			
Time End	638	255	508	124	0,14		653	377	666	302	0,59			
Accidents	1,11	1,08	0,88	0,92	0,65		0,47	0,71	0,125	0,35	0,3			

surgeons of varying levels of expertise participated in the experiments. The age of participants ranged from 26 to 39 years. Five participants were female, four were male.

The following parameters were recorded: experiment identifier, subject gender, subject age, subject preferred hand, type of controller (with / without haptic feedback) and order of the experiment. The following signals were recorded at 60Hz: joint positions of 1) endoscopic master q_{em} , 2) endoscopic slave q_{es} , 3) grasper master q_{gm} , 4) grasper slave q_{gs} , 5) status of the foot pedals $S = [s_g, s_e, s_i]^T$, 6) forces at the trocar w_{tr} , 7) forces at the grasper handler w_h , and 8) forces at the grasper tip w_{tip} .

Laparoscopic psychomotor skills can be assessed by different metrics computed from recorded time series. Here, all acquired data was post-processed to compute metrics that tell something about the applied forces, the paths that were followed by the grasper, instants and duration of laser and clutching actions. Also the smoothness of the motion or uncontrolled collisions that took place are gauged. Collisions are counted when the tools, laparoscope and grasper. Table I summarizes the

data grouped by level of expertise of the surgeon and by type of controller used. Mann-Whitney test results are shown along each metric. Other metrics with less significance are reported in [2].

CONCLUSION AND DISCUSSION

Most significant differences caused by the controller used (unilateral / haptic feedback) are found on metrics “Max Force” and “Mean force”. Specially, novice surgeons present a more delicate behavior (‘max’ $P < 0,01$ and ‘mean’ $P = 0,03$) when using the bilateral controller (a.k.a. haptic feedback). Licensed surgeons also benefit from this controller, however their largely trained skills let them limit interaction forces even with the unilateral controller. The number of accidents was observed to decrease ($P = 0,04$). Many subjects stated that the force felt with the haptic feedback was making them more cautious and that it was acting as a barrier to avoid perforations on contact with the model. Surgeons also preferred to use a bilateral controller when working with ESE.

Looking at the differences between expertise groups, separating data coming from unilateral and bilateral controllers, one can guess a tendency to lower (improve) the scores of all the presented metrics. The number of samples is, however, small (18 novices, 12 licensed; several repetitions per subject) to find the differences statistically significant. We expect that with a further collection of data from ESE, these metrics, and others, could be used to assess the learning process of laparoscopy students.

REFERENCES

- [1] N. Enayati et al., “Haptics in robot-assisted surgery: Challenges and benefits,” *IEEE Reviews in Biomedical engineering*; 2016; vol. 9:49-65.
- [2] S. Portoles-Diez et al., “Evaluation of Haptic Feedback on Bimanually Teleoperated Laparoscopy for Endometriosis Surgery,” *IEEE TBME*, 2018 [Submitted].



Figure. 2. Photograph of tomato model marked with green pen; the part of exocarp that needs to be ‘surgically’ removed from the mesocarp.

Soft and Inflatable Hand Rehabilitation Device with Haptic Perception, Evaluation of Applied Forces

J. Konstantinova^{1*}, C. Y. Zhang^{2*}, K. Althoefer¹

¹*Centre for Advanced Robotics @ Queen Mary (ARQ), Queen Mary University of London, UK*

²*Royal College Of Arts, London, UK*

j.konstantinova@qmul.ac.uk

INTRODUCTION

This work presents a soft and inflatable hand rehabilitation device that is able to perceive forces applied during interaction. The proposed rehabilitation device aims to improve hand and finger functionality for patients with hand impairment, such as arthritis or carpal tunnel syndrome, and for those who need post stroke rehabilitation, as well as general physiotherapy exercises after hand injuries [1]. There are several directions how robotics contributes to upper-limb rehabilitation, such as virtual reality [2] that focuses on motion development only, as well as exoskeletons and prosthetics [3], [4] that can be not convenient to use or require complex calibration. The proposed device:

- Is designed to assist in rehabilitation of hand motor skills for hand rehabilitation;
- Can adapt the stiffness of the system to stimulate desired grasping force;
- Is able to provide feedback to the physiotherapist regarding progress of the patients.

One of the benefits of the proposed rehabilitation device is the possibility to use it for different operation modes that focus on several types of exercises. Namely, the device can be used for separate exercises at different stiffness levels, for reactive mode that adapts stiffness of the rehabilitation device based on the applied force, as well as for finger extension when device dynamically inflates and deflates.

MATERIALS AND METHODS

Main components of the rehabilitation device are as follows: soft inflatable device with the spherical shape, pneumatic system used for device actuation, and a force sensing system to evaluate user interaction forces. Force and torque sensor FT17 (force range ± 50 N for lateral forces, and ± 70 N for normal force; IIT, Italy) is used to measure forces during exercising with a rehabilitation device. Moreover, the design of the device allows the use of various force sensors, including low-cost solutions, for real-world rehabilitation applications.

The rehabilitation device described in this work can be operated using different pneumatic pressures – from fully deflated to inflated state with maximum of 2 Bar (Figure 1). The pneumatic system consists of a compressor and a pressure regulator valve (ITV1000 series, maximum operating pressure of 3 Bar), and it is connected to an inflatable chamber of the rehabilitation device. Input pressure of the rehabilitation device is controlled based

on the measurements of an applied force during exercising, as well as depending on the mode of operation.

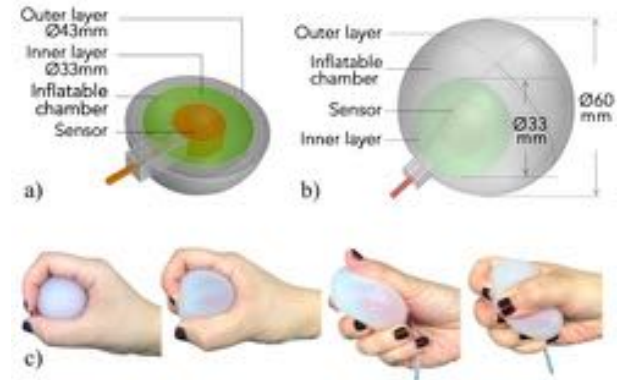


Figure. 1. Design of soft and inflatable post-stroke rehabilitation device: a) uninflated rehabilitation device, b) inflated to 2 Bar rehabilitation device, c) hand interaction with the rehabilitation device.

The outer diameter of the deflated device is 43 mm. This dimension was chosen to be approximately half of mean hand breadth measure of 85 mm, obtained in [5], in order to ensure palm wrapping around the spherical shape of the rehabilitation device. The outer diameter of a fully inflated sphere is 60 mm. The prototype was fabricated using soft and stretchable EcoFlex0030 silicone with tensile strength of 200 psi and 900% of elongation at break (Smooth-On Inc., US). The rehabilitation device consists of two chambers (Figure 1) – inner layer that fixes force and torque sensor to measure interaction forces, and chamber that is used for inflation. The outer diameter of the inner chamber is 33 mm. The outer layer of a silicone was selected to be 5 mm thick in order to avoid ballooning effect.

RESULTS

This section discusses experiments that were performed to design and evaluate a soft and inflatable post-stroke rehabilitation device. In order to study the desired stiffness of an inflatable rehabilitation device, we test grasping force that is required to deform a soft therapy putty that is typically used as a passive hand exercising method for post-stroke patients and patients with other hand impairments. The material of a therapy putty can have different stiffnesses that varies depending on the needs of patients [6]. It is required to understand what are the highest forces that can be exerted by human hand

* Authors have contributed equally.

during exercising. Therefore, we focus on evaluation of a desired grasping force for material with highest and medium stiffness. In order to perform this experiment, a six degrees-of freedom force and torque sensor (FT17, IIT) was embedded in a spherical shape therapy putty, as shown in Figure 2. As a result, the sensor was covered with a 3 cm layer of material to enable deformation. Sharp edges of the sensor were not detectable due to thick layer of the material. Six healthy subjects were invited to perform experiments. They were instructed to perform deformations of a therapy putty. In order to avoid any specific behaviors, subjects were not given instructions to apply any specific forces.

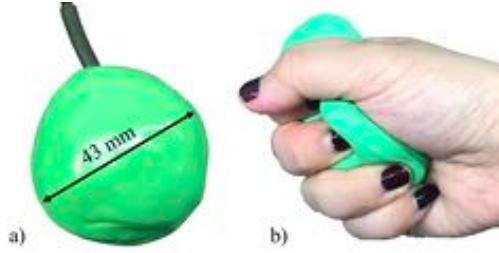


Figure 2. Evaluation of applied forces during hand exercises: a) sensor embedded in the medium stiff therapy putty, and b) deformed therapy putty during exercises.

Soft and inflatable nature of a device allows to implement various levels of material stiffness, as it was discussed in the previous section. Further on, the forces applied to the rehabilitation device is evaluated. We tested device in fully deflated state, as well as applying pressure of 1 and 2 Bar. To compensate for the effect of pressure on the sensor measured force magnitude is biased. Figure 3 shows the feedback of force magnitude recorded during exercising with a therapy putty, as well as a rehabilitation device at different levels of inflation. Moreover, the results of force magnitude recorded during experiments with subjects is analyzed. The main criteria of evaluation are mean and maximum forces, as well as the average peak width. Maximum pressure is used to characterize the maximum force that can be exerted by a subject during a single grip. The average peak width characterizes the mean length of a grip in seconds during interaction. This parameter can also be used for evaluation of an ability to exert certain forces for a given period of time. High peak width corresponds to grasps of high strength, while shorter peak width corresponds to faster motion of exercise. Table I summarizes the results obtained during experiments with therapy putty and rehabilitation device. It was observed that the results are similar for stiff and medium stiff therapy putty with the average maximum applied force of 37.7 and 35.3 N, respectively. However, the rehabilitation device in deflated state stimulates users to exert higher average mean force of 6.7 N. This is also combined with the highest average peak width of 1.8 seconds. It can be observed that the rehabilitation device in inflated state stimulates users to apply lower forces, but at the higher rate. This demonstrates that the rehabilitation device can be successfully used both for strength exercises and for dexterity training when fast manipulation is required.

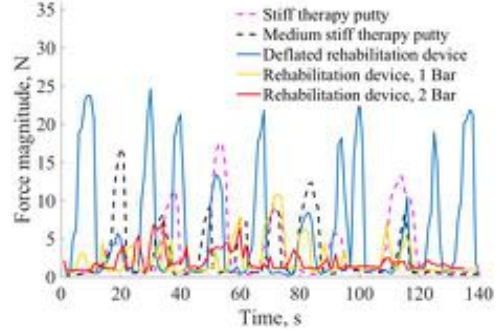


Figure 3. Sample force magnitude for one subject recorded during exercising with therapy putty (dotted lines) and soft rehabilitation device (solid lines) - sample pattern of force magnitude applied by a selected subject.

TABLE I. RESULTS OF FORCE EVALUATION

Type of Device	Evaluation criteria		
	Average mean force, N	Average maximum force, N	Average peak width, s
Stiff therapy putty	4.9	37.7	1.69
Medium stiff therapy putty	5.1	35.3	1.62
Rehabilitation device, deflated	6.7	31.8	1.80
Rehabilitation device, 1 Bar	3.8	16.5	1.01
Rehabilitation device, 2 Bar	3.3	12.0	0.82

CONCLUSION AND DISCUSSION

In this paper we presented design and evaluation of a concept prototype of soft and inflatable hand rehabilitation device with haptic perception. The presented work is focused on the evaluation of the applied force during user interaction. In future work, we are planning to evaluate the functionality of the proposed device involving patients with hand impairment.

ACKNOWLEDGEMENT

This work was supported in part by the EPSRC National Centre for Nuclear Robotics project (EP/R02572X/1) and the Innovate UK WormBot project (104059).

REFERENCES

- [1] R.W.Bohannon, "Muscle strength and musclettraining after stroke," *Journal of Rehabilitation Medicine*, vol. 39, no. 1, pp. 14–20, 2007.
- [2] A. Henderson, N. Korner-Bitensky, and M. Levin, "Virtual Reality in Stroke Rehabilitation: A Systematic Review of its Effectiveness for Upper Limb Motor Recovery," *Top. Stroke Rehabil.*, vol. 14, no. 2, pp. 52–61, 2007.
- [3] R. Bogue, "Exoskeletons and robotic prosthetics: A review of recent developments," *Ind. Rob.*, vol. 36, no. 5, 2009.
- [4] Z. Yue, X. Zhang, and J. Wang, "Hand Rehabilitation Robotics on Poststroke Motor Recovery," *Behavioural Neurology*, vol. 2017, 2017.
- [5] T. M. Greinger, "Hand Antropometry of U.S. Army Personnel," 1989.
- [6] R. M. Gibbon, "Monitor putty with increasing stiffness," US5693689A, 1997.

Contact Force Measurement for Medical Ultrasound Imaging

Ata Otaran, Halime Gulle, Stuart Miller, Ildar Farkhatdinov

Queen Mary University of London, UK

a.otaran@qmul.ac.uk

INTRODUCTION

Ultrasound imaging is a non-invasive diagnostic method used to see internal body structures such as tendons, muscles, bones and other organs. This imaging technique is based on utilizing high frequency sound waves. Measurement of amplitudes and travel durations of reflected ultrasound waves enable continuous imaging of the inner tissues. Applying the right amount of pressure to a patient's body with the ultrasound probe during imaging is crucial for retrieving high quality images. Usually medical students learn correct ultrasound probe operation by trial and error until they acquire sufficient probe manipulation skills. Measuring interaction probe-patient body contact forces can be handy for monitoring and improving the ultrasound imaging training. In this paper we describe our approach to measure contact forces with the help of inexpensive but efficient sensing devices.

Previously, several other force measurement ultrasound probe designs were proposed for various purposes. In [1] and [4] a single degree-of-freedom (DoF) force feedback tele-echography devices to increase the availability of sonographers were described. In [2], a six-DoF force sensor was used to investigate the importance of repeatability of force profiles during separate medical imaging instances to keep the tissue deformation due to pressure of the probe constant. In [3], a hand-held probe with 6-DoF force measurement was proposed for understanding sonographer injuries which is a very serious problem affecting more than at least 80% of the correspondents in surveys carried out in [5] and [6]. A handheld and robot mounted system for replacing the CT and X-ray imaging with ultrasound, for needle insertion guidance tasks was presented in [7].

In contrast to previous works, present work demonstrates a low-cost and easily attainable single-DoF force sensing solution for ultrasound imaging. The developed interface can be easily manufactured, mounted to the ultrasound probe and used by research and teaching facilities, sonographers and even practicing students.

MATERIALS AND METHODS

The design of the force feedback interface is optimized for attainability of the interface. All of the parts are either off the shelf or can be attained using a desktop type 3D-printer without requiring any expensive machining. The current design version was specifically developed for SonoSite HFL38X type ultrasound transducer. However, our design can be easily updated to support other probes.

Figure 1 shows the top view (A) and general view (B) of the probe with our force measuring interface mounted on it. The developed interface is composed of two 3D printed parts: a fixed base which is attached to the base of the probe, and a passive moving part; a handle which can move back and forth during imaging. Both parts are connected with mechanical springs. The moving handle is supported by plastic caster ball bearings to reduce friction and provide smoothness of sliding movements. As a result, the movement of the slider is restricted to the longitudinal axis using caster wheels.

The force sensing is performed on the longitudinal axis of the device by measuring the displacement of the moving part (slider) w.r.t. the base. The displacement is estimated using a hall effect sensor and two magnets (shown in Figure 1A). Figure 2 demonstrates the arrangements of the two permanent magnets and the Hall-effect sensor in our interface. The output analogue signal from the Hall-effect sensor is sampled with analogue-to-digital converter (ADC) and is used to estimate the displacement of a magnet attached to the moving slider w.r.t. to the non-moving Hall-effect sensor. The estimated displacement of the moving part is then used to calculate the contact force, assuming that the spring's stiffness is constant and known. A detailed description of this force estimation technique and related calibration can be found in [8].

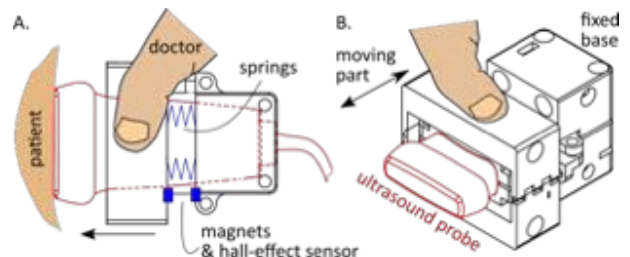


Figure 1. The developed contact force measuring interface mounted to the ultrasound imaging probe.

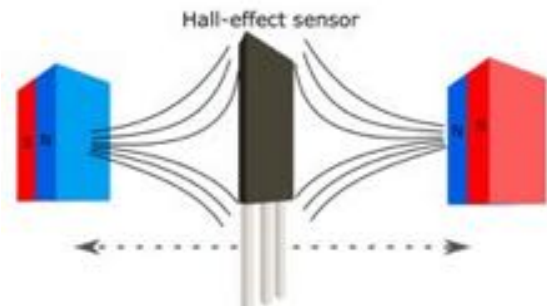


Figure 2. Schematics demonstrating the use of a Hall-effect sensor and two permanent magnets to measure displacement.

RESULTS

We have manufactured, assembled and tested the contact force measuring interface with SonoSite HFL38X ultrasound imaging probe. The key components and the assembly of the interface are shown in Figure 3A-B. The stiffness of the extension springs used in the interface is approximately 4.76 N/mm. The maximal displacement is 16 mm. Therefore, the maximal available force reading is 76 N which is sufficient for most of the sonography tasks. The force sensing resolution, using a low-cost 10-bit ADC is estimated to be around 0.3 N.

Figure 3C shows the estimated contact force during the operation of the probe. A user pushed against a soft material (simulated a human body) with the probe for about 3 seconds. The plot demonstrates that the measurements are not noisy and the developed interface can be used as a reliable tool to monitor the probe usage.

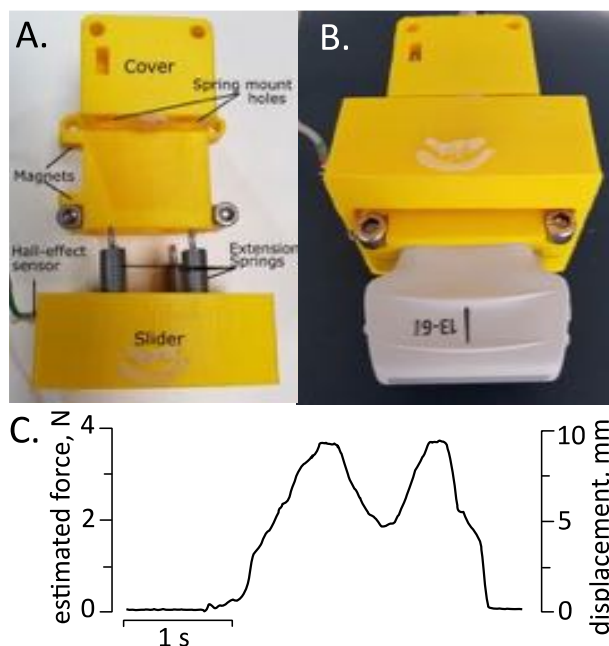


Figure. 3 A) Disassembled and labeled image of the cover and slider. B) Fully assembled and ready to use version of the device with the probe. C) A sample Force vs. Time reading attained with the device.

CONCLUSION AND DISCUSSION

The developed system can be efficiently used to monitor interaction forces applied by a probe to a patient's body. Such systems can be used to improve medical students training leading to better ultrasound imaging. Our solution is low-cost and is easy to maintain. However, current design requires further improvements. For instance, the force resolution can be improved. The force sensing resolution is directly related to the stiffness of the force sensing elements, quality of the hall-effect sensor, and the resolution of the ADC. The stiffness of the compliant prismatic joint can be changed by replacing the springs with softer or harder ones. For instance, tissues where maximum pressure is relatively low can benefit from a softer force sensing unit for increase in resolution.

Additional problems with Hall-effect sensors include significant measurement noise. However, since ultrasound imaging is done with relatively low frequency movements and constant contact with the human skin helps damp out high frequency vibrations, usage of low pass filters with relatively lower cut-off frequencies used in many force feedback systems is possible.

The future works include improvement of the sliding mechanism, minituarisation and design optimisation.

REFERENCES

- [1] S. Chadli, N. Ababou, A. Ababou, N. Djelal and N. Saadia, "A removable device for axial force and orientation measurement on medical ultrasound probe," International Multi-Conference on Systems, Signals & Devices, Chemnitz, 2012.
- [2] R. Burcher, J. Noble, L. Man, A System for Simultaneously Measuring Contact Force, Ultrasound, and Position Information for use in Force-Based Correction of Freehand Scanning, IEEE Trans. on Ultrason., Ferroelectrics and Freq. Control, 52(8) pp. 1330-42, 2005
- [3] M. W. Gilbertson and B. W. Anthony, An ergonomic, instrumented ultrasound probe for 6-axis force/torque measurement, in Proc. IEEE 35th Annu. Int. Conf. Eng. Med. Biol. Soc., 2013, pp. 140–143
- [4] M. Marchal, J. Troccaz, A One-DOF Free-Hand Haptic Device for Robotic Tele-Echography. Studies in Health Technology and Informatic Series, IOS Press, 98, pp. 232-233, 2004.
- [5] I. Pike, A. Russo, J. Berkowitz, J. Baker, V. Lessoway, The prevalence of musculoskeletal disorders among diagnostic medical sonographers, J Diagn Med Sonography 1997;13:219–227
- [6] K. Evans, S. Roll, J. Baker, Work-Related Musculoskeletal Disorders (WRMSD) Among Registered Diagnostic Medical Sonographers and Vascular Technologists: A Representative Sample, Journal of Diagnostic Medical Sonography, Vol 25, Issue 6, pp. 287 – 299, 2009.
- [7] Y. Noh, R.J. Housden, A. Gómez, C.L. Knight, F. Garcia, H. Liu, R. Razavi, K.S. Rhode, K. Althoefer, An ergonomic handheld ultrasound probe providing contact forces and pose information. 37th Annual International Conference of the IEEE Engineering in Medicine and Biology Society (EMBC), 5773-5776, 2015.
- [8] A. Otaran, O. Tokatli, V. Patoglu, (2016) Hands-On Learning with a Series Elastic Educational Robot. In: Bello F., Kajimoto H., Visell Y. (eds) Haptics: Perception, Devices, Control, and Applications. EuroHaptics 2016. Lecture Notes in Computer Science, vol 9775. Springer.

Development of a non-contact device for detecting small animal breathing in dedicated whole-body imaging instruments based on fibre optics and CCD camera

Dalia Osman¹, Gilbert Fruhwirth², Rhode Kawal¹, Yohan Noh¹,

¹Department of Biomedical Engineering, King's College London, UK

²Department of Imaging Chemistry and Biology, King's College London, UK

(Corresponding author): yohan.noh@kcl.ac.uk

INTRODUCTION

During whole body imaging procedures for preclinical research, mice are placed under anaesthetic, which incurs physiological effects. These must be regulated. Respiration rate is an effective way to monitor the wellbeing of the animal and an is a good indication of the depth of anaesthesia, helping to avoid hypothermia, or involuntary muscle movement [1]. The normal breathing rate of mice under anaesthesia is 55-60 *breaths per minute* (bpm) [2], up to 120-180 bpm in lighter levels of anaesthesia [3].

There are many current methods that are used to monitor respiration in small animals; many of these require contact with the body[4] and are very bulky. Some also require excess equipment such as filters and amplifiers [5]. The novel device proposed in this project uses a low cost, non-contact respiration monitor that is potentially compatible with all imaging modalities. It aims to be easy to integrate onto animal imaging beds, and does not require extra circuits for filtering.

DESIGN METHOD AND NON-CONTACT BREATHING DETECTION DEVICE

1. Non-Contact Breathing Detection Device: Breathing motion will be detected using multi-pairs of fibre optic cables to detect light intensity variations that will be converted to a breathing waveform. The fibre pairs will be positioned above the animal (Figure 1); these emit and receive light off the surface of the mouse. A Keyence Sensor (FS-N11MN) is used as a light source (630nm wavelength), and reflected light is captured using a CCD camera (XCSource) into successive images. As the mouse is respiring, the light intensity that is reflected from the surface of the mouse will vary with a certain frequency.

2. Continuous Light Intensity Measurement from Image: Images captured by the camera are passed through a median filter to reduce noise, then converted to greyscale. Each 8-bit pixel greyscale image is averaged to give a single greyscale light intensity value. This is repeated for each frame, to give a continuous series of analogue values, that vary in real time, as the distance between the surface of the mouse and the fibre pairs vary with breathing motion. These values are plotted to give a breathing waveform [6].

3. Light Intensity Model: The Gaussian distribution of light is the way in which light spreads from the emitting fibre, as described in [7]. The light that spreads radially reduces in intensity exponentially with increasing distance away from this fibre source. This means light can be modulated by changing distance to the reflecting surface; this is a crucial part of the way this device works.

OPTIMISATION

1. Optimisation Experiment: It is important to find the optimal positioning for the pairs of fibres and the distance away from the surface of the mouse, so that they may be sensitive to small breathing displacements of the abdomen. The set up in Figure 2 shows a pair of fibre cables fixed onto fibre holders that may be turned at different angles and distances apart. They are mounted onto a linear actuator that moves away from a reflecting surface. As this happens, reflected light travels down to the lens of the camera, where successive images are captured, filtered and converted to an analogue greyscale value. For a given fibre position, the light intensity response is measured for a displacement of up to 10mm away from the reflecting surface. The system is covered with a black box to eliminate external light (Figure 2).

2. Optimisation Result: Figure 3 displays examples of results gained from the optimisation experiment, showing the light intensity response over displacement. There was a significant difference between intensity responses of white fur compared to black fur surface. Steep responses over a small distance were considered as optimal positioning, for example as shown in the highlighted yellow section in Figure 3.

SIMULATION

1. Breathing Simulation Experiment: Using the optimal fibre pair positions, these were to be used this in a more realistic breathing simulation experiment. This involved using a toy mouse model and fitting it with a balloon (Figure 4). The balloon is pumped through a rotary to linear system. The stepper motor rotates a lever that is connected to a syringe, which pumps air into the balloon to produce uniform breathing motion. This was done to

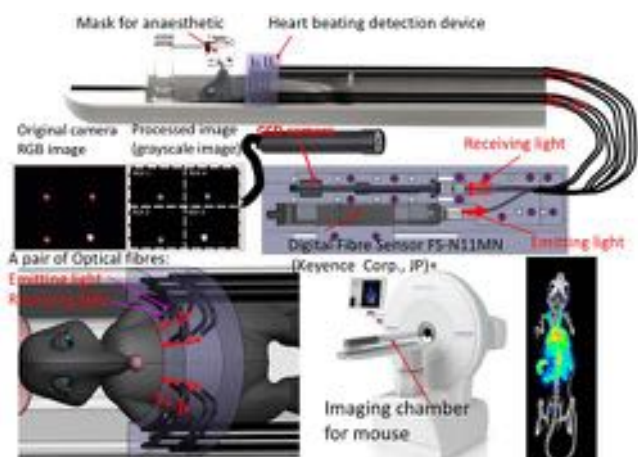


Fig.1 : Design – Proposed respiration monitor system with nanoScan/PET CT small animal imager (Mediso Ltd., Hungary)

test breathing frequencies in the range of 50-200 bpm. Light intensity measurements were recorded to produce a breathing waveform over time. From this the breathing rate can be found and compared to the true pumping rate.

2. Breathing Simulation Experiment: Figure 5 displays some measurements of the simulation experiment using the optimal fibre positions at 50 bpm.

DISCUSSION AND CONCLUSION

A suitable fibre position found for a black reflecting surface was at a 80° fibre separation, at 2mm apart; while for lighter reflecting surfaces this was at 100° , 18mm apart. By calculating the breathing rates from the recorded waves over a period of time (Figure 5), these values were found to be close to the correct breathing rate that was being simulated. This was true for low breathing rates, where the measured values were 0.2-1.8% higher than the simulated breathing rate (50bpm). This shows that the device was able to detect low breathing rates correctly within a degree of accuracy. The camera used in this device was unable to sample high frequencies,

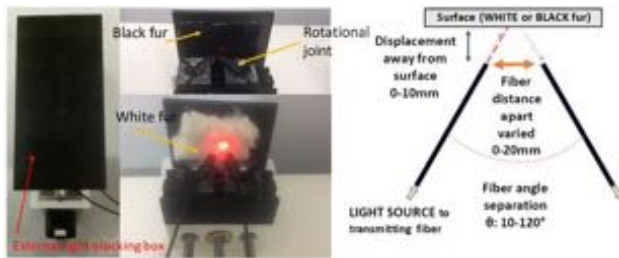


Fig 2. Optimisation experiment: Fibres (2.2mm PE Jacket, OMC Ltd., UK) are placed at varying positions. Different reflecting surfaces are tested using black/white fur.

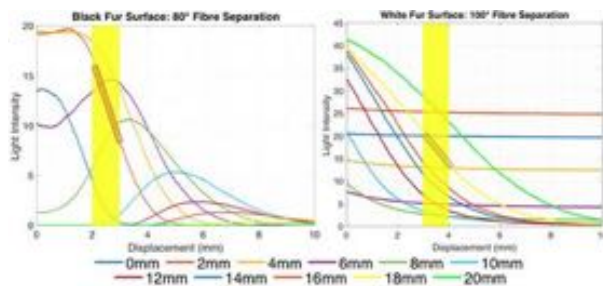


Fig 3. Optimisation Results: Graphs show light intensity response with increasing displacement away from a black (left) and white (right) reflecting surface. Each line represents certain gap between fibres. This is repeated for many different angles.

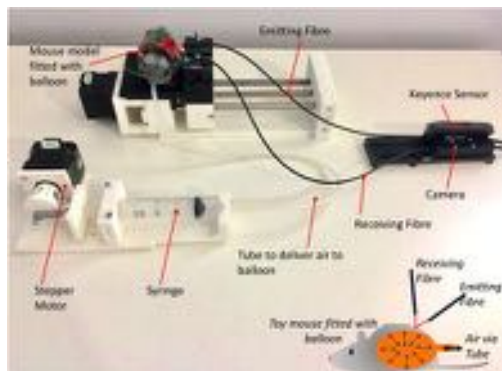


Fig.4 Simulation Experiment: Breathing waveform recorded by measuring light intensity variations during the simulated breathing.

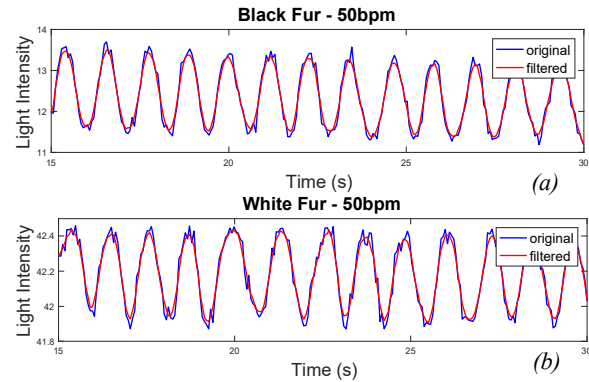


Fig.5: Breathing Simulation results using optimal position. (a) & (b) show results using black fur surface and white fur surface at 50bpm

therefore failed to accurately measure higher breathing rates where values measured from recorded waves were up to 27% lower than the true simulated breathing rate. To conclude, it can be said that the non-contact fibre optic based respiratory detection device proposed can be used to monitor respiration of small animals. This was done by finding optimal fibre pair positions and testing on a simulated breathing rate of a model mouse. This showed that breathing rate can successfully be measured at lower rates, following the common breathing rates of mice while under anaesthetic. However, the device is unable to measure higher breathing rates such as 180-200 bpm, due to the low frame rate of the CCD camera used. Furthermore, the low pass averaging filter was unsuitable for the higher breathing rates, and should be replaced with filters such as a Kalman filter. This device allows the signal to be filtered and amplified by software, and can be easily integrated onto imaging beds, by designing a fibre holder with the optimised fibre position. To take this further, a clinical trial should be conducted and compared to other devices. This device could in future be integrated into gating systems or used in anaesthesia delivery systems based on respiration rate, and may have applications in non-invasive monitoring in humans.

REFERENCES

- [1] A. J. Ewald, M. Egeblad, et al., "Monitoring of Vital Signs for Long Term Survival Of Mice Under Anesthesia", Cold Spring Harbour Protoc. ; 2011(2); pdb.prot5563.
- [2] L. Schroder, C. Faber, "In Vivo NMR Imaging Methods and Protocols", (2011) Springer eBook.
- [3] I. J. Hildebrandt, W. A. Weber, et al., "Anaesthesia and other considerations for in Vivo imaging of Small Animals", ILAR Journal, Vol. 49, Issue 1, pp 17-26, Jan 2008.
- [4] R. Sablong, O. Beuf, et al., "An optical Fibre-Based Fating Device for Prospective Mouse Cardiac MRI", IEEE, Vol 61, Issue 1, pp. 162-170, 2014
- [5] K. H. Hermann, J. R. Reichenbach, et al., "MRI Compatible small animal monitoring and trigger systems for whole body scanners", Zeitschrift für Medizinische Physik, Vol. 24, Issue 1, pp. 55-64, 2014
- [6] Y. Noh, K. Althoefer, et al., "Image-Based Optical Miniaturized Three-Axis Force Sensor for Cardiac Catheterization", IEEE SENSORS Journal, Vol. 16, No. 22, pp. 7924-7932, 2016.
- [7] P. Polygerinos, P. Puangmali, T. Schaeffter, R. Razavi, L. D. Seneviratne, K. Althoefer, "Novel Miniature MRI Compatible Fibre Optic Force Sensor for Cardiac Catheterization Procedures", 2010 IEEE International Conference on Robotics and Automation, pp. 2598-2603, 2010

Development of an Innovative Sleeve-Based Robotic Catheter Driver

O. Al-Ahmad¹, M. Ourak¹, J. Smits¹, S. Jeanquart¹, N. Deserranno¹, F. Bernhard², Y. Kassahun², B. Yu¹ and E. Vander Poorten¹

¹KU Leuven University, Department of Mechanical Engineering, Leuven, Belgium,

²Robotics Innovation Center (DFKI GmbH), Bremen, Germany

omar.alahmad@kuleuven.be

INTRODUCTION

Cardiovascular diseases (CVD) form the most common cause of death worldwide [1]. Minimally Invasive Surgery (MIS) and robotic catheterization are becoming more popular therapies to treat CVD. MIS approaches are especially attractive as they significantly aid in reducing intra- and post-procedural complications [2]. Radio-frequency Ablation (RFA) by means of catheterization interventions is a rather common procedure within this context. One of its applications is in the treatment of Atrial Fibrillation (AF). However, this procedure is not risk-free. Some of the complications may include inflammation, cardiac perforation and cerebrovascular accidents [3]. It is therefore crucial to develop assistive technologies that help minimize risks and aid interventionalists in achieving maximum success rates. Robotic catheter driver systems have been developed within this framework. Systems like the SenseiTM and the MagellanTM from Hansen Medical or the Niobe[®] driver from Stereotaxis are commercially available. These systems usually work with special types of catheters and are expensive. Most catheter drivers mainly rely either on friction rollers and belt transmissions [4]–[6] or mechanical gripping and translation [7]–[9]. A disadvantage of these drive methods is that they apply large stresses locally upon the catheter and may cause damage to the catheter itself or its internal components (sensors, actuators or wirings). The focus of this paper is on a new type of catheter driver that uses pneumatically-actuated sleeve-based grippers (see Figure 1). These grippers exert evenly distributed forces along the length of the catheter, preventing damage and slippage.

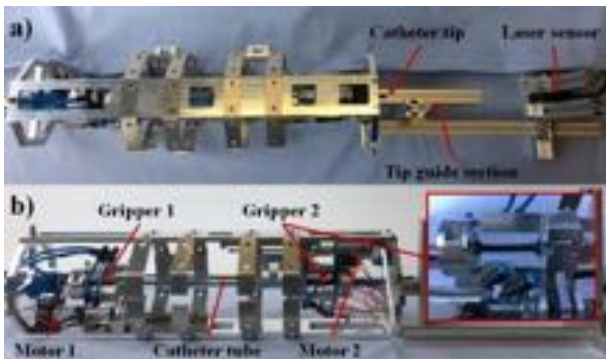


Figure 1. Catheter driver system with pneumatically-actuated sleeve-like grippers, a) top view b) side view.

MATERIALS AND METHODS

The catheter driver is required to achieve an infinite continuous stroke resulting in the smooth translation of

the catheter. In order to achieve this continuous motion, an optimized gripping strategy must be developed. This strategy combines the efficient gripping of the sleeve-like grippers and their corresponding translation. The gripping mechanism and strategy are outlined below.

Gripping mechanism: A braided sleeve fitted within the pneumatic cylinders (FESTO ADVC-6-10-A-P) is tensioned when the cylinders extend. The sleeve's elongation causes a reduction in its diameter, hence permitting contact between the sleeve and the embedded catheter. In effect, the distributed contact force creates large friction between the sleeve and the catheter so that slippage is prevented. The gripper block (incorporating the pneumatic cylinder and the sleeve) is mounted onto a guiding rail. A ball screw mechanism is used for the translation of the gripper blocks, and the complete system is able to rotate around its (and the sleeves') central axis.

Gripping strategy: The grippers are placed on opposite sides such that they approach each other when extending-/translating. The translation strategy of the catheter is somewhat similar to peristaltic motion and is explained as follows (see Figure 2): 1) starting from the home position, gripper 1 grips and gripper 2 releases 2) both grippers start to move *inwards* (gripper 1 at speed (V) and gripper 2 at speed ($V \cdot \alpha$), where $\alpha > 1$) 3) gripper 2 reaches the end of its stroke 4) just before gripper 1 reaches the end of its stroke, gripper 2 moves *outwards* in the same direction as gripper 1 at speed (V) 5) gripper 2 grips (both grippers are now gripped) 6) gripper 1 reaches the end of its stroke and releases 7) both grippers move *outwards* (gripper 2 at speed (V) and gripper 1 at speed ($V \cdot \alpha$), where $\alpha > 1$). The cycle is then repeated until the desired catheter tip position is reached.

Other gripping-based systems [7], [8] have limited strokes, where a temporary interruption in gripping is required to return the gripper to its home position and continue translation. This means that there will be a delay at the end of each stroke before resuming motion. On the other hand, the control strategy outlined in this paper provides for a unique advantage. It allows for continuous smooth motion where at any given moment, at least one of the two grippers is gripped (especially interesting in the proximity of the beating heart). Hence, the catheter's position is controlled at all times. This type of control has not been implemented before in such applications. The logic and control of the driving mechanism was based on a Finite State Machine (FSM) approach. LabVIEW 2016 software and the NI CompactRIO were used for the implementation. A cascaded controller was implemented to control the grippers' linear position.

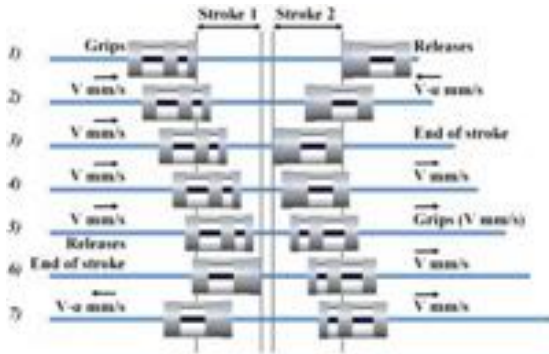


Figure 2. Illustration of the catheter gripping strategy.

RESULTS

Early experiments have shown that friction forces applied to the catheter (by the sleeve) allow it to withstand axial loads up to 10.8 N. This is more than sufficient for this type of application. The translation mechanism was tested using the catheter driver shown in Figure 1. A laser sensor with an accuracy of around 40 microns was used to measure the distance between the catheter tip and the sensor (position ground truth). A targeted travel range of 200 mm was set. Each gripper has a stroke of 70 mm, meaning that about 3 cycles are required to reach the setpoint. The measured position and tracking error are shown in Figure 3.

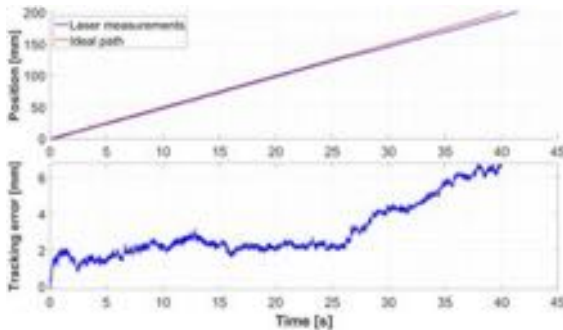


Figure 3. Catheter tip position measured by the laser sensor throughout the different cycles.

The results are encouraging as they show a proper linear increase in position over time. In addition, the tracking error between the ideal path (at the desired speed = 5 mm/s) and the actual travelled path shows reasonable deviation. The cause for this deviation is due to the fact that the speed of the catheter tip is not exactly 5 mm/s. Therefore, the deviation (error) between the actual tip position and the ideal path would increase over time. More importantly, there are no evident peaks or jumps in position when the gripping/ungripping action occurs between cycles. This is due to the fact that the transition between grippers only occurs when both grippers are gripped and moving at the same speed (dynamic re-gripping). The position error at the end of the cycles was less than 0.1 mm indicating the driver's high positional accuracy. Figure 4 shows the position and speed measurements of the individual grippers as measured from the encoders. The electrovalve control signals are also shown to indicate when the cylinders are gripped. In

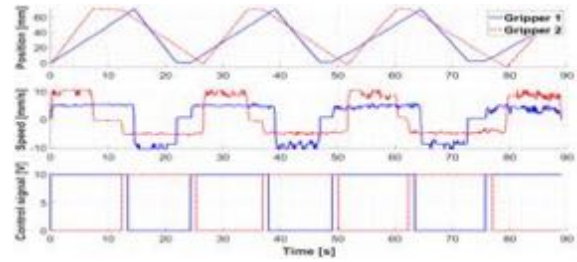


Figure 4. Position, speed and electrovalve control signal plots.

this case however, a position setpoint of 420 mm was set (this corresponds to 6 cycles). This was done to have a better illustration of the cycles. The behavior shown in Figure 4 does indeed correspond to the translation mechanism described in the previous section (see Figure 2). In this case, α was chosen to be 2. This can be seen in the plots where speed values fluctuate between 0, 5 and 10 mm/s (in both directions of course).

CONCLUSION AND DISCUSSION

A new type of catheter driver system was developed and evaluated in this paper. A control strategy for gripping-/ungripping between cycles was implemented to minimize positional error and maintain a constant speed at the catheter tip. The results are promising as they illustrate a smooth linear increase in catheter tip position. The positional accuracy of the system indicates the driver's potential use for intricate cardiothoracic surgeries. The repeatability is yet to be investigated. A further characterization of the grippers is intended (especially in relation to applied forces). An improvement to the mechanical components of the driver system is intended to achieve better positional accuracy at higher speeds.

REFERENCES

- [1] WHO, World Heart Federation, and World Stroke Organization, "Global Atlas on Cardiovascular disease prevention and control," 2011.
- [2] M. Mirabel *et al.*, "What are the characteristics of patients with severe, symptomatic, mitral regurgitation who are denied surgery?," *Eur. Heart J.*, vol. 28, no. 11, pp. 1358–1365, 2007.
- [3] J. Sra, "Atrial fibrillation ablation complications," in *Journal of Interventional Cardiac Electrophysiology*, 2008, vol. 22, no. 2, pp. 167–172.
- [4] T. Wang *et al.*, "Remote-controlled vascular interventional surgery robot," *Int. J. Med. Robot. Comput. Assist. Surg.*, vol. 6, no. 2, pp. 194–201, 2010.
- [5] S. Guo *et al.*, "A novel active catheter system for ileus treatment," in *Proceedings of the IEEE International Conference on Automation and Logistics, ICAL 2008*, 2008, pp. 67–72.
- [6] Y. Fu *et al.*, "Development of a novel robotic catheter system for endovascular minimally invasive surgery," in *2011 IEEE/ICME International Conference on Complex Medical Engineering, CME 2011*, 2011, pp. 400–405.
- [7] F. Arai *et al.*, "New catheter driving method using linear stepping mechanism for intravascular neurosurgery," *Proc. 2002 IEEE Int. Conf. Robot. Autom. (Cat. No.02CH37292)*, vol. 3, no. May, pp. 2944–2949, 2002.
- [8] E. Marcelli *et al.*, "A novel telerobotic system to remotely navigate standard electrophysiology catheters," in *Computers in Cardiology*, 2008, vol. 35, pp. 137–140.
- [9] S. B. Kesner and R. D. Howe, "Position control of motion compensation cardiac catheters," *IEEE Trans. Robot.*, vol. 27, no. 6, pp. 1045–1055, 2011.

Fulcrum effect on stiffness virtual fixtures at distal tip

Caspar Gruijthuijsen, Gianni Borghesan, Emmanuel Vander Poorten

Department of Mechanical Engineering, KU Leuven, Belgium

firstname.lastname@kuleuven.be

INTRODUCTION

In Minimally Invasive Surgery (MIS), the incision point acts as a fulcrum about which the surgical instrument pivots. The presence of this incision point, or fulcrum point, is a central aspect in MIS. Robotic MIS approaches deal with this point in various ways. Remote Center of Motion (RCM) and Local Center of Motion (LCM) mechanisms create a mechanical constraint that imposes pivoting behavior around the incision point, as soon as an alignment procedure has been completed. Virtual RCM approaches replace the mechanical constraint by a soft, programmed constraint. Finally, there are configurations with a back-drivable wrist (BW), where the instrument is attached to a wrist that can act as a passive joint. Upon motion of this wrist's center, the instrument passively reorients itself to comply with the fulcrum constraint.

In shared control situations where surgeon and robot comanipulate the instrument, the BW approach has the advantage of being very close to surgical practice without robotic assistance. There is no alignment procedure required and the surgeon can freely manipulate the instrument, with a small added impedance, even in case of power breakdown.

To apply virtual fixtures, such as a virtual wall, at the distal tip of the instrument, Vitrani *et al.* show that two approaches are possible with BW systems [1]. On one hand, an active wrist (AW) approach can be pursued, where the robot exerts the exact wrench from the virtual fixture on the instrument, while the fulcrum constraint is satisfied by the back-drivability of the robot. On the other hand, a passive wrist (PW) approach applies only pure forces on the instrument, but requires knowledge of the fulcrum position and a lever model. While algorithms such as [2] allow for fast and reliable estimation of the fulcrum position, for safety considerations it makes sense to resort to the AW approach when the fulcrum position is lost or not (yet) detected. Even though the PW and AW approach are fundamentally different in terms of actuator effort and PW theoretically cannot apply forces on the incision point, Vitrani shows that in practice both approaches yield equivalent levels of contact force and a similar user experience [1].

This consideration indicates that both control approaches are interchangeable and raises the question whether it can be advantageous to combine them to address challenging control conditions, especially as an AW setup allows PW control without hardware alterations. This work elaborates this combination, concentrating on the fulcrum effect, i.e. the distortion of the magnitude and orientation of forces and displacements between the distal and proximal ends of the surgical instrument.

FULCRUM MODEL

The fulcrum can be modeled with the following relations:

$$\begin{aligned}\frac{\delta p_{p,x}}{l_o} &= -\frac{\delta p_{d,x}}{l_i} = -\delta \theta_{p,y} = -\delta \theta_{d,y} \\ \frac{\delta p_{p,y}}{l_o} &= -\frac{\delta p_{d,y}}{l_i} = \delta \theta_{p,x} = \delta \theta_{d,x} \\ \delta p_{p,z} &= \delta p_{d,z} \\ \delta \theta_{p,z} &= \delta \theta_{d,z}\end{aligned}$$

As Fig. 1 illustrates, l_o is the instrument length outside the patient and l_i the instrument length inside. $\delta \mathbf{p}$ represents infinitesimal translations and $\delta \boldsymbol{\theta}$ infinitesimal rotations, at the proximal (subscript p) and distal side (subscript d) of the fulcrum. The lever ratio is defined as:

$$a = \frac{l_i}{l_o}$$

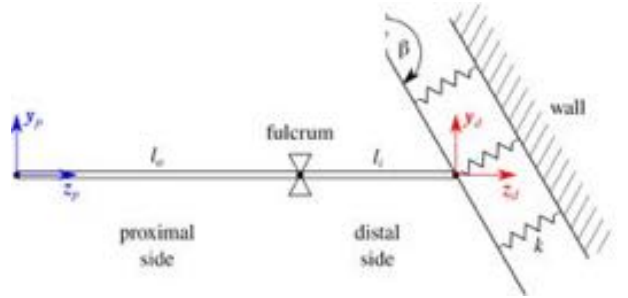


Figure. 1. Definition of fulcrum frames and parameters. The instrument tip contacts a virtual wall of stiffness k at angle β .

From these relations, the fulcrum mapping between proximal and distal displacements (or reciprocally forces) can be derived:

$$\delta \mathbf{p}_d = \mathbf{J}_f \delta \mathbf{p}_p$$

with

$$\mathbf{J}_f = \begin{bmatrix} -a & 0 & 0 \\ 0 & -a & 0 \\ 0 & 0 & 1 \end{bmatrix}$$

The fulcrum also introduces coupling between the linear and rotational displacements (and reciprocally forces). The coupling between a proximal twist $\delta \mathbf{x}_p$ and a proximal infinitesimal translation $\delta \mathbf{p}_p$ is:

$$\delta \mathbf{x}_p = \mathbf{J}_{cpl} \delta \mathbf{p}_p$$

with

$$\mathbf{J}_{cpl} = \begin{bmatrix} 1 & 0 & 0 & 0 & -1/l_o & 0 \\ 0 & 1 & 0 & 1/l_o & 0 & 0 \\ 0 & 0 & 1 & 0 & 0 & 0 \end{bmatrix}^T$$

FULCRUM MAPPING OF A STIFFNESS MATRIX

Suppose now that a virtual wall of stiffness k is to be rendered at the distal tip of the surgical tool. Generally, such distal stiffness can be expressed by the matrix:

$$\mathbf{K}_d = \begin{bmatrix} ks_\beta^2 s_\gamma^2 & -ks_\beta^2 s_\gamma c_\gamma & ks_\beta s_\gamma c_\beta \\ -ks_\beta^2 s_\gamma c_\gamma & ks_\beta^2 c_\gamma^2 & -ks_\beta c_\beta c_\gamma \\ ks_\beta s_\gamma c_\beta & -ks_\beta c_\beta c_\gamma & kc_\beta^2 \end{bmatrix}$$

with β the wall inclination as in Fig. 1 and γ the rotation angle of the wall about the instrument z-axis. The sine and cosine of β, γ are abbreviated as s_β, s_γ and c_β, c_γ , respectively. Using the fulcrum mapping \mathbf{J}_f , this stiffness matrix can be mapped to the proximal side [3]:

$$\begin{aligned} \mathbf{K}_p &= \mathbf{J}_f^T \mathbf{K}_d \mathbf{J}_f \\ &= \begin{bmatrix} a^2 ks_\beta^2 s_\gamma^2 & -a^2 ks_\beta^2 s_\gamma c_\gamma & aks_\beta s_\gamma c_\beta \\ -a^2 ks_\beta^2 s_\gamma c_\gamma & a^2 ks_\beta^2 c_\gamma^2 & -aks_\beta c_\beta c_\gamma \\ aks_\beta s_\gamma c_\beta & -aks_\beta c_\beta c_\gamma & kc_\beta^2 \end{bmatrix} \end{aligned}$$

Analysis of the eigenvalues and eigenvectors of these two rank-1 stiffness matrices \mathbf{K}_d and \mathbf{K}_p reveals that the fulcrum mapping corresponds to a rotation and a scaling of the stiffness matrix. This can be derived from the eigendecompositions of both stiffness matrices:

$$\begin{aligned} \mathbf{K}_d &= \mathbf{R}_d \text{diag}(0,0,k_d) \mathbf{R}_d^T = \mathbf{R}_d \text{diag}(0,0,k) \mathbf{R}_d^T \\ \mathbf{K}_p &= \mathbf{R}_p \text{diag}(0,0,k_p) \mathbf{R}_p^T = s_f \mathbf{R}_p \text{diag}(0,0,k) \mathbf{R}_p^T \\ &\quad \downarrow \\ \mathbf{K}_p &= s_f \mathbf{R}_p \mathbf{R}_d^T \mathbf{K}_d \mathbf{R}_d \mathbf{R}_p^T = s_f \mathbf{R}_f \mathbf{K}_d \mathbf{R}_f^T \end{aligned}$$

From distal to proximal side, the desired stiffness k is scaled by $s_f = a^2 s_\beta^2 + c_\beta^2$ and rotated by $\mathbf{R}_f = \mathbf{R}_p \mathbf{R}_d^T$, where \mathbf{R}_f is composed of the eigenbases of the symmetric matrices \mathbf{K}_p and \mathbf{K}_d . It is clear that the fulcrum effect distorts both the directionality and the magnitude of a stiffness matrix between the proximal and distal side.

From the perspective of proximal actuator effort, it becomes challenging to render the stiffness $k_p = s_f k$ when $\beta \rightarrow \frac{\pi}{2}$ and $a \gg 1$. This corresponds to deep instrument insertion with the wall force perpendicular to the instrument axis.

REDUNDANT ACTUATORS

In the PW scenario, only linear actuators acting on the wrist are available, which might be insufficient for large k_p . Now, consider the AW scenario, where rotational wrist actuators are also available to produce moments on the instrument. Thanks to the coupling between translations and rotations, as introduced by the fulcrum, the actuator effort to generate k_p can be shared by both the linear and rotational actuators.

To this end, assume an idealized robot is available that can produce a homogeneous stiffness $\mathbf{K}_l = k_l \mathbf{I} \leq \hat{k}_l \mathbf{I}$ with its linear actuators and a homogeneous stiffness $\mathbf{K}_r = k_r \mathbf{I} \leq \hat{k}_r \mathbf{I}$ with its rotational actuators, without stability issues. Using the fulcrum coupling, the available proximal stiffness \mathbf{K}_a that this robot can render yields:

$$\mathbf{K}_a = \mathbf{J}_{cpl}^T \text{diag}(\mathbf{K}_l, \mathbf{K}_r) \mathbf{J}_{cpl} = \begin{bmatrix} k_l + \frac{k_r}{l_o^2} & 0 & 0 \\ 0 & k_l + \frac{k_r}{l_o^2} & 0 \\ 0 & 0 & kl \end{bmatrix}$$

Comparison of the available \mathbf{K}_a and desired \mathbf{K}_p for the most challenging wall inclination ($\beta = \frac{\pi}{2}$) shows that the coupling between the redundant actuators augments k_l by k_r/l_o^2 , thus allowing a larger realizable k_p . As different combinations of k_l and k_r yield the same k_p , a possible criterion for choosing k_l and k_r equalizes the ratios to their prespecified maxima \hat{k}_l and \hat{k}_r :

$$w = \frac{k_l}{\hat{k}_l} = \frac{k_r}{\hat{k}_r}$$

Starting from this criterion and a desired stiffness k_p in the xy -plane, the ratio w can be determined as:

$$k_p = k_l + \frac{k_r}{l_o^2} = w \left(\hat{k}_l + \frac{\hat{k}_r}{l_o^2} \right) \Rightarrow w = \frac{l_o^2}{\hat{k}_l l_o^2 + \hat{k}_r} k_p$$

For a proximal displacement $\delta \mathbf{p}_p = \mathbf{J}_f^{-1} \delta \mathbf{p}_d$ in the xy -plane, it follows that the total actuator effort \mathbf{f}_p can be distributed over the linear and rotational actuators:

$$\begin{aligned} \mathbf{f}_p &= k_p \delta \mathbf{p}_d = k_l \delta \mathbf{p}_d + \frac{k_r}{l_o^2} \delta \mathbf{p}_d = \mathbf{f}_{p,l} + \mathbf{f}_{p,r} \\ &\quad \downarrow \\ \mathbf{f}_{p,l} &= k_l \delta \mathbf{p}_d = k_l \frac{\mathbf{f}_p}{k_p} = w \hat{k}_l \frac{\mathbf{f}_p}{k_p} = \frac{1}{1 + \hat{k}_r/l_o^2 \hat{k}_r} \mathbf{f}_p \\ \mathbf{f}_{p,r} &= \frac{k_r}{l_o^2} \delta \mathbf{p}_d = \frac{k_r}{l_o^2} \frac{\mathbf{f}_p}{k_p} = \frac{w \hat{k}_r}{l_o^2} \frac{\mathbf{f}_p}{k_p} = \frac{\hat{k}_r/l_o^2 \hat{k}_r}{1 + \hat{k}_r/l_o^2 \hat{k}_r} \mathbf{f}_p \end{aligned}$$

CONCLUSION

This work discussed back-drivable wrist robots, a very user-friendly type of surgical robot that satisfies the fulcrum constraint with a back-drivable wrist. These robots are controlled using either a passive wrist (PW) or active wrist (AW) strategy. If, e.g. for safety reasons, an AW is required, the available hardware allows to apply the PW approach as well. By combining AW and PW control, it becomes possible to realize stiffer virtual fixtures. It is analyzed how the redundant actuators are optimally combined in this case.

REFERENCES

- [1] Vitrani MA, Poquet, C, Morel G. "Applying Virtual Fixtures to the Distal End of a Minimally Invasive Surgery Instrument." IEEE Transaction on Robotics; 2017; 33(1):114-123.
- [2] Gruijthuisen C, Dong L, Morel G, Vander Poorten E. "Leveraging the Fulcrum Point in Robotic Minimally Invasive Surgery." IEEE Robotics and Automation Letters; 2018; 3(3); 2071-2078.
- [3] Salisbury JK. "Active Stiffness Control of a Manipulator in Cartesian Coordinates" in Proceedings of 19th IEEE Conference on Decision and Control; 1980; 95-100.

An Endoscopic Laser Scanner for Soft Tissue Microsurgery

Alperen Acemoglu and Leonardo S. Mattos

*Department of Advanced Robotics, Istituto Italiano di Tecnologia, Genova, Italy
alperen.acemoglu@iit.it*

INTRODUCTION

The development of the CO₂ laser in 1964 [1] brought an alternative approach to perform incisions on soft tissues. Laser surgeries provide many advantages such as minimal bleeding by coagulation of the small blood vessels, the sterilization of the wound and the absence of post-operative edema [2]. However, even though laser-based microsurgery have been recognized as a better treatment alternative to the traditional methods, thermal damage and tissue carbonization during ablation are still limiting factors for delicate fiber-based operations. On the other hand, since 1993 free-beam laser scanners have been developed and used for char-free soft tissue ablation. The first application was in rectal surgery [3]. The results achieved proved that fast and homogeneous movement of the laser on the tissue minimizes thermal damage and char formation on tissue surrounding the ablation site.

Our recent efforts focused on developing a miniaturized laser scanner to bring the benefits of modern free-beam scanners to fiber-based endoscopic applications. The goal is to enable high-quality tissue ablations in hard-to-reach surgical sites. For this, we proposed a magnetically actuated laser fiber scanner [4]. The system provides high-speed scanning and non-contact ablations, and can be coupled to either a diode [5] or a CO₂ [6] surgical laser source.

In this paper, we focus on the performance characterization of the magnetic laser scanner, conducting workspace and repeatability assessments and evaluating the advantages of high-speed scanning in fiber-based soft tissue ablations.

MATERIALS AND METHODS

The magnetic laser scanner was designed as an end-effector module for a continuum robotic arm. The main design objective is to provide precise laser positioning and scanning control at the tip of a flexible robotic arm. The system includes a flexible optical fiber for delivering the high-power surgical laser to the distal end of the tool, a permanent magnet attached to the optical fiber, four electromagnetic coils, and two optical lenses to focus the laser beam on a target. The basic working principle relies on the fact that the laser spot position changes on the target surface when the optical fiber is bent. In this design, magnetic actuation is used to bend the fiber.

A proof-of-concept device was manufactured as follows: The cylindrical base of the electromagnetic coils, lens and fiber holders were manufactured with 3D printing (see Fig. 1). Four ferromagnetic coil cores were placed

circumferentially on this cylindrical base orthogonal to each other. Then, electromagnetic coils were wound on the cores with a thin copper wire. The optical fiber was fixed to a fiber holder. An axially magnetized ring permanent magnet was attached to the optical fiber. Lens holders were attached to the cylindrical base which holds the electromagnetic coils. The optical lenses were chosen to keep a 30 mm distance between the tip of the magnetic laser scanner and the target surface. This optical system can produce a laser spot diameter of 0.57 mm on the target (focal length = 30 mm).



Figure. 1. Prototype components (a) and assembled prototype (b) of magnetic laser

EXPERIMENTS AND RESULTS

Workspace

The aim of this experiment was to define the maximum limits of the workspace of the magnetic laser scanner. To this end, a set of current values, I_y and I_z , were fed to the coil pairs. Then, the laser spot positions in the yz -plane and the position (d) – current (I) correlations were calculated. Fig. 2 presents sample laser spot positions achieved with current values varying between ± 0.165 A in y - and z -axes. The position of the laser spot changes linearly with the current (Fig. 3). This range of current values resulted in a workspace almost 4×4 mm² in size.

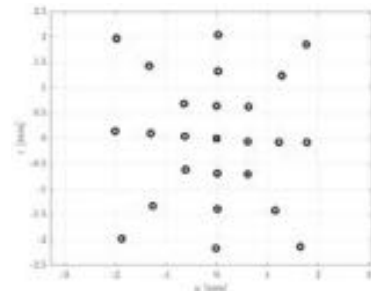


Figure. 2. Sample laser spot positions for different current values on the target surface. Black square in $[0, 0]$ represents the reference point, i.e., the initial laser position on the target for currents $I_y = 0$ and $I_z = 0$.

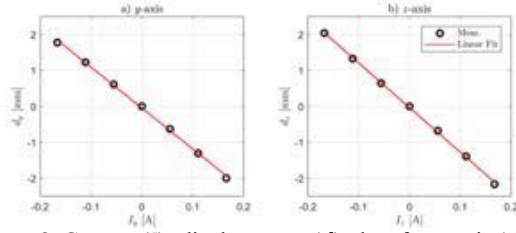


Figure 3. Current (I)-displacement (d) plots for y-axis (a) and z-axis (b).

Repeatability

Repeatability is an important criterion for laser microsurgery. During computer-controlled repetitions of predefined intra-operative trajectories, the laser spot should travel exactly on the same path in order to guarantee accurate ablations. In order to measure the repeatability of trajectories, a 2D trajectory with an '8' figure was executed at 1 Hz and repeated 10 times. In this experiment, the first pass was accepted as the reference trajectory, allowing the computation of the RMSE for the subsequent passes of the laser spot.

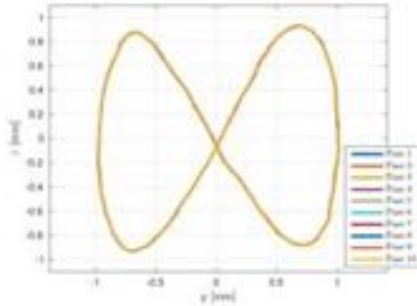


Figure 4. Current (I)-displacement (d) plots for y-axis (a) and z-axis (b).

Fig. 4 depicts the results from the repeatability assessment considering the '8' figure (number of passes, $n = 10$). The calculated average RMSE for repeatability trials was $21 \pm 10 \mu\text{m}$. Thus, the system shows very high repeatability and is, therefore, suitable for accurate laser control during microsurgery.

Soft-tissue ablation experiments

The prototype presented in Fig. 1 was updated to be used with a CO_2 laser source instead of the original diode laser to take advantage of the know superior quality of CO_2 laser for soft tissue microsurgery. A waveguide with $750 \mu\text{m}$ core diameter replaced the previous silica fiber, and new ZnSe lenses were used for laser focusing. Ablation experiments were then performed in three different conditions: a) ablations with a bare waveguide, b) non-contact ablations with focusing optics, and c) high-speed and non-contact ablations to assess the quality of the ablations with different functionalities. Condition a) corresponds to the current state of the art in flexible fiber laser surgery, and thus provide the baseline for assessing the benefits of the proposed scanner.

The results of the ablation experiments are depicted in Fig. 4. Average ablation width for 'bare waveguide' condition was approximately $700 \mu\text{m}$, whereas it was 435 and $420 \mu\text{m}$ for the 'non-contact' and 'non-contact +

scanning' conditions, respectively (Fig. 5). These results show that coupling the system with focusing optics leads to smaller laser spot, resulting in narrower ablations.

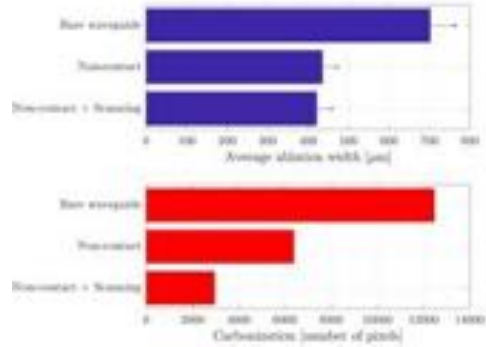


Figure 5. Average ablation widths and tissue carbonization amounts for the ablations with a) Bare waveguide, b) Non-contact, and c) Non-contact + Scanning conditions.

Additionally, results show that the most tissue carbonization was observed for the 'bare waveguide' condition and the least was in 'non-contact + scanning' condition (Fig. 5). Comparison of the 'non-contact' and 'noncontact+ scanning' conditions shows that scanning feature decreases the tissue carbonization.

CONCLUSION AND DISCUSSION

An endoscopic laser scanner was proposed to be used in soft tissue surgeries. Magnetic actuation of an optical fiber demonstrated to be fast and highly accurate. Moreover, high-speed scanning proved to increase the quality of the ablations also in endoscopic applications. The scanning decreases thermal damage to surrounding tissue, while focusing optics provides narrower tissue ablations than those performed with a bare waveguide. Experimental results show that endoscopic laser scanning systems have great potential to improve the quality of the microsurgery in terms of precision and thermal damage. Future work will focus on integration of the endoscopic laser scanner with flexible robotic arm to enable use in real endoscopic surgeries.

REFERENCES

- [1] C Kumar N Patel. Continuous-wave laser action on vibrational-rotational transitions of CO_2 . Physical review, 136(5A):A1187, 1964.
- [2] Marc Rubinstein and William B Armstrong. Transoral laser microsurgery for laryngeal cancer: a primer and review of laser dosimetry. Lasers in medical science, 26(1):113–124, 2011.
- [3] David A Arnold, Michael Slatkine, and Eliezer Zair. Swiftlase: a new technology for char-free ablation in rectal surgery. Journal of clinical laser medicine & surgery, 11(6):309–311, 1993.
- [4] Acemoglu, A., Deshpande, N., and Mattos, L. S., "Towards a Magnetically Actuated Laser Scanner for Endoscopic Microsurgeries". Journal of Medical Robotics Research, 3(02), 1840004.
- [5] Acemoglu, A., and Mattos L. S., "Magnetic Laser Scanner for Endoscopic Microsurgery," In Robotics and Automation (ICRA), 2017 IEEE International Conference on, pp. 4215-4220, IEEE.
- [6] Acemoglu, A., and Mattos L. S., "Non-Contact Tissue Ablations with High-Speed Laser Scanning in Endoscopic Laser Microsurgery", 40th Annual International Conference of the IEEE Engineering in Medicine and Biology Society (EMBC'18) to be held at the Honolulu, HI, USA, July 17-21, 2018.

A SIMPLE surgical robot concept: a bimanual single-port system with intrinsic force-sensing capability

T.J.C. Oude Vrielink, A. Darzi, G.P. Mylonas

*hARMS Lab, Department of Surgery and Cancer, Imperial College London
t.oude-vrielink15@imperial.ac.uk*

INTRODUCTION

The CYCLOPS concept is a surgical robotic device that uses a cable-driven parallel mechanism (CDPM) to achieve dexterous manipulation of multiple instruments in the human body [1]. CDPMs are known for their high force lifting capabilities, low inertia and therefore high velocities. In addition, CDPMs have applications of variable size, including haptic interfaces and stadium camera systems, to the largest radio telescope in the world. The adaptable workspace makes CDPMs good candidates for deployable systems. These desirable characteristics have led to the inception of the CYCLOPS concept as the first CDPM technology proposed for minimally invasive surgery (MIS) [1].

The first CYCLOPS system that was developed for intraluminal gastrointestinal surgery, offers bimanual dexterity and high forces (up to 46N) for performing endoscopic submucosal dissection [2]. Additionally, the neuroCYCLOPS [3] and microCYCLOPS [4] are variation of the CYCLOPS concept for port-based minimally invasive approaches, including removal of deep-seated brain tumours through a transparenchymal tissue dilator. In addition to the increased dexterity, the force sensitivity and autonomous operation of CDPMs has been demonstrated in MIS. In one investigation, the positional accuracy of autonomous motion was assessed for use in transoral laser surgery. In a low-friction configuration, the system showed highly desirable characteristics in terms of accuracy (0.1974 ± 0.1345 mm error) and repeatability [5]. A third prototype was developed as an instrument for the daVinci® surgical robot, aiming for autonomous endomicroscopic tissue scanning. Force sensitivity of up to 0.2N was seen as one key aspect to provide appropriate contact between the tissue and the probe [6]. The force sensitivity also was seen as essential for safe interactions during autonomous motions. At our laboratory another investigation is currently evaluating the use of the force sensitivity for haptic feedback for tumour detection with palpation [7].

This abstract introduces SIMPLE, a new concept which uses a CDPM combining the aforementioned advantages and applying these to single-incision laparoscopic surgery (SILS). SIMPLE stands for Single-Incision MicroPort LaparoEndoscopic surgery. It aims at providing accurate force sensing and highly dexterous bimanual instrument handling within the abdomen, through a virtually scarless approach.

THE SIMPLE CONCEPT

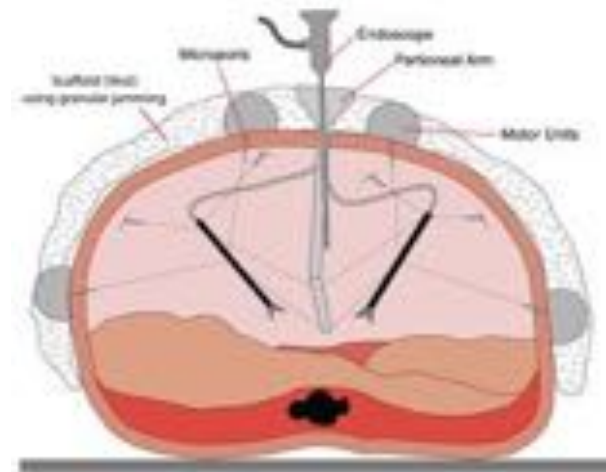


Figure 1 – The SIMPLE concept, using microports to guide (part of) the actuation cables through the abdominal wall into the pneumoperitoneum. The external scaffold, here shown as a granular jamming vest, is used to support the cables and the integrated motor units.

The concept shown in Fig. 1 relies on the use of microports to directly guide actuation cables from the motors – external to the body – to the instruments inside a cavity of the body. The motors are placed on an external scaffold structure, able to withstand actuation forces. A third element is the use of an internal peritoneal arm, which is inserted through a single incision and used for delivery of the surgical instruments, the endoscope and part of the actuation cables. For a scarless approach, either the umbilicus or natural orifice transluminal access methods (similar to NOTES) can be used.

The microports are similar to standard needles and their size is determined by the 0.19mm high-strength (13kgf payload) spectra cables currently in use. Needle sizes of 26 gauge (0.46mm outer diameter) or larger, provide a working channel large enough for the cable. The microports, as other percutaneous approaches, provide a scarless access to the body. In addition, the direct cable pathway provides low friction, which is essential for high control accuracy and force sensitivity.

The workspace of the system depends highly on the cable entry points, and thus on the position of the microports. Similar to conventional laparoscopic surgery, repositioning the ports is important to change the workspace to one of the many different surgical

procedures performed intra-abdominally. A remote centre-of-motion mechanism (RCM) is used to orientate the needles in the desired angle and minimise forces on the abdominal wall. The centre of motion is chosen to be halfway the thickness of the abdominal wall to reduce tissue deformation by the tissue. Also, the outer scaffold structure must provide the ability to reconfigure the position of the ports. Variable stiffness surfaces, like a granular jamming structure, are ideal candidates for creating an adaptable outer scaffold structure that can be moulded to each patient and allow for repositioning of the motors for different workspaces. Other candidates for the external scaffold include thermoplastic materials with a low glass-transition temperature, able to mould around the body in their compliant phase and rigidify shortly after. Thermoplastic materials with these properties are already commonly used for the customization of orthoses and prosthesis.

CURRENT STAGE OF DEVELOPMENT

The current design, still undergoing manufacturing, is shown in Fig. 2. The generated pneumoperitoneum is based on a simulated and validated insufflation model using a human pre-operative CT scan. The system is designed using the umbilicus as entry port, with a 25mm diameter. The EndoEye Flex 3D (Olympus, Japan) is used for visualization. Twelve tendons required for control of both instruments, of which six are guided into the body along the peritoneal arm, whereas the other six are guided using the microports. Low-friction PTFE tubing and pulleys are used to guide the tendons via the motors placed on the peritoneal arm to the entry points at the distal end of the arm.

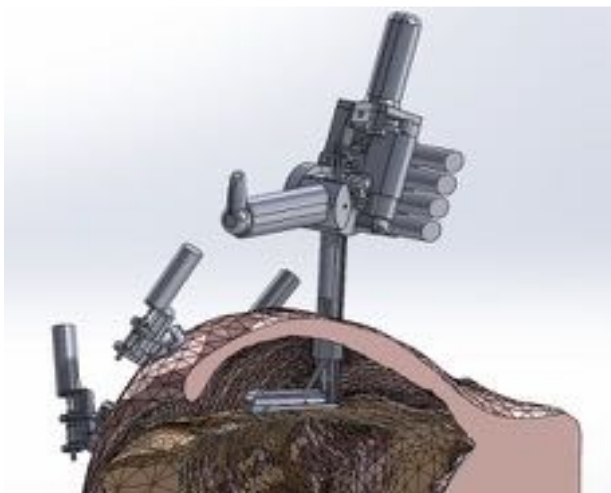


Figure 2 – A render of the current design of the system with the peritoneal arm, and the motor units with RCM mounted around the insufflated abdomen.

CONCLUSIONS & DISCUSSION

The current concept is aimed at providing a highly dexterous bimanual tele-operated system with high force sensitivity and safe autonomous capabilities. This is based on previously validated instrument dexterity, force sensitivity and positional accuracy [2,5,6]. An important aspect for guaranteeing these qualities is low-friction

transmission. The microport access method can provide the low friction and gives a large and customizable workspace. In addition, an external scaffold close to the body provides the ability to adjust the patient position after scaffold placement and a small OR footprint, which remains a relevant issue when considering current surgical robotic systems.

That noted, the system will need to be further scrutinized once the prototype has been fully developed, to show the real opportunities for this approach for MIS. Aside from the obvious advantages the system can provide in surgery, a number of clinical challenges will need to be assessed. Rapid conversion from MIS to open surgery is essential in emergency situations and the design should allow for this. In such situations, the tendons through the microports can be easily cut/released and the peritoneal arm retracted. A second challenge is the assembly of the six percutaneous cables to the surgical end-effectors within the body. Clever mechanisms exist to enable quick and robust connections, and one source of inspiration for the system is seen in minimally invasive suturing, in particular suturing devices used for mesh anchoring in pelvic mesh repair, e.g. Capio SLIM (Boston Scientific) that allows anchoring and needle placement. Such mechanisms can allow for cable assembly inside the body. An alternative approach is by inserting the microports from the inside through the abdominal wall, and then attaching cables outside of the body. Future development will show which approach is best suited for assembly.

This work is supported by the NIHR Imperial BRC and the ERANDA Rothschild Foundation. The SIMPLE concept is a patent pending technology (GB 1806943.5)

REFERENCES

- [1] Mylonas, G. P., Vitiello, V., Cundy, T. P., Darzi, A., & Yang, G. Z. *CYCLOPS: A versatile robotic tool for bimanual single-access and natural-orifice endoscopic surgery*. ICRA 2014, 2436-2442.
- [2] Oude Vrielink, T.J.C., Darzi, A., Mylonas, G.P., *ESD CYCLOPS: a new robotic surgical system for GI surgery*, ICRA 2018, 150-157.
- [3] Oude Vrielink, T.J.C., Kahn, D.Z., Darzi, A., Mylonas, G.P. *NeuroCYCLOPS: a novel system for endoscopic neurosurgery*, Hamlyn Symposium on Medical Robotics 2016, 36-37.
- [4] Oude Vrielink, T.J.C., Darzi, A., Mylonas, G.P., *microCYCLOPS: A robotic system for microsurgical applications*, CRAS 2016, 32-33.
- [5] Zhao, M, *Development of a simulation environment for a novel cable-driven parallel bimanual robot for single access surgery*, MRes Thesis, Imperial College London, 2016.
- [6] Miyashita, K., Oude Vrielink, T., Mylonas, G. (2018). A cable-driven parallel manipulator with force sensing capabilities for high-accuracy tissue endomicroscopy. *International journal of computer assisted radiology and surgery*, 13(5), 659-669.
- [7] Saracino, A, Oude Vrielink, TJC, Menciassi, A., Sinibaldi, E, Mylonas, G, *Haptic-enabled palpation for intraoperative tumor detection using a cable-driven parallel manipulator*, in press CRAS 2018.

Motion-based skill analysis in a fetoscopic spina-bifida repair training model

A. Javaux¹, L. Joyeux², J. Deprest², K. Denis¹, E. Vander Poorten¹

¹Department of Mechanical Engineering, KU Leuven, Leuven, Belgium

²Department of Development and Regeneration, KU Leuven, Leuven, Belgium

allan.javaux@kuleuven.be

INTRODUCTION

Spina bifida aperta is an anomaly of the spinal cord found in newborns characterized by an apparent closure defect of a vertebra leading to leakage of cerebrospinal fluid. Percutaneous fetoscopic patch coverage of spina bifida aperta [1] is a prenatal repair which consists of placing a patch on the back of the fetus with a minimally invasive approach. In addition to the well-known surgical difficulties of minimally invasive surgery (MIS), fetal surgeons must deal with a fragile environment with the lives of two patients at stake. Thus, high-fidelity training environments are demanded.

For this purpose, the fetal surgery team of UZ Leuven has developed a reproducible simulation training model for spina bifida single-port fetoscopy to allow trainees overcome the learning curve before performing the surgery on larger animal models or in the clinic. Quantifying this learning curve in an objective and automated manner is of big interest.

This paper presents the training model and presents the measurement setup and the tools installed to allow an objective characterization of the learning curve.

MATERIALS AND METHODS

The training model simulates the surgical steps of a standardized two-layer spina bifida fetoscopic repair in New Zealand rabbits (Fig.1). The abdominal cavity is insufflated with CO₂ to mimic the insufflated uterus of the patient. The dilated stomach of the rabbit serves as a representation of the back of the fetus. An assistant manipulates an endoscope to capture the surgical scene

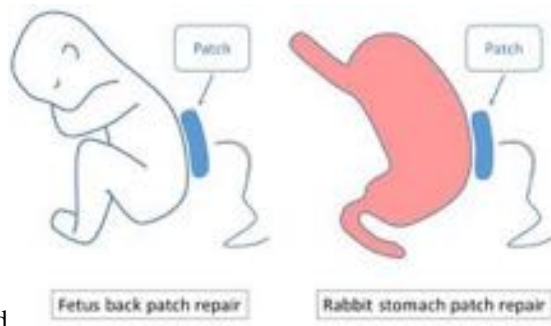


Figure 1 Representation of spina bifida aperta repair on a fetus by suturing a patch on the back (Left). Representation of simulated spina bifida aperta repair in a rabbit by suturing a patch on its stomach (Right).



Figure 2 Picture of training model and instrument tracking setup.

while the surgeon accomplishes the surgical task in a bimanual fashion. The endoscope and two surgical instruments are inserted through a single-port instrumentation. The complex surgery is divided into 10 steps which are accomplished by employing in total 6 different instruments. This paper focuses on a specific step: patch suturing. It consists of placing a non-resorbable patch on the rabbit's stomach (i.e. the back of the fetus) and suturing the edges to it in order to ensure impermeability.

An instrument tracking device was installed around the training model in order to capture the position of the different instruments over time (Fig. 2). On the handle of each instrument and endoscope, a 6-DOF electromagnetic tracker (Aurora from NDI, Canada) was placed. The motions of the endoscope and the single-port were tracked as well. The NDI Planar Field Generator was positioned specifically for each rabbit in order to cover the majority of the instruments workspace.

The position signals were processed and analyzed with a MATLAB program. Classic motion-based skill metrics such as path length and movement arrest period ratio at 50% speed threshold (MAPR50) [2,3] were computed. Clinical outcomes were also measured and reported previously [4]. Three main metrics were put forward: total operation time, patch watertightness and an OSATS score [5] (evaluated by an expert while supervising the fetoscopic videos). To characterize the learning curve and competency, the cumulative sum (CUSUM) analysis was computed. This statistical technique of sequential analysis detects change in an individual's performance [6], thus helping us gaining knowledge on the number of trials required for achieving competency on this training model. For this statistical test, a composite binary outcome was defined as a clinically-acceptable

watertight repair in less than 150 minutes with an OSATS of at least 19. Based on literature, acceptable and unacceptable success rates for watertightness repair were set at 90.6% and 82% respectively.

RESULTS

One right-handed laparoscopic surgeon trained on 34 rabbits while being assisted by different endoscope assistants. The CUSUM analysis (Fig.3-Top) concluded that the surgeon achieved competency after 17 cases (*learning phase*) and maintained it for the remaining rabbits (*competency phase*). During the latter phase, the surgeon's CUSUM scores C+ and C- must stay between the two thresholds (H0 and H1) based on the abovementioned success rates. The analysis of motion data reveals more insight on the surgeon's performance. As a first analysis, only the motions of the dominant (right) hand's instrument were analyzed during the patch suturing. Each studied sample began when the patch was ready to be sutured and ended after the last knot. The motions were not considered whenever one of the instruments or the endoscope were taken out of the cavity, for e.g. cleaning the lens of the camera. Only 29 sessions were successfully recorded. The first 5 recordings suffered from high magnetic disturbance due to a metallic element which was removed afterwards. The evolution of path length and MAPR50 over the different trials are depicted in Fig. 4. For comparison, the OSATS score is also represented (Fig. 5).

CONCLUSION AND DISCUSSION

When observing the motion metrics, each metric has a similar trend and 3 different phases may be identified. First, metrics vary significantly until a stabilization is observed between trials 16 and 27. This approximatively corresponds to the end of the learning and competency phase detected by the CUSUM analysis. After that, an apparent decrease of performance happens for cases 28 to 30, until another stabilization for the remaining period. It is important to place the different operations in context in order to explain these different phases. The trials 5 until 28 took place over a period of two consecutive weeks. The cases 29-35 were conducted in two days but only took place 6 weeks later. This might explain the loss of performance shown by the motion metrics. Additionally, case 28 experienced an unusual event: stomach bleeding. This event was taken care by the surgeon to the detriment of the task. When observing the OSATS evolution, this qualitative assessment may not be deduced.

This analysis shows that motion data contains useful additional information. Further investigations must take place to add quantitative support to these conclusions.

ACKNOWLEDGEMENTS

We thank R. S. Degliuomini, M. P. Eastwood, A. Ahmad, T. Micheletti, G. Callewaert, L. Van der Veecken, G. Van den Bergh, P. De Coppi for their contribution to this work.

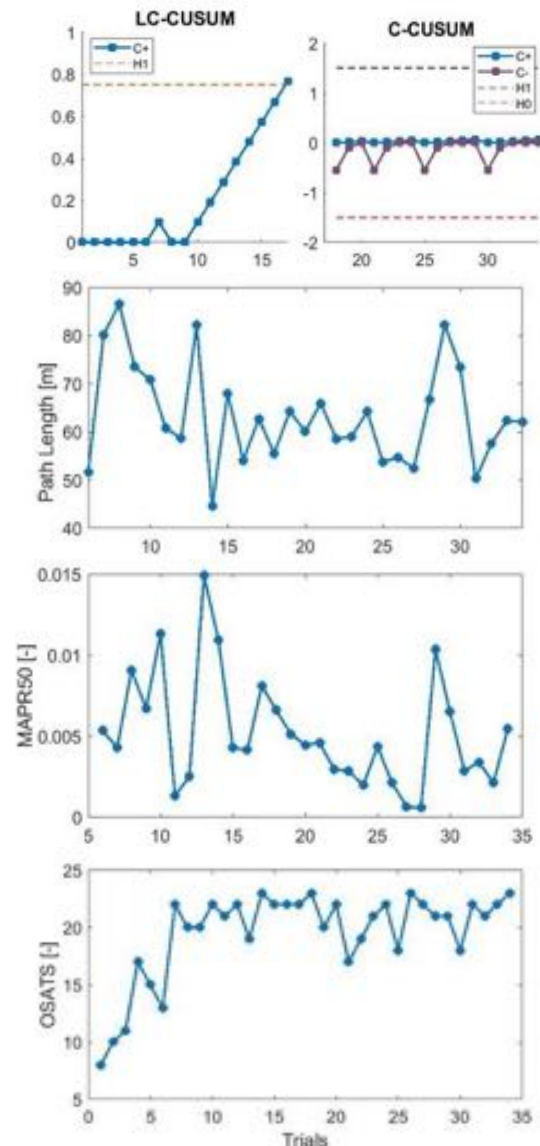


Figure 3 The learning curve (LC) and competency (C) CUSUM analysis test with scores C+ and C- (Top) . The evolution of metrics of path length and MAPR50. The evolution of the OSATS score over the different trials (Bottom).

REFERENCES

- [1] Kohl T., et al. Percutaneous fetoscopic patch closure of human spina bifida aperta: advances in fetal surgical techniques may obviate the need for early postnatal neurosurgical intervention. *Surgical endoscopy*. 2009;23.4: 890-895.
- [2] Cotin, S., et al. Metrics for laparoscopic skills trainers: the weakest link!. In *International conference on medical image computing and computer-assisted intervention*. 2002;2488:35-43.
- [3] Rohrer, et al. Movement smoothness changes during stroke recovery. *Journal of Neuroscience*, 2002;22(18):8297-8304.
- [4] Joyeux L., et al. Learning curve analysis in a rabbit training model simulating spina bifida fetoscopic repair by single access. *Annual Conference of the International Fetal Medicine and Surgery Society 2018 (recently accepted)*.
- [5] Martin, J. A., et al. Objective structured assessment of technical skill (OSATS) for surgical residents. *British journal of surgery* 1997;84.2: 273-278.
- [6] Khan, Nuzhath, et al. Measuring the surgical 'learning curve': methods, variables and competency. *BJU international*. 2014;113.3:504-508.

Towards actuating soft robotic manipulators for MIS using stiffness-controllable low melting point material

Samuel Suchal¹, Alberto Arezzo², Mark Miodownik¹, Sarah Spurgeon³,

Helge Wurdemann¹

¹*Department of Mechanical Engineering, University College London, UK*

²*Department of Surgical Sciences, University of Torino, Italy*

³*Department of Electrical and Electronic Engineering, University College London, UK*

Email of corresponding author: samuel.suchal.12@ucl.ac.uk

INTRODUCTION

There is an emerging trend towards soft robotics due to its extended manipulation capabilities compared to traditionally rigid robot links, showing promise for an extended applicability to new areas. One of these areas is Minimally Invasive Surgery (MIS) [1]. During minimally invasive procedures, laparoscopic instruments are inserted through Trocar ports which are in turn inserted into a patient's abdomen through small incisions allowing surgeons to carry out surgical interventions inside the patient's body [1]. In particular during colorectal surgery, clinicians have observed considerable challenges when conducting keyhole procedures (such as the Total Mesorectal Excision (TME)) due to the limited manoeuvrability of the available surgical tools which are mostly rigid [2].

It has been reported that soft robotics has great potential to overcome the aforementioned limitations [3]. A soft manipulator structure for MIS is beneficial because of increased dexterity and a more gentle interaction with soft tissue; decreased risk of injury to healthy tissue is the main benefit of interest. The large number of Degrees of Freedom (DoFs) of a soft, continuum robot provides ease of navigating around organs inside the patient's body towards the target, rather than "cutting through".

However, as a result of the inherent property of soft materials, the ability to control/obtain higher overall stiffness when required is yet to be further explored. One of the most widely investigated methods to achieve stiffness variation has been realised by embedding material inside a soft manipulator able to change stiffness (i) when vacuum pressure is applied (e.g., granular and layer jamming) [4] or (ii) when exposed to thermal energy [5]. Commonly, chambers that contain stiffness-controllable material are integrated in addition to fluidic actuation chambers.

In this abstract, we propose to use a thermally tuneable composite, a low melting point alloy (LMPA), to hydraulically actuate a soft manipulator and, at the same time, control its stiffness. Here, we describe the setup of our proposed system and present initial results of the stiffness analysis of our LMPA embedded into a silicone chamber.

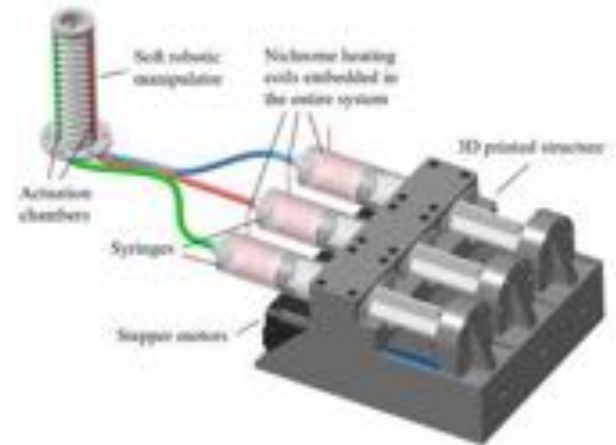


Figure 1. CAD drawing of the LMPA actuation and stiffening device: Three motorised syringe pumps include integrated nichrome heating coils allowing to melt the LMPA which is used to simultaneously actuate and stiffen a soft robotic manipulator.

MATERIALS AND METHODS

The overall setup of our proposed system is shown in Figure 1. The simultaneous actuation and stiffening device consists of three motorised linear rails. Each rail is made of a 10 ml syringe (Terumo Corporation, Shibuya, Tokyo, Japan), fixed on a 3D printed structure made of VisiJet EX200 resin (3D Systems, Rock Hill, SC, US). The movement of the plungers is regulated by a Nema 17 non-captive linear stepper motor with anti-rotation mechanism (17HS5001-100D8). A tube connects each motorised linear rail with each actuation chamber of a soft robotic manipulator as described in [6]. Considering the geometry of each syringe and the specifications of the motors, an amount of 0.008ml fluid is approximately delivered into each actuation chamber by a single step. Hence, the volume of each chamber can constantly be monitored by simply counting the number of executed steps.

Nichrome heating coils (BLOCK, DE, Ø0.6mm nickel chrome resistance wire) are integrated into each syringe allowing to transfer thermal energy to the LMPA (Lens Alloy 117 – melting point of 47.2°C) which is used as an actuation and stiffening material. When electrical current is run through the nichrome wires, the achieved heat results in the LMPA to melt. When the LMPA is

liquefied, the motorised syringe pump can be used to hydraulically actuate and navigate the soft robotic manipulator.

RESULTS

To determine the characteristics of the silicone embedded LMPA and provide initial proof-of-concept results, we integrated a cylindrical LMPA element of 5 mm diameter and 95 mm length into a silicone cylinder of 11 mm diameter and 100 mm length. The silicone body was made of EcoFlex 00-50. This arrangement constitutes a simplified, one-dimensional case of the proposed arrangement shown in Figure 1 above. A motorised linear rail was equipped with a Miniature 17 mm Force-Torque Steel sensor (model series 1000) from Fondazione Istituto Italiano di Tecnologia. The force sensor mounted on the linear rail was then moved towards the tip of the silicone/LMPA cylinder, applying forces as shown in the illustration in Figure 2. A force-displacement curve was obtained for the loading and unloading sequence when deflecting the tip by a maximum of 3 mm. As shown in Figure 2, a maximum force of approximately 0.45 N is achieved when the LMPA is in its solid state.

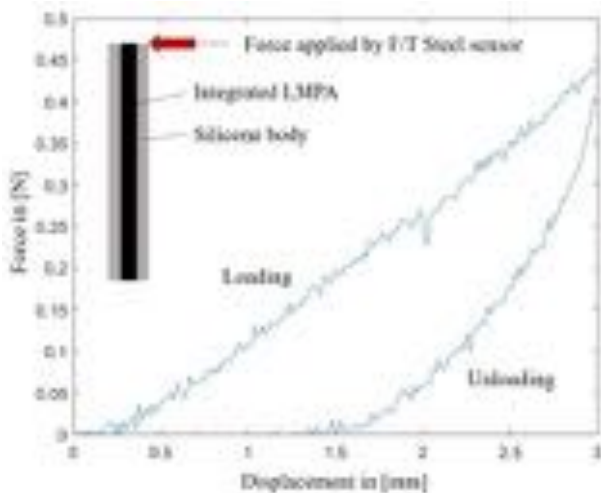


Figure 2. Loading and unloading force-displacement curve of a cylindrical LMPA element integrated into a silicone body.

CONCLUSION AND FUTURE WORK

We conclude that the proof-of-concept work shows great promise in both stiffness range and control strategy compared to solutions that integrate actuation chambers and additional stiffening chambers. Hence, we are able to miniaturise soft, stiffness-controllable robotics. Secondly, our method allows adding additional material that is used for stiffening when the soft robot bends or elongates. Commonly, material used for stiffening will distribute within the allocated chamber but might not fill the entire space during actuation resulting in lack of stiffness-controllability. Our proposed approach provides a solution using stiffness material as an actuation means. However, the concept outlined above has its challenges. Compared to manipulators only using LMPAs as a stiffening mechanism, where only a small amount of alloy is required to be heated, in this concept, the entire actuation system needs to be thermally activated which

may negatively impact the actuation time. Since the alloy used in this work does not have a wide industrial usage, its properties such as phase composition, thermal cycling performance, performance in fatigue are not well documented. Material characterisation will be required to identify key data that will ease and drive the design process and the control strategy to be employed. Despite the challenges outlined above and the ever-present fabrication challenges that haunt the field of soft robotics, we believe that the advantages of combining actuation and stiffening mechanism which has only previously existed as two separate entities will make a valuable contribution to the field of soft, stiffness-controllable robotics.

ACKNOWLEDGEMENT

This work is supported by the Engineering and Physical Sciences Research Council (grant number: EP/N509577/1) and by Springboard award of the Academy of Medical Sciences (grant number: SBF003\1109:).

REFERENCES

- [1] J. Fras, J. Czarnowski, M. Macias, J. Glowka, M. Cianchetti, and A. Menciassi, "New STIFF-FLOP module construction idea for improved actuation and sensing," *IEEE International Conference on Robotics and Automation*, pp. 2901-2906, 2015.
- [2] M. Cianchetti, T. Ranzani, G. Gerboni, T. Nanayakkara, K. Althoefer, P. Dasgupta, and A. Menciassi, "Soft robotics technologies to address shortcomings in today's Minimally Invasive Surgery: The STIFF-FLOP approach," *Soft Robotics*, vol. 1(2), pp. 122-131, 2014.
- [3] A. Arezzo, Y. Mintz, M.E. Allaix, S. Arolfo, M. Bonino, G. Gerboni, M. Brancadoro, M. Cianchetti, A. Menciassi, H.A. Wurdemann, Y. Noh, K. Althoefer, J. Fras, J. Glowka, Z. Nawrat, G. Cassidy, R. Walker, M. Morino, "Total mesorectal excision using a soft and flexible robotic arm: a feasibility study in cadaver models", *Surgical Endoscopy*, vol. 31(1), pp. 264-273, 2016.
- [4] A. Jiang, T. Aste, P. Dasgupta, K. Althoefer, and T. Nanayakkara, "Granular jamming with hydraulic control," in *ASME International Design Engineering Technical Conferences & Computers and Information in Engineering Conference*, 2013.
- [5] H. Abidi, A. Tonazzini, M. Cianchetti, D. Floreano, A. Menciassi, "Low Melting Point Alloy Based Stiffening of a Soft Robot", *International Congress of the Society for Medical Innovation and Technology*, 2017.
- [6] H. Abidi, G. Gerboni, M. Brancadoro, J. Fras, A. Diodato, M. Cianchetti, H.A. Wurdemann, K. Althoefer, A. Menciassi, "Highly Dexterous 2-module Soft Robot for Intra-organ Navigation in Minimally Invasive Surgery", *The International Journal of Medical Robotics and Computer Assisted Surgery*, vol. 14(1), pp. e1875, 2017.

Educational Workshop for Image-Guided Therapy and Medical Robotics

John O'Neill, Sébastien Ourselin, Christos Bergeles, Tom Vercauteren

School of Biomedical Engineering and Imaging Sciences, Kings College London, London, UK

john.j.o'neill@kcl.ac.uk

INTRODUCTION

Hands-on teaching of image-guided therapy and medical robotics typically faces challenges related to securing access to specialised devices. The tutorial developed by Pace et al. [1] described a reproducible and practical workshop using a LEGO robot and open-source software to expose students to many key aspects of medical robotics. However, the LEGO NXT robot kit used in that workshop was retired in 2013, when the replacement LEGO EV3 kit was released. Additionally, the version of the Slicer software package that the workshop used was replaced with another major revision, 4.0, in 2011 [2]. Therefore, it was desired to modernize the workshop to work with the latest LEGO robot kit (The EV3) and the latest version of Slicer (version 4.8), while maintaining the accessible and open-source nature of the original workshop. We present a version 2.0 of the accessible workshop for image-guided therapy and medical robotics including a new LEGO robot design.

MATERIALS AND METHODS

The following physical items are required to perform the tutorial:

- **LEGO Robot:** Model #31313, ~350 USD;
- **LEGO Ultrasonic:** Model #45504, ~30 USD;
- **LEGO Bricks:** Model #10698, ~60 USD;
- **MicroSD Card:** 2GB-32GB, ~10 USD;
- **Synthetic Tumour:** Spongy Ball, ~1 USD;
- **Computer/Laptop:** Could be provided by student. Requires USB port, administrator privileges and a MicroSD card device.

These items total approximately 450 USD, assuming a suitable laptop is available. Detailed instructions for running the workshop as well as the code are available at github.com/NifTK/LegoIGTWorkshop. Additional required software includes the ev3dev Debian operating system for the LEGO robot [3] and Slicer [4]. The custom software written for the workshop is written in Python for both the LEGO robot and the Slicer module, with the two communicating over a TCP socket. This allows the robot to communicate via USB, Bluetooth or WiFi and removes the need for the student to compile software. The same LEGO Phantom design and

Computed Tomography (CT) scan was used from the previous system developed by Pace et al. [1], which allowed the use of the same instructions for the phantom. However, the EV3 system differs significantly from the NXT system, meaning that the robot had to be redesigned from scratch. This new robot design can be seen in the left of Figure 1.



Figure 1. Overview of the proposed LEGO EV3 robot (left) and LEGO Phantom (right).

The Python module loads with a default registration, which can be used to have the robot insert a needle analogue to any point selected on the CT scan in Slicer. The Python module and CT scanned phantom are shown in Figure 2. The Python module also allows the user to create a custom registration, fitting a spatial transformation using three or more point matches and the least squares method [5]. The user manually moves the robot to touch certain points recording the point in robot space, then pairs those points with fiducials in the CT scan to create a rigid registration. Then this improved registration can be used to control the robot more accurately regardless of the initial position of the robot relative to the phantom.

RESULTS

The workshop was run with 8 graduate students at University College London in the Medical Physics and Biomedical Engineering department as illustrated in Figure 3.

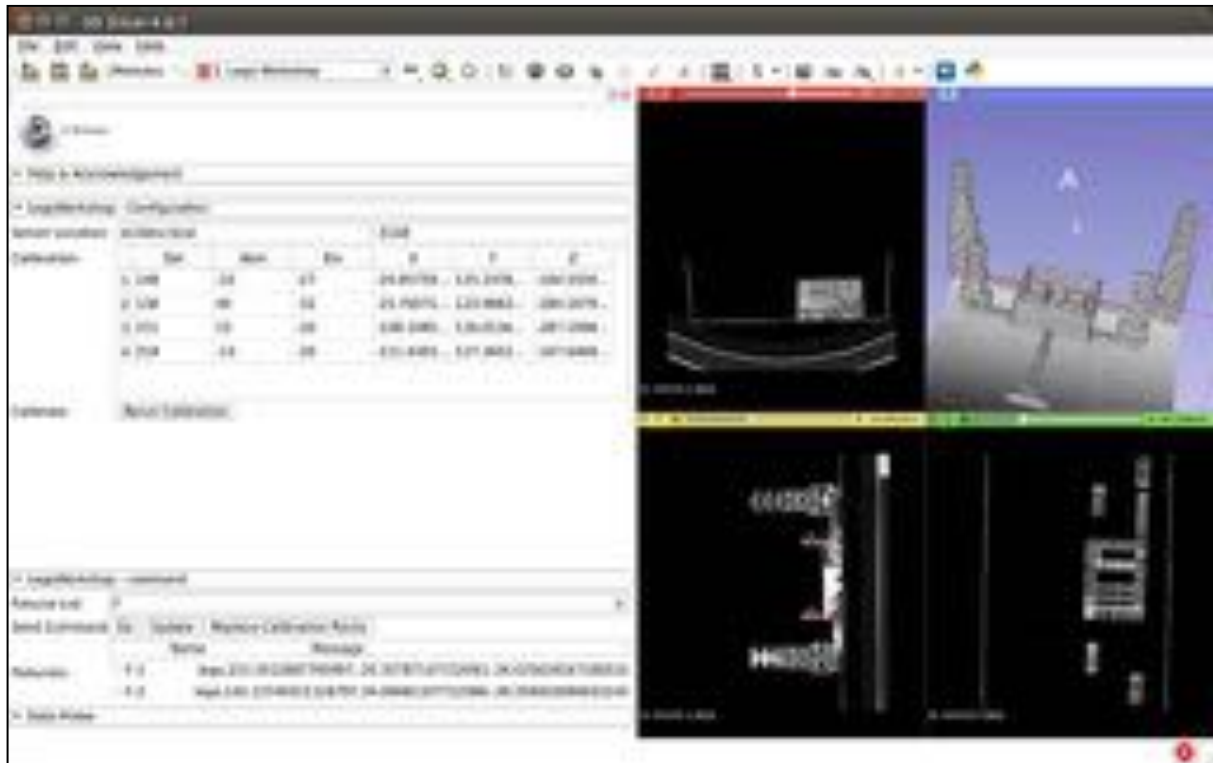


Figure. 2. Screenshot of Slicer 4.8 with the Python module and CT scan loaded.

The students worked in three groups of two to three students. They took approximately 1.5 hours to assemble the LEGO phantom and robot from scratch, and another 0.5 hours get the robot connected to the computer and running with the predefined registration. The remaining hour was used by the students to attempt custom registrations for their robot. This did seem to noticeably increase the accuracy of the needle actuation, although it was still limited by the accuracy of the motors, giving approximately 1 cm targeting error.

DISCUSSION

The workshop was performed with graduate students, but it would likely be appropriate for undergraduate or high school students to illustrate the concepts of image guided therapies. The software could be preloaded on a laptop if the students aren't expected to be able to set up the software and networking. Also, as the LEGO assembly process takes a rather long time, the robot or the phantom could be fully or partially preassembled.

The workshop code and instructions are open sourced at github.com/NifTK/LegoIGTWorkshop, and we fully encourage other groups to run the workshop and provide feedback in order to improve the workshop and the instructions.

ACKNOWLEDGMENTS

This work was supported by Wellcome [203145Z/16/Z] and EPSRC [EP/L016478/1; NS/A000050/1].

This work was performed at the Wellcome / EPSRC Centre for Interventional and Surgical Sciences at University College London



Figure. 3. Students from University College London perform the updated workshop.

REFERENCES

- [1] Danielle F Pace, Ron Kikinis, and Nobuhiko Hata. An accessible, hands-on tutorial system for image-guided therapy and medical robotics using a robot and open-source software. In Open Science Workshop (MICCAI), 2007.
- [2] Andriy Fedorov, Reinhard Beichel, Jayashree Kalpathy-Cramer, Julien Finet, Jean-Christophe Fillion-Robin, Sonia Pujol, Christian Bauer, Dominique Jennings, Fiona Fennessy, Milan Sonka, et al. 3D slicer as an image computing platform for the quantitative imaging network. *Magnetic resonance imaging*, 30(9):1323–1341, 2012.
- [3] R Hempel and D Lechner. Ev3dev. Available: <http://www.ev3dev.org>, 2017.
- [4] The Slicer Community. 3D Slicer. Available: <http://www.slicer.org>, 2017.
- [5] K Somani Arun, Thomas S Huang, and Steven D Blostein. Least-squares fitting of two 3-D point sets. *IEEE Transactions on pattern analysis and machine intelligence*, (5):698–700, 1987.

FCNN-based segmentation of kidney vessels - Towards constraints definition for safe robot-assisted nephrectomy

S. Moccia^{1,2}, S. Foti³, S.M. Rossi³, I. Rota³, M. Scotti³, S. Toffoli³, L.S. Mattos³,
E. De Momi³, E. Frontoni²

¹*Department of Advanced Robotics, Istituto Italiano di Tecnologia, Genoa (Italy)*

²*Department of Information Engineering, Università Politecnica delle Marche, Ancona (Italy)*

³*Department of Information, Electronics and Bioengineering, Politecnico di Milano, Milan (Italy)*
sara.moccia@iit.it

INTRODUCTION

Nephrectomy requires careful surgical actions in order to remove tumoral tissue while avoiding the damaging of major vessels such as the renal artery [1]. Robotic nephrectomy is emerging as a powerful solution to avoid vessel damaging through active-constraints (AC) control [1]. To provide AC control, sensitive vascular structures have to be detected in real-time in intra-operative images.

A well established literature on vessel segmentation exists. Vessel-segmentation approaches can be divided in: (i) vessel enhancement, (ii) model-based methods, (iii) tracking, and (iv) machine-learning (ML) approaches [2]. Recently, successful segmentation approaches are mainly based on ML strategies based on fully-convolutional neural networks (FCNNs). FCNNs allows to tackle inter- and intra-patient variability, as well as noise and illumination variation in the images.

The goal of this paper is to investigate the use of FCNN for vessel segmentation in laparoscopic images acquired during nephrectomy procedures.

MATERIALS AND METHODS

The FCNN investigated in this work is the U-Net [3]. U-Net is made of 9 processing steps, which form a contractive and an expansive path. The paths are symmetric to each other. The contractive path acts as feature extractor, while the expansive one performs up-convolution and segmentation. The U-Net used in this paper has only 5 of the original 9 processing steps to lower the segmentation computational cost while preserving segmentation performance [4]. The steps in the contractive path are made of 3x3 convolutional and 2x2 max pooling kernels. The expansive path has 3x3 convolutional and 2x2 up-sampling kernels. The peculiarity of U-Net is the presence of copy layers. The copy layers were introduced in [3] to link the contracting and the expansive path, as to retrieve the information lost in the contracting path and take it into account while performing object localization.

The segmentation of the renal artery – which is recognized as one of the most critical structures in the

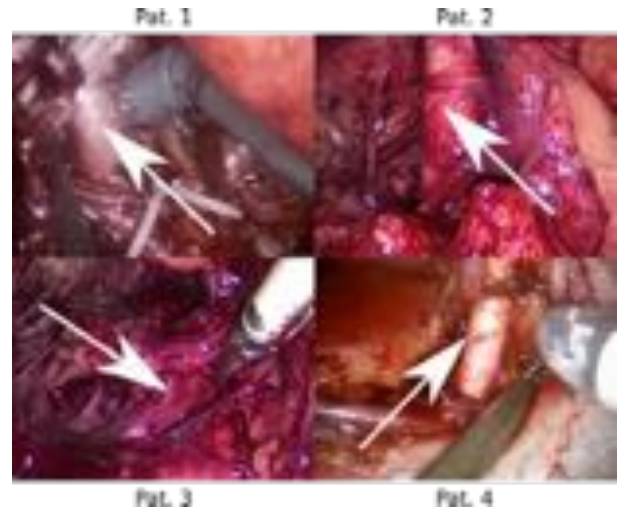


Figure 1: Sample images. Arrows indicate the renal artery.

clinical literature [1] – was studied deploying a deep neural network. However, to the best of authors knowledge, no renal arteries dataset was available to train the FCNN. For this reason, a new dataset was created. It consisted of laparoscopic images manually extracted and labeled from 4 videos of robot-assisted partial nephrectomy, relative to 4 different patients. The images were extracted in such a way that the renal artery was clearly visible in the camera field of view. The number of extracted frame was 65 for the first patient (Pat. 1), 100 for the second one (Pat. 2), 30 for the third one (Pat. 3) and 123 for the last one (Pat. 4). Images size was 640x480 pixels for Pat. 1, 1280x720 for Pat. 2, and 854x480 for Pat. 3 and Pat. 4. Black borders were removed from the images, that were then resized to 296x220 pixels to smooth noise and reduce both processing time and memory usage. The image labeling process involved 4 expert subjects, that manually drew vessel contours using MATLAB 2018A. Challenges in the dataset included: different illumination levels, noise in the images, varying laparoscope pose with respect to the renal artery and high variability in both inter-patient artery architecture and location. Sample images acquired from different patients are shown in Fig. 1.

	PPV	TPR	DSC	LR
P1-Pat. 1	0.8021	0.8564	0.8284	0.001
P1-Pat. 2	0.8555	0.4693	0.6061	0.001
P1-Pat. 3	0.8195	0.4208	0.5561	0.001
P1-Pat. 4	0.3626	0.7448	0.4878	0.0025
P2	0.7543	0.3814	0.5066	0.003

Table 1: Performance of the two protocols (**P1** and **P2**). For **P1**, results are shown for each of the four patients.

Two segmentation protocols were investigated. The first protocol (**P1**) aimed at evaluating the U-Net performance when training and testing were performed on different images from the same subject. Despite **P1** is not applicable in the actual clinical practice, it allowed investigating the segmentation performance in a trivial scenario. The images from each patient were randomly shuffled and divided in training (90%) and testing (10%).

The second segmentation protocol (**P2**) aimed at investigating the generalization power of U-Net when segmenting images from different patients. Thus, the images from the four patients were merged and randomly shuffled. Also in this case, the 90% of the images were used for training and 10% for testing. Prior to training, data augmentation was performed (9 linear and non-linear transformations were applied).

To train U-Net for the two protocols, the cross-entropy was used as loss function. Adam [5], a method for efficient stochastic optimization, was used as optimization algorithm. The initial learning rate (LR) was set to 0.001, after a trial-and-error procedure. Mini-batch gradient descent technique was used as a trade off between training convergence time and memory usage. Batch size was set equal to 5. TensorFlow (<https://www.tensorflow.org/>) was used for training and testing purposes.

The U-Net segmentation performance was quantitatively evaluated with respect to manual vessel tracing in terms of positive predictive value (PPV), true positive rate (TPR) and dice similarity coefficient (DSC).

RESULTS

The results relative to P1 and P2 are shown in Table 1. The best segmentation performance was achieved by **P1** for the first patient (Pat. 1). Sample segmentation images are shown in Fig. 2.

CONCLUSION AND DISCUSSION

As can be observed in Table 1, the best result was achieved for **P1-Pat. 1** with a DSC equal to 82.84%.

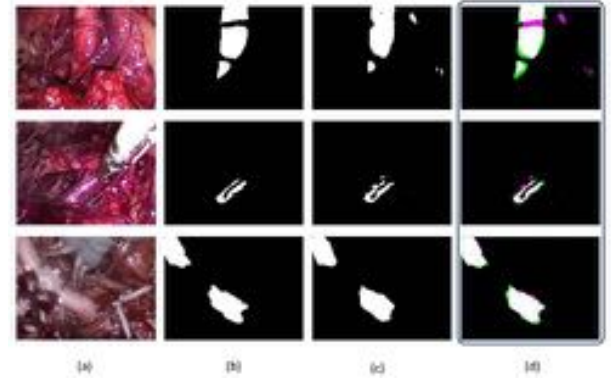


Figure 2: Sample images of U-Net segmentation outcomes. (a) original images, (b) ground-truth manual segmentations, (c) U-Net segmentation outcomes, (d) comparison between ground-truth and segmentation outcomes: false positives and false negatives are represented in magenta and green respectively.

In fact, Pat. 1 images were less challenging with respect to the remaining three patients (Pat. 2, Pat. 3 and Pat. 4), where the presence of cauterization smoke and the movement of the renal artery, caused by the interaction with surgical tools, increased the segmentation challenges. The resulting DSC of 50.66% obtained in P2, reflected the variability between different patients.

Improving the segmentation performance and tackling inter-patient variability by building a larger dataset, could be the natural continuation of the project in view of translation into clinical practice. Finally, instead of performing single-frame segmentation, temporal information could be exploited to track the vascular structures in time and improve segmentation performance [6].

REFERENCES

- [1] MacLennan, Steven, et al. "Systematic review of oncological outcomes following surgical management of localised renal cancer." *European Urology* 61.5 (2012): 972-993.
- [2] Moccia, Sara, et al. "Blood vessel segmentation algorithms - Review of methods, datasets and evaluation metrics." *Computer Methods and Programs in Biomedicine* 158 (2018): 71-91.
- [3] Ronneberger, Olaf, Philipp Fischer, and Thomas Brox. "U-net: Convolutional networks for biomedical image segmentation." *International Conference on Medical image computing and computer-assisted intervention*. Springer, Cham, 2015.
- [4] S. Moccia, et al. "Toward Improving Safety in Neurosurgery with an Active Handheld Instrument," *Annals of Biomedical Engineering* (Accepted for publication).
- [5] Kingma, Diederik P., and Jimmy Ba. "ADAM: A method for stochastic optimization." *arXiv preprint arXiv:1412.6980* (2014).
- [6] Coskun, Huseyin, et al. "Long short-term memory kalman filters: Recurrent neural estimators for pose regularization." *arXiv preprint arXiv:1708.01885* (2017).

Advanced User Interface for Augmented Information Display on Endoscopic Surgical Images

Simone Foti¹, Andrea Mariani¹, Thibaud Chupin¹, Diego Dall'Alba³, Zhuoqi Cheng², Leonardo Mattos², Darwin Caldwell², Paolo Fiorini³, Elena De Momi¹, Giancarlo Ferrigno¹

¹*Departement of Electronics, Information and Bioengineering, Politecnico di Milano, Milano, Italy.*

²*ADVR, Istituto Italiano di Tecnologia, Genova, Italy,*

³*Altair Robotics Lab, University of Verona, Verona, Italy,*
simofoti@gmail.com

INTRODUCTION

Robotic surgery has come to the forefront in the last decades mainly because this technology can provide enhanced dexterity and 3D perception of the surgical field. These advantages turn into a surgical approach that is easier for surgeons and, ultimately, into better surgical outcomes for patients [1]. The incorporation of real-time sensing technologies during complex medical procedures is an essential component for future surgical robotic platforms. Despite the specific type of advanced sensing technology, the introduction of novel sensing requires proper integration in the standard surgical interface to be used effectively [2].

In this work, we present an advanced user interface (AUI) able to provide the surgeon with additional information about the operational field of view. In particular, we retrieved information from the kinematics of a robotic tool and from an electric bio-impedance (EBI) measurement system for tissue classification. These data constitute the input for augmented reality (AR) visualization of the surgical scene.

MATERIALS AND METHODS

The AUI is based on the Unity3D cross platform game engine, which provides an easy way to create complex graphics in space. The integration with a ROS-based robotic device is achieved by creating a C++ native plugin. It provides a simple C interface exposed to C# scripts. The virtual world created in Unity (see Fig. 1) is close to the real surgical setup. In this world, the real stereo-endoscope is modeled by two juxtaposed cameras (${}^V C_L$ and ${}^V C_R$) that record a textured plane each. The two textures (I_L and I_R) are mutually visible by the virtual cameras and they are continuously updated with the images recorded during the medical procedure. The virtual environment preserves the depth perception of the surgical scene and allows the projection of additional information (e.g. user interfaces, 3D models or point-clouds). The graphical user interface (GUI) is placed close to the virtual cameras, such that it can be seen in both their fields of views without being

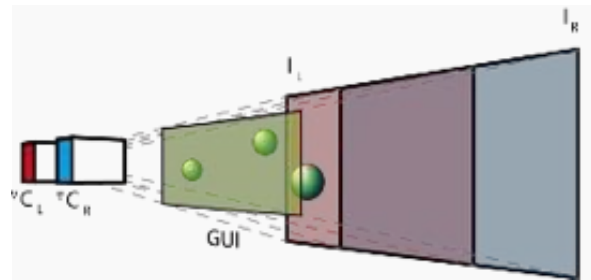


Figure 1. The AUI virtual environment: two virtual cameras (${}^V C_L$ and ${}^V C_R$) record a textured plane each, where the textures (I_L and I_R) are the images obtained with the real endoscope. The GUI is placed close to the cameras, while 3D objects are positioned between the textured planes and the GUI.

occluded by other objects.

Registration is fundamental to correctly overlap spatial-related information to the endoscopic images. We achieve this goal by measuring a set of fiducial points on a ChArUco board (i.e. a checkerboard augmented with fiducial visual markers). These points have known coordinates in the *world frame* (the one of the board). Then we place the tip of the robotic tool on each fiducial point of the ChArUco board and we record the corresponding coordinates in the robotic frame. Quaternion matching method [3] is applied to estimate the transformation between the tool and the world reference frame. In addition, the camera coordinate frame is registered to that of the *world frame* through online extrinsic calibration of the camera. Finally, the transformation between the camera and the tool is obtained by combining the previously estimated transformations. Expressing the tool coordinates in the camera reference frame, the AUI can provide position-related information to the surgeon.

In this study, the AUI is used to assist the surgeon to understand the tissue type in contact with the surgical tip. To identify the type of tissue, we use the EBI sensing technology. Then, a dot is marked in a predefined color on the AUI to represent the corresponding tissue type.

As shown in Figure 2(A), the EBI measurement system integrates a single chip with the proximal end of

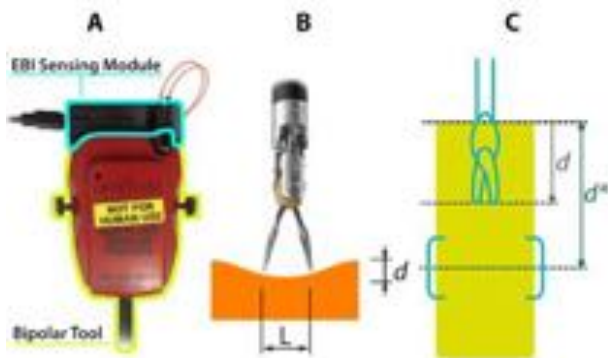


Figure 2. (A) The EBI measurement system integrated with the Maryland Bipolar Forceps. (B) The factors influencing the electrical impedance. (C) Visual feedback on the insertion depth as it appears in the final AUI.

a bipolar tool. For instance, we used the standard Maryland bipolar forceps (Ref. 400172) available for the da Vinci Research Kit (Intuitive Surg.Inc.). The EBI measurement depends on several variables including the jaw opening distance (L) and the insertion depth (d) (see Fig. 2.B) [4]. In fact, different jaw opening angles of the forceps are related to different current densities applied to the tissue, and thus result in different EBI values. This opening angle is accessible from the robot joint encoders and it is taken into account while performing the tissue classification. In addition, pressing the tissue can change both the intracellular and extracellular tissues' impedances. Here, an optimal insertion depth (d^*) was defined to obtain reliable tissue classification [5]. Therefore, the correct position of the surgical tool with respect to the tissue surface is essential: this information can be provided to the surgeon by means of a visual feedback on the AUI.

RESULTS

The final AUI allows to (i) communicate the result of the classification in text form, (ii) provide a visual feedback on the insertion depth (Fig. 2.C) and (iii) create a tridimensional point on the touching site of the tooltip to mark the classified tissue type.

A preliminary experiment was designed to verify the proposed system (Fig. 3). Four types of porcine tissues (i.e. muscle, fat, liver and lung) were used to construct a realistic surgical scene. The designed AUI was found very helpful since on-site tissue type can be detected in real time. Also, visual feedback on the tool insertion depth assures a more accurate tissue identification. In terms of classification marks positioning, the calibration method allowed to obtain an accuracy (reprojection error) of the order of millimeters.

CONCLUSION AND DISCUSSION

In this preliminary work we presented a novel AUI to improve the surgeon understanding of EBI sensing data. The AUI provides integrated AR data visualization and

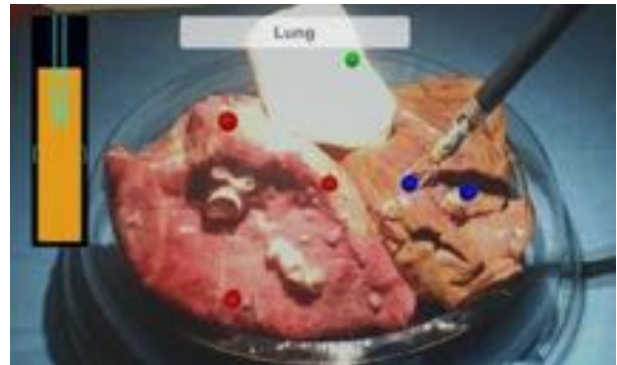


Figure 3. The AUI visualization components: the lateral bar provides a visual feedback of the insertion depth and it turns green when the optimal distance is reached; the upper central box contains the classification outcome in text form.

indications of the surgical tool positioning to obtain consistent measurements. It allows to map the surgical scene with information of the tissues touched by the tooltip. The map might be particularly useful if the visual feedback provided by the endoscope fails (e.g. in case of bleeding, blurred camera or smoke in the field of view). Most importantly, the map could help in tumors resections because EBI sensing has been demonstrated to discriminate between healthy and cancerous tissues [6], which is difficult to be achieved by the only visual inspection.

This study is a part of the EL.I.S.A. project which aims to apply EBI sensing for various surgical applications and future work will focus on improving hardware and software components with the objective of testing the proposed approach with in-vivo experiments. A relevant improvement would be the implementation of tracking algorithms to adjust the position of the classification dots in case of tissue displacement.

ACKNOWLEDGEMENTS

This work has been partially supported by Project 732515 – SMARTsurg – H2020-ICT2016-1 and Project 742671 – ARS – H2020-ERC2017-3.

REFERENCES

- [1] Maeso et al, Efficacy of the Da Vinci Surgical System in abdominal surgery compared with that of laparoscopy: a systematic review and meta-analysis, *Ann Surg.*, 2010.
- [2] Taylor et al., *Medical robotics and computer-integrated surgery*, Springer handbook of robotics, 2016.
- [3] Umeyama, Least-squares estimation of transformation parameters between two point patterns, *IEEE Transactions on Pattern Analysis and Machine Intelligence*, 1991.
- [4] Martinsen et al., *Bioimpedance and bioelectricity basics*, Academic press, 2011.
- [5] Dodde et al., Bioimpedance of soft tissue under compression, *Physiol. Meas.*, 2012.
- [6] Laufer et al., Electrical impedance characterization of normal and cancerous human hepatic tissue, *Physiol. Meas.*, 2010.

ORPlanner - Towards Enhanced Operating Room Planning Tools

M. Stacey¹, S. Muscroft¹, A. Chow¹, J. Nehme¹, D. Stoyanov^{1,2}

¹Digital Surgery Ltd, 230 City Road, EC1V 2QY, London, UK.

²Dept. Of Computer Science, University College London, Gower Street, WC1E 6BT, London, UK.

mark@touchsurgery.com

INTRODUCTION

Operating room (OR) planning and setup for different procedures involves the positioning of equipment, instruments and complex devices. This needs to be done to optimise the ergonomics of the entire operating team with the environment. OR setup can be substantially different, depending on the available surgical infrastructure, procedure type and surgical teams' technique. The setup of the OR can be a contributing factor to the efficiency of a surgical procedure by allowing more effective coordination between the various roles and by expediting the overall time taken to complete an operation [1, 2].

Because the layout of an OR can vary for each procedure and can be subject to change mid-procedure as equipment layouts are altered to facilitate different stages of the operation, it is important to support better preparation and execution of the OR management [3]. A system allowing the recording and recalling of these layouts is needed to allow the correct initial setup of the OR. This can be the case in dynamic healthcare economies where OR staff rotate and are not always given sufficient time to plan and learn the optimal theatre management, a frequent occurrence in National Health Service (NHS) systems. However, the current state-of-the-art for recording OR layout is a simplistic line drawing on paper stored in Kardex files, showing the preferences of each surgeon for individual procedures. There are digital tools currently available that allow the design and configuration of an OR but these tend to be for visualising new OR equipment installations for design and sales purposes (for example, Stryker ByDesign [4]) rather than allowing per procedure documentation of a changing OR layout.

In this pilot study, we present a touchscreen tablet and augmented reality (AR) capable solution whereby different users can create, edit and visualise OR layouts. Our system is based on a framework that can be deployed across platforms and can thus facilitate team engagement and interaction prior to each case within an easy to manage delivery application.

MATERIALS AND METHODS

The OR planner has been developed in Unity3D (version 2018.1) to allow real-time rendering and manipulation of 3D assets across multiple platforms.

The advantage of this framework selection is that it can be deployed across common mobile platforms that are typically available to OR staff but can also be delivered through novel virtual reality (VR) and AR systems, which are emerging.

Mobile Implementation: The OR layout planner view on a tablet (Apple 12.9-inch iPad Pro) can be seen in Figure 1. This is the most practical deployment method for the entire theatre team, as planning and setup views can be distributed before the procedure to all mobile devices. Initial creation and subsequent editing of the layout is done via a simple touch interface on the tablet, which is ideally suited to moving and rotating objects. The layout can be edited and viewed on the tablet in orthographic or perspective overhead views. There is also capability embedded to view the layout from multiple positions within the OR.



Figure 1. iPad screenshot of overhead orthographic view of an example OR layout setup for a sleeve gastrectomy procedure showing the positioning of the patient, OR staff, equipment and devices.

AR Implementation: Figure 2 shows an OR layout being viewed on an AR headset (Microsoft HoloLens), which allows the user to view the OR layout from any angle. The layout can be viewed at 1:10 scale and 1:1 scale. After editing on the iPad, the layouts are sent via a network connection to the HoloLens for viewing within a better spatial context setting.



Figure. 2. HoloLens image capture of 1:10 scale view of an OR layout, which can be linked to the layout displayed in Figure 1.

Assets and Features: The planner currently uses 3D art assets from the Digital Surgery studio asset library as well as the OR bundle from the Unity Asset Store. Different assets can be easily incorporated; if specific assets are not available, a generic object can be added and labelled by the user. The application features a design mode to allow tailoring to different OR sizes, shapes and features. The planner allows the user to enter custom room dimensions allowing the OR within the planner to match dimensions of the room being used. OR layouts can be saved in the planner and then loaded for reference or subsequent editing.

PRELIMINARY RESULTS

Initial feedback was sought from a surgical team based at University College London Hospital focusing on orthopaedic surgery as well as a team from St Mary's Hospital, Imperial College Healthcare NHS Trust, specialising in bariatrics. The assessment from OR staff who used the planner was that this will be a useful reference tool. The benefit of having the planner placed near the scrub nurse board allowing it to be referenced before any operation setup begins was recognised. This would enable the correct room layout to be set up according to the preferences for a specific room, procedure and surgeon.

It was noted that the planner would not be needed for staff who are frequently in the same ORs. However, it is often the case that staff are coming in from other clinics or agencies as locums; in this

scenario the planner would prove useful. Additionally, if the application included movement ranges and additional features about the functionality and mobility of the equipment, this would be helpful especially with new devices.

CONCLUSION AND DISCUSSION

This pilot developed and assessed the initial feasibility and interest in a set of easy to use digital tools to allow virtual 3D visual representations of OR layouts to be created. It investigated if this would prove useful to OR staff.

It is likely that support tools for OR planning will be increasingly important to theatre management, especially as robotic surgical devices are introduced and the correct positioning and layout of this equipment will become key to the efficiency of the OR. Future work could extend the planner to allow a variety of more advanced features, including:

- Visualisation of radiation zones for equipment that uses energy emission or detection;
- Visualisation of zones of action for OR staff and potential ergonomic optimisation procedures;
- Visualisation of sterile and non-sterile zones that define the sterility barrier;
- Situational and hazard training alongside risk process management and mitigation.

The delivery of such possible features can be achieved via distribution of the OR planner to OR staff's devices in order to support different working schedules and practices. A key challenge will be validation and evaluation studies to assess usability and future development.

REFERENCES

- [1] Qureshi M, Buckle P and Hanna G. "Use of incident reporting to inform theatre design and surgical practice". In: Improving Patient Safety 2008 'From Safe Design to Safe Practice'. Eds Hignett S, Norris B, Catchpole K, Hutchinson A and Tapley S. Publ Ergonomics Society, England, pp. 191-195
- [2] Bayranzadeh S, Joseph A, San D, Khoshkenar A, Taaffe K, Jafarifiroozabadi R, Neyens DM. "The Impact of Operating Room Layout on Circulating Nurse's Work Patterns and Flow Disruptions: A Behavioral Mapping Study". *Journal of Health Environments Research & Design*; 2018; 1-15.
- [3] Barbagallo S, Corradi L, de Ville de Goyet J, et al. "Optimisation and planning of operating theatre activities: an original definition of pathways and process modeling". *BMC Medical Informatics and Decision Making*. 2015;15:38.
- [4] Stryker ByDesign:
<https://www.stryker.com/us/en/communications/products/room-design.html>

Haptics-enabled palpation for intraoperative tumour detection using a cable-driven parallel manipulator

A. Saracino^{1,2}, T.J.C. Oude Vrielink³, E. Sinibaldi², A. Menciassi¹, G. Mylonas³

¹*The BioRobotics Institute, Scuola Superiore Sant'Anna, Pontedera, Italy*

²*Center for Micro-BioRobotics@SSSA, Istituto Italiano di Tecnologia, Pontedera, Italy*

³*hARMS Lab, Department of Surgery and Cancer, Imperial College London, London, UK
a.saracino@santannapisa.it*

INTRODUCTION

In current Robotic Minimally Invasive Surgery (RMIS) systems, haptic feedback is not available at the master site, which is considered as one of the main criticisms of da Vinci surgical system (Intuitive Surgical, Sunnyvale, CA), the most widely adopted surgical robot in the operating theatres. Kinaesthetic and tactile cues useful to distinguish tumoral lumps, blood vessels and nerves, which are commonly stiffer than the surrounding tissue, are therefore absent. Surgical manoeuvres affected include palpation for tumour detection [1]. Restoring realistic haptic sensation may therefore allow performing procedures typically requiring an open-surgery approach using MIS or RMIS. Intraoperative palpation can help early detection of cancer that can lead to an increase in the survival rate of patients. For these reasons, investigations have been conducted to convey the force sensation to the surgical robot master controller. Approaches include machine learning-based methodologies [2] and the use of ad-hoc palpation probes [3]. In previous works, a cable-driven parallel robot (CDPR) for minimally invasive applications was presented (CYCLOPS, [4, 5]). This system can be customised to various surgical needs, being procedure- and patient-specific. The main contribution of the work presented here is to demonstrate the intraoperative haptic feedback offered by the CYCLOPS and provide quantitative and qualitative performance metrics. To this end, we performed a pilot user study to compare the outcomes of a palpation test-case, performed with and without force feedback. Tissue - probe interaction forces are here detected in an economical way, without relying on any tip-attached F/T sensors.

MATERIALS AND METHODS

A CYCLOPS robotic system assembly was augmented with force sensing capabilities and teleoperated with a haptic device to perform the tasks. The experimental setup is depicted in Figure 1. Six cables were used for the manipulation of the end-effector in five degrees of freedom (DoF). Each cable is controlled by a brushless DC motor (2232-024BX4 22F 25:1, Faulhaber GmbH & Co.KG, Germany), mounted on an aluminium frame surrounding the system. The tension in each cable was measured via a pulley connected to a loadcell (LCL-020, Omega Ltd, UK), and mounted directly at the

actuation motor, similar as found in earlier work [5]. The system is controlled via an EtherCAT communication layer, with a soft real-time Linux computer as control input (Ubuntu 14.04, patched with low-latency kernel 3.13.0) at a 1 kHz frequency. A Geomagic Touch haptic controller (Geomagic Touch, 3D Systems, USA) is used to control the position and display the haptic feedback to the user. The end-effector is controlled in the 3 DoF in which the haptic device is able to provide feedback (x,y,z). The loadcells are digitized using an Instronet i100 device, connected to a single-board Windows PC (LattePanda) and sent over UDP to the Linux PC.

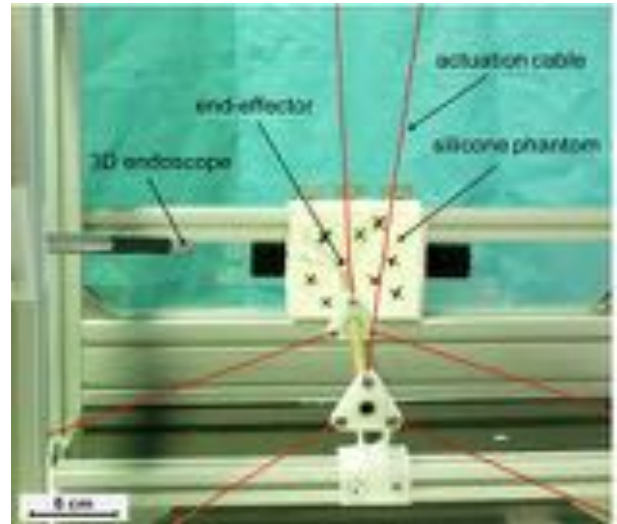


Figure 1 – The experimental setup (cables have been artificially enhanced to assist visibility)

The external load on the device is calculated by modelling the end-effector as free-floating object with six forces acting on it due to the cables, one due to the gravity and another as external load. As the cable tension is measured, and the direction of this force on the end-effector is derived from the known end-effector pose, the force vectors of the cables are known. As a result, the external load of the cable can be directly calculated using the equilibrium equations. The external load is forwarded to the user after multiplication with a haptic gain scalar. In the below experiments the derived external load was multiplied by a factor of 0.3. A 3D endoscope (Endoeye Flex 3D, Olympus, Japan) was used for visualization during the experiments.

Silicone soft tissue phantoms (Ecoflex 00-30, Smooth-On) with stiffer embedded spheres sized 15 mm (PDMS, Sylgard 184, 1:10 mixing ratio, Dow Corning) were moulded to realistically mimic healthy biologic tissue with stage T1 tumours in it.

A user study was designed to compare performances and subjective workloads during a palpation tasks in two experimental conditions: visual feedback only and visual plus haptic feedback available. Performances were evaluated in terms of nodule detection sensitivity (based on the user's skill in detecting harder structures in the phantom and possible presence of false positives) and exploration behaviour (maximum applied force). Indeed, haptic feedback potential benefits in RMIS include lower applied forces, thus leading to a decrease in tissue damage during the task. Subjective workload was measured through NASA-TLX questionnaire, while the user's preference between the two presented conditions was determined by a questionnaire in the Likert scale. Users were asked to fill in both questionnaires at the end of the experimental session.

An indentation/tapping palpation technique was preferred over a continuous sliding one, supported by published evidence that this provides better inference on specimen stiffness [6]. Therefore, after a 5-minute training, users were asked to indent the phantom in specific marked points, following a direction of indentation normal to the phantom surface, and to report to the investigator the perceived presence or absence of harder spheres. Experimental conditions were randomized to avoid any learning effect.

RESULTS

A pilot user study was conducted on n=6 subjects (aged 21-27), all of them PhD/Mres engineering students. The results of the quantitative metrics are shown in Table 1. These results show that with the current feedback method and population size, no significant difference is found between the visual and the visual + haptics experimental conditions. Qualitative evaluation using the Likert scale for testing user-friendliness, usability and intuitiveness showed 76±13.7% preference in performing the task with haptic feedback.

CONCLUSION AND DISCUSSION

This study has proven that specific performance metrics during a palpation task benefit from the restoration of the haptic feedback at the master site. While, with the current implementation, the users showed clear preference for the task with haptic feedback, the quantitative measures do not confirm this benefit. This contradiction may be related, in the first instance, to the lack of any surgical background of the involved subjects. Other possible explanations, indicated also by some users, refer to the nature of the task being subjective and often based on relative perception of stiffness when comparing current force feedback with a previous measure. In particular, this seemed challenging when multiple nodules are placed directly after each other, which sometimes caused confusion and doubt to

Table 1 – Quantitative results of the pilot user studies (n = 6).

	Detection sensitivity	False positives (0-1 range)	Fmax [N]
Only visual	0.57 ± 0.32	0.1 ± 0.17	2.69 ± 0.41
Visual + Haptic	0.6 ± 0.3	0.23 ± 0.15	2.64 ± 0.5
p-value	0.79	0.1	0.56

the participant. A second aspect indicated by the participants was their inexperience with the combined visual and haptic feedback in robotics, and their expectation that a longer training time would increase their performance.

Ongoing work calls for haptic sensation improvement by compensating for cable slackness at higher indentation depths, which can jeopardize the fidelity of force rendering. Moreover, we are currently conducting the study with the involvement of robotic/laparoscopic surgical trainees (ST3 and above, n=22 to date). This study is already shifting the results towards a clear quantitative evidence of haptic feedback improving task performance. When completed, the two studies will also provide better insight on the observed differences between subjects of engineering and surgical background.

Nonetheless, this work demonstrates a first implementation of a novel and economical approach that allows to quantify probe-tissue interaction forces using a surgical CDPR.

This work is supported by the NIHR Imperial BRC.

REFERENCES

1. Talasaz, A. and R.V. Patel. *Remote palpation to localize tumors in robot-assisted minimally invasive approach*. in *Proc. IEEE Int'l Conf. Robotics and Automation*, pp. 3719-3724, 2012.
2. Garg, A., et al. *Tumor localization using automated palpation with Gaussian Process Adaptive Sampling*. in *IEEE International Conference on Automation Science and Engineering*, pp. 194-200, 2016.
3. Herzig, N., et al., *A Variable Stiffness Robotic Probe for Soft Tissue Palpation*. *IEEE Robotics and Automation Letters*, 2018. **3**(2): p. 1168-1175.
4. Oude Vrielink, T.J., et al., *ESD CYCLOPS: a new robotic surgical system for GI surgery*, in *ICRA 2018*.
5. Miyashita, K., T. Oude Vrielink, and G. Mylonas, *A cable-driven parallel manipulator with force sensing capabilities for high-accuracy tissue endomicroscopy*. *International Journal of Computer Assisted Radiology and Surgery*, pp 659-669, 2018.
6. LaMotte, R.H., *Softness discrimination with a tool*. *J Neurophysiol*, 2000. **83**(4): p. 1777-86.

Force Sensing for Measuring Vaginal Wall Interaction Forces during Laparoscopic Sacrocolpopexy

J. De Smet^{1,3}, J. Deprest², A. Thys³, E. Vander Poorten¹

¹KU Leuven, Department of Mechanical Engineering, Leuven, Belgium

²UZ Leuven, Department of Development and Regeneration, Leuven, Belgium

³Hephaestus Surgical, Aarschot, Belgium

jef.desmet@kuleuven.be

INTRODUCTION

Pelvic organ prolapse (POP) is defined as any abnormal descent of organs through the vagina. Clinically visible POP occurs in up to 50% of parous women in their forties, half of them being symptomatic [1], [2]. The descent of these organs is caused by structural damage to the supporting ligaments and muscles of the pelvic floor. In sacrocolpopexy (SC) the vaginal vault and/or cervix is fixed by means of a graft to the anterior longitudinal ligament over the sacrum. It has been shown to be the most effective surgery for treating apical vaginal defects [3]. Today, SC can be performed in a minimally invasive (MIS) way and is then called laparoscopic sacrocolpopexy (LSCP). During LSCP, there are at least three people needed to perform the intervention: a surgeon who uses long, slender instruments to dissect and suture tissue; an assistant to manipulate a laparoscope so that the patient's internals can be visualized and a second assistant who uses a *vaginal manipulator* to position and tension the vaginal vault. Until now, the interaction forces between the manipulator device and the vaginal wall are unknown. The assistant occasionally over-tensions the vaginal wall, which leads to rupture [4], [5]. In order to quantify the interaction with the vaginal wall, a force sensor (Figure 1) has been developed. Its functioning is evaluated here.

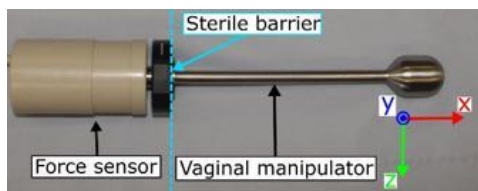


Figure 1: Force sensor on vaginal manipulator to measure interaction forces between the vaginal manipulator's head and the vaginal wall during LSCP; measurement is done according to visualized coordinate system; a sterile drape is placed between the screw connection of the vaginal manipulator and the force sensor to maintain a sterile barrier.

MATERIALS AND METHODS

The design of the sensor is based on a double Maltese cross configuration which allows for isotropic sensitivity by determining the proper distance between the crosses, which is 50mm in this case. The cross structures have a thickness of 0.8mm and can withstand forces up to 90N before mechanical failure, which is

prevented by safety stops. The sensor's housing is appropriately dimensioned to provide a comfortable grip for the manipulating assistant who has to hold the device for more than three hours at a time under heavy loads. The sensing elements are placed at the instrument handle so that all electronics stay outside the patient's body. This is convenient for guaranteeing electrical safety and to avoid complex sterilization approaches which might damage the sensor. During surgery the sterile barrier is maintained by a plastic sterile cover which is placed between the force sensor (non-sterile) and the vaginal manipulator (steam sterilization at 136°C). The vaginal manipulator is made out of biocompatible stainless steel 304. Only this part comes in contact with the patient. The sensor can measure forces in three degrees of freedom (DOF), namely F_x , F_y and F_z , which is sufficient for the application since interaction torques are expected negligible during vaginal vault manipulation. Each Maltese cross is equipped with strain gauges (Figure 2) to convert the deformation, caused by the applied loads, to a voltage output. Three full Wheatstone bridge circuits are applied, whereby each bridge output voltage represents a load direction thanks to proper positioning of gauges.

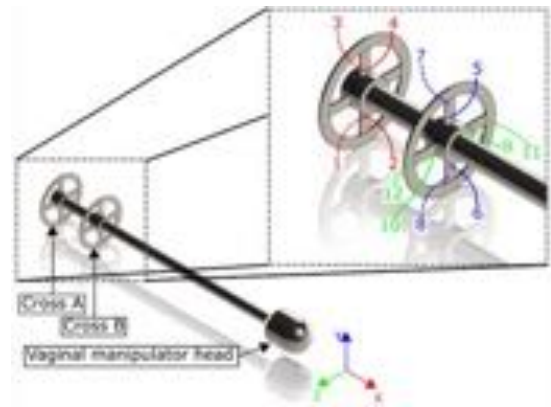


Figure 2: Double Maltese cross structure attached to the proximal side of the vaginal manipulator and Wheatstone bridge configuration for each measuring axis: x-axis in red; y-axis in blue and z-axis in green; dotted lines point to the backside of the cross structures.

Ideally the resulting calibration matrix \mathbf{K} that maps strains to forces should be a diagonal matrix due to the decoupled design. The sensor is characterized in lab-environment by clamping it subsequently in different orientations so that loads can be applied along respectively x-, y- and z-axis (Figure 3). The calibration

matrix \mathbf{K} , accuracy, precision and coupling between axes are evaluated by loading each axis five times over its calibration range, and taking the average of 5000 measurement samples (obtained at 1kHz) per loading step. The calibration range for the x-axis (axial loads) is $\pm 30\text{N}$ and $\pm 10\text{N}$ for y- and z-axis (radial loads). Axial forces are considered to be bigger than radial forces since the vaginal manipulator is mainly moved inwards along the center axis of the vaginal vault during tensioning. This causes a bigger axial reaction force of the vaginal tissue compared to radial forces.

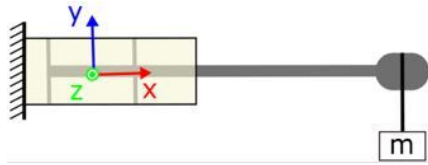


Figure 3: View upon calibration setup, known masses (m) are suspended along the different coordinate axes while the sensor's housing is clamped.

RESULTS

Without calibration, the sensor already shows proper decoupled behavior for the bridge voltage outputs. After multiplying with calibration matrix \mathbf{K} :

$$\mathbf{K} = \begin{bmatrix} 127 & 0.979 & -0.630 \\ 8.70 & 91.3 & -1.22 \\ 0.963 & 1.33 & 81.1 \end{bmatrix} \times 10^3, \quad (1)$$

the decoupling is enhanced even more.

The accuracy is calculated as the average error between the known applied load and the force output reading after application of \mathbf{K} . The standard deviation on the accuracy measurement is then used as a measure for the precision. The obtained accuracy and precision are respectively $2.73\% \pm 1.85\%$ for the x-axis, $2.66\% \pm 1.55\%$ for the y-axis and $2.63\% \pm 1.43\%$ for the z-axis for a full range. Figure 4 shows the difference between the sensor output before and after calibration.

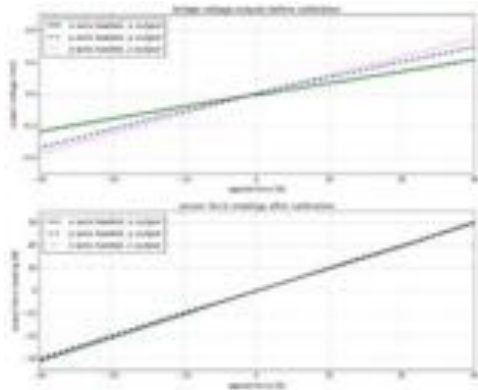


Figure 4: Relation between load and raw sensor outputs (above) and calibrated outputs (below).

Table 1 shows the remaining force output of the non-loaded axes while applying a maximal reference load (30N on x-axis, 10N on y- and z-axis) on a first axis. The results are the averaged values of the non-loaded axes during the accuracy measurement recordings.

Table 1 - Coupling between axes after calibration. A reference load is applied stepwise on a first axis over its calibration range. The remaining force outputs of the non-loaded axes are averaged as a measure of cross-sensitivity.

	F_x [N]	F_y [N]	F_z [N]
F_x ref	/	-0.249	0.334
F_y ref	0.624	/	-0.529
F_z ref	0.623	-0.327	/

CONCLUSION AND DISCUSSION

A force sensor to measure vaginal wall interaction forces during SC was designed and tested in a lab-environment. The range of loads used to calibrate the sensor is bigger than the expected range of interaction forces to make sure that all *in-vivo* situations can be measured correctly. The sensor has been made by design such that it allows decoupled measurement. Imperfections in manufacturing (e.g. small deviations in locations where strain gauges were glued) were reduced by determining an adequate calibration matrix. Indeed, the calibration matrix \mathbf{K} has a number of off-diagonal elements confirming the fact that the sensor was not perfectly decoupled by design. After applying the calibration matrix it was found that the size of the coupled force measurements is reduced to stay below 4% of the sensor range. Given the purpose of the sensor, the obtained accuracy and precision are deemed within limits to give a first idea about the actual applied *in-vivo* interaction forces. Ethical Committee approval has been obtained to use the sensor in a clinical trial to measure and register vaginal wall interaction forces during SC on 30 patients. Results of this trial will be of great value for future developments in the field of (robotic) assistive technology for SC.

REFERENCES

- [1] C. Glazener *et al.*, "Childbirth and prolapse: long-term associations with the symptoms and objective measurement of pelvic organ prolapse," *BJOG An Int. J. Obstet. Gynaecol.*, vol. 120, no. 2, pp. 161–168, 2013.
- [2] L. C. Turner, K. Kantartzis, J. L. Lowder, and J. P. Shepherd, "The effect of age on complications in women undergoing minimally invasive sacral colpopexy," *Int. Urogynecol. J.*, vol. 25, no. 9, pp. 1251–1256, Sep. 2014.
- [3] C. Maher, B. Feiner, K. Baessler, and C. Schmid, *Surgical management of pelvic organ prolapse in women*. Cochrane Database Syst Rev., 2013.
- [4] O. Eskandar, J. Hodge, and S. Eckford, "Strangulated small bowel through vaginal vault rupture: late complication of abdominal sacrocolpopexy," *Gynecol. Surg.*, vol. 7, no. 1, pp. 67–70, Feb. 2010.
- [5] Y. Halwani, V. Nicolau-toulouse, J. Oakes, J. Leipsic, R. Geoffrion, and S. M. Wiseman, "Transvaginal strangulated small intestinal hernia after abdominal sacrocolpopexy: case report and literature review," *Hernia*, vol. 17, no. 2, pp. 279–283, 2013.

Design and Evaluation of an Intraoperative Safety Constraints Definition and Enforcement System for Robot-Assisted Minimally Invasive Surgery

Luca Vantadori, Andrea Mariani, Thibaud Chupin, Elena De Momi, Giancarlo Ferrigno

Department of Electronics, Information and Bioengineering, Politecnico di Milano, Milan, Italy
luca.vantadori@mail.polimi.it

INTRODUCTION

Most of the studies and progresses in surgery have focused on minimizing the invasiveness of surgical procedures. In the last decades, there has been a significant methodological shift in several surgical procedures: surgeons do not directly see and, especially, do not directly touch the anatomical structures on which they operate. In fact, advances in video imaging, endoscopic technology and robotic instrumentation have made a definite transition from open to minimally invasive surgery possible [1]. However, surgical robots are still tele-operatively controlled by the healthcare professional and the human error remains considerably high. In minimally invasive surgery, even when performed with a robotic device, the most common complication is accidental damage to nerves, veins and arteries [2]. This may cause dysfunctions, heavy bleeding and affect the outcomes of the surgical procedure. To address this issue, we developed and tested a system for the intraoperative definition of safety constraints which generates a repulsive force on the robotic tool when it tries to enter the constrained region.

MATERIALS AND METHODS

Safety constraints can be defined as “control strategies” that can be used in robot-assisted manipulation tasks to assist the procedure by anisotropically regulating motion [3]. This is achieved by comparing the robotic tool position with respect to known restricted regions and then modulating the master command to prevent the manipulator from entering those regions.

The implementation of the constraint enforcement method is achieved by placing a virtual damped spring between the robotic tool and the constrained volume. The viscoelastic enforcement function is

$$\mathbf{f}_p = k_p(\mathbf{p}_d - \mathbf{p}_c) + k_d(\dot{\mathbf{p}}_d - \dot{\mathbf{p}}_c)$$

where \mathbf{f}_p is the constraint force vector, k_p and k_d are the proportional and derivative gains, and \mathbf{p}_d and \mathbf{p}_c are the current and desired tool position respectively. If the robotic tool is out of the constrained region, the desired position is coincident with the actual one and the force will be nil; in case it violates the constraint, the desired tool position is set to be the nearest point on the surface of the bound region, then creating the virtual linkage which finally generates the repulsive force (Fig. 1).

To generate the constrained region, the system allows the surgeon to define an intraoperative area above the

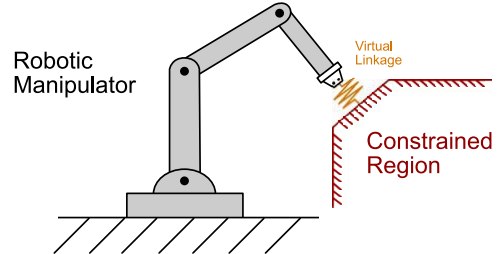


Figure 1. The safety constraints generate a repulsive force thanks to the virtual linkage.

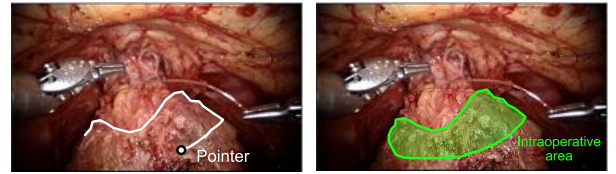


Figure 2. By moving the pointer, the surgeon can draw the safety area freehand.

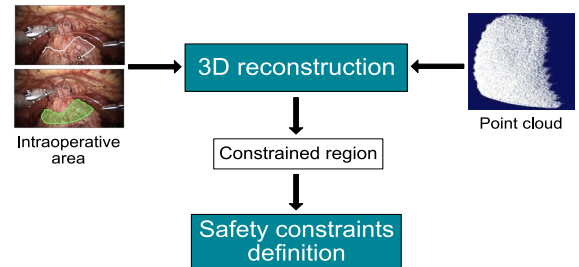


Figure 3. Operating scheme of the system.

patient’s anatomical structures. This is achieved by moving a pointer, shown on the surgical console viewer, with the same master controllers the surgeon uses to perform the surgical procedure (Fig. 2).

During the surgical procedure, a point cloud of the patient’s anatomical structures is produced by exploiting the disparity map between the images of a stereoscopic camera. The previously drawn area is projected to identify the portion of the point cloud belonging to the anatomical structure that the surgeon intends to select. In this way, a repulsive force is generated to prevent the robotic tool from entering the constrained volume, thus avoiding damage to the selected anatomical structures (Fig. 3).

To validate the system, we exploited the da Vinci Research Kit master console (Intuitive Surg. Inc.) and a virtual simulation environment we previously developed [4]. A virtual partial nephrectomy simulation was created with anatomically correct models of a renal tumour and renal arteries, both placed on a stand-in for the kidney

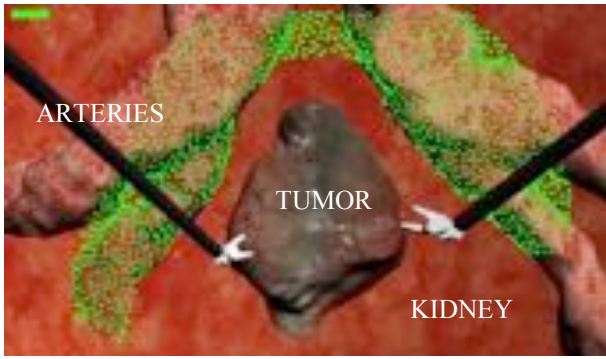


Figure 4. The virtual partial nephrectomy simulation. The constrained region is represented by the selected points coloured in green. Their colour changes from green to red according to the safety area - tool distance.

(Fig. 4). Ten volunteer candidates (with no experience with robotic tele-operation) were asked to perform the removal of the tumour by using virtual tools whilst trying to avoid the collision of the robotic tool with the renal arteries. Each participant performed the task 6 times, alternately under two different modalities: in the first unconstrained modality, the tumour removal is carried out without any feedback; in the second constrained modality, the candidate has to define an area enclosing the renal arteries so that the execution of the task is supported by the force feedback generated from the surface of the constrained region, as well as visual aids indicating the distance between the tool and the safety region. The proportional and derivative gains of the viscoelastic enforcement function were set to 1000 N/m and 10 N*s/m, while the maximum constraint force was imposed to be 4 N. In order to quantify the outcomes, the mean number of collisions of the robotic tool with the renal arteries, the mean total duration of the collisions (in seconds), the mean percentage of healthy tissue improperly removed in addition to the tumor (defined as the difference between the removed tissue surface and the tumor surface divided by the tumor surface) and the mean task execution time (in seconds) were analysed for each candidate and each modality. Due to the small sample size, non-parametric statistical significance tests were used to compare the performance of the users in the constrained and unconstrained task. The Wilcoxon rank sum test was then employed in MATLAB. Statistically significant effects were assessed at $p < 0.05$.

RESULTS

The distributions of the number of collisions, the total collisions time and the percentage of removed healthy tissue for the *constrained* and *unconstrained* task are shown in Figure 5 and their median values are reported in Table 1. The results suggest that the safety constraints have enhanced the accuracy in performing the task compared to the *unconstrained* case, reducing all the parameters. Furthermore, safety constraints reduced the variability of the performance among the users compared to the *unconstrained* sets. Finally, the average task time (considering only the duration of the tumour removal) show that users completed the constrained task faster:

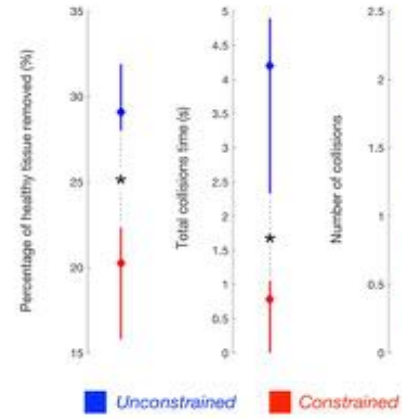


Figure 5. The accuracy metrics are reported in terms of median (diamond marker) and 25th – 75th percentiles (vertical bar) across the subjects.

	Unconstrained	Constrained	p
Number of collisions	1.75	0.50	<0.001
Total duration of collisions (s)	4.20	0.78	0.0013
% of healthy tissue removed	29.09	20.25	<0.001
Task execution time (s)	40.81	36.58	<0.001

Table 1. Task performance metrics median values across the users in the unconstrained and constrained mode.

32.6 sec. if *constrained*. vs. 40.8 sec. if *unconstrained*, $p < 0.001$. This can implicitly imply ease of use of the system and reduction of cognitive load.

CONCLUSION AND DISCUSSION

We presented a system for the intraoperative definition of viscosity-based constraints on a safety area. We tested this system on a virtual reality task and the results showed higher performances in terms of accuracy and time with respect to the traditional unconstrained case. This research focused only on a small group of candidates. For a higher statistical determinism, it will be necessary to carry out experiments involving a larger sample size. Additionally, repeating the study on medical participants would increase the impact on the research field.

ACKNOWLEDGEMENTS

The current work is part of the “SMARTsurg” (SMart weArable Robotic Teleoperated surgery) project, which has received funding from the European Union’s Horizon 2020 research and innovation programme.

REFERENCES

- [1] M. M. Hammoud et al., *To the point: medical education review of the role of simulators in surgical training*, American Journal of Obstetrics and Gynecology, 2008.
- [2] A. Okamura, *Haptic Feedback in Robot-Assisted Minimally Invasive Surgery*, Current opinion in urology, 2009.
- [3] S. A. Bowyer et al., *Active Constraints/Virtual Fixtures: A Survey*, IEEE Transactions on Robotics; 2014; 30:138-157.
- [4] N. Enayati et al., *A Framework for Assisted Tele-operation with Augmented Reality*, CRAS: Joint Workshop on New Technologies for Computer/Robot-Assisted Surgery, 2017.

Design of an ergonomic upper gastro-intestinal endoscopic device for gastric cancer diagnosis

Manish Chauhan¹, James Chandler¹, Pietro Valdastrì¹ and Keith Obstein²

¹Storm Lab, University of Leeds, ²Vanderbilt Institute for Surgery and Engineering
Email: (m.chauhan, j.h.Chandler, p.valdastrì)@leeds.ac.uk

INTRODUCTION

Gastroscopy or upper gastrointestinal (GI) endoscopy is a common diagnostic procedure, which is used for investigating medical conditions like difficulty in swallowing, persistent abdominal pain. It also finds its use in diagnosing stomach ulcers, gastro-esophageal reflux disease and treating bleeding ulcers, blockage in the esophagus, non-cancerous growth and cancerous tumors. Its general procedure involves pushing the flexible end of an endoscopic device with onboard camera (Gastroscope) down the patient's throat through the esophagus into the stomach for visual inspection (Refer Fig. 1(a)). This introduction of gastroscope involves two actions, (i) **tool articulation control**; and (ii) **tool feeding**. As seen in Fig. 1(a), both these actions are simultaneously performed by the medical practitioner with dedicated single hand use to each task. Additionally, gastroscope requires use of expensive and bulky equipment, trained personnel, costly reprocessing cost \$160 per procedure [1]. These issues were successfully addressed with design of a low cost, disposable continuum endoscope which was principally based on piston driven parallel bellows (referred as the Bellowscope) [1].

Figure 1(b) shows the intuitive design of the Bellowscope. It comprises of a continuum handle which pressurizes three syringe pistons for achieving corresponding bellow articulation. Based on feedback received from medical practitioners, its use during gastroscope involves use of dedicated twin hand control only for the device (Fig. 1(b)). For the task of feeding the flexible camera tube into the patient, the user must leave tool control and shift to tool feeding task. This continuous change of hands while task control is counter-intuitive while performing gastric screening. Secondly, the articulating camera end of this device is based on parallel actuation of three separate bellows. These bellows being soft are less stiff in comparison to the commercial devices (Fig. 1(c)). Low stiffness leads to increased vibration while introducing the Bellowscope into the stomach as the camera gets deflected by meeting internal organs which leads to shaky image quality.

To articulate the Bellowscope, pressurized air is forced through syringes, causing the bellows to expand relative to one another thereby inducing bending. However, since air is a compressible fluid, its pressurized action does not lead to the proportional articulation/bending angle in comparison to commercial counterparts (Refer Fig. 1(c)).

The reason for this is elastic nature of the bellows which blows up in expansion and desired air quantity spreads within that expanded cross-section. The following work presents design of a novel interface which addresses the above-mentioned disadvantages of the Bellowscope.



Figure 1: Upper GI endoscopic device challenges; (a) Tool control and feeding with traditional the gastro scope [2]; (b) Twin hand control of the Bellowscope [1]; (c) Comparison of range of motion and stiffness between traditional gastro scope with the Bellowscope.

DESIGN OF UPPER GI ENDOSCOPIC DEVICE

The improved design of the Bellowscope comprises of the following key components.

(a) The Integrated Bellows:

With an aim to control the vibrational and poor range of motion (Fig. 2(a)), the proposed design of the bellows comprises of an integrated structure which is a combination of three inter-twined air channels. The Bellowscope shown in Fig. 1(c) have $\phi 13.68\text{mm}$ diameter and a maximum articulation angle of 37° [1]. The inter-twined air channels in the proposed bellows allows smaller diameter, $\phi 6.8\text{mm}$. The bellows are molded together to form a stiffer, hygienic and smooth structure as each air channels support the structure to provide a complete articulation (from 80° to 180°) as seen in Fig. 2(b). The proposed bellows were made out of dragon skin 20 silicone (tensile strength of 3.79MPa) [3]. With a cylindrical profile of length 45mm , the stiffness of the bellows was estimated by modeling it as a cantilever ($k = \frac{3EI}{L^3}$). Where, E , I and L refers to the

elastic modulus, moment of inertia and length of the bellows. Stiffness of 13 N/m was estimated for the proposed bellows. This stiffness allowed an onboard camera for vibration less inspection.

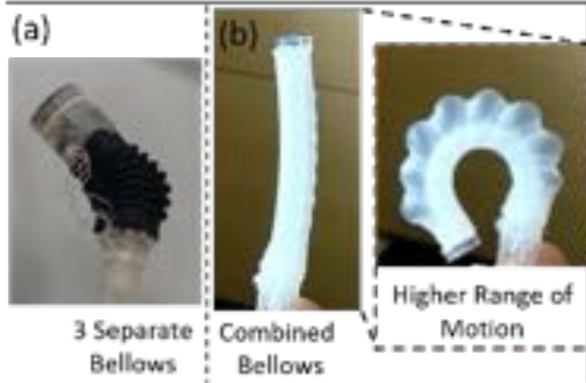


Figure 2: Improved design of the bellows (a) 3 separate bellow design; (b) Combination of bellow design and its improved range of motion and stiffness.

(b) *Device Interface design:*

The design of the device interface was done to promote single hand tool control. This was achieved by combining the actuation of the two air channels in the bellows through a specially synthesized cam follower mechanism (Refer Fig. 3). These cams were designed to actuate the pneumatic syringes such that full stroke of syringe causes complete articulation of the bellows. As seen, two cams are placed along same shaft at an angular offset of 120°. With this arrangement, the two air channels of the bellows are actuated in sequence. The actuation of the cam is done with a common rotation knob. The cam surfaces are designed to follow cycloidal motion such that there is smooth operation while actuating the bellows to its maximum articulation angle as seen in Fig. 2(b). Equation 2 expresses the position of piston in syringes (y) while pushing (referred as rising, θ_{ri}) air to actuate bellows.

$$y = L \left(\frac{\theta}{\theta_{ri}} - \frac{\sin(2\pi\theta)}{\theta_{ri}} \right) \quad (2)$$

Where θ and L is the rotation angle of cam for corresponding rise of piston in the syringe. Equation 1 is utilized to have linear relationship between cam rotation and syringe movement. A cycloidal cam surface profile leads to zero velocity and acceleration of piston at the beginning and the end of piston stroke. This makes bellow actuation smooth without jerks. Equation 3 and 4 represents the velocity (v) and acceleration (a) numerically. Here ω refers to the angular velocity of cam rotation.

$$v = \omega L \left(\frac{1}{\theta_{ri}} - \frac{\cos(2\pi\theta)}{\theta_{ri}} \right) \quad (3)$$

$$a = \omega^2 L \frac{4\pi^2}{\theta_{ri}^2} \frac{\sin(2\pi\theta)}{\theta_{ri}} \quad (4)$$

Gastroscopy involves active control for complete scanning the stomach inner walls. Such control is possible with the provision of the third syringe which is actuated with help of a slider crank (SC) mechanism. This mechanism is specially synthesized to achieve accurate control over bellow. A linear relationship is maintained between push button motion (input) and corresponding articulation of bellow (output). The SC mechanism is housed in a compact ergonomic grip. As seen in Fig. 3 inset, the user thumb actuates two syringes simultaneously with the help of the rotation knob. The third air channel of the bellows are controlled with index finger actuation of the push button. Hence, user could dedicatedly use single control over the tool articulation and again use the other hand for feeding the bellows into the patient stomach.



Figure 3: Novel Interface design of gastro-endoscope

CONCLUSION AND DISCUSSION

The above work presents design of a novel interface for a gastrointestinal endoscopic device which is the improved design for an earlier presented device [1]. An integrated bellow design actuated through specially synthesized cam and SC mechanism is presented. An ergonomic interface design is done to maintain clinical workflow of traditional gastroscopy. An enhanced workspace (up to 180°), stiffness (13 N/m) while articulation is achieved with integrated bellow design. Future work would involve introduction of an instrument channel through the device for performing in-situ/in-vivo biopsy.

REFERENCES

1. Garbin, N., et al. *A disposable continuum endoscope using piston-driven parallel bellow actuator*. in *Medical Robotics (ISMR), 2018 International Symposium on*. 2018. IEEE.
2. hirurgija, G.I., Accessed on 10th August 2018. <https://www.invita.rs/services/gastroscopy/?lang=en>.
3. Silicone, D.s., Accessed on 10th August 2018. <https://www.smooth-on.com/products/dragon-skin-20/>.

Human-Robot Shared Control for Split-Site Interaction and Disabled Assistance

Alaa Al-Ibadi^{1,2}, Samia Nefti-Meziani¹, and Steve Davis¹

¹Computing, Science and Engineering, University of Salford,

²Computer Engineering Department, University of Basrah,
a.f.a.al-ibadi@edu.salford.ac.uk

INTRODUCTION

The context where the robot will be used leads to understanding the interaction requirement among the robots and between the human and robot. This includes the number of humans and robots to be used, the task to be solved, and in several cases, the human is expected to assist the robot in overcoming the limitation in robot performance [1]. Numerous factors are nominated for the robot to be successful, such as the repetition to reach regular quality, the speed and the force of manufacturing robots, reduction of the task hazards, decrease of the force required and flexibility in programming [2].

The estimated number of multi-task robots around the world is about 1,664,000 as reported by the International Federation of Robotics (IFR) statistical analysis [3]. The industrial robots continue to develop in both safety and productivity; moreover, while they have evolved in their functionality, safety is a hugely significant concern [2].

Since the risk of injury is the most crucial factor for the human-robot interaction, the soft robotics technologies provide significant alternatives for rigid robots. The soft actuators that made as a human-like muscle such as the pneumatic muscle actuators (PMA) are used to design such type of robots. The main advantages of the PMA are the high force in comparison of its weight, multiple degrees of freedom (DOF) without joints, small workspace required and it is safe for human-robot collaboration [4].

MATERIALS AND METHODS

In this paper, the self-bending contraction actuator (SBCA) by Al-Ibadi, et al. [5] is used to design a single actuator continuum robot arm. The specifications for this actuator are listed in Table 1. The small size of the SBCA is used to develop a 4-fingers soft gripper, and it is mounted to the end of the soft robot arm.

Table 1. The specifications of the bending PMA

L_0 (m)	Rubber thickness (m)	Braided thickness (m)	Rubber diameter (m)
0.6	1.1×10^{-3}	0.5×10^{-3}	26.5×10^{-3}
Rubber stiffness(N/m)	Rod length (m)	Rod thickness (m)	Rod width (m)
545	0.6	0.003	0.025

L_0 is the length of the SBCA at relaxed condition (no pressure). Fig. 1.a-c shows the design and the implementation for the continuum arm and the gripper respectively.

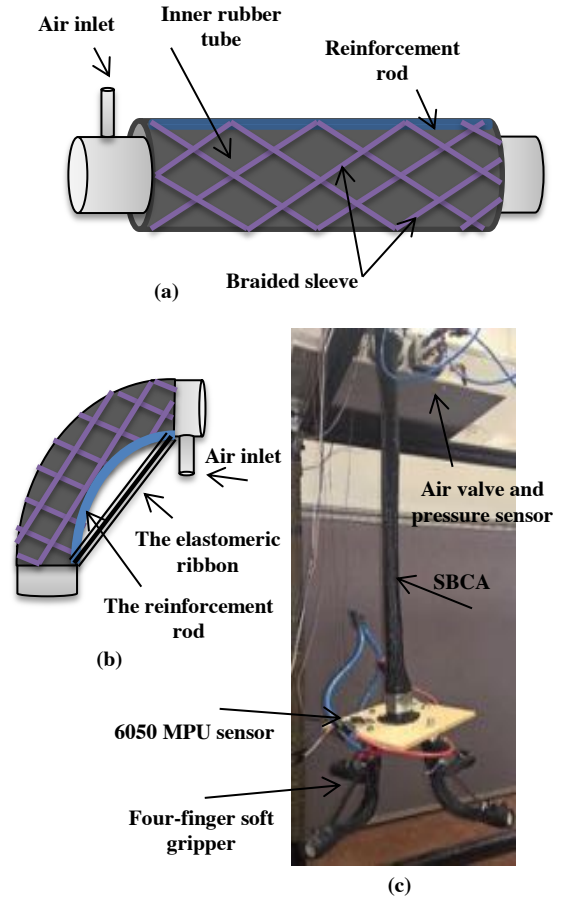


Figure 1. The bending continuum arm. (a) The structure of the SBCA. (b) The design of the soft finger. (c) The entire soft arm with soft gripper and

In order to control the grasping force and the bending angle of the proposed continuum arm by a split-site or disabled human arm, four sensors are used in both the human and the soft robot arms. Two 6-axis motion tracking (MPU 6050) sensors, an air pressure sensor and flex sensor and they are mounted as shown in Fig. 1.c and Fig. 2.

The flex sensor is mounted on the index finger as illustrated in Fig. 2 and it is connected to the pressure sensor to control the grasping process via Arduino Mega 2560 and a neural network (NN).

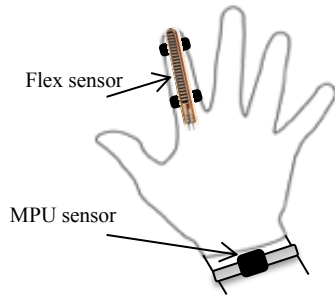


Figure 2. The sensor layout on human

The NARMA-L2 NN-controller by Matlab R2016a is used of 9-neurons in one hidden layer, 3-delayed plant inputs, 2-delayed plants outputs and it is trained by (trainlm) for 100 Epochs. The mean square error (MSE) for the training, testing and validating data is about 10^{-7} . The NN is trained by the relationship between the resistance of the flex sensor and the pressure of the soft gripper. A no grasping state (zero pressure) is assumed at the relaxed condition for the index finger and 300 kPa air pressure in each finger in the soft gripper at fully closed of the human hand.

One MPU sensor is mounted on the top of the soft gripper and the second MPU is worn as a bracelet closed to the wrist. Bending the human arm send a reference bending angle to control the bending angle of the soft robot arm. Fig. 3 illustrates the flow chart for the human-controller-robot system (HCRS).

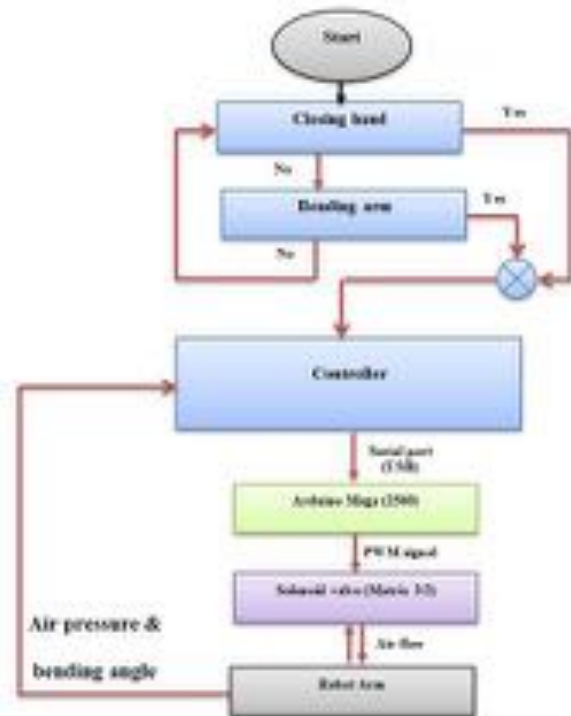


Figure 3. The flowchart of the human-controller-robot system.

RESULTS

Fig. 4 shows the step response at 0.25 Hz at root mean square error equal to 0.2° .

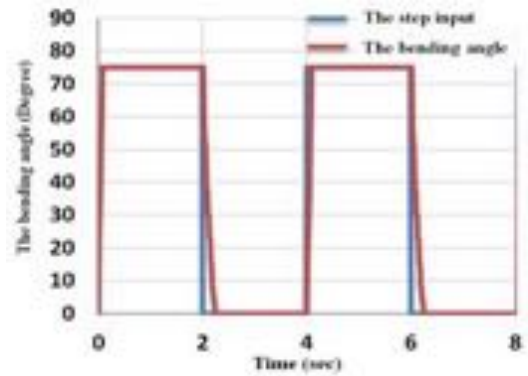


Figure 4. The step response at 0.25 Hz.

Fig. 4 shows the robustness of the controller to send the commands from the human arm to the robot to grasp and bend.

The proposed system is used either to control the robot arm which is not in the safe area for a human being or to assist an elderly/disable person to grasp and move objects by a safe robot arm. The disability is restricted by the ability to close the hand partially and bend the forearm in small degrees. The HCRS transfer these movements to full grasping and bending.

CONCLUSION AND DISCUSSION

Using the soft robot arm close to human is safe due to the softness and the light weight of its material.

The proposed human-controller-robot system (HCRS) provides a full controlled operation to move the continuum arm by an operator by wearing the flex and the MPU sensors. As well as help the person has difficulties to grasp and move the objects.

REFERENCES

- [1] K. Severinson-Eklundh, A. Green, and H. Hüttenrauch, "Social and collaborative aspects of interaction with a service robot," *Robotics and Autonomous Systems*, vol. 42, pp. 223-234, 2003.
- [2] J. Fryman and B. Matthias, "Safety of industrial robots: From conventional to collaborative applications," in *Conference on Robotics; Proceedings of ROBOTIK 2012; 7th German 2012*, pp. 1-5.
- [3] IFR International Federation of Robotics. (2015, 09/06/2016). *World Robotics 2015 Industrial Robots*. Available: <http://www.ifr.org/industrial-robots/statistics/>
- [4] A. Al-Ibadi, S. Nefti-Meziani, and S. Davis, "Cooperative project by self-bending continuum arms," in *Automation and Computing (ICAC), 2017 23rd International Conference on*, 2017, pp. 1-6.
- [5] A. Al-Ibadi, S. Nefti-Meziani, and S. Davis, "Active soft end effectors for efficient grasping and safe handling," *IEEE Access*, 2018.

A Long Short-Term Memory Network for Vessel Detection with a Steerable Needle

Vani Viridyawan¹, and Ferdinando Rodriguez y Baena¹

¹*Department of Mechanical Engineering, Imperial College London, UK,
f.rodriquez@imperial.ac.uk*

INTRODUCTION

During percutaneous interventions in the brain, puncturing a vessel can cause life threatening complications. To avoid this risk, current research has been directed towards the development of steerable needles. However, there is a risk that vessels of a size which is close to or smaller than the resolution of commonly used preoperative imaging modalities (0.59 x 0.59 x 1 mm) would not be detected during procedure planning, with a consequent increase in risk to the patient. One such steerable needle design, first demonstrated by Frasson et. al. [1] and referred to as a Programmable Bevel Tip Needle (PBN), incorporates a multi-segment, flexible design which is inspired by the egg laying channel of certain insects. The current embodiment of the PBN is manufactured using a biocompatible polymer with an outer diameter of 2.5 mm. The needle has two lumens in each of its four segments, which can be used as a conduit to deliver drugs or as the working channel for imaging modalities based on optical fibers.

In our previous study [2] we have shown that vessel detection is possible with our technology, coupled with a commercial laser-Doppler flowmetry (LDF) system. The LDF sensor detects a vessel by measuring the Doppler shift effect in the light refracted by the moving blood cells flowing within it. Since the laser light is randomly scattered in the tissue, it is challenging to determine the source of the signal, and thus determining the perfusion value of blood flow is not possible [3]. Therefore, the perfusion measurement is a relative value with an arbitrary unit (AU). Since a perfusion value corresponds to many vessel positions, in [2], successive measurements combined with a lookup table of the inverse perfusion value (measured under controlled conditions with varying parameters) were used to determine the axial (d) and off-axis (r) distance from the tip of the probe to the vessel (Figure 1). Based on r and d values of two LDF probes, the vessel pose could be predicted. However, this method only works for a given pair of tissue and vessel properties (e.g. a 0.6 mm vessel diameter with 5 mm/s flow velocity rate).

Under real conditions, neither the vessel nor the tissue properties are known beforehand. Hence, in this work, we propose a feasibility study where a Long Short-Term Memory (LSTM) network is employed to infer information about vessel diameter (ϕ) and position (r, d) based on successive measurements of an LDF probe. LSTM is an effective network to capture the long-term dependency of sequential data [4]. Here, the perfusion

values recorded while the needle is moving are considered as sequential data to feed the network.

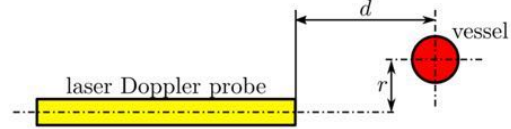


Figure 1. Axial distance d and off-axis distance r from the tip of the probe to a vessel

MATERIALS AND METHODS

LSTMs require a large number of training data sets. Therefore we used Monte-Carlo simulations [5] to model measurements from the LDF system. The simulations were compared to characterization results of a 0.6 mm diameter vessel phantom. The phantom mimics the optical properties of grey matter (reduced scattering coefficient $\mu'_s \approx 0.75 \text{ mm}^{-1}$). The phantom was made by adding 3 g/L of titanium dioxide (TiO_2) into 4.5 % weight gelatin [6]. The blood surrogate was 3.5% fat milk diluted in water to obtain 25% volume fraction.

The simulation was then extended to model the perfusion value for 0.3, 0.6, 0.9 mm diameter vessels, with μ'_s equal to 0.55, 0.75 and 0.95 mm^{-1} . The flow velocities were set at 10, 15, and 20 mm/s. For each set of optical properties, the perfusion values were simulated at off-axis positions ranging from 2 to 0 mm in 0.2 increments and at axial positions ranging between 0.75 to 4.05 mm in 0.3 mm increments. For each vessel diameter, the maximum and the minimum simulated perfusion value at a certain vessel position from the needle tip were recorded. Since the vessel parameter and tissue optical properties can be any value between the maximum and minimum values of the parameters used for the simulation, for the training dataset, the perfusion value at one position was generated based on a random number uniformly distributed between the maximum and the minimum perfusion value at that point. In this proof-of-concept, we assumed that only a single vessel is ever detected by the probe.

The LSTM was used to predict vessel parameters $V(r, d, \phi)$ based on perfusion measurements $\text{Perf}_1, \text{Perf}_2, \dots, \text{Perf}_i$. Mathematically this is equivalent to computing

$$P(V(r, d, \phi) | \text{Perf}_1, \text{Perf}_2, \dots, \text{Perf}_i)$$

The LSTM consists of 2 layers, with 100 nodes in each layer. A dropout value of 0.5 was used to avoid overfitting. We then discretised the measurement range of the sensors with 0.1 mm resolution for three diameters (0.3, 0.6, and 0.9 mm). The total number of classes was 660. The training datasets consisted of 30,000 samples, with 30 steps per sample. Each step corresponds to a 0.3 mm difference in d . Since the minimum radius of

curvature of PBN is 70 mm while the maximum d that can be detected by the sensor is only ≈ 2 mm, we modelled the insertion as a straight insertion (no changes in r value in the successive positions). This is because the change in r corresponding to the maximum curvature, with 2 mm difference in d , is less than the resolution used for the discretisation of the sensor.

RESULTS

Figure 2 shows the comparison between the simulated and measured perfusion values. To ease comparisons, all perfusion values were normalised against the perfusion value at 0.75 mm axial and 0.00 mm off-axis position. The simulation shows good agreement with the experiments. Table I shows the confusion matrix of the prediction. For the correctly predicted diameter, the root-mean squared errors (RMSE) of the position prediction are 0.14, 0.19, and 0.27 mm for 0.3, 0.6, and 0.9 mm diameter, respectively. Figure 3 shows an example of the perfusion values from the experiments and its prediction. The network should choose the correct diameter of the vessel: 0.3 mm (top row), 0.6 mm (middle row), and 0.9 mm (bottom row). After successive measurements, the network can predict the diameter and position of the vessel correctly.

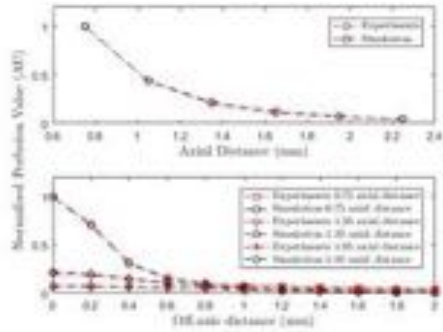


Figure 2. Comparison between normalised simulation and experimental perfusion values

Table I. Confusion matrix of the prediction; ND: No detection

		Predictions			
		ND	0.3	0.6	0.9
Actual	ND	0.975	0.007	0.011	0.007
	0.3	0.031	0.804	0.122	0.043
	0.6	0.049	0.061	0.724	0.166
	0.9	0.038	0.019	0.21	0.732

CONCLUSION AND DISCUSSION

As can be seen in Table I, there are several cases where a vessel is predicted in the no-detection area state. Further

analysis shows that it is in the area close to the maximum detection range of the sensor. The LSTM network is able to predict the possible diameter of the vessel with its position. This prediction can still be done even though the optical properties of the tissues and the properties of the vessels are not known. Even though we trained the network using simulation data, as can be seen in Figure 3, it can be used to predict experimental measurements correctly.

Even though here we could predict the vessel position from a single probe, we still do not know the vessel pose in three dimensional space. It is because there are many possible vessel poses that can have a pair of off-axis and axial distances. In order to remove this ambiguity, we could use multiple forward looking sensors [2]. This will be part of our future work. Additionally, during the insertion, in this study we assumed that the vessel is static, while it is possible to account for the effect of a moving vessel within the model. Previously, we used a high resolution material tracking setup based on Particle Image Velocimetry (PIV) to investigate tool tissue interactions [7]. By combining this method with a vessel embedded within the sample, we could predict the movement of the vessel during insertion. This work will also be part of future work.

REFERENCES

- [1] L. Frasson, et. al., "Biologically inspired microtexturing: investigation into the surface topography of next-generation neurosurgical probes," *Conf. Proc. Annu. Int. Conf. IEEE Eng. Med. Biol. Soc. IEEE Eng. Med. Biol. Soc. Annu. Conf.*, vol. 2008, pp. 5611–4, Jan. 2008.
- [2] V. Virdyawan, et. al., "Laser Doppler sensing for blood vessel detection with a biologically inspired steerable needle," *Bioinspir. Biomim.*, vol. 13, no. 2, p. 26009, 2018.
- [3] I. Fredriksson, "Model-based quantitative laser Doppler flowmetry in skin," *J. Biomed. Opt.*, vol. 15, no. 5, p. 057002, 2010.
- [4] K. Greff, et. al., "LSTM: A Search Space Odyssey," *IEEE Trans. Neural Networks Learn. Syst.*, vol. 28, no. 10, pp. 2222–2232, 2017.
- [5] F. de Mul, et. al., "Laser Doppler Velocimetry and Monte Carlo simulations on models for blood perfusion in tissue," *Appl. Opt.*, vol. 34, no. 28, pp. 6595–6611, 1995.
- [6] H. G. Akarçay, et. al., "Determining the optical properties of a gelatin-TiO₂ phantom at 780 nm," *Biomed. Opt. Express*, vol. 3, no. 3, p. 418, 2012.
- [7] A. Leibinger, M. J. Oldfield, and F. Rodriguez y Baena, "Minimally disruptive needle insertion: a biologically inspired solution," *Interface Focus*, vol. 6, no. 3, p. 20150107, 2016.

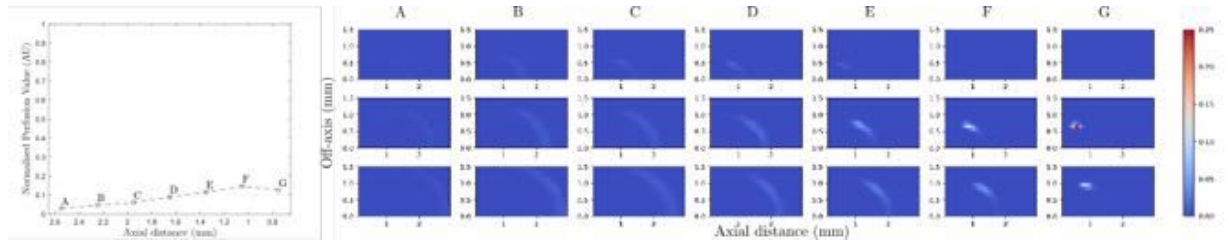


Figure 3. The probability of vessel diameter and positions (right) after successive measurements (left): y axis - off-axis distance; x axis - axial distance; top row: 0.3 mm diameter, middle row: 0.6 mm diameter, bottom row: 0.9 mm diameter. The actual diameter of the vessel was 0.6 mm, at the end of the insertion the actual position of the vessel was at 0.67 mm off-axis and 0.75 mm axial distance. The perfusion data were taken from experiments.

Gesture Classification in Robotic Surgery using Recurrent Neural Networks with Kinematic Information

E.B. Mazomenos¹, D. Watson², R. Kotorov² and D. Stoyanov¹

¹ *Wellcome/EPSRC Centre for Interventional and Surgical Sciences, Department of Computer Science, University College London, London, U.K.*

² *Trendalyze Inc., London, U.K.*

INTRODUCTION

The integration of robotics in minimally-invasive surgery has witnessed remarkable increase over the previous decade. Breakthrough innovations in robotic technology, imaging and sensing facilitated the design of novel surgical systems for a number of different operations (laparoscopy, endovascular surgery). Prime example is the da Vinci Surgical System (dVSS; Intuitive Surgical Inc., Sunnyvale, CA, USA) used nowadays in many laparoscopic resection procedures (prostatectomy, cholecystectomy, nephrectomy) while it is constantly expanding to other surgical domains.

The use of robotic technology offers significant operational advantages like increased maneuverability, reduction of tremor and more precise tool positioning thus minimising intra-operative risk and trauma ultimately leading to a reduction in recovery times [3]. The continuous development of image-guided robotic surgery creates a need for new surgeons to go through analogous training for this type of surgery in order to master the necessary dexterous and technical skills. The currently practiced method of surgical training is heavily-based on expert supervision, with faculty surgeons reviewing and evaluating performance through manually assessing global rating scales and task specific checklists. The scoring procedure requires significant amount of time and it is also subjective and prone to interobserver variability. Subsequently, it has been advocated that novel objective methods, focusing on competency metrics should be developed for evaluating surgical trainees. Typically, robotic surgical systems, like the dVSS, have the ability to record both video and tool kinematic parameters (joints pose). This offers the possibility for analysing surgical procedures and developing objective performance methods based on the manipulation pattern of surgical tools. Procedures can be broken down to sequential surgical tasks which can be further partitioned to autonomous activities termed as “gestures”. It has been reported that the ability to recognize surgical gestures can be further exploited for performance assessment [1].

In this work we introduce the application of Recurrent Neural Networks (RNNs) on surgical kinematic data, for the classification of gestures in three fundamental surgical tasks (suturing, needle passing knot tying). The developed RNN-based classifier achieves close to 60%

average classification accuracy for all three tasks when trained and tested with dVSS kinematic data from the same operator. Our preliminary work indicates that this type of artificial neural networks can be the building blocks in gesture classification systems which can form the basis for further developing automated skill assessment methods in robotic surgery.

MATERIALS AND METHODS

The JHU-ISI Gesture and Skill Assessment Working Set (JIGSAWS) is a publicly available surgical dataset comprising of video and kinematic data from the execution of three basic surgical tasks (suturing, knot tying and needle passing) with the dVSS on bench-top models by eight surgeons (subjects) of varying level of expertise [1, 2]. All subjects performed each task five times. The stereo video output of the dVSS endoscopic camera module was captured at 30fps in 640x480 resolution. The kinematic data contain 3D position, orientation, velocity and gripper angle values from both the master and slave, left and right manipulators totaling 76 motion-related parameters. The two datastreams are synchronised with the same sampling rate.



Figure. 1. The three surgical tasks performed in JIGSAWS: from left to right – Suturing; Needle Passing; Knot Tying.

A vocabulary of subtasks (gestures) is also formulated for representing each task in JIGSAWS. A surgical gesture is considered as a single action that completes a clearly identifiable step. Gestures are completed sequentially, and their entire sequence comprises the overall task. Fifteen different gestures are defined in JIGSAWS and used to manually annotate the dataset in such a way that each temporal datapoint (video and kinematics) is assigned a single gesture. The list of gestures in JIGSAWS is:

- (G1) reaching for the needle with right hand;
- (G2) positioning the tip of the needle;
- (G3) pushing needle through the tissue;
- (G4) transferring needle from left to right;
- (G5) moving to center of workspace with needle in grip;
- (G6) pulling suture with left hand;

- (G7) pulling suture with right hand;
- (G8) orienting needle;
- (G9) using right hand to help tighten suture;
- (G10) loosening more suture;
- (G11) dropping suture and moving to end points;
- (G12) reaching for needle with left hand;
- (G13) making C loop around right hand;
- (G14) reaching for suture with right hand;
- (G15) pulling suture with both hands.

RNNs is a class of neural networks that their structure includes directed connections along a sequence, like a graph, allowing information to persist. Each node in an RNN has a time-varying activation value and each connection between nodes carries a modifiable weight. A standard building block of RNNs is a Long-Short Term Memory (LSTM) unit. This comprises of the input and output stages and the internal cell as illustrated in Figure 2.

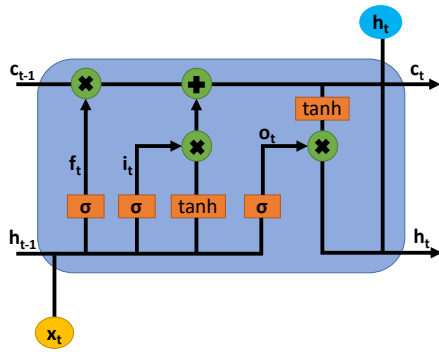


Figure. 2. The fundamental LSTM unit.

For our multi-label classification problem we design an RNN using an LSTM block with an internal dimension of 128 followed by a fully-connected (FC) layer with softmax activation that concatenates the LSTM output and produces the classification result. The dimension of the FC layer is set to the number of gestures that we intend to classify. To minimise overfitting we employ dropout in the LSTM block with a value of 0.3. Our investigation takes place with the kinematic information of each subject separately for each task. This resulted to the dense layer having variable dimension since each subject may perform the task using a different number of gestures and in situations gestures not present in the nominal sequence as defined in JIGSAWS.

Our intention was to initially evaluate the ability of the RNN to classify the surgical gestures of each individual subject, in the three tasks, only using data from that particular subject. We therefore collated the kinematics from all executions that a subject performed on each task and used the 80%-20% rule to separate the data into a training and testing dataset. Through experimentation we identified that the inclusion of the gripper angle value diminishes performance, hence we chose to disregard this parameter from both the master and slave and perform our investigation with the remaining 72 kinematic variables. The gesture annotations were used

as the ground truth labels. For training the RNN the cross-entropy was set as the loss function and gradient descent optimization with adaptive moment estimation was performed to obtain the weights of the LSTM connections. The RNN network was trained for 15 epochs with a batch size of 64.

RESULTS

The performance of the RNN was evaluated using as accuracy metric the percentage of correct gesture classification over the total number of gesture annotations. Table 2 lists per subject and average accuracy results for the three tasks.

Table 1. Classification accuracy results (subject 6 had no annotations for the Needle Passing task)

Subject	Suturing	Needle Passing	Knot Tying
1	63.22%	72.20%	57.28%
2	63.10%	70.89%	82.70%
3	75.70%	36.86%	69.23%
4	64.50%	56.80%	56.15%
5	64.49%	79.49%	24.03%
6	59.80%	-	76.18%
7	67.66%	47%	52.05%
8	73.69%	76.76%	58.73%
Average	66.52%	62.85%	59.54%

CONCLUSION AND DISCUSSION

In this paper we have demonstrated that RNNs have considerable potential as building blocks in robotic surgical gesture classification systems. The ability to partition surgical tasks into simple gestures can be exploited in the development of objective performance assessment methods. Results show that close to 60% average classification accuracy can be achieved with a simple RNN-based gesture classifier. Future efforts will focus on boosting classification performance by developing hybrid, combining Convolution Neural Networks and RNNs, learning-based systems that combine both kinematic and video information.

REFERENCES

- [1] N. Ahmadi et al., "A Dataset and Benchmarks for Segmentation and Recognition of Gestures in Robotic Surgery", in IEEE Trans Biomed Eng, vol. 64 (9), pp. 2025-2041, Sep. 2017.
- [2] Yixin Gao et al., "The JHU-ISI Gesture and Skill Assessment Working Set (JIGSAWS): A Surgical Activity Dataset for Human Motion Modeling", In Modeling and Monitoring of Computer Assisted Interventions (M2CAI) – MICCAI Workshop, vol 3 2014.
- [3] C. Bergeles and G. Z. Yang, "From Passive Tool Holders to Microsurgeons: Safer, Smaller, Smarter Surgical Robots", in IEEE Trans Biomed Eng, vol. 61(5), pp. 1565-1576, May 2014.

Incision Port Displacement Modelling Verification in Minimally Invasive Surgical Robots

I. Sayyaddelshad , E. Psomopoulou , S. Abeywardena , A. Tzemanaki , and S. Dogramadzi

Bristol Robotics Laboratory, University of the West of England, Bristol, United Kingdom

INTRODUCTION

Robot-assisted minimally invasive surgical procedures are long and complex involving large expert teams that perform a plethora of tasks required for the successful completion of surgery. Since the mid-80s, robotic assistance involved a surgeon to teleoperate surgical tools providing no automation or autonomy in its performance. Enabling surgical robots for automation could provide more precision and speed while obviating the need for long surgical training to carry out unwieldy tasks. This paper considers one aspect of using robotic instruments to autonomously perform precision motion in robot-assisted laparoscopic surgery where robotic instruments go through trocars inserted through the patient's skin. The experience shows that the elasticity of the skin causes displacements of the incision ports which can result in localization and motion errors, thus, creating inaccuracy in robot performance by moving the instrument in undesirable directions. The offline calibration that calculates exact kinematic parameters does not account for online errors due to interactions with the unstructured environment [1]. Some approaches use force sensors in the trocar or in the robot to minimize interactions at the port or passive joints between the instrument and the robot end-effector to assess more accurately the instrument pose [2, 3]. Another way to approach the issue is by measuring the position of the instrument tip using cameras or magnetic position trackers. Such measurements eliminate the problem of errors in the forward kinematics, but do not directly solve the problem of errors in the inverse kinematics and position control. In [4], authors present online estimation of the local Jacobian using position information to reduce the effects of errors in inverse kinematics. However, this approach is sensitive to significant motion in a single direction.

In order to analyse the aforementioned error at the incision port, this research study aims at modelling incision port displacements and the instrument as a single link manipulator attached to a flexible joint. Our first objective is to experimentally emulate the surgical instrument motion through a surgical trocar inserted in artificial skin in order to highlight kinematic error induced by the elasticity of the skin.

MATERIALS AND METHODS

The experiments were conducted using the setup shown in Figure 1. A DaVinci surgical instrument was attached to the flange of a KUKA LBR iiwa robotic arm and passed through a trocar inserted in the incision port of the artificial skin. The experiments were carried out considering the incision port as a fulcrum point, i.e. the arm was controlled to rotate the instrument shaft around the incision port in a single direc-

tion by an angle of 10° . The experiments were performed for 7 different lengths of the shaft below the skin surface $l = [13\ 15\ 17\ 19\ 21\ 23\ 25]\text{ cm}$, three times for each length. In order to determine induced kinematic errors, optical reflective markers were placed on the endpoint of the tool and on the incision port to track their positions using a Polaris (NDI) sensor.

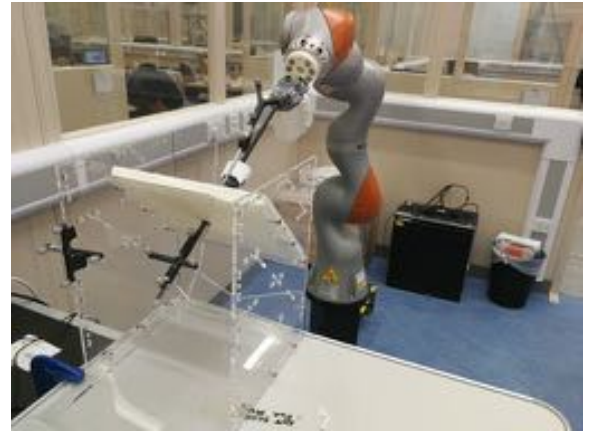


Figure 1: Experimental setup at Bristol Robotics Laboratory

RESULTS

Figure 2 shows the tool (blue lines) and the incision port (red lines) endpoints in the Cartesian space for one of the experiments where the instrument shaft was 19 cm below the skin. The initial pose of the shaft is denoted by grey lines while the pose of the shaft at the end of the motion is denoted by black lines. The arrows show the motion direction of the tool endpoint. The solid lines correspond to the positions calculated using forward kinematics whereas the dashed lines correspond to the positions measured by the Polaris sensor. The significant error between the positions renders the incision port non-rigid (detail in Figure 2). Figure 3 shows the Euclidean norm of the position errors of the tool endpoint and the incision port with respect to the different lengths of the shaft beneath the skin. The bars represent the minimum and maximum error values recorded in the experiments. For a single experiment, Table 1 shows statistical features of the incision port position displacements when the instrument's length is 13 cm below the skin.

MATHEMATICAL MODEL

In this section, we present a fundamental model, a single-link manipulator with a flexible joint, to define the error of the end-effector position induced by the incision port displacement. The schematic view of the flexible joint manipulator is depicted in Figure 4. It is clear that the system has two de-

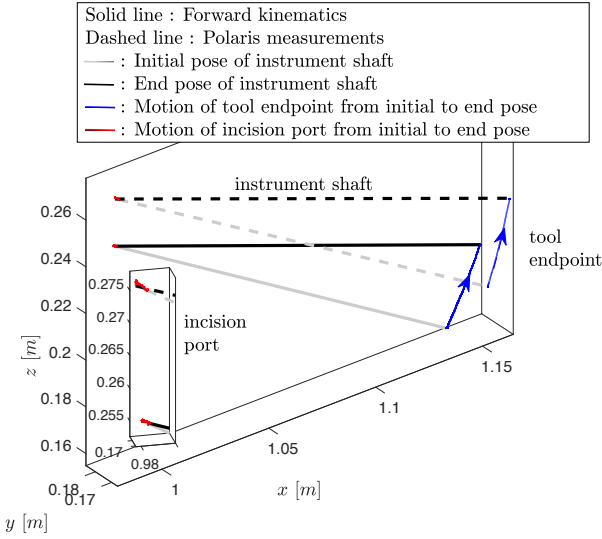


Figure 2: Motion of tool endpoint and incision port in the Cartesian space. Comparison between positions calculated using forward kinematics and positions measured by Polaris. (Experiment time: 5 seconds)

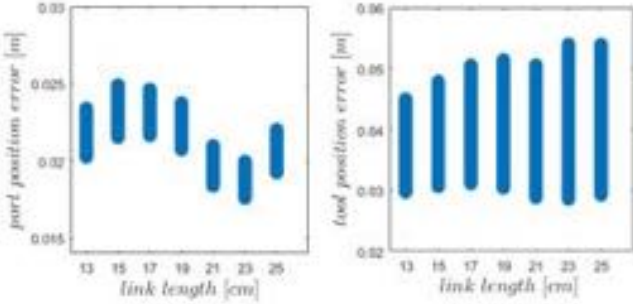


Figure 3: Min-max values of the Euclidean norm of position errors with respect to the shaft length that is below the skin (Left: incision port. Right: tool endpoint)

Error Statistics [cm]	
Mean	2.19
Minimum	2.06
Maximum	2.31
Mode	2.06
Standard Deviation	0.000733

Table 1: Error statistics

degrees of freedom corresponding to the rotation of the motor shaft with respect to a coordinate frame fixed to the base, and the rotation of the flexible joint with respect to the motor. The generalized coordinates are therefore the angular position of the motor θ_m and the angular displacement of the flexible joint θ_f (see Figure 4). The state-space representation of the system is:

$$\begin{aligned}
 \dot{x}_1 &= x_2 \\
 \dot{x}_2 &= \frac{k_s}{J_m} (x_3 - x_1) + \frac{1}{J_m} \tau \\
 \dot{x}_3 &= x_4 \\
 \dot{x}_4 &= \frac{-k_s}{J_l} (x_3 - x_1) + \frac{mgl}{2J_l} \sin x_3
 \end{aligned} \quad (1)$$

where $[x_1, x_2, x_3, x_4] = [\theta_m, \dot{\theta}_m, \theta_l, \dot{\theta}_l]$ is the state vector, τ is motor torque, l and m are length and mass of the link, respectively. In order to validate the proposed model, experimental

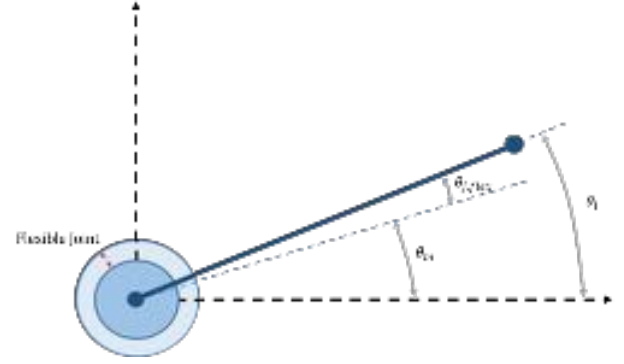


Figure 4: Flexible Joint

tests are needed where all inherent system parameters, such as the motor moment of inertia J_m and spring stiffness k_s , can be calculated. However, experimental model validation is an extension of the current study.

CONCLUSION AND DISCUSSION

According to Figure 3 it is clear that there is a significant error in the position of the incision port (an average of 2 cm) which in turn induces a larger error in the position of the tool endpoint (an average of 4 cm). The larger error in the tool position might also be a consequence of the instrument shaft's inherent flexibility. Noise and other factors can also affect the accuracy of the sensor's measurements, which according to the manufacturer is 0.35 mm RMS. Nevertheless, these error values can be critical in some MIS applications where much higher precision would be required (e.g. cardio-vascular or ENT surgery). Consequently, a model that incorporates these displacements is needed for accurate position control. This displacement at the incision port can be modelled as a single link flexible-joint planar manipulator as depicted in Figure 4, where flexible joint motion represents the undesired incision port motion.

ACKNOWLEDGEMENTS

This work has received funding from the European Union's Horizon 2020 research and innovation programme under grant agreement No 732515.

REFERENCES

- [1] R. A. Beasley, R. D. Howe and P. E. Dupont, "Kinematic Error Correction for Minimally Invasive Surgical Robots," Proceedings of the IEEE International Conference on Robotics & Automation, New Orleans, LA, 2004.
- [2] N. Zemiti, G. Morel, T. Ortmaier and N. Bonnet, "Mechatronic Design of a New Robot for Force Control in Minimally Invasive Surgery," in IEEE/ASME Transactions on Mechatronics, vol. 12, no. 2, pp. 143-153, 2007.
- [3] B. Willaert, B. Corteville, D. Reynaerts and H. Van Brussel, "A Mechatronic Approach towards Bilateral Teleoperation for Keyhole Surgery" International conference on New Actuators, pp. 144 - 147, 2012.
- [4] M. Jgersand, "Visual servoing using trust region methods and estimation of the full coupled visual-motor Jacobian" IASTED Applications of Robotics and Control, pp. 105-108, 1996.

Monocular 3D Reconstruction of the Colon Using CNNs Trained on Synthetic Data

A. Rau¹, F. Chadebecq¹, P. Riordan², D. Stoyanov¹

¹*Wellcome / EPSRC Centre for Interventional and Surgical Sciences (WEISS), University College London*

²*Digital Surgery, London, UK*

a.rau.16@ucl.ac.uk

INTRODUCTION

Colorectal cancer is the third most common cancer worldwide and is rising in incidence. Indicators or precursors to cancerous tissue development can be detected as polyps and removed during colonoscopy. However, complete, endoscopic colon investigation is still challenging and often regions of the colon are not fully examined resulting in high polyp miss rates [1]. Improving the endoscopist's ability to detect abnormal tissue through computational or biphotonic techniques and also to navigate within the colon and reference the position of the camera within the anatomy are significant clinical needs. Better navigation within the colon relies on the ability to map the 3D environment and localize the endoscope within it, but while computer vision advances make this possible in many applications, it has yet to be achieved reliably in endoscopic examination.

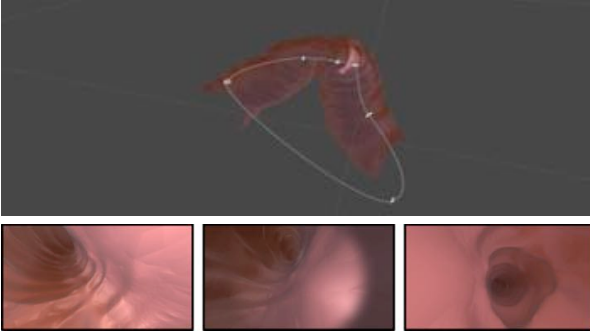


Figure. 1. Colon segment observed within the *Unity* simulation environment (top) with camera trajectory and examples of the endoscopic inside view of the virtual colon (bottom) with different material and lighting configurations generating views from the simulated colon environment.

With recent advances in deep learning, data driven approaches are leading the performance tables in vision based environment mapping. One problem with applying such approaches to endoscopy is that ground truth data is not available to train any CNN models. An appealing alternative, the use of synthetic data, has recently been reported for predicting depth during colonoscopy [2]. After training on simulation, a transformer network, that learns to generate a synthetic representation of real RGB images is used to adapt to real data. Despite promising results the ability of the network to handle real images can still be improved and needs further investigation.

In this paper, we take a different approach and learn directly from the properties that synthetic and real colons have in common, namely, their shape. In synthesizing images with different light/material-configurations, we emphasize the importance of learning

a shape prior based on depth instead of using hand modelled assumptions or regularization, as is often used in shape-from-shading, for example. Our experiments with different state-of-the-art algorithms [3,4,5] show that when lighting conditions change, the prediction capability of networks fail and the models lose any understanding of tubular shape. We therefore first learn from depth maps a statistical model that describes the shape of the colon. During training, we then penalize predictions of the CNN that, according to the learned shape model, have a small probability.

MATERIALS AND METHODS

Data Generation: Using the game engine *Unity*, we generate simulated endoscopic renderings of a 3D mesh, which is based on a CT scan of a human colon. We simulate an endoscopic camera with an attached light source that follows a trajectory through the colon (Figure 1). According to a frames/sec rate RGB images and corresponding depth maps, scaled to a depth $\in [0,1]$, are recorded. To obtain a larger data set, we randomly displace and rotate the camera relative to its initial path during render passes.

We generate RGB images using different materials by varying colors and reflection properties (Figure 1). We also vary lighting settings, in particular color, brightness, and angle of the virtual endoscopic illumination. We keep camera parameters constant to ensure the geometry of the colon is consistent and our simulated camera field of view is 140 degrees, consistent with real endoscopes. Our training data consists of nine subsets, each of which is a combination of one out of three material settings and one out of three lightening settings. In total, we generate roughly 11,000 images with depth ground truth.

Shape classification: Distinct from stereo images, where geometrical inference can be drawn from the relation of the position of a landmark in the image pair, estimating depth from a single image is highly ill posed. However, we can benefit from knowledge that the colon has an approximately tubular shape.

Therefore, we first estimate the direction of the lumen in a single image. We use K-means to cluster the depth maps into five groups, which results in for humans distinguishable clusters that depend on the curvature direction of the lumen (Figure 2). Given the clusters, we train a network based on ResNet-50 [6] to classify RGB images into one of the five classes with 89% accuracy. This allows us to classify new images without known depth map and estimate the location of the vanish point.

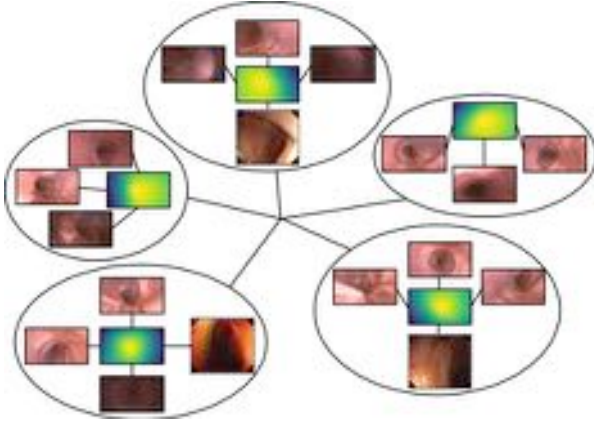


Figure 2. Mean depth maps of five clusters with examples from the training set. Yellow indicates areas of high depth while blue indicates areas of low depth. Real images that were assigned to the clusters using our classification network, are indicated through a dashed frame.

Depth Estimation: Our architecture is based on two components (Figure 3). We predict the depth based on ResNet-50 followed by a sequence of upscaling layers according to [7] and simultaneously impose a shape that adheres to a statistical model describing the distribution over the depth maps in the training set. A simple approach is using the Maximum Likelihood estimate assuming a Gaussian distribution. To this end, we compute the mean depth of each cluster. During training, we pass the cluster index to the loss function and compute the squared difference between the initial depth estimation and the mean of the given cluster. The final loss function takes into account how close the estimated depth is to both, ground truth and expected shape.

We train our network on six out of the nine subsets in our data set, leaving out all sets that were derived from one of the three lightening settings. The remaining three sets serve as our test set. This allows us to analyze the robustness of the learned model towards changes in illumination. We train each network for 15,000 iterations with a batch size of 32, using Adam optimizer with a learning rate of 10^{-4} . While training takes 18h, depth prediction during test time takes both networks 0.11 sec per image on one NVIDIA TITAN Xp GPU.

RESULTS

While training on ResNet-50 yields a mean distance between ground truth depth and prediction of 0.112 on the test set, our networks yields an error of 0.110, where the maximum depth in the training set is rescaled to 1. Estimating the scale, this roughly corresponds to a mean distance between estimation and ground truth of 9.0 mm on ResNet-50 vs. 8.8 mm on our network. Although the total error on the test set is similar for both networks, we can observe a different source for mistakes. In particular, our network performs better on images that are close to the mean of the cluster (Figure 4a) but fails on images that are outliers (Figure 4b) where the network falsely tries to enforce a tubular shape.

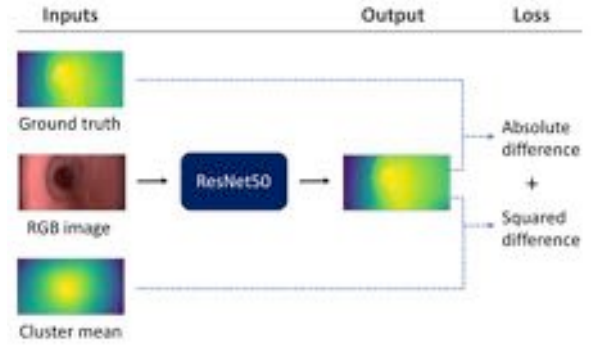


Figure 3. Network architecture for depth estimation combining the ResNet-50 output to a classifier.

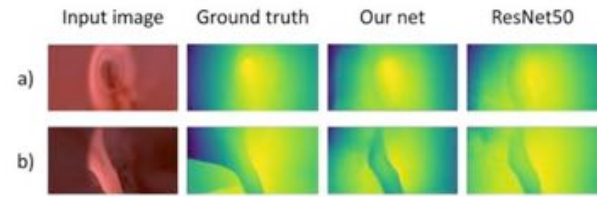


Figure 4. Comparison results between the output of our model and the direct output of ResNet-50.

CONCLUSION AND DISCUSSION

In this paper we present a method that allows us to train a Convolutional Neural Network to predict depth from a single image without the need of real ground truth data. We describe a procedure to create training data in a virtual environment and propose a network architecture that attempts to limit the drawbacks of using synthetic data by enforcing shape consistency. However, our underlying shape model is trivial and fails to cover the variety of shapes found in the test set, which results in a mean distance of several millimeters between ground truth and prediction. Our future work will focus on a more elaborate statistical model incorporating the joint distribution of nearby pixels instead of considering each pixel independently.

REFERENCES

- [1] Van Rijn, Jeroen C., et al. "Polyp miss rate determined by tandem colonoscopy: a systematic review." *The American Journal of Gastroenterology* 101.2 (2006): 343.
- [2] Mahmood, Faisal, and Nicholas J. Durr. "Deep learning and conditional random fields-based depth estimation and topographical reconstruction from conventional endoscopy." *Medical Image Analysis* (2018).
- [3] Visentini-Scarzanella, Marco, et al. "Deep monocular 3D reconstruction for assisted navigation in bronchoscopy." *CARS* (2017).
- [4] Laina, Iro, et al. "Deeper depth prediction with fully convolutional residual networks." *3DV IEEE* (2016).
- [5] Godard, Clément, Oisín Mac Aodha, and Gabriel J. Brostow. "Unsupervised monocular depth estimation with left-right consistency." *CVPR* (2017).
- [6] He, Kaiming, et al. "Deep residual learning for image recognition." *CVPR* (2016).
- [7] Laina, Iro, et al. "Deeper depth prediction with fully convolutional residual networks." *3DV IEEE* (2016).

Power Augmentation and Rehabilitation Exoskeleton Robot based on Variable Stiffness Soft Actuators

Hassanin Al-Fahaam¹, Samia Nefti-Meziani¹, Steve Davis¹

¹*Autonomous Systems and Robotics Research Centre, School of Computing/ Science and Engineering, The University of Salford, Manchester, United Kingdom.*

h.s.h.al-fahaam@edu.salford.ac.uk

INTRODUCTION

Power assistive and rehabilitation robots have increased in number particularly to assist physically weak elderly individuals and disabled people who have neurological damage to improve their quality of life and independence [1]. So as to provide the exoskeleton wearer with comfort and safety, physical human-robot interaction has a significant role and includes various aspects such as transmission of power, actuation, anatomical differences between users, necessary degrees of freedom (DOF), dexterity, compliance and kinematics [2].

MATERIALS AND METHODS

This research uses both contracting and extending pneumatic muscles. The contracting artificial muscles are constructed from a woven sleeve, length 11 cm and 6 mm in diameter; a latex bladder 11 cm length and 5 mm diameter with two 3D printed terminals, one with a closed end and the other with a hole for the application of air. Fig 1 shows the proposed contraction artificial muscle with different supplied pressures.

The extensor artificial muscles use the same braid sleeve but with length 42.5 cm and diameter 8 mm and the same bladder with 17 cm length and 8 mm diameter. As the resting length of the braid is longer than the bladder it must be compressed when forming the muscle. Fig 2 shows the proposed extensor muscle at different pressures. It can be seen that the extensor muscle increases in length as pressure is applied.

We have developed a novel bending artificial muscle from the extending muscle by reinforcing one side of it with strong thread and leaving the other side free. Fig. 3 shows the bending muscle with different applied pressures. It can be seen that when pressure is increased to the bending muscle, the bending angle increases in proportion to the increase in pressure.



Figure 1. The contraction muscle with different pressures

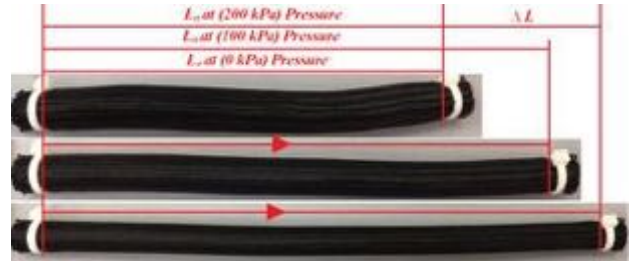


Figure 2. The extensor muscle with different pressures



Figure 3. The bending artificial muscle.

RESULTS

The characteristic relationship between the applied pressure and the displacement of the contracting muscle is illustrated in Fig. 4. Fig. 5 shows the relationship between pressure and displacement of the extensor artificial muscle.

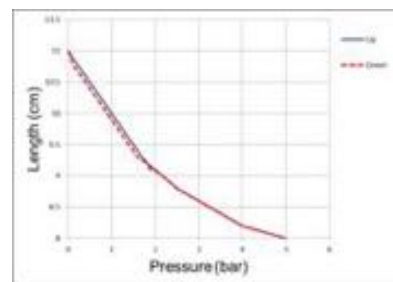


Figure 4. The contraction muscle with different pressures

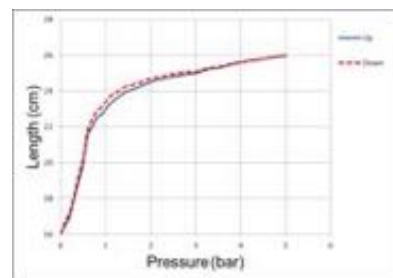


Figure 5. The extensor muscle with different pressures

A novel variable stiffness soft actuator has been developed. To produce this we have combined the contraction and bending artificial muscles together. The contraction muscles are connected with their terminals to the extensor muscle sleeve by small cable ties as shown in Fig. 6 (a). Fig. 6 (b) illustrates flexion of the actuator when pressurising only the bending muscle. When the contractor muscles are also pressurised they act against the bending muscle to restore the actuator to its straight configuration as shown in Fig. 6 (c). This antagonistic operation of the muscles allows the stiffness of the bending actuator to be adjusted. In result of controlling the pressures of all muscles together, the stiffness of the bending actuator is controllable. The maximum bending angle is approximately 160° at 3 bar pressure or above as shown in Fig. 7. The novel actuator contains two contracting actuator elements which act at different positions along the extensor muscle's length. Fig. 6 (d & e) demonstrates how bending of the terminal and root ends of the actuator can be achieved separately by actuating the bending muscle along with the root contractor (for terminal part bending) and the terminal contractor (for root section bending). The achievable bending angles of the root and terminal sections of the actuator are approximately the same and the bending angle is as shown in Fig. 7.

An exoskeleton glove has been developed based on the proposed variable stiffness actuator discussed above, as shown in Fig. 8. Four fully variable stiffness actuators were sewn onto a non-stretchable fabric glove. These four actuators are placed on the back side of the glove aligned with the index, middle, ring and the little fingers. The thumb is fitted with a single bending extensor artificial muscle.

This novel glove design is defers from most other soft actuated gloves by its actuators capable of bending in two segments in addition of hole actuator bending, but in other gloves, only the full actuator bending. Controlling the bending segments of the actuator provides the glove to perform more rehabilitation movements as shown in Fig. 9.



Figure. 6. Fully variable stiffness soft actuator

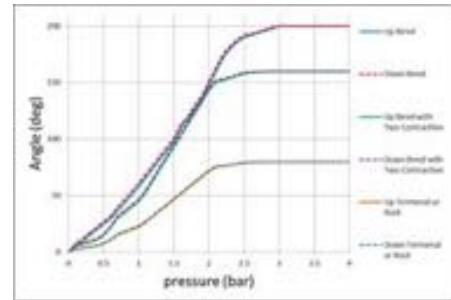


Figure. 7. The bending angles of the fully variable stiffness actuator



Figure. 8. The contraction muscle with different pressures

Fig. 9 demonstrates how the glove can also be used to achieve typical rehabilitation movements such as full grasp (a), straight grasp (b), hook grasp (c), and table top (d). Depending on the rehabilitation exercises required the glove can be programed to perform many exercises by controlling the pressure inside each actuator.



Figure. 9. The contraction muscle with different pressures

CONCLUSION AND DISCUSSION

This study demonstrates the preparatory phases of building up a wearable power augmentation and rehabilitation exoskeleton soft glove which uses novel variable stiffness soft pneumatic actuators.

REFERENCES

- [1] H. Al-Fahaam, S. Davis, and S. Nefti-Meziani, "The design and mathematical modelling of novel extensor bending pneumatic artificial muscles (EBPAMs) for soft exoskeletons," *Robotics and Autonomous Systems*, vol. 99, pp. 63-74, 2018.
- [2] H. Al-Fahaam, S. Davis, S. Nefti-Meziani, and T. Theodoridis, "Novel soft bending actuator-based power augmentation hand exoskeleton controlled by human intention," *Intelligent Service Robotics*, pp. 1-22, 2018.

Toward effective three-dimensional control of an epicardial wire robot

S. Dan¹, Y. Ren¹, N. A. Bustos¹, N. A. Wood¹, M. J. Passineau², R. J. Moraca², C. N. Riviere¹

¹The Robotics Institute, Carnegie Mellon University, Pittsburgh, Pennsylvania, USA

²Allegheny General Hospital, Pittsburgh, Pennsylvania, USA
camr@ri.cmu.edu

INTRODUCTION

Heart failure (HF) is a leading cause of mortality, afflicting up to 23 million people worldwide [1]. This pathology costs the United States healthcare system nearly 30 billion dollars each year, and the life expectancy of those afflicted with HF is less than 5 years for nearly 50% of patients [2]. A growing understanding of myocardial dysfunction and gene transfer technology has led to the promise of effective gene therapy drugs for HF. While such gene therapies have shown promise in preclinical tests, the effectiveness is influenced by the amount of gene transferred to the tissue, which is dependent on the delivery method. Recent clinical trials of gene therapy for HF have yielded disappointing results, pointing to the need for improved delivery techniques [1].

To address this need, we developed a parallel wire robot for epicardial injection of gene therapy, which was tested previously in the porcine model using a control system based on planar kinematics [3]. The present paper describes ongoing work to extend the control system to a prolate spheroidal geometry that better approximates the shape of the heart.



Figure 1. Epicardial parallel wire robot, shown on balloon.

MATERIALS AND METHODS

Epicardial parallel wire robot

Cerberus (Fig. 1) is a parallel wire robot or cable-driven robot [4] developed to conduct minimally invasive cardiac interventions quickly and efficiently over a large workspace. Cerberus is designed to be inserted using a subxiphoid approach, enabling access to the heart while avoiding the pleural space. The parallel cable-driven robot incorporates three suction bases and an injector head intended to house a needle for intramyocardial injections. Two of the suction bases are at the ends of flexible arms and the third is at the base of both arms. Once inserted, the flexible arms expand into a triangular shape and adhere to the surface of the

beating heart. Cables from each base connect to the injector head and move it within the triangular support structure by changing the cable lengths. This end-effector platform design involving parallel wires allows quick movement over the workspace. This design also shares the general benefits of organ-mounted robots, providing a platform that is approximately motionless in the frame of reference of the beating heart [5].

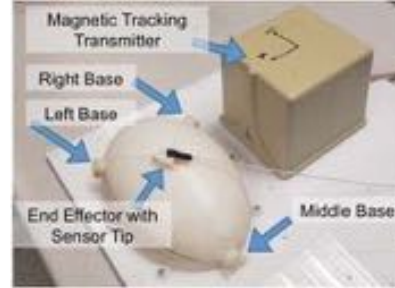


Figure 2. Epicardial wire robot on prolate spheroid testbed. (Here bases are affixed permanently, rather than via suction).

Control system

Current work focuses on incorporating prolate spheroidal kinematics into the parallel force/position control system of Cerberus, for more accurate approximation of cardiac geometry (Fig. 3). This involves implementation of an inverse geodesics algorithm for the prolate spheroid, and development of a method to find the desired tension distribution at a given end-effector location.

The tabletop instrumentation [3] uses a 6-degree-of-freedom electromagnetic tracker to localize the injector head, rotary encoders to measure changes in cable length, and load cells to measure cable tension.

Given a desired location for the injector head, the corresponding wire lengths are determined by solving

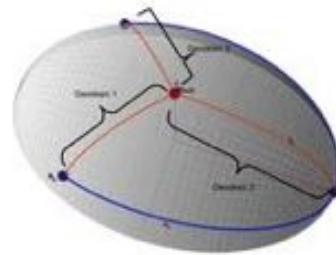


Figure 3. Geodesics to be solved to determine wire lengths for inverse kinematics of the epicardial parallel wire robot. Suction bases are depicted in blue, and the movable injector head in red.

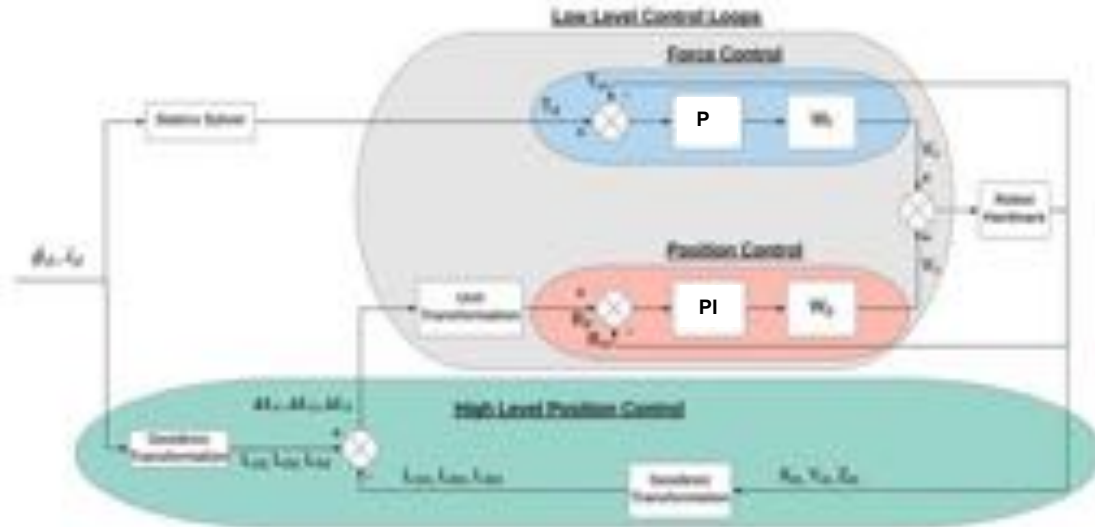


Figure 4. Parallel force/position control. Low-level control is performed on a microcontroller, and high-level control on a PC. Wire lengths L are controlled to reach a desired latitude ϕ_d and longitude λ_d .

an inverse geodesics problem via Newton's method [6]. The statics are then solved, given the orientation of the cables, to determine an appropriate set of cable tensions that is within reasonable limits for the safety of the patient and the device. A parallel force/position control system is then used to position the injector head (Fig. 4). Proportional-integral control is used in the position loop, and proportional control in the force loop [3], with $W_f/W_p = 0.25$.

The system was tested with the rectangular pattern of 12 targets indicated by the blue markers in Fig. 5. The injector head was commanded to the full set of targets in sequence.

RESULTS

Results for the pattern of 12 targets are presented in Table I and Fig. 5.

TABLE I. EXPERIMENTAL RESULTS

Error	Mean	Standard deviation
x (mm)	1.34	1.05
y (mm)	1.21	0.8
z (mm)	0.97	0.94
Latitude (°)	0.50	0.55
Longitude (°)	1.53	1.04

CONCLUSION AND DISCUSSION

In this limited dataset on the prolate spheroid, the system has achieved positioning accuracy superior to our previous planar results [3]. For real-world implementation, it will be necessary to develop accurate means for intraoperative localization of the three suction bases. Subsequent future work will include duplication of similar results with a larger dataset, and comparison of the performance of this system with a system based on true cardiac geometry.

ACKNOWLEDGMENTS

Funding provided by National Institutes of Health (grant no. R01HL078839).



Figure 5. Experimental results. Targets are marked in blue, and recorded locations in green.

REFERENCES

- [1] J.-S. Hulot, K. Ishikawa, and R. J. Hajjar, "Gene therapy for the treatment of heart failure: promise postponed," *Eur Heart J*, vol. 37, no. 21, pp. 1651–1658, 2016.
- [2] S. Ylä-Herttuala and A. H. Baker, "Cardiovascular gene therapy: Past, present, and future," *Mol Ther*, vol. 25, no. 5, pp. 1095–1106, 2017.
- [3] A. D. Costanza, M. S. Breault, N. A. Wood, M. J. Passineau, R. J. Moraca, and C. N. Riviere, "Parallel force/position control of an epicardial parallel wire robot," *IEEE Robot Autom Lett*, vol. 1, no. 2, pp. 1186–1191, 2016.
- [4] R. L. Williams and P. Gallina, "Translational planar cable-direct-driven robots," *J Intell Robot Syst*, vol. 37, pp. 69–96, 2003.
- [5] N. A. Wood, D. Schwartzman, M. J. Passineau, R. J. Moraca, M. A. Zenati, and C. N. Riviere, "Beating-heart registration for organ-mounted robots," *Int J Med Robot*, p. e1905, 2018.
- [6] C. F. F. Karney, "Algorithms for geodesics," *J Geod*, vol. 87, no. 1, pp. 43–55, 2013.

Soft Wearable Glove for Tele-Rehabilitation Therapy of Clenched Hand/Fingers Patients

T. Abrar, F. Putzu, K. Althoefer

*Centre for Advanced Robotics @ Queen Mary, Queen Mary University of London
(t.abrar; f.putzu; k.althoefer)@qmul.ac.uk*

INTRODUCTION

One of the primary causes of disability in adults is stroke [1]. Patients who survived a stroke normally undergo therapy of 1-2 sessions of 30 minutes every day which gradually reduces to 1-2 session per week [1]. To enable training at home with home-based systems, tele-rehabilitation was introduced in 1998 [1]. Haptics-enabled Robotic Rehabilitation systems are used for two purposes; (1) assistive therapy to physically support the patient's movements to improve agility and motion range, and (2) resistive therapy which opposes the patient's movement, to build strength by building up musculature [2].

Patients suffering from impaired hand function due to neurological disorders often caused by stroke require assistive therapy, at least in the beginning, to improve their hand motion capability and range. This leads to new research and technology requirements in the area of soft wearable gloves for hand rehabilitation. A robotics glove can help patients in improving hand function by conducting commonly performed activities of daily life including grasping and pinching of objects. Hang *et al.* [3] discuss the emerging trend of hand robotics devices that are wearable. Simple wearable structure devices, using soft and compliant materials, without complex mechanical parts; make them suitable for close interaction with the patient.

To mimic the actuation of an actual hand, two main approaches can be explored: (1) tendon-driven actuation or (2) hydraulic or pneumatic actuation in an elastomeric structure. Researches also make use of shape memory alloys as pulleys for tendons [4]. However, such systems may have to deal with the problems related to the friction caused by cable movement and arrangement of cables due to different hand sizes and dimensions [5]; also, shape memory alloys suffer from hysteresis. Another recent approach is to use a 3D printed glove that consists of bidirectional linear soft actuators and soft orifice valves producing 180N force at 100kPa [6].

CONCEPT

The aim is to design a soft glove for hand rehabilitation that can be used in daily life applications and improve the hand performance with regards to opening the hand for grasping and pinching. Here, the two-essential parameters for a pneumatic glove are considered to be improved: (1) Weight: the literature suggests that the weight of a glove worn by a patient should not exceeds 500g; therefore, our wearable system is designed in a way that its weight is below the given threshold; (2) Pressure: research data collected from biomechanics literature [6],

[7] indicate that a glove is supposed to be better in performance if the force achieved at the finger-tip is around 10N or more. Greater force usually means higher pressure requirements – this commonly increases the whole system in terms of glove size and weight. Taking these two parameters (weight & pressure) into consideration, our system is designed in a way that it operates at 2bar pressure, which can be achieved through commercially available micro pumps.

The effect of changing any of the two above factors can be visualized with respect to the "Time". If the pressure is kept constant, then by changing the weight the time for opening the finger will also change. Similarly, when the weight is kept constant, then by changing the internal pressure the time for opening the finger will also change.

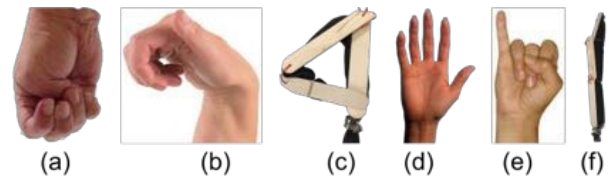


Figure 1: Soft finger glove imitating finger states (a) clenched fingers with closed fist (b) clenched fingers with open palm (c) soft glove in clenched state (d) stretched human hand (e) stretched human finger (f) stretched soft finger glove.

This study is part of a larger project aiming to develop complete hand exoskeletons for rehabilitation. In this paper, we focus on developing a soft wearable finger (weight 3.4g) as part of the long-term vision to create wearable gloves (weight under 50g) that can help patients in physical hand therapy. Our approach aims at creating an exoskeleton that helps the patient to straighten their finger from a bent state finger to an extended finger state, as shown in Figure 1. In achieving this task pneumatic pressure is used. The outcome of this research will be instrumental for the development of a complete rehabilitation glove, since the developed technology can be replicated for all fingers in a similar manner.

The proposed finger exoskeleton has a cylindrical sleeve structure. A single sleeve is made from the ripstop fabric. To avoid air leaking air from the stitched fabric areas, the stitched side was coated with a thin layer of latex.

An experimental study to show feasibility without harming a human subject, three links, functionally comparable to a finger's phalanges, were attached to the finger exoskeleton and behaved like fingers during the experimental study. When inflating the cylindrical sleeve of the finger exoskeleton, it acts as an actuator; valuable information can be achieved from the movement of links. Under the condition when no pressure is applied, the

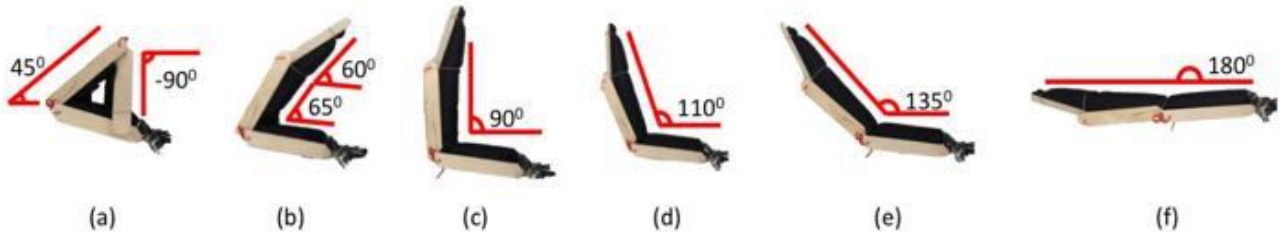


Figure 2: Step by step visualisation of finger from flexed to relaxed state; (a) when the finger is curled, and no pressure is applied. (b) a small amount of air pressure is applied, and the finger starts opening; this opening of the finger continues along (c), (d) & (e); (f) the finger is fully stretched and straight with all the phalanges being aligned.

exoskeleton adapts its shape to the configuration of the finger, i.e. it assumes a curled shape, Figure 2(a). When pressurized, the exoskeleton sleeve extends and forces the finger into a straightened configuration. Hence, the proposed exoskeleton will provide aid to patients whose fingers are predominantly in a closed position and straighten the attached finger, Figure 2(b-f). Once the patient is in the right position to grasp an object, the pressure is removed, and the exoskeleton applies no more force on the finger which then returns to its curled position because of the patient's illness and a grasp can be accomplished.

The aim of this exoskeleton is to provide therapy exercise and assistance with finger movements of a patient from flex state (when the finger is curled) to relax state (when the finger is straight). Noted that the exoskeleton doesn't apply any grasping force, it only assists the finger to open and close. So, by helping in grasping means it help in hand to be in good position i.e. positing of fingers are open.

EXPERIMENT

To measure the tip pulling force of our exoskeleton, weights were attached at the tip and the exoskeleton sleeve was filled with air. The direction of the force that the weight exerts on the tip is in a way that it opposes the finger to open. The experiment was repeated with a range of weights, starting at 0g and increasing at increments of 100g. The tests were devised to indicate how much time and pressure will the glove need to straighten the attached finger model as a function of different tip weights simulating different opposing forces that vary across patients.

RESULTS

The results of our experiment are shown in the graph of Figure 3. The time taken by the different joints to reach their final straightened configurations is shown in line graphs where every bar shows the finger response for a separate weight attached at the tip.

Whereas, the bars from Figure 3 also indicates that with an increase in weights, the time required by the middle phalange of the finger increases with respect to the time gradient of the distal phalange. This can be due to inertia; the distal phalange requires more time to straighten due an increase in weight. The middle phalange, once in motion, carries that momentum and does not require more time to get straight.

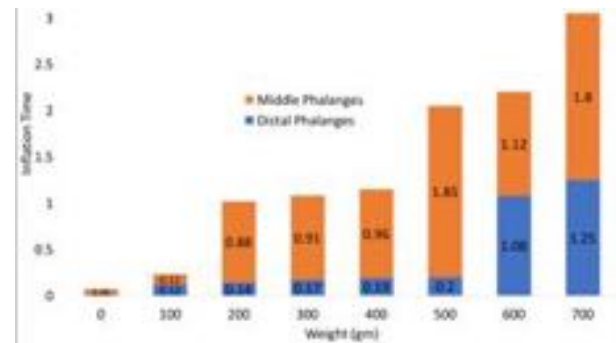


Figure 3: Time graph of each joint to change its state from a curled to a straightened state as a function of weights attached at the fingertip.

CONCLUSIONS

The experiments showed that a suitable performance could be achieved with weights in the range of 0g to 700g. An additional test performed at 800g showed that the proposed exoskeleton was incapable of moving this high load. We conclude that for the given pressure (2bar), a fingertip force of 7N can be achieved. If higher forces are required, higher air pressures should be used.

ACKNOWLEDGEMENTS

This work was supported in part by the EPSRC in framework of the NCNR (National Centre for Nuclear Robotics) project (EP/R02572X/1) and WormBot project by Q-Bot.

REFERENCES

- [1] A. Alamri, M. Eid, R. Iglesias, S. Shirmohammadi, and A. El Saddik, "Haptic Virtual Rehabilitation Exercises for Poststroke Diagnosis," *IEEE Trans. Instrum. Meas.*, vol. 57, no. 9, pp. 1876–1884, Sep. 2008.
- [2] Atashzar, S. Farokh, Mahya Shahbazi, Mahdi Tavakoli, and Rajni V. Patel. "A new passivity-based control technique for safe patient-robot interaction in haptics-enabled rehabilitation systems." In *Intelligent Robots and Systems (IROS)*, 2015 IEEE/RSJ International Conference on, pp. 4556–4561. IEEE, 2015.
- [3] H. K. Yap, N. Kamaldin, J. H. Lim, F. A. Nasrallah, J. C. H. Goh, and C.-H. Yeow, "A Magnetic Resonance Compatible Soft Wearable Robotic Glove for Hand Rehabilitation and Brain Imaging," *IEEE Trans. Neural Syst. Rehabil. Eng.*, vol. 25, no. 6, pp. 782–793, Jun. 2017.
- [4] Z. Yao, C. Linnenberg, A. Argubi-Wollesen, R. Weidner, and J. P. Wulfsberg, "Biomimetic design of an ultra-compact and light-weight soft muscle glove," *Prod. Eng.*, vol. 11, no. 6, pp. 731–743, Dec. 2017.
- [5] H. K. Yap, J. H. Lim, F. Nasrallah, and C.-H. Yeow, "Design and Preliminary Feasibility Study of a Soft Robotic Glove for Hand Function Assistance in Stroke Survivors," *Front. Neurosci.*, vol. 11, Oct. 2017.
- [6] J. Yi, X. Chen, and Z. Wang, "A Three-Dimensional-Printed Soft Robotic Glove With Enhanced Ergonomics and Force Capability," *IEEE Robot. Autom. Lett.*, vol. 3, no. 1, pp. 242–248, Jan. 2018.
- [7] Polygerinos, Panagiotis, Kevin C. Galloway, Emily Savage, Maxwell Herman, Kathleen O'Donnell, and Conor J. Walsh. "Soft robotic glove for hand rehabilitation and task specific training." In *Robotics and Automation (ICRA)*, 2015 IEEE International Conference on, pp. 2913–2919. IEEE, 2015.

Using current measurement to estimate palpation and grasping forces in robot-assisted minimally invasive surgery

A. Tzemanaki, S. Abeywardena, E. Psomopoulou, C. Melhuish, S. Dogramadzi

*Bristol Robotics Laboratory, University of the West of England, Bristol, UK
Antonia.Tzemanaki@brl.ac.uk*

INTRODUCTION

Robot-assisted minimally invasive surgery (RAMIS) has gained popularity in recent decades through use of the da Vinci master-slave surgical system offering improved vision, precision and patient recovery time compared to traditional MIS [1]. However, certain shortcomings prevent RAMIS from fulfilling its maximum potential, including the lack of haptic feedback provided to the surgeon [2]. Attempts have been made to develop sensorised surgical instruments as a means to detect interaction forces during RAMIS and provide surgeons with haptic feedback. However, the size of force sensors and incision ports, the sterilisation of tools at high temperature as well as the disposable nature of surgical tools have so far prevented integration of end-effector/tissue force sensing in RAMIS [3, 4].

Force estimation algorithms that do not require sensing hardware at the operating site include visual estimation of the shaft deformation [5], modelling of surgical tool-tissue interaction [6] and the use of motor current, among others. Sang et al. modelled the dynamics of a da Vinci robot and, in conjunction with measured motor current, estimated the external force applied at the tip of the surgical tool [7], while Zhao and Nelson created a 3 degrees-of-freedom (DOF) surgical grasper prototype with joint dynamics modelled as individual linear 2nd order systems to estimate external forces [8]. These methods require some form of modelling and simplification (e.g. neglecting friction) which can affect the estimation accuracy. Further, the complexity of these algorithms may not allow for suitable update rates required for haptic feedback, thus affecting the system's overall stability and transparency.

In this work, we propose an alternative method to force estimation in a RAMIS context, using the real-time measurement of the instrument motor current. Off-the-shelf force sensors are characterised and then used to determine the correlation between the motor current and the applied force in palpation and grasping with DaVinci forceps.

MATERIALS AND METHODS

A load cell (CZL635, Phidgets, 49 N range) and a capacitive force sensor (SingleTact, 45 N range) were characterised through use of calibration masses. The load cell was orientated with its sensitivity axis in the direction of gravity and masses were hung from it. For the SingleTact sensor, a 3D printed (Nanocure, Envisiontec) hemispherical dome was attached to one

side of the sensing element. Calibration masses were placed on top of a 1-DOF beam-pivot structure with their weight applied directly on the dome-sensor, placed underneath the beam and on high precision scales. In both cases, the associated voltage was recorded.

The sensors were then used to measure grasping and palpating forces exerted by the gripper of DaVinci forceps as shown in Fig. 1a-b. For grasping, two 3D printed (TangoPlus, Stratasys) hemispherical domes were attached to either side of the SingleTact sensor for even distribution of the applied load.

The instrument has 3 DOF, controlled by 4 motors: 2 for the pitch and roll and 2 for the yaw and grasping of the jaws. For the grasping and palpation experiments, the jaws of the forceps were actuated by 2 DC motors (Maxon, 3.89mNm, 62:1 reduction). The motors' shafts were connected to the gearbox of the instrument via the blue fixtures in the custom-made interface shown in Fig. 1c-d, while the pitch and roll were kept constant (red fixtures). During palpation, the two motors had equal current, while during grasping the motors had equal magnitude of current while turning in opposite directions.

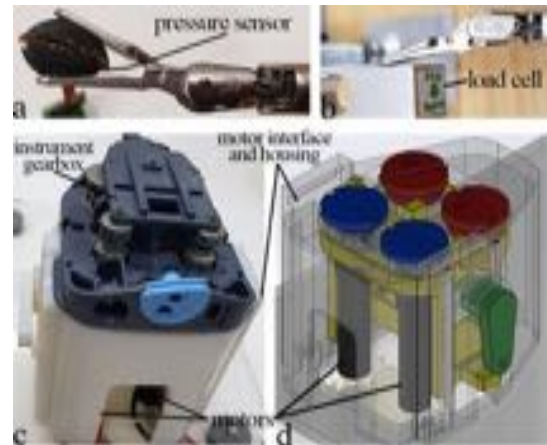


Figure 1. Da Vinci forceps **a)** grasping the dome-sensor, **b)** applying vertical force to the load cell, **c)-d)** with a custom-made housing for the motors

RESULTS

For both sensors, the characterisation experiments were repeated 3 times and the resulting voltage averaged with a standard deviation of 0 (CZL635) and 0.0022 (SingleTact) (Fig. 2). The load cell has a linear relationship between force and voltage with an R^2 value of 1; while the SingleTact sensor has a cubic relationship between force and voltage with an adjusted R^2 of 0.9988. To map the measured force to the motors' current, the motors were driven using current control: sensor readings

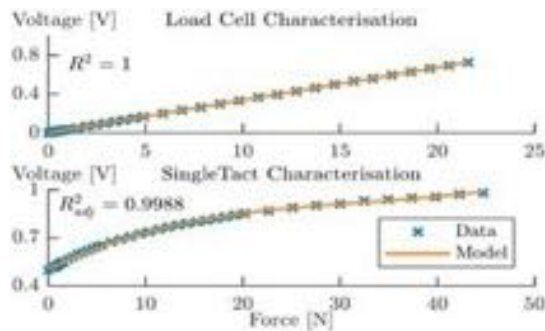


Figure 2. Characterisation of the force sensors

were taken for every 0.1mA increase of the current between 10-309mA (maximum continuous current of the motors). The grasping and palpation experiments were each repeated ten times. The results were then filtered using smoothing splines (smoothing parameter in the range of [0.5, 0.53]) and averaged with standard deviation of 0.63 (grasping) and 0.12 (palpation). Fig. 3 shows that there is a linear relationship between current and force for the grasping, while the mapping during palpation can be modelled with a cubic polynomial.

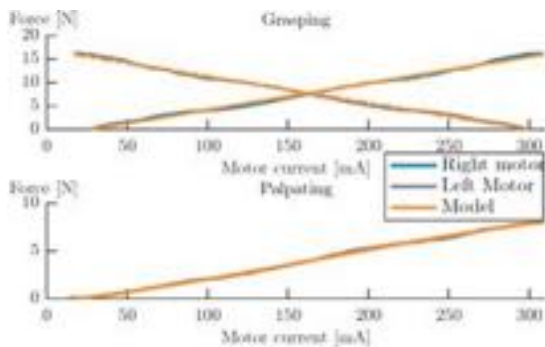


Figure 3. Mapping of the motors' current to the grasping and palpating forces of the gripper for both motors controlling its right and left jaw

CONCLUSION AND DISCUSSION

The maximum (averaged) forces recorded were 17 N for grasping and 8 N for palpation, which were lower than expected. This was due to friction and the coupling of the instrument's cable-driven system [9] between the mechanisms responsible for the grasping/yaw and those for the roll and pitch. In this experiment, roll and pitch were kept constant (red fixtures in Fig. 1). Furthermore, the forceps used in these experiments was a retired Da Vinci instrument, with cables not operating in their nominal capacity.

Nevertheless, the results suggest that correlation between motor current and forces exerted by the end-effector can be found for both grasping and palpation. This is highly beneficial in surgical applications where due to miniaturisation and sterilisation of surgical instruments, attaching sensors directly to the end-effector has not yet offered an acceptable solution. Furthermore, the results show that palpation is possible by pushing with the grasper without having to grasp the tissue as previously done in [8], which can be more intuitive for the surgeon.

Our further work includes extending our testing to different surgical tasks where force and pressure estimation can improve surgical performance. This will mean combining all instrument DOF (including roll and pitch) as well as examining leverage effects caused by the point of grasping (distance from the tip of the instrument) and can be further applied to instruments with different articulation and actuation mechanisms such as finger-like tools [10].

ACKNOWLEDGMENTS

This work was supported by the European Union's Horizon 2020 research and innovation programme under grant agreement No 732515.

REFERENCES

- [1] A. R. Lanfranco, A. E. Castellanos, J. P. Desai, and W. C. Meyers, "Robotic surgery: A current perspective", *Annals of Surgery*, vol. 239, no. 1, pp. 14-21, 2004.
- [2] A. M. Okamura, "Haptic feedback in robot-assisted minimally invasive surgery", *Current Opinion in Urology*, vol. 19, no. 1, pp. 102-107, 2009.
- [3] P. Puangmali, K. Althoefer, L. D. Seneviratne, D. Murphy, et al., "State-of-the-art in force and tactile sensing for minimally invasive surgery", *IEEE Sensors*, vol. 8, no. 4, pp. 371-381, 2008.
- [4] A. J. Spiers, H. J. Thompson, and A. G. Pipe, "Investigating remote sensor placement for practical haptic sensing with EndoWrist surgical tools", in *IEEE World Haptics Conference*, 2015, pp. 152-157.
- [5] Q. J. Lindsey, N. A. Tenenholz, D. Lee, and K. J. Kuchenbecker, "Image-enabled force feedback for robotic teleoperation of a flexible surgical tool", in *Proceedings of the IASTED International Conference on Robotics and Applications*, 2009.
- [6] A. M. Okamura, C. Simone, and M. D. O'Leary, "Force modeling for needle insertion into soft tissue", *IEEE Transactions on Biomedical Engineering*, vol. 51, no. 10, pp. 1707-1716, 2004.
- [7] H. Sang, J. Yun, R. Monfaredi, E. Wilson, et al., "External force estimation and implementation in robotically assisted minimally invasive surgery", *The International Journal of Medical Robotics and Computer Assisted Surgery*, vol. 13, no. 2, 2017.
- [8] B. Zhao and C. Nelson, "Sensorless force sensing for minimally invasive surgery", *Journal of Medical Devices*, vol. 9, no. 4, pp. 041012:1-14, 2015.
- [9] C. Y. Kim, M. C. Lee, R. B. Wicker, and S.-M. Yoon, "Dynamic modeling of coupled tendon-driven system for surgical robot instrument", *International Journal of Precision Engineering and Manufacturing*, vol. 15, no. 10, pp. 2077-2084, 2014.
- [10] Tzemanaki, A., Fracczak, L., Gillatt, D., Koupparis, et al, "Design of a multi-DOF cable-driven mechanism of a miniature serial manipulator for robot-assisted minimally invasive surgery", In the 6th *IEEE International Conference on Biomedical Robotics and Biomechanics*, 2016, pp. 55-60.

Free-view Gaze Controlled Image Navigation: One application of a Perceptually-enabled Smart Operating Room

A.A. Kogkas, A. Ezzat, A. Darzi, G.P. Mylonas

*hARMS Lab, Department of Surgery and Cancer, Imperial College London, UK
a.kogkas15@imperial.ac.uk*

INTRODUCTION

Medical imaging is an essential part of day to day operating. As such, alternative touch free navigation systems have been developed aimed at maximising accessibility to important surgical information required during surgery [1]. In addition to this, touch free navigation systems may reduce transmission of infections through physical contact between users and computer/keyboard interfaces [2]. Moreover, such systems are hoped to deliver a comfortable and seamless interface for enhanced surgeon experience.

Current image navigation systems are predominantly hand gesture controlled, such as the Gestix which uses 2D cameras to identify predetermined hand movements to view images on a monitor [3]. 3D based systems such as the Brainlab relies on cameras to capture gestures [2]. Voice based command systems such as the HERMES VRI have been trialled in laparoscopic surgery and shown faster operating times [4]. Other authors have reported combined hand gesture and voice commands to deliver practical image navigation tools [2].

Eye-tracking methodology has the potential to provide a “third hand” and a seamless way to allow “perceptually enabled” interactions with the surgical environment. However, screen based eye-trackers considerably restrict the head movement of the user within a very small volume. The Tobii EyeX eye tracker is one such example with an operating distance of 450-800 mm, a maximum screen size of 24 inches and a visual angle working range of $\pm 18^\circ$ on the x-axis and $\pm 10.5^\circ$ on the y-axis [5]. This restriction may disadvantage the user's positional flexibility to complete specific tasks, and thus diminish the usability of screen based eye tracker systems. Instead, eye tracker based navigation systems need to be reliant on the user's head/body position in space to reflect the natural user movements in theatre [6].

More recently, we have introduced the *Perceptually-enabled, Smart Operating Room* concept based on a novel real-time framework for theatre-wide and patient-wise 3D gaze localisation in a simultaneous and unrestricted/mobile fashion. An extension of this framework is presented here, that allows hands-free gaze-driven interactions with the environment and a screen. The framework is expected to facilitate seamless and meaningful integration of human and technology in the theatre for improved safety, collaboration and clinical outcome.

In this study, we present a novel eye gaze controlled image navigation system which is touch free and does not rely on hand or voice commands.

MATERIALS AND METHODS

The core functionality of the real-time framework presented in [7]–[9] is to provide the user's 3D point of regard in space. It relies on estimating the pose of the scene/RGB camera of the wearable eye-tracker in the world frame and tracing the gaze ray provided by the eye-tracker on the head frame of reference, on the 3D reconstructed space. For the work presented here, the head pose is estimated with the employment of the OptiTrack motion capture system. This method was preferred as it allowed to focus on the evaluation of the application by eliminating several sources of potential errors [7]. Spherical markers are mounted on the eye-tracker to form an asymmetric rigid body and allow OptiTrack to provide its unique 6 degrees of freedom (DOF) pose in space. The rigid transformations between the rigid body – eye-tracker scene camera (Y) and OptiTrack – world coordinate system (X) is estimated by solving the hand-eye calibration problem $AX = YB$ [10].

A screen displaying medical images from an inventory file is positioned in the operating theatre and its four corners and respective 3D coordinates are manually indicated. By using the hybrid macro/micro-scale model presented in [11], the mode (macro or micro) and the 2D screen fixation (for micro mode) is provided as output (Fig.1). To demonstrate the capabilities of the framework, an essential image navigation application is implemented: the screen is segmented into a grid of three rows and four columns, equally distributed along the screen's height and width respectively. A fixation with a dwell time over 1.5 sec on the cell defined by the middle row and the first column (2, 1) triggers the display of the previous image, on the cell defined by the middle row and the last column (2, 4) triggers the display of the next image and rest of the fixations do not trigger any alternation on the screen.

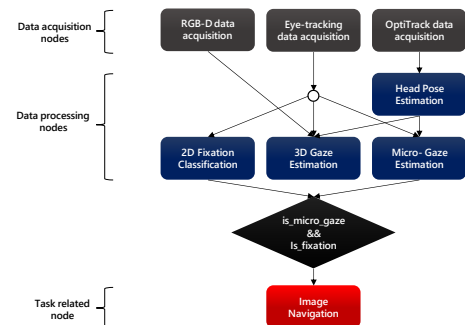


Figure. 1. System overview: the framework is implemented in the Robot Operating System (ROS) with C++ and each module represents a node.

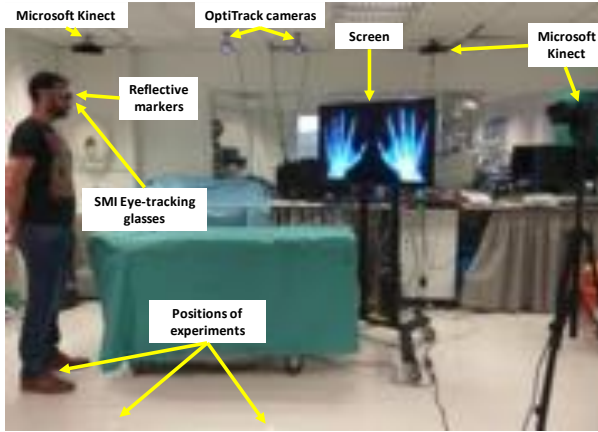


Figure 2. The experimental setup.

For eye-tracking, the wireless SMI (SensoMotoric Instruments GmbH) glasses are used and for RGB-D sensing, the Microsoft Kinect v2. For head pose tracking the OptiTrack motion capture system is used, with two Prime 13 cameras. For the image navigation application, a 42" LG screen with 1920x1080 px resolution is used.

EXPERIMENTAL SETUP

Our framework was evaluated with the experimental setup shown in Fig.2. The subjects were asked to perform 2 tasks from 3 different positions, 1.5 m, 2 m, and 2.5 m from the screen. In the first task, the subjects were being instructed to display the previous/next image in random order defined by the instructor before the experiment, using their natural gaze, for 20 times in each position. In the second task, the subjects were instructed to fixate for 5 sec on 12 equally distributed points displayed on the screen, starting from top left to bottom right. 3 subjects, 2 males and 1 female, 26-29 years old, normal uncorrected vision, took part in the study.

RESULTS

The success rate of the instructed actions, the delay of the action activation and the accuracy of the micro-scale fixations (2D fixations on screen) are evaluated.

In the first task, the success rate is calculated as the success rate of the instructed actions within a time threshold of 5 sec. The delay is calculated as the time between the instruction given and the image navigation system trigger for the successful attempts. In the second task, the accuracy of the fixations is estimated as the Euclidean distance between the on-screen target coordinates and the estimated 2D fixations and presented as a percentage of the screen resolution.

The results summarized in Table 1 show the delay and the error averaged over all subjects. The delay is 2.12 sec (including the 1.5 sec dwell time required for the trigger), the error is 1.27% and the success rate is 92.3%.

DISCUSSION

An application of the Perceptually-enabled Smart Operating Room has been presented, which allows touchless control of a screen in a free-viewing fashion. Preliminary evaluation of its accuracy and performance is deemed satisfactory. The study supports our hypothesis that our

Table 1: Delay and error averaged over all subjects.

	Mean	SD	Upper
Delay of activation, incl. trigger (sec)	2.12	0.58	3.11
Micro-scale fixation error (%)	1.27	0.44	1.72

free-view gaze framework enables the surgeon to control screens in the operating theatre, without restricting their position in space.

Our immediate plans involve implicit tracking of multiple screens in the operating theatre, which will allow further flexibility to the surgeon during the operation. Moreover, further screen-based gaze-contingent applications will be developed, based on the picture archiving and communication system (PACS) and the OR.NET framework [12]. This will facilitate the integration of our framework with real clinical applications and its deployment to multiple operating theatres.

AAK is supported by the NIHR Imperial Biomedical Research Centre (BRC).

REFERENCES

- [1] A. Mewes, B. Hensen, F. Wacker, and C. Hansen, "Touchless interaction with software in interventional radiology and surgery: a systematic literature review," *Int. J. Comput. Assist. Radiol. Surg.*, pp. 1–15, 2016.
- [2] L. C. Ebert, G. Hatch, G. Ampanozi, M. J. Thali, and S. Ross, "You Can't Touch This: Touch-free Navigation Through Radiological Images," *Surg. Innov.*, vol. 19, no. 3, pp. 301–307, 2012.
- [3] J. P. Wachs, H. I. Stern, Y. Edan, M. Gillam, J. Handler, C. Feied, and M. Smith, "A Gesture-based Tool for Sterile Browsing of Radiology Images," *J. Am. Med. Informatics Assoc.*, vol. 15, no. 3, pp. 321–323, 2008.
- [4] G. E. H. El-Shallaly, B. Mohammed, M. S. Muhtaseb, A. H. Hamouda, and A. H. M. Nassar, "Voice recognition interfaces (VRI) optimize the utilization of theatre staff and time during laparoscopic cholecystectomy," *Minim. Invasive Ther. Allied Technol.*, 2005.
- [5] A. Gibaldi, M. Vanegas, P. J. Bex, and G. Maiello, "Evaluation of the Tobii EyeX Eye tracking controller and Matlab toolkit for research," *Behav. Res. Methods*, 2017.
- [6] R. Johnson, K. O'Hara, A. Sellen, C. Cousins, and A. Criminisi, "Exploring the potential for touchless interaction in image-guided interventional radiology," *Proc. 2011 Annu. Conf. Hum. factors Comput. Syst. - CHI '11*, no. May, pp. 3323–3332, 2011.
- [7] A. A. Kogkas, A. Darzi, and G. P. Mylonas, "Gaze-contingent perceptually enabled interactions in the operating theatre," *Int. J. Comp. Assist. Radl. Surg.*, pp. 1–10, 2017.
- [8] A. A. Kogkas, A. Darzi, and G. P. Mylonas, "Gaze-Driven Human-Robot Interaction in the Operating Theatre," in *6th Joint Workshop on New Technologies for Computer/Robot Assisted Surgery (CRAS)*, 2016, p. 103.
- [9] M.-Y. Wang, A. A. Kogkas, A. Darzi, and G. P. Mylonas, "Free-View, 3D Gaze-Guided, Assistive Robotic System for Activities of Daily Living," *arXiv Prepr. arXiv1807.05452v2*, 2018.
- [10] M. Shah, "Solving the Robot-World/Hand-Eye Calibration Problem Using the Kronecker Product," *J. Mech. Robot.*, vol. 5, no. 3, p. 31007, Jun. 2013.
- [11] A. A. Kogkas, M. H. Sodergren, A. Darzi, and G. P. Mylonas, "Macro- and Micro-Scale 3D Gaze Tracking in the Operating Theatre," in *The Hamlyn Symposium on Medical Robotics*, 2016, p. 100.
- [12] F. Kühn and M. Leucker, "OR.NET: Safe Interconnection of Medical Devices," in *Foundations of Health Information Engineering and Systems*, 2014, pp. 188–198.

Augmented Reality Based External Fixation Fracture Reduction Training

P. Riordan¹, S. Muscroft¹, M. Stacey¹, A. Inwood¹, L. Greenlee¹, R. Connaghan¹, S. Oussedik³, D. Stoyanov^{1,2}

¹Digital Surgery Ltd, 230 City Road, EC1V 2QY, London, UK

²Dept. Of Computer Science, University College London, Gower Street, WC1E 6BT, London, UK

³Dept. Orthopaedics, University College London Hospital, Euston Road, NW1 2BU, London, UK

paul.riordan@touchsurgery.com

INTRODUCTION

Complex orthopaedic surgical procedures require spatial cognitive skills to orient instruments, position imaging device planes, and determine optimal placement of implants. Because costs and volume inherently limit the availability and access options to anatomy laboratories and to operating rooms, students are typically required to supplement their knowledge with traditional 2D resources, such as lecture slides, textbooks, and videos [1]. These are not optimal to support the development of the deeper understanding and coordination skills necessary to manage advanced equipment such as C-Arms.

The use of augmented reality (AR) simulations potentially allows for the teaching of complex 3D spatial skills outside of a live surgery environment, removing the possibility of student errors having consequences on patients, and encompassing a virtual instructor who is dedicated to education [2]. Simulation based learning has been shown to be a valid and effective tool in education of operative performance [3][4][5]. In this paper, we present an AR Hololens training experience for an external fixation fracture reduction procedure. It used holograms overlaid onto a prosthetic leg with guidance to correctly position a C-Arm with respect to the anatomy, visualisation of suggested viewing orientation, and also radiation exposure fields around the setup.

MATERIALS AND METHODS

The Hololens application was built using the Unity engine (Unity Technologies, USA), which allows flexible rendering of 3D content and provides support for interfacing with the device's sensor system to input/output audio and use of the built-in cameras for localisation.

All holographic content is registered onto the prosthetic limb, with the aim of giving the experience a clinical context and to enhance the user's spatial

cognition. A Vuforia (PTC Inc., Boston, MA) image target is viewed by the Hololens camera to provide an initial registration (Figure 1). The user can 'Air tap' and drag using a system of manual alignment nodes to further refine alignment after the automatic registration. The experience thereafter relies upon the Hololens internal SLAM system to maintain hologram alignment.



Figure. 1. Hololens capture of Vuforia alignment marker (shown on left of draped table), and visualisation of the radiation exposure around the C-Arm.

Throughout the full AR training experience, the user is guided to the correct position using footprint holograms and 3D spatial audio. The experience guides the user on how to position the C-Arm over the leg, and allows the user to observe the radiation exposure levels (Figure 1). Holograms of a fractured tibia, nervous system, and cardiovascular system are overlaid on the prosthetic leg and can be controlled using voice to activate different layers. The user is shown the safe zone for pin insertion, and can see how insertion in these zones avoids damage to the surrounding anatomy (Figures 2 & 3).

The experience concludes with a holographic animation depicting drill assembly and construction of the external fixation frame onto the prosthetic, and an animation of the fracture reduction being performed. A hologram of the cross-section of the anatomy demonstrates how a correct pin insertion

angle will avoid damage to the surrounding muscles and tissues. The pin angle is controlled by the user's gaze direction (Figure 3).

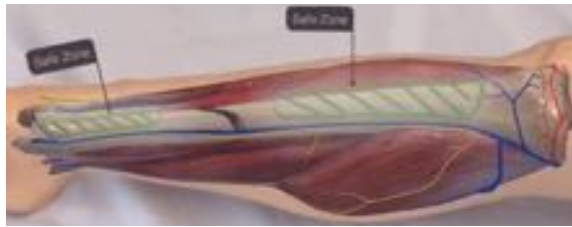


Figure. 2. Hololens viewpoint capture of safe zones and anatomy overlayed onto the prosthetic limb from Figure 1 showing the level of detail we can display in AR.

USER STUDY

Initial feedback was sought from an orthopaedic surgical team at University College London Hospital. Their qualitative preliminary assessment was that this AR experience could improve the quality of education for surgeons for this procedure prior to having live OR experience.

A further study was performed on a group of 8 people who had no prior experience with this procedure. The participants rated each feature on how useful they consider the content for training purposes.

RESULTS

Feature	Mean usefulness 1 (poor) to 5 (good)
C-Arm positioning	3.8
Radiation exposure	4.3
Pin guidance	4.6
Drill/frame assembly	3.9
Fracture reduction anim	4.5

All participants found the experience engaging, and undemanding, without any experience of fatigue or strain on their visual system.

Radiation exposure, pin guidance, and fracture reduction animations received high score, indicating that the experience supported the development of understanding during those aspects of external fixation. Mixed feedback was received for the ergonomics of the Hololens headset, due to weight, size, and comfort of fit, which are known as traditional pinch points for AR headsets.



Figure. 3. Hololens capture of pin and cross-section guide

CONCLUSION AND DISCUSSION

The study shows how an AR surgical training guide can be an engaging format for improving the spatial cognition skills for complex surgical procedures. AR training guides have the potential to be a cheaper and more accessible alternative to traditional methods such as 'see one, do one, teach one' and cadaver labs. The ability to view anatomy in novel ways may improve the educational effectiveness. A more detailed quantitative study will be undertaken to assess a user's understanding after using this AR experience compared to traditional teaching materials.

Future work would be to extend this experience to a live surgical setting using live patient scans. Current limitations are ergonomics and pricing of Hololens devices, which will be mitigated as the technology advances. The experience will also be ported to mobile devices running ARKit or ARCore for wider usability and accessibility.

REFERENCES

- [1] Messier E, Wilcox J, Dawson-Elli A, Diaz G, Linte CA. 2016. "An interactive 3D virtual anatomy puzzle for learning and simulation - Initial demonstration and evaluation." *Stud Health Technol Inform* 220:233–240.
- [2] Kamphuis C, Barsom E, Schijven M, Christoph N. Augmented reality in medical education? *Perspect Med Educ*. 2014;3(4):300–311
- [3] Haubruck P, Nickel F, Ober J, Walker T, Bergdolt C, Friedrich M, Müller-Stich BP, Forchheim F, Fischer C, Schmidmaier G, Tanner MC. "Evaluation of App-Based Serious Gaming as a Training Method in Teaching Chest Tube Insertion to Medical Students: Randomized Controlled Trial" *J Med Internet Res* 2018;20(5):e195
- [4] Barsuk JH, Cohen ER, Mikolajczak A, Seburn S, Slade M, Wayne DB. Simulation-based mastery learning improves central line maintenance skills of ICU nurses. *J Nurs Adm*. 2015;45(10):511–517. 13.
- [5] Huang, Cynthia Y et al. "The Use of Augmented Reality Glasses in Central Line Simulation: 'see One, Simulate Many, Do One Competently, and Teach Everyone.'" *Advances in Medical Education and Practice* 9 (2018): 357–363.

Design, Fabrication and Testing of an Inflatable Variable Stiffness Retractor Prototype for Minimally Invasive Colorectal Surgery

S.A. Agha¹, A. Abidali¹, K. Althoefer¹, M.A. Taha² M.H. Shaheed¹

¹*School of Engineering and Materials Science, Queen Mary University of London*

²*National Bowel Research Centre, Blizard Institute, Barts & the London School of Medicine and Dentistry, Queen Mary University of London*

s.a.gha@qmul.ac.uk

INTRODUCTION

Surgical intervention is a well-established and viable treatment option for an array of colorectal disorders ranging from severe constipation, anal injuries, unnatural cracks and tears as well as colorectal cancer. In contrast to traditional open bowel surgery involving a large incision, minimally invasive surgical procedures require key-hole incisions of 5-12mm each [1]. This results in less pain for patients, faster recovery, reduced risk of post-operative infection and improved cosmesis [2].

Retraction of anatomical structures is an essential part of any surgical procedure; the objective is to provide the surgeon adequate access to the target pathology without causing damage to surrounding structures. The constraints posed by key-hole access necessitates specialised retraction devices such as the polyarticular snake retractor (which consists of small rigid segments), the fan retractor (composed of multiple blades). Retraction with ties and slings, magnetic retractors and gravity assisted retraction are also well documented [3]. Gravity assisted retraction achieved via patient positioning can pose anaesthetic challenges and cardiorespiratory issues. The inflatable atraumatic retractor described by O'Shea et al. [4] was developed to restrain the small intestine and retain retraction gained by patient positioning such that the patient can be returned to the level position for the rest of the surgery. This is effectively a sling type retractor capable of applying only tension.

The retractor prototype developed in this study is a 3:1 scale inflatable, variable stiffness device aimed at facilitating minimally invasive surgery. The apparent stiffness of the retractor is controllable to achieve good tissue-instrument contact properties by maintaining suitable force distribution over the tissue but also retaining sufficient rigidity to support the load presented by the anatomical structure being retracted. The conflicting nature of these requirements necessitates scrutiny of the factors that influence the apparent stiffness of the system. Besides being conformal and adaptive, an inflatable retractor can also be shrunk to enable passage through a surgical cannula [5].

MATERIALS AND METHODS

The inflatable retractor prototype consists of a latex balloon, an enveloping sheath of Icarex ripstop fabric, a pneumatic fitting, nylon strings and a plastic support stem. The latex balloon is attached to the pneumatic

fitting with some liquid latex between them to ensure the connection remains airtight. The inextensible Icarex fabric forms the outer layer of the retractor and fits over the latex balloon to restrict its expansion. A hexagonal recess in the retractor stem houses the pneumatic fitting. The inextensible outer layer is placed over the base piece (stem) and is locked in place using a small cylindrical piece. The retractor stem was 3D printed with PLA plastic at a resolution of 0.04mm, and has small grooves for passage of the nylon strings.



Figure 1. Components of the inflatable retractor prototype

By constraining the expansion of the balloon, the outer layer determines the shape and size of the device. The retractor stem provides the base for the balloon to push against, and the nylon strings are used as tendons to apply a pull on the outer layer, to which they are attached. Similar to the role of antagonistic muscles in biological systems, the tendons are used to achieve controlled bending of the retractor by shortening the retractor length on one side while the tension from the inflated balloon keeps the rest of the retractor body fully extended. Two sets of three tendon strings with equal radial spacing (120° apart) are utilised; one set at the top and second at the middle of the retractor. For a given profile, the stiffness of the device is mainly a function of the applied internal pressure. The tendons can, however, be used to augment the system stiffness. Nylon thread is chosen for the combination of its tensile strength and low friction property.

The two profiles investigated in this study were:

- Cylindrical profile
- Palm-shape profile

Both prototype profiles are shown in figure 1. The diameter of the stem is the critical dimension of the system as it is rigid and needs to be small enough to go through the trocar port. The inflatable portion can be shrunk for insertion and retrieval. The palm-shape profile utilises this property as its distal end is wider than its proximal end connected to the retractor stem. Hence the surface area presented for tissue contact is not restricted

by the size of the trocar port. The cylindrical profile presents a simple geometry which similarly can have a diameter different from the diameter of the stem.

Three sets of tests were carried out on the fabricated prototypes:

- Material limits – pull tests on both the Icarex fabric and the nylon string.
- Tendon operation – to ascertain the effectiveness of the tendons in achieving bending.
- Deflection – to assess the load bearing capacity of each retractor at different inflation pressure and loaded at right angle to its un-deflected axis.

The material limits and deflection tests were performed on an instron tensile testing machine.

The principal stresses experienced by the outer layer in resisting the applied pressure are determined by analysing it as a thin-walled pressure vessel.

RESULTS

For all tendon pull tests performed the nylon string was observed to fail before breakage of the articulation point or the Icarex fabric to which it was attached. The nylon strings (1.08mm wide by 0.06mm thick) failed at a load of 22.11N (SD = 0.595N). Tensile testing of a 48mm wide Icarex specimen showed two linear regions of the load-extension plot and failed at a load of 129.6N, indicating a specific strength of 2.7N/mm.

As expected, the tendon tension required to induce bending of the retractor body increased progressively with increase in internal pressure. It was observed that both tendon sets produced identical bending outcome, that is; bending close to the proximal end of the inflatable end effector (figure 2a).

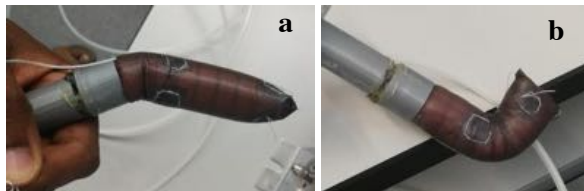


Figure 2. Controlled bending of retractor body. Tendon tension applied: a. after inflation b. before inflation

Figure 2b shows the result of applying tendon tension to the retractor before applying internal pressure to the device. The retractor retains this deflection even after the tendon tension is released indicating high static friction (stiction) resulting from the tendons being pressed between the latex balloon and Icarex material.

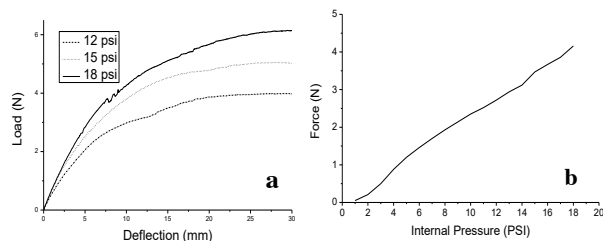


Figure 3. Loading behaviour of the cylindrical retractor. a. load-deflection plot at three pressures. b. variation of load-bearing capacity with pressure for 10mm deflection

The load-deflection behaviour of each prototype showed good repeatability. As expected the stiffness of the retractor increased with increased pressure, the change in load bearing capacity was, however, more pronounced for higher deflections (fig 3a). For the same deflection, the change in stiffness showed a linear correlation with applied internal pressure (fig 3b).

DISCUSSION AND CONCLUSION

By analysing the cylindrical retractor as a thin-walled pressure vessel, the circumferential and longitudinal stress on the outer Icarex fabric layer were found to be 1.40 N/mm and 0.70 N/mm respectively at 18psi. By using the ultimate strength obtained from the Icarex tension test, the present configuration will rupture at a pressure of 34.8psi. The burst pressure of the retractor increases with decreasing diameter hence, higher pressures are possible for a smaller system.

The load-deflection behaviour of the palm-shape retractor prototype was similar to that of the cylindrical device given that most of the bending is attributable to the compression of the device at the proximal end. The palm-shape profile, however, presented greater stiffness in the lateral bending compared with dorsoventral flexure indicating that not all the resistance to bending happens at the most proximal end. Further work is required to predict the bending stiffness from applied pressure and physical dimensions.

For effective flexure control the stiction encountered needs to be limited. It is expected that this will be achieved by isolating the tendons from the latex.

The combination of the device geometry and the ability to control the stiffness of the system is expected to result in improved biomechanical compatibility between tissue and instrument. The next step of this study will include numerical modelling and simulation for performance predictions, automatic control and miniaturisation.

REFERENCES

- [1] M. H. Whiteford, S. W. Lee, M. Mutch, S. Steele, and H. Ross, "Minimally Invasive Approaches to Colon and Rectal Disease," *Springer*, pp. 15–25, 2015.
- [2] M. Pascual, S. Salvans, and M. Pera, "Laparoscopic colorectal surgery: Current status and implementation of the latest technological innovations," *World J. Gastroenterol.*, vol. 22, no. 2, pp. 704–717, 2016.
- [3] N. Ladwa, M. S. Sajid, N. K. Pankhania, P. Sains, and M. K. Baig, "Retraction techniques in laparoscopic colorectal surgery: A literature-based review," *Color. Dis.*, vol. 15, no. 8, pp. 936–943, 2013.
- [4] C. O'Shea *et al.*, "Design, development and evaluation of an inflatable retractor for atraumatic retraction in laparoscopic colectomy," *Ann. Biomed. Eng.*, vol. 42, no. 9, pp. 1942–1951, 2014.
- [5] A. Stilli, H. A. Wurdemann, and K. Althoefer, "Shrinkable, stiffness-controllable soft manipulator based on a bio-inspired antagonistic actuation principle," *IEEE Int. Conf. Intell. Robot. Syst.*, no. Iros, pp. 2476–2481, 2014.

Development of a Soft Inflatable Structure with Variable Stiffness for Hand Rehabilitation

F. Putzu¹, T. Abrar¹, K. Althoefer¹

¹*Centre for Advanced Robotics @ Queen Mary, Queen Mary University of London,
(f.putzu; t.abrar; k.althoefer)@qmul.ac.uk*

INTRODUCTION

Stroke is one of the main causes of death worldwide, more precisely, in the UK, stroke is classified as the fourth cause of death; around 7% (40,000 people per year) of all deaths are caused by stroke [1-2]. Survivors, estimated between 55% and 75%, suffer from a number of disabilities, including those affecting the upper limbs. In order to recover the lost ability or parts of it, a rehabilitation programme is usually recommended. In order to improve their mobility, patients affected by neurological disorders caused by stroke need assisted rehabilitation therapy; indeed, physiotherapists plan a rehabilitation programmes based on intensive daily training of repetitive movements.

In the last decade, a large number of 'roboticists' focused their research on the development of devices that could be used for post-stroke rehabilitation.

Different approaches have been explored, the three main concepts are based on robotic assisted devices, pneumatic devices and Virtual Reality (VR) based devices or a combination of them.

Hadi et al. [3] developed a wearable glove for hand rehabilitation and assistance using shape memory alloys, able to exert more than 40N at the finger's tip. While, Connelly et al. [4] used a different approach creating a pneumatic glove that works with pressurized air up to 10psi, paired with a virtual environment representation (using a VR headset) allowing patients to perform different exercises. Along similar lines, Alamri et al. [5] proposed 5 different VR based exercises that could be performed employing the CyberGrasp System [6] composed of three different hardware pieces: the CyberGlove, which allows to read the spatial hand coordinates and recreates a realistic virtual avatar; the CyberGrasp providing force feedback at the fingers tips of the patient, and the CyberForce armature that simulates inertia in order to give a more realistic experience to the patient.

A simpler solution has been presented by Sebastian et al. [7] where a soft robotic haptic interface with variable stiffness, made of silicon material combined with a Kevlar threading is used; this system is grabbed by the patient and can work in two different modalities (1) isometric and (2) constant pressure.

In our paper, a similar approach to the last presented will be introduced – a low-cost and user-friendly design of a soft inflatable structure with adjustable stiffness has been chosen that can be used in clinical or home settings.



Figure 1 Soft Inflatable Device; Folded state (left), inflated state (right)

MATERIALS AND METHODS

The soft structure presented in this paper utilizes air pressure to extend the fingers of a patient. The air pressure can be varied allowing us to adjust the stiffness as required for an exercise. A combination of fabric and natural rubber (NR) has been employed in order to realize an airtight bladder. The fabrication process is outlined below. The first step was to sketch the outline of desired inflatable structure on the fabric as shown in Fig. 2a. Then two identical fabric parts were cut out. Subsequently, the finger supports (rings) were sewn on to the top part of the structure, the seams have been sealed from the internal part with NR and only after the curing time, the bottom part has been attached employing a sewing machine. Again, the external seam has been sealed using NR from the outside. A small pipe of 2mm (external diameter) has been inserted into the fabric bladder allowing the injection of air.

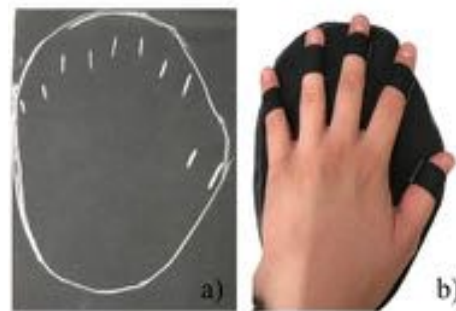


Figure 2 a) Drawing on the fabric, b) Hand attached to device using finger supports

In order to provide pressured air, an air compressor must be employed. The control of the airflow is achieved using a pressure regulator placed between the compressor and the pneumatic device. The pressure regulator can be programmed allowing the patient to perform the rehabilitation in both ways, actively and passively.

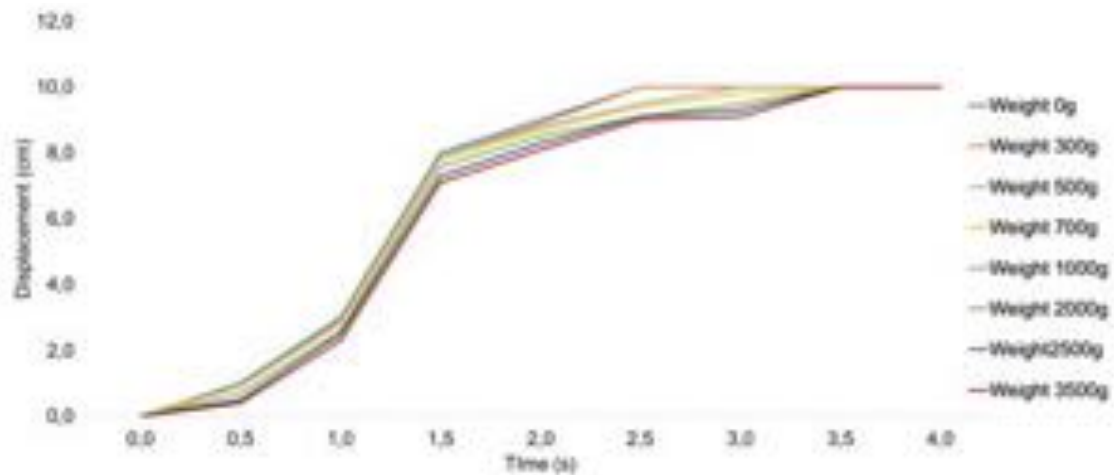


Figure 4 Force exerted over a fixed time (4 sec) and constant pressure (1Bar)

The proposed structure is low-cost and could be used in the comfort of the patient's home, with no need to go every day to the hospital or the desired structure to do the rehabilitation training, a portable compressor is needed.

RESULTS

In order to understand and show the strength of the device experiments have been carried out. The set-up is explained in Fig. 5.

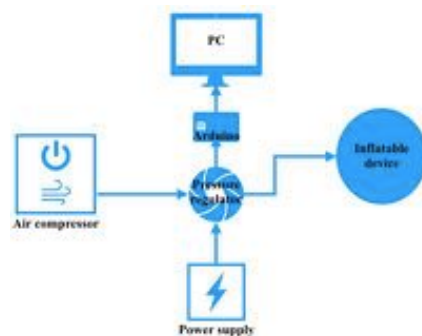


Figure 5 Experiment set-up

The air compressor provides pressurized air at 1Bar, while the pressure regulator connected to an Arduino board, controls the airflow and the pressure inside the device. Different calibration weight has been placed on top the device in order to characterize the exerted force. The maximum force achieved is 34N as shown in Fig. 4, the range of weights used have been successfully lifted by the device, reaching the maximum displacement permitted by the fabric which represents the main physical constrain of the system. Different trials have been carried out in order to understand what is the maximum pressure that the device can hold, it has been noticed that inflating the system with more than 4Bar leads to the bursting of the device.

CONCLUSION AND DISCUSSION

In future it is expected to improve the overall system starting from the wearability, embedding Velcro straps into the finger supports, making it easier to strap on the

device and customized it for different patients, especially for people who suffer from the clenched fist syndrome; in this case it will be possible to wear the system with no need to manually pre-stretch the patient's fingers. At the moment the limitation of the system is that all the fingers achieve the same displacement but a multi-chambers system have been thought to be realized in order to be able to have different level of extension of the fingers.

ACKNOWLEDGMENTS

This work was supported in part by the EPSRC in framework of the NCNR (National Centre for Nuclear Robotics) project (EP/R02572X/1) and WormBot project by Q-Bot.

REFERENCES

- [1] Stroke.org.uk. (2018). Stroke Statistic 2017. Available at: https://www.stroke.org.uk/sites/default/files/state_of_the_nation_2017_final_1.pdf.
- [2] nhs.uk. (2018). Stroke. [online] Available at: <https://www.nhs.uk/conditions/stroke>.
- [3] Hadi, A., Alipour, K., Kazeminasab, S. and Elahinia, M. (2017). ASR glove: A wearable glove for hand assistance and rehabilitation using shape memory alloys. *Journal of Intelligent Material Systems and Structures*, 29(8), pp.1575-1585.
- [4] Atashzar, S., Shahbazi, M., Tavakoli, M. and Patel, R. (2017). A Passivity-Based Approach for Stable Patient-Robot Interaction in Haptics-Enabled Rehabilitation Systems: Modulated Time-Domain Passivity Control. *IEEE Transactions on Control Systems Technology*, 25(3), pp.991-1006.
- [5] Alamri, A., Eid, M., Iglesias, R., Shirmohammadi, S. and El Saddik, A. (2008). Haptic Virtual Rehabilitation Exercises for Poststroke Diagnosis. *IEEE Transactions on Instrumentation and Measurement*, 57(9), pp.1876-1884.
- [6] [Online]. Available: http://www.immersion.com/3d/products/cyber_grasp.php
- [7] Sebastian, F., Fu, Q., Santello, M. and Polygerinos, P. (2017). Soft Robotic Haptic Interface with Variable Stiffness for Rehabilitation of Neurologically Impaired Hand Function. *Frontiers in Robotics and AI*, 4.

Medical Virtual Reality Palpation Training using Ultrasound Based Haptics and Image Processing

Luis Andrés Puértolas Bálint, Kaspar Althoefer

*Centre for Advanced Robotics @ Queen Mary, Queen Mary University of London
(l.a.puertolasbalint@qmul.ac.uk, k.althoefer@qmul.ac.uk)*

ABSTRACT

Palpation is still considered one of the most important techniques used by medical practitioners to diagnose disease in a patient. As part of their training, medical students are taught palpation and must learn how best to interpret the interaction between their hands and the patient's body. Through several studies at different medical schools, it has been shown that virtual reality (VR) can speed up the training process [1]. Most current VR training systems use visual feedback only [2]. It has been recognized that using other feedback modalities can further improve the experience and the training outcome. Recently emerging ultrasound-based haptic devices show promise in this context. In this paper, we propose a new approach that fuses standard visual virtual reality, palpation and an ultrasound haptic-based system providing touch sensation to the user's hands. This is a preliminary study showing promise in augmenting VR with haptics for palpation, providing the user an enhanced interaction with the training material.

INTRODUCTION

There is consensus that palpation is a useful examination technique allowing medical practitioners to diagnose different illnesses in patients, including musculoskeletal, neurological, lymphatic, gastrointestinal and other systems [3]. A trained doctor can easily identify a range of illnesses just by applying pressure to different parts of the body and interpreting the tactile response received during palpation.

Different palpation techniques are applied, including both gentle and firm pressure, circular motions, etc. During palpation, the doctor gets haptic feedback that is related to the behaviour of the examined tissue, organ or body part. The tissue/body behaviour in turn is influenced by its pathological state. Different illnesses modify the body's tissue and organ tactile response in different ways. A medical practitioner with appropriate experience can categorise these through the physical examination and can, firstly, distinguish healthy tissue areas from diseased ones and, secondly, provide a good estimate on the type and extent of disease.

Because of the diagnostic importance of palpation, palpation training is an essential part of the medical student curriculum [4]. Traditionally, students are instructed by experienced doctors on how to conduct the palpation procedure on volunteers. Through observation, the palpation instructor can direct the trainee and improve

the technique and the interpretation of the touch sensations experienced.

Virtual Reality (VR) packages, especially those that use VR goggles, have proven to be very useful in supporting the training of palpation [1]. However, most current systems rely on visual feedback only: this is an extreme shortcoming when learning manual tasks such as palpation which relies so heavily on tactile feedback. This paper proposes a new approach augmenting visual VR with haptics. In our work, we use a haptic ultrasound system to provide the sensation of touch to the user's fingers and hands in a medical environment. We propose that with this haptics addition the user will experience a greater immersion, further accelerating the training progress. In the work described here the user will experience the physical interaction with a patient's body and receive haptic feedback when in contact with the body informed by mechanical tissue behaviour. Programming the extended VR environment, the haptic feedback can provide different responses depending on the patient's simulated illness. Our work is not intended to make the personal training from an experienced practitioner obsolete, but to provide a useful and low-cost training add-on that will accelerate the trainee's learning of essential palpation tasks.

HAPTICS AND VIRTUAL REALITY

In the created simulator, the user sees a virtual patient and their own body, especially their hands. The projection of the user's body is achieved with the help of 3D sensors, Leap Motion and Kinect V2, determining the user's body parts in space and with respect to the location of the virtual body. The user can interact with the environment and can grasp instruments, like a wireless stethoscope (such as the Steethe™ which we rendered here). The training procedure investigated is to palpate the body with one hand and place the stethoscope with the other hand on different body parts.

We aim for a realistic immersion within the virtual environment. When the user sees their own body in VR combined with some sense of touch and interaction, the resulting perception in the human's mind reinforces the feeling of immersion. To further heighten user immersiveness, our VR system is programmed in a way that the user's hands cannot penetrate the patient's body or other objects in the simulated world – this creates the additional illusion of physical interaction in the user [5][6]. We observe that the discrepancy between the free movement of the user's hand and the artificially blocked

movement displayed to the user through the modified visual VR simulation fools the user's mind and makes the interaction with the patient body more believable. Combining this illusion (also referred to as pseudo haptics) with a haptics ultrasound device proves to further help the user to immerse themselves into the scenario and adds to realism of the simulation with clear benefits for the intended training [7].

METHODS AND MATERIALS

The aim of this study was to test the feasibility of the proposed approach. The hypothesis is that combining pseudo haptics in the visual space with haptics through ultrasound will provide the user with increased immersiveness. To test this hypothesis, we created a setup consisting of the following main components: a computer with a fast rendering GPU, and Facebook's Oculus Rift goggles a haptic ultrasound system (Ultrahaptics Touch Development Kit). The computer system can run the visual simulation at an acceptable framerate of 90 FPS which is the maximum rendering speed that the Oculus Rift can handle. With a view on portability to allow installation of palpation training systems in an easy way, the chosen computer was a modified Alienware R3 laptop with the following specifications: Processor: Intel Skylake Core i7-6700HQ CPU, quadcore, 8 thread 2.6 GHz, 3.5 GHz turbo, 16 GB RAM and a dedicated video card, GeForce 970m. The costs of all system components were below £4000.

Several tests were conducted to show the effect of the different components of the system with regards to the feeling of user immersion. Users were instructed to use the system (palpating the body and applying the stethoscope) with and without the haptics as additional feedback modality.



Figure 1: Grabbing the stethoscope (A) Placing the stethoscope on the patient's chest and palpating the patient (B).

CONCLUSIONS

The results from the conducted tests show that a sense of immersion was created by the visual collisions (pseudo haptics) programmed into our virtual environment. Recognising the importance of seeing one's own body parts when interacting with the environment was an important aspect of this study. This feeling of interaction was further emphasised when adding the haptic ultrasound device. Users observed a marked increase in immersiveness. These results are qualitative, but clearly show that a simple and low-cost setup can be used to create a palpation training environment for aspiring doctors. The proposed simulator where the user can see himself or herself, gets a sense of touch through ultrasound-based haptics as well as pseudo haptics has the potential to be used as a medical training tool.

FUTURE WORK

We plan to extend our system by providing feedback on aspects such as heartbeat, blood pressure and breathing. We aim to incorporate this into the ultrasound haptics feedback system, but also to add audio feedback (such as sounds of heartbeat through the stethoscope) to further improve the realism of our training system, reinforcing the representation of different illnesses through associated sounds. We are also planning to integrate tomographic images with the virtual human, whose organs will be distinguished by their relative density. Further, we intend to incorporate soft tissue biophysical properties such as density and deformation [8].

ACKNOWLEDGEMENT

This work was supported by BALTECH Pty Ltd (Ballarat Technologies), CONACYT, Queen Mary University of London.

REFERENCES

- [1] Kale, Somesh. "Medical Learning and Training using VR." *International Journal for Research in Applied Science and Engineering Technology*, 6(6), 2018.
- [2] Coles, Timothy R., Dwight Meglan, and Nigel W. John. "The Role of Haptics in Medical Training Simulators: A Survey of the State of the Art," *IEEE Trans. on Haptics*, 4(1), 2011.
- [3] Geisel School of Medicine - On Doctoring: Year II Resources. [Online]. http://geiselmed.dartmouth.edu/ed_programs/course_resources/ondocoring_yr2/index.shtml
- [4] A Touch of Sense [Online]. http://abrahamverghese.com/images/NarrativeMatters_July2009.pdf
- [5] Li, M., Ridzuan, M.B., Sareh, S., Seneviratne, L.D., Dasgupta, P. and Althoefer, K., "Pseudo-haptics for rigid tool/soft surface interaction feedback in virtual environments." *Mechatronics*, 24(8), 2014.
- [6] Bekrater-Bodmann, Robin, Jens Foell, Martin Diers, Sandra Kamping, Mariela Rance, Pinar Kirsch, Jörg Trojan et al. "The importance of synchrony and temporal order of visual and tactile input for illusory limb ownership experiences—an fMRI study applying virtual reality." *PloS one* 9(1), 2014.
- [7] Sim, F. and Mackie, P., "Sight—the most critical sense for public health?" *Public health*, 129(2), pp.89-90, 2015.
- [8] VertExmotion - Asset Store [Online]. <https://assetstore.unity.com/packages/tools/animation/vertexmotion-23930>

Fetoscopic Scene Orientation Estimation From a Single 2D Image Using Convolutional Neural Networks

A. Ahmad¹, C. Gruijthuisen¹, M. Ourak¹, J. Deprest², T. Vercauteren³, E. Vander Poorten¹

¹*KU Leuven University, Department of Mechanical Engineering, Leuven, Belgium*

²*University Hospital Leuven, Department of Development and Regeneration, Leuven, Belgium*

³*King's College London, Imaging and Biomedical Engineering, London, United Kingdom*
mirzaawais.ahmad@kuleuven.be

INTRODUCTION

Open womb surgery for prenatal therapy is an extreme option which may induce severe side effects on both the fetus and the mother. Minimal invasive surgery (MIS) is in general, less strenuous than open surgery. Unfortunately, the current tools and techniques are not optimized for the unique environment of the womb. Fetoscopy is one of the tools used in prenatal MIS, which allows the physician to have a direct visual assessment of the in-utero environment and the fetus. The primary advantage that fetoscopy offers is the decreased chance of preterm delivery, which is a main cause of fetal loss. Fetoscopy requires only a small incision in the uterine wall, contrary to hysterotomy, decreasing the procedure induced morbidity significantly [1].

This abstract deals with the use of the fetoscopic instruments in photocoagulation therapy using lasers for Twin-to-twin Transfusion Syndrome (TTTS). TTTS has become one of the most common fetoscopic operations today. In this operation, anastomosing vessels on the shared placenta are identified and coagulated using a laser [2]. Figure 1 shows the use of rigid scopes in current techniques, which have a few short comings including: inability for orthogonal orientation of the fetoscope and laser in case of anterior placenta; the need to change scopes over different interventional stages and image instability in the absence of motion compensation when carried out at close proximity to prevent inadvertent ablation or tissue contact and feto-placental hemorrhage [3].

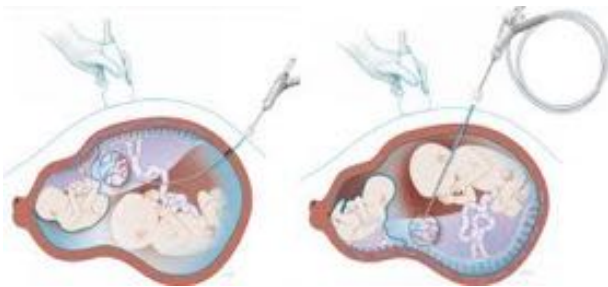


Figure. 1. Semi-rigid curved and straight fetoscopes being used for laser coagulation therapy for TTTS. Courtesy of UZ Leuven.

The aim of this research is to develop sensing and control techniques for a fetoscope with actuated flexible distal tip to help the clinician to control the distance and orientation of the distal tip autonomously. This sensing technique will be used as a feedback to control the autonomous distal tip. Such shared control operation would reduce the mental load on the clinician who only has to focus on navigation. The quality of the ablation could also benefit from improved distance and orientation management.

MATERIALS AND METHODS

In the design of a new medical instrument, size is a crucial criteria. Adding extra sensors to the instrument can take more space hence increasing the diameter of the instrument. It is ideal to use the already existing sensing on the instrument, i.e. the camera, to avoid the need for a new sensing component. This work proposes to use Convolutional Neural Networks (CNN) to estimate the orientation of the placenta with respect to the fetoscope. Figure 2 (left) shows a fetoscopic image of a placenta. The human brain can deduce the relative orientation of the placenta due to the visual cues such as light intensity.

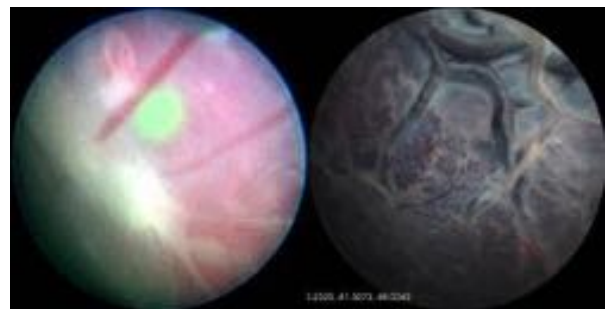


Figure. 2. Fetoscopic image of placenta at an inclination relative to the camera (left), a simulated image of a placenta at an inclination relative to the virtual camera (right) .

We propose that if enough images with ground truth orientation data are generated, a CNN may be trained to predict the orientation when given a single 2D fetoscopic image. Image processing techniques such as PCA can be used to estimate the orientation but are not always reliable on all types of data. This research investigates the performance of CNN combined with image processing techniques. An approach was devised to train and test the proposed CNN on a simulated environment. Figure 2

(right) shows a simulated image of an inclined placenta taken from the virtual camera.

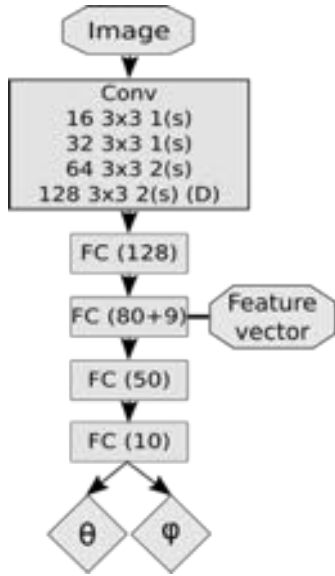


Figure. 3. A diagram of the proposed CNN, Conv block is 4 convolutional layers, here number preceding (s) is stride and (D) represent dropout layer. NxN is the size of kernel and the number preceding the kernel size is the number of filters. FC is fully connected layer.

The simulated dataset is well-distributed and can be created in huge numbers with no human cost. The virtual image can easily be changed with any placenta image in order to diversify the scale the dataset.

Figure 3 shows the proposed CNN model which is inspired from the work presented by Olmschenk *et. al* [4]. An image is given as input to the network and two angles are received as outputs. It can also be seen in Figure 3 a feature vector is connected to the second fully connected layer. This feature vector improves the network's learning by providing extra features from the image. Each image is converted to binary at a threshold value, and the PCA is calculated of the white pixel cloud. This feature vector contains the eigenvalues, eigenvectors, center and the volume of the white pixel mass.

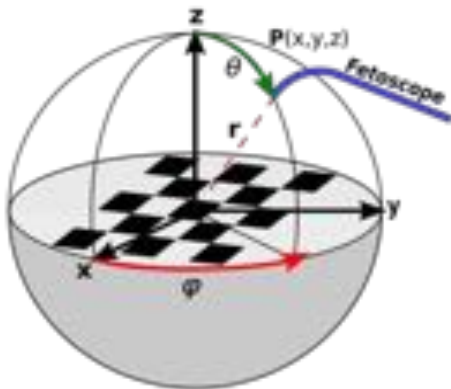


Figure. 4. Orientation information of the image plane with respect to the fetoscope in spherical coordinates.

Figure 4 shows how the orientation of the image plane with respect to the camera is defined in a spherical coordinate system. The three unique spherical coordinates (r, θ, Φ) can be found using simple trigonometry. For the back propagation in training the network, a loss function needs to be formulated that would accommodate the jumps in angular outputs. A prediction that might be close to ground truth may cause high loss because of the cyclic nature of angles. Therefore, the distance in spherical coordinates between the target (ground truth) point and the predicted point is used as a loss function.

$$loss = \|P_{target} - P_{pred}\|$$

RESULTS

The network was trained over 27000 images with 200x200 pixels. The results in Table 1. represent the loss of testing, calculated as RMS loss function, after running 20 training epochs. It can be seen that the network was able to predict the value of θ without the introduction of the feature vector. Meanwhile the network improved to predict the value of Φ with feature vector.

Output	Average Test Error - RMSLoss (Radians)	
	Without Feature Vector	With Feature Vector
θ	0.14	0.14
Φ	0.32	0.26

Table. 1. Average test loss of the CNN after 5 training epochs.

CONCLUSION AND DISCUSSION

It is clear from the results that the network was able to perform well for one of the angles, predicting it within an acceptable range of 0.17 radians. However, a significant improvement is needed for the second angle. The network might face troubles converging because of the duplication of inputs vs outputs. Therefore, extra features are needed to make the relationship between inputs and outputs unique. This argument seems already supported by the effect of introducing the feature vector.

REFERENCES

1. Yang, Edmund Y., and N. Scott Adzick. "Fetoscopy." *Seminars in laparoscopic surgery*. Vol. 5, No. 1. Sage CA: Thousand Oaks, CA: Sage Publications, 1998.
2. Senat, Marie-Victoire, et al. "Endoscopic laser surgery versus serial amnioreduction for severe twin-to-twin transfusion syndrome." *New England Journal of Medicine* 351.2 (2004): 136-144.
3. Huber, A., et al. "Laser coagulation of placental anastomoses with a 30° fetoscope in severe mid-trimester twin-twin transfusion syndrome with anterior placenta." *Ultrasound in Obstetrics and Gynecology: The Official Journal of the International Society of Ultrasound in Obstetrics and Gynecology* 31.4 (2008): 412-416.
4. Olmschenk, Greg, Hao Tang, and Zhigang Zhu. "Pitch and Roll Camera Orientation from a Single 2D Image Using Convolutional Neural Networks." *Computer and Robot Vision (CRV), 2017 14th Conference on*. IEEE, 2017.

Fuzzy Logic Control of a Tele-Robotic Manipulator Assistant for Laparoscopic Surgery

Ololade O. Obadina¹, Mohamed A. Thaha², Kaspar Althoefer¹, M. Hasan Shaheed¹

¹*School of Engineering and Materials Science, Queen Mary University of London, UK.*

²*Blizard Institute, Barts and The London School of Medicine & Dentistry, Queen Mary University of London, UK.*

o.o.obadina@qmul.ac.uk

INTRODUCTION

Current surgical robots utilize the master-slave (MS) technology to operate using small-scale interventions that require highly precise and reliable control systems, in order to perform accurate surgical tasks [1]. While conventional linear control systems like PID control are easy to implement and operate in a wide range of conditions [2], their performance deteriorates when applied to nonlinear robot systems. Without adequate control in these surgical MS robot systems, the presence of a large tracking error and time delay between the surgeon's master console and the patient side slave console can become catastrophic and possibly lead to complications. Thus, there is a demand for nonlinear control systems that is precise, capable of minimizing tracking error and reducing time delay, as well as reducing the effect of disturbances (such as tremor and shaking of the surgeon's hands) in laparoscopic surgical robot systems.

Several non-linear control methods exist [3], [4], however, majority of these techniques require an accurate knowledge of the robot system to be modeled, which in most cases is impractical. Fuzzy logic control (FLC), however, is robust for non-linear systems [5] and does not require accurate knowledge of the robot manipulator's parameters. These FLC systems are designed to mimic the intuitive decision making process of humans, and these systems decisions are based on a knowledge base that comprises of fuzzy IF-THEN rules [6]. While FLCs have many advantages, the issue of deciding what parameters to use for FLCs is rather cumbersome and often requires an expert's input. To solve this problem, intelligent optimization algorithms such as Particle Swarm Optimization [5] and Bees Algorithm [7] have been proposed to tune fuzzy logic controllers for robot trajectory control. To the best of the authors' knowledge, very little investigation has been reported in the tuning of FLCs parameters using the swarm based Whale Optimization Algorithm (WOA) [8] for application on a master-slave robot manipulator system.

This paper, thus, presents a simulation study of a simplified fuzzy logic control approach that uses Gaussian membership functions for a high precision tracking control of a potential MS surgical robot assistant system. The performance of the proposed FLC

is further improved by tuning the input and output scaling factors of the FLC using the Whale Optimisation Algorithm (WOA).

MATERIALS AND METHODS

The MS robot assistant manipulator used in this study was developed at Queen Mary University of London (See Figure.1). The system consists of a master and slave manipulator consoles and a robot control system. The modeled system has four degrees-of-freedom (4-DOF) namely Joints 0, 1, 2 and 3, which signify the base, shoulder, elbow and wrist joints respectively, and a gripper for grasping a laparoscopic tool or camera. As control is implemented in joint space, each joint will be independently controlled. The dynamics of the slave robot manipulator is first derived using the Euler-Lagrange technique [9], and is described mathematically as:

$$\tau = D(\theta)\ddot{\theta} + C(\theta, \dot{\theta}) + G(\theta) \quad (1)$$

where: $D(\theta)$, $C(\theta, \dot{\theta})$, $G(\theta)$, θ and τ represent the inertia matrix, Coriolis and centrifugal terms, gravity terms, the robot's joint angles and the control driving torque, respectively.

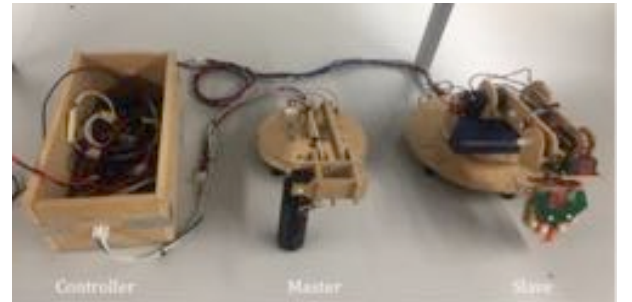


Figure. 1 The 4-DOF Master-Slave Robot Manipulator System

The designed Mamdani-type fuzzy controller comprises of three inputs and one output. These inputs are: error (e), change in error (ce) and integral error (ie), while the output is referred to as the control voltage (U). The overall output of the FLC is a function of three inputs, and is described mathematically as:

$$U(t) = K_u * \left[f \left(K_p e(t), K_d \frac{de(t)}{dt} \right) + K_i \int e(t) dt \right] \quad (2)$$

where: $e(t)$ is the tracking error; K_p , K_i , K_d and K_u are the proportional, integral, derivative and output scaling

factors respectively. The universe of discourse of all inputs and output are normalised within the range $[-1,1]$. The fuzzification of inputs and defuzzification of the output are characterised by Gaussian MFs. As the number of MFs for the inputs and output increases, the computation time of FLCs also increases. So, to reduce computation time, the proposed FLC design is simplified by using a total of 9 MFs namely $\{Ne, Ze, Pe\}$ for the error input, $\{Nce, Zce, Pce\}$ for the change in error input, and $\{Nu, Zu, Pu\}$ for the control voltage output. Due to page limitations, only the MFs of the control voltage output are shown in Figure. 2. The fuzzy control rules governing the fuzzy inference system are presented in Table 1.

Table. 1: Fuzzy Logic Control Rules

	Ne	Ze	Pe
Nce	Nu	Nu	Zu
Zce	Nu	Zu	Pu
Pce	Zu	Pu	Pu

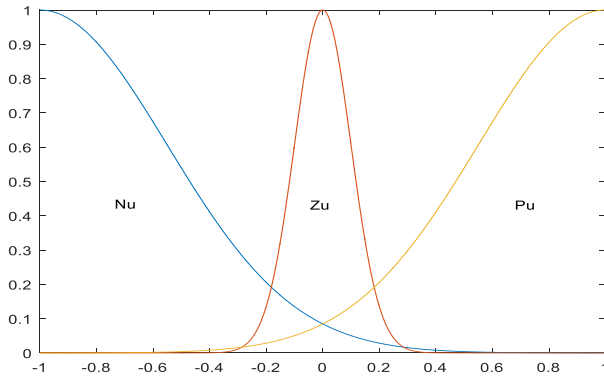


Figure. 2. Membership functions of output voltage

RESULTS AND DISCUSSION

The modeling of the robot manipulator system, and the design and testing of the developed FLC were implemented offline in the MATLAB/Simulink environment.

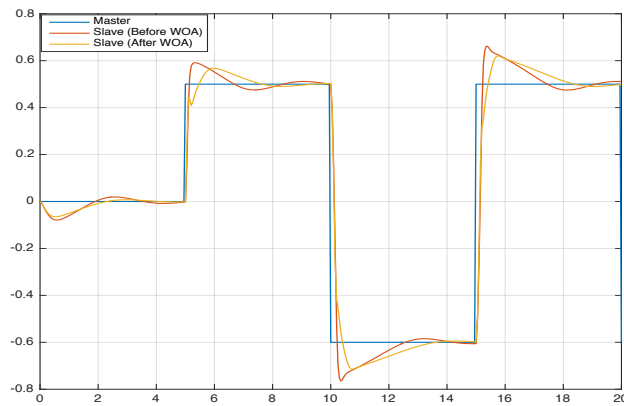


Figure. 3. Output Response of Joint 1 (Shoulder Joint)

The tracking performance of the shoulder joint before and after optimisation is shown in Figure. 3. The slave manipulator is seen to have a relatively smooth response

as it accurately tracks the trajectory commands of the master manipulator. The response after optimisation shows a small improvement in the reduction of the overshoot. Quantitatively speaking, there is a 6% improvement in terms of mean square error (MSE). The MSE of the output response before optimisation is 0.0213 while the MSE after using whale optimisation algorithm is 0.02.

CONCLUSION & FUTURE WORK

This paper presents a simplified fuzzy logic control approach for a potential MS surgical robot assistant system. Simulation results from the shoulder joint show that the approach is feasible with a good tracking performance. Also, using WOA to tune the FLC's scaling factors shows a 6% improvement in terms of MSE. Future work will include practical implementation of this approach, and tuning the MFs of the presented FLC with other optimization algorithms.

REFERENCES

- [1] S. J. Song, Y. M. Choi, D. H. Lee, C. B. A. JoJaesoon, and Youngho, 'Comparative Study of Fuzzy PID Control Algorithms for Enhanced Position Control in Laparoscopic Surgery Robot', *J. Med. Biol. Eng.*, vol. 35, no. 1, pp. 34–44, 2015.
- [2] S. J. Song, J. W. Park, J. W. Shin, D. H. Lee, J. Choi, and K. Sun, 'A Comparative Study of Fuzzy PID Control Algorithm for Position Control Performance Enhancement in a Real-time OS Based Laparoscopic Surgery Robot BT - 13th International Conference on Biomedical Engineering, ICBME 2008, December 3, 2008 - December 6, 20', vol. 23, pp. 1090–1093, 2009.
- [3] Z. Song, J. Yi, D. Zhao, and X. Li, 'A computed torque controller for uncertain robotic manipulator systems: Fuzzy approach', *Fuzzy Sets Syst.*, vol. 154, no. 2, pp. 208–226, 2005.
- [4] K. D. Young, V. I. Utkin, and U. Ozgiiner, 'A Control Engineer's Guide to Sliding Mode Control', *IEEE Trans. Control Syst. Technol.*, vol. 7, no. 3, pp. 328–342, 1999.
- [5] Z. Bingül and O. Karahan, 'A Fuzzy Logic Controller tuned with PSO for 2 DOF robot trajectory control', *Expert Syst. Appl.*, vol. 38, no. 1, pp. 1017–1031, 2011.
- [6] T. Dao and C. Chen, 'Tuning Fuzzy-Logic Controllers', in *Fuzzy Logic - Controls, Concepts, Theories and Applications*, E. Dadios, Ed. InTech, 2012, p. 428.
- [7] D. T. Pham, A. H. Darwish, E. E. Eldukhri, and S. Otri, 'Using the Bees Algorithm to tune a fuzzy logic controller for a robot gymnast', *2007 Innov. Prod. Mach. Syst.*, 2007.
- [8] S. Mirjalili and A. Lewis, 'The Whale Optimization Algorithm', *Adv. Eng. Softw.*, 2016.
- [9] J. J. Craig, *Introduction to Robotics: Mechanics and Control 3rd*, vol. 1, no. 3. 2004.